MODELLING MUCO-CILIARY TRANSPORT IN THE LUNG

by

DAVID JOHN SMITH

A thesis submitted to
The University of Birmingham
for the degree of
DOCTOR OF PHILOSOPHY

School of Mathematics

University of Birmingham

December 2005

ABSTRACT

This thesis is concerned with modelling the liquid lining of the airways, which is transported towards the pharynx by beating cilia. It is not understood whether the ciliated epithelium normally absorbs water. Surface area decreases moving up the bronchial tree but the depth of the periciliary liquid (PCL) remains constant, hence if there is significant flux of PCL up the bronchi, there must be absorption by the epithelium. Theoretical analyses of cilia have previously concluded that flux of PCL is small, however experiments appear to show significant transport of PCL. In chapter 1 we review the biology of the muco-ciliary system, previous modelling and the conflict between theory and experiment. In chapter 2 we present a 'traction layer' model of the fluid flow, assuming no absorption by the epithelium, which provides insight into the mechanisms by which efficient mucus transport does or does not occur. Pressure gradients caused by surface and interface tension are crucial to maintaining efficient transport. From justified parameter values we predict mucus transport rates of $40\ \mu\mathrm{m/s}$, close to that observed in cultures, and very small mean PCL transport. In chapter 3 we discuss the problem of modelling the cilia as discrete objects. We consider the PCL as a fluid bounded by two parallel plates, the epithelium and the mucus interface. We extend models of cilia in a confined domain using a Stokeslet and dipole distribution in the near-field and an averaged Stokeslet distribution in the far-field, so that a numerical solution can be found efficiently. We calculate solutions that are accurate in both the near and far-fields. There is significant positive transport of PCL during the recovery stroke, indicating how the traction layer model may be improved. In chapter 4 we model tracer dispersion experiments with a two dimensional advection-diffusion model which is solved numerically. Steady and oscillatory profiles from chapter 2, together with other suggested profiles are used for the advective flux. It is found that a plane Couette flow in the PCL is sufficient to reproduce experimental results, and that the profiles of chapter 2 produce results remarkably close to experiment, however further work is needed to clarify the problem fully.

ACKNOWLEDGEMENTS

I would like to thank my supervisors Prof. J. R. Blake and Dr. E. A. Gaffney for their continued guidance and encouragement and for patiently reading many drafts and revisions of papers and this thesis. In particular I would like to thank them for their mathematical and scientific background knowledge, their help with programming, mathematical precision and presentation, and their emphasis on physical and biological insight.

I also gratefully acknowledge the EPSRC for financial support.

This thesis was typeset using LaTeX 2_ε and various packages, in particular the chapter headings were produced with a modified version of fncychap.sty by U. Lindgren, the skeleton file was written by Dr. C. Watson.

I would like to thank those whose comments and questions, particularly in seminars at the University of Birmingham, have helped me in improving and developing this work. I would also like to thank faculty, staff and students in the Department of Applied Mathematics and the Cystic Fibrosis Pulmonary Treatment and Research Centre, UNC Chapel Hill and other members of the interdisciplinary group for their insight, and I would like to thank Profs. R. C. Boucher and C. W. Davis for arranging a fascinating visit, and allowing me to see the hTBE cultures.

I would like to thank my girlfriend Lylah Haynes for assistance with typesetting, but more importantly for her support and for making the last three and a half years so much more fulfilling.

Finally, I would like to thank my family for their encouragement throughout my life.

CONTENTS

LIST OF FIGURES

LIST OF TABLES

CHAPTER 1

INTRODUCTION

1.1 Mucus, cilia and the ciliated epithelium

The airways of the lung are protected from inhaled dust, bacteria and other harmful substances by an extremely thin surface layer of liquid ($\sim$ 5–20 μm), as shown in Figure 1.1. This liquid consists of a watery serous fluid, or 'periciliary liquid' (PCL) which is directly in contact with the epithelium, and overlying highly viscous and non-Newtonian mucus. The mucous layer is mainly comprised of water and glycosylated mucin proteins, secreted by specialised cells. In order to remove harmful material, the mucous layer is transported along the airways and out of the lungs by the action of a dense mat of microscopic cilia, whereupon it is swallowed or expectorated. Each mature ciliated cell may have up to 200 cilia, at a density of 6–8 $\mu\mathrm{m}^{-2}$ (Sleigh et al., 1988). Figure 1.2 shows a very simplified diagram of the ciliated epithelium, showing the main cell types: ciliated and goblet cells. The goblet cells do not protrude significantly from the epithelium and occur in proportion 1:5 with ciliated cells (Sleigh et al., 1988).

Failure of the muco-ciliary clearance system results in harmful complications such as those suffered by cystic fibrosis (CF), asthma and chronic obstructive pulmonary disease (COPD) patients. In order for such illnesses to be treated successfully, it is important that the fluid dynamics of the airway surface liquid (ASL) be well understood. However, there is still con-

troversy over some very basic aspects of muco-ciliary transport. In particular it is unknown whether there is significant transport of PCL along the airways and consequent absorption of PCL by the epithelium. The velocity profiles predicted by most theoretical analyses are significantly different from those which experimentalists have recently claimed to have observed (Matsui et al., 1998b). This may be due to the basic difficulty in modelling a very large array of bodies beating in a fluid, the non-Newtonian nature of the mucus, the problems of studying *in vivo* ciliated epithelium, the presence of osmotic effects and the complex interaction between the cilia and the mucus–PCL interface. It is especially difficult to obtain data on the PCL since the layer is so thin ($\sim 5\,\mu\mathrm{m}$). It is also possible that the interpretation of the experimental results needs to be reappraised. In this chapter we review existing knowledge of the biology of cilia, mucus and the muco-ciliary system, relevant mathematical modelling, and finally the recent experimental work of Matsui et al. (1998b), which conflicts with most theoretical analyses of fluid transport in the lung. We then briefly discuss ways in which experimental and theoretical work may be reconciled, and summarise the structure of this thesis.

Propulsive cilia were observed as early as 1675 on micro-organisms by the Dutch microscopist van Leeuwenhoek. They were first discovered in higher organisms in the 1830s by Purkinje and Valentine in the oviduct walls of vertebrates, and airway cilia were studied soon after by Sharpey (Rivera, 1962). They can be observed throughout most of the animal kingdom in, amongst others, the digestive, excretory, respiratory and reproductive systems.

Cilia are known to have a similar external and internal structure to eukaryotic flagella and spermatozoan tails (Sleigh et al., 1988, see, for example). Both are beating appendages with a '9+2' internal structure of constant length fibrils. The '9' refers to nine outer 'double fibrils' which, given a supply of ATP, will slide relative to each other, bending the cilium. The '2' refers to two central microtubules which are linked to the other fibrils by lateral projections. There also exist rotating 'primary cilia' with a '9+0' internal structure which may be responsible for symmetry-breaking flows in embryo development (Nonaka et al., 2002). The term 'cilium' as

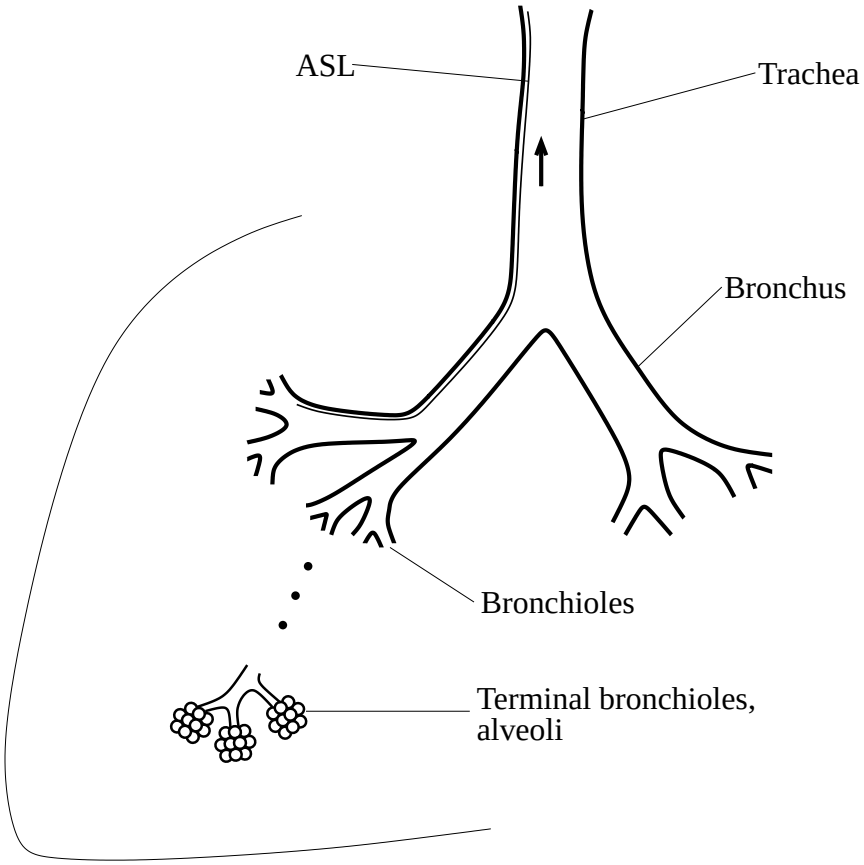

Figure 1.1: Schematic diagram of the lungs—not to scale.

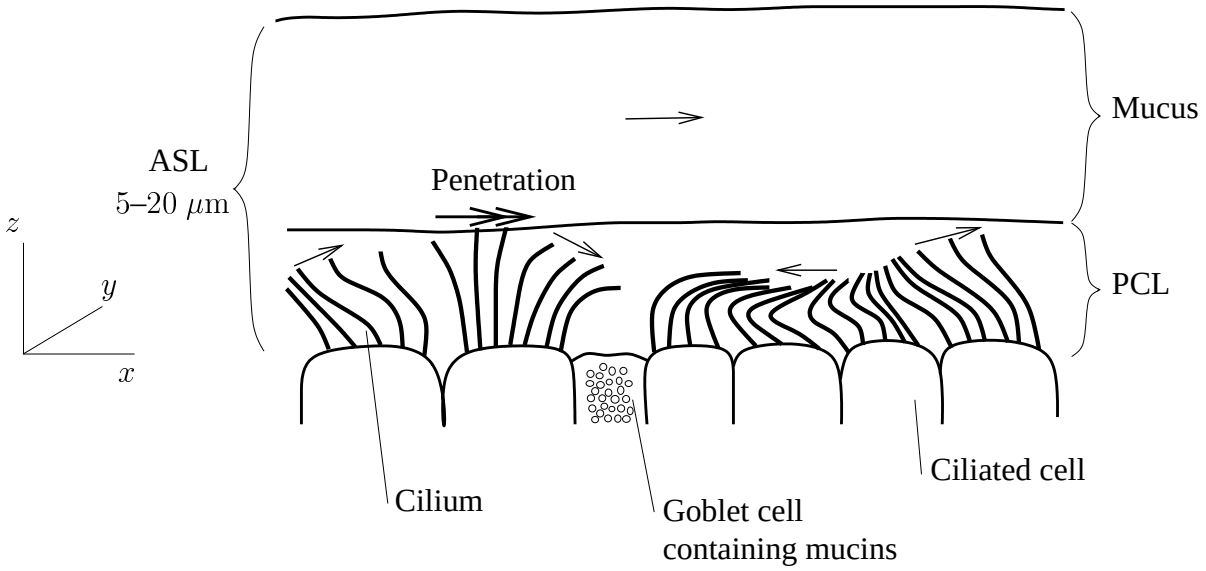

Figure 1.2: Illustration of the bronchial epithelium, showing the ASL consisting of the lower PCL containing a dense mat of cilia, and the upper mucous layer. Two of the main cell types, are shown—ciliated and mucus-secreting goblet cells. Penetration of the mucous layer by the cilia during the forward part of the beat cycle causes a mean forward flow of mucus. The coordinate system used in this thesis is shown on the left—the x direction is the direction of mucus transport, the y direction is in the direction of the metachronal wavefront (into the paper) and the z direction is normal to the epithelium. The actual gaps between cells on the epithelial surface are not as large as shown in this illustration, as can be seen in the micrographs of Sanderson and Sleigh (1981).

opposed to ‘flagellum’, is generally used for organelles moving fluid perpendicular to their axes, usually being arranged in dense arrays. It seems likely that cilia evolved from flagella because of the hydrodynamic advantages of having many cilia beating in coordination (Sleigh, 1962; Gueron and Levit-Gurevich, 1999).

The ciliary beat is considered to have two phases - an ‘effective stroke’ during which the cilium is relatively straight, and rotates forwards, propelling fluid in the direction of propulsion, and a ‘recovery stroke’ in which the cilium bends close to the epithelium and returns more slowly to its initial position. In ciliated micro-organisms, each cilium beats slightly out of phase with its neighbours, in such a way that a ‘metachronal wavefront’ propagates along the ciliated surface. In the lungs the metachronal wave is less well-defined and extends over shorter distances than in water propelling organisms—this seems to be because the cilia are ‘clawing along’ a semi-solid layer of mucus, rather than smoothly propelling lower viscosity water (Sanderson and Sleigh, 1981). In the lungs, the metachronal wave travels in the opposite direction to the effective stroke. This is known as an ‘antiplectic wave’. This has important implications for the type of models that may be appropriate (Blake, 1972). It is still not understood how metachronism is initiated, and whether ciliary beating is subject to signalling mechanisms. Gueron and Liron (1992, 1993) have shown that metachronism can occur spontaneously as a result of hydrodynamic coupling. However, the fact that clearance of fluid is greatly reduced in the absence of mucus has led to the suggestion that muco-ciliary clearance cannot occur without signalling between secretory and ciliated cells (Boucher, 1994). This signalling could be due to calcium waves, paracrine messengers or a combination of the two (Salathe et al., 1997).

The ciliary beat frequency has been measured at between 6 and 15 Hz in humans, the wide range likely being due to experimental artifacts, to the presence or absence of mucus, and possibly because beat frequency may be regulated by the autonomic nervous system, although this has not been demonstrated in animals other than the frog (Salathe et al., 1997). Beat frequency may also be reduced by bacterial infection (Salathe et al., 1997), certain drugs or by recent

exposure to tobacco smoke (Rivera, 1962).

Mucus is a non-Newtonian fluid—it does not display a simple linear relationship between stress and rate of strain, the consequence being that the normal linear Stokes flow equations used to model very low Reynolds number flow do not apply. Many studies have been made of the rheological properties of mucus, and a brief review is given in §2.4.2. Extracting, storing and testing mucus samples in a way which preserves the *in vivo* conditions and provides accurate information is a considerable task. From the perspective of modelling transport rates, some important properties are viscoelasticity—a time dependent response to stress, shear-thinning (pseudoplasticity)—dependence of viscosity on shear rate, and spinnability—the ability of a sample to be drawn out into a long thread. In §2.4.2 we find that the effective viscosity of mucus under oscillations characteristic of the muco-ciliary system is around 50 times that of water.

Although most modelling work, detailed in §1.3, has treated mucus as a very viscous Newtonian fluid, Liron and Rozenson (1983) argued that consideration of the mucous layer as a non-Newtonian fluid was vital to understanding its transport. They cited experimentally based evidence such as that published by Meyer and Silberberg (1980) who, by investigating transport on the mucus-depleted frog palate, found that by varying the dynamic storage modulus of mucus added to the palate they achieved different levels of transport. They argued that '...a system which functions as mucus must possess a significant number of relaxation mechanisms ... at least 10 times larger than the period of the ciliary beat...' They also cited the fact that the gel-like nature of the mucus was essential for transport. According to Ziegler and Foegeding (1990) a 'gel' is '...a continuous network of macroscopic dimensions immersed in a liquid medium exhibiting no steady-state flow'. King (1980) found that restoration of transport is achieved not only by mucus, but also by a guaran gel. He found that below the 'gel point', no transport occurred, but as the consistency was increased to just above this point, almost full transport was restored. Silberberg (1983) gave a mathematical argument that, due to the timescale of tip

penetration, the behaviour of the mucus on this scale was effectively elastic, suggesting that a realistic tip-penetration model cannot simply model mucus as a Newtonian fluid.

Certain issues regarding the muco-ciliary system have been difficult to resolve. The question of whether the tip of the cilium must penetrate the mucous layer in order to ensure efficient transport has long been in doubt. Theoretical analysis by Fulford and Blake (1986) suggested that penetration was not necessary except in case of high ciliary inactivity. Winet et al. (1984) performed experiments on frog epithelial cultures using fluorescent polystyrene spheres to measure the flow profiles in a liquid culture above the mucus surface, and also with the mucus replaced by an RPMI^{+} control medium. They concluded that cilia penetration was not necessary for positive transport, unless there were mucus 'flakes' in contact with ciliostatic patches. However, micrograph studies by Sanderson and Sleigh (1981) and Puchelle et al. (1987) provide evidence that penetration of the mucous layer usually does occur. Kerem et al. (1999) have suggested that the mucous layer acts as a 'reservoir', absorbing excess liquid from the PCL to ensure that the mucous layer does not 'float off' the cilia tips. In the study presented in chapter 2, we model the propulsive interaction of the cilia with the mucous layer by 'penetration', and produce results that show striking parallels with this experimental study.

It has also been suggested that the classical two-fluid model shown in Figure 1.2 may be incorrect. In certain species, a thin surfactant lipid layer has been observed between the PCL and the mucous layer (Yoneda, 1976). It may therefore be important to take into account interfacial effects when modelling flow in the ASL. It has also been suggested that the distinction between the mucous layer and the PCL may not be that clear, and that mucins form an entangled gel throughout the ASL, with high concentration in the 'mucous layer' and lower concentration in the 'serous layer', the dilution resulting from epithelial ion and water transport (Boucher, 1994).

The problem that first motivated this study is that of whether there are significant osmotic flows through the epithelium. Boucher (1994) suggested that flow of water through the epithelium due to osmosis may be present, in order to maintain isotonic conditions in the ASL, as

explained in §1.4. Osmotic pressure gradients have not been a feature of any of the mechanical models of ciliary transport, and may make a significant contribution to the flow in the PCL (Blake and Gaffney, 2001). As explained in §1.4, Boucher's team have demonstrated (Matsui et al., 2000) that the osmotic permeability of human airway epithelia is relatively high, consistent with an isotonic ASL, and in (Matsui et al., 1998b) found evidence of high axial transport of PCL, which is strongly suggestive of significant liquid absorption by the epithelium. In this thesis we develop a models in which osmotic flows are neglected, in order to test whether such a system could produce tracer transport results consistent with the experiments of Matsui et al. (1998b).

1.2 Physical parameters of the muco-ciliary system

Below we very briefly review some experimental findings regarding physical parameters of the mucus and cilia, that will be used in our modelling studies. International Commission on Radiological Protection and Measurements (1994) quote mean values of $5\ \mu\mathrm{m}$ and $6\ \mu\mathrm{m}$ for the thickness of the mucous and PCL in the bronchus respectively. Puchelle et al. (1998) estimated that the depth of penetration of the cilium into the mucous layer was $0.5\ \mu\mathrm{m}$. Toskala (1994), summarising existing research reported a cilium diameter of $0.2\ \mu\mathrm{m}$, corresponding to a radius of $0.1\ \mu\mathrm{m}$, and a cilium length of 5–7 $\mu\mathrm{m}$. Sleigh et al. (1988) quoted 5–6 $\mu\mathrm{m}$ for cilium length and 6–8 $\mu\mathrm{m}^{-2}$ for cilium density; this corresponds to a cilium spacing of 0.35–$0.41\ \mu\mathrm{m}$. As discussed above, cilia beat frequency may vary from 6–$15\ \mathrm{Hz}$.

Based on the above data, and on typical values previously used in theoretical studies (Fulford and Blake, 1986; Liron, 1978), Table 1.1 lists values of typical parameters that will be used in this thesis. Since the precise values are likely to vary between individual cilia, between different parts of the lung, between species, between individuals and over time, it is not possible to be exact, and indeed we have chosen certain parameters for analytic simplicity, for instance $5.4 = 6 \times 0.9$, so that the penetration depth is $0.1\times$ the cilium length. In chapter 2 we investigate

L	cilium length	$6\ \mu\mathrm{m}$
h	thickness of PCL	$5.4\ \mu\mathrm{m}$
H	thickness of ASL	$10\ \mu\mathrm{m}$
$H-h$	thickness of mucous layer	$4.6\ \mu\mathrm{m}$
$L-h$	depth of cilium penetration	$0.6\ \mu\mathrm{m}$
σ	cilia beat frequency	$10\ \mathrm{Hz}$
r_0	cilium radius	$0.1\ \mu\mathrm{m}$
d	cilium spacing	$0.3\ \mu\mathrm{m}$

Table 1.1: Characteristic length and timescales for the muco-ciliary system. Further physical parameters such as viscoelasticity and surface tension are given and discussed in depth in chapter 2.

the effect of varying certain parameters in order to model the effect of disease or drugs, in particular through the mucous layer thickness and the cilia beat frequency.

1.3 Previous theoretical models of ciliary transport

The earliest attempt to model muco-ciliary flow mathematically was that of Barton and Raynor (1967), modelling the cilium as a rigid rod which automatically shortens during the recovery stroke. The force exerted by each rod as it oscillated was calculated by considering each rod to be composed of infinitesimally short cylindical sections, perpendicular to the epithelium. The force could then be found using Oseen's linearised equation of motion, which led to an analytical solution for the mean transport and mean shear stress. This approach had several limitations, in particular, the motion of the cilia was not accurately modelled and the metachronal wave was not included (Blake, 1973b). They also assumed that the effective and recovery strokes were of equal duration, something that has been shown to be untrue experimentally, however correcting this would not be difficult. They assumed that viscosity varied linearly from the epithelium to the top of the mucous layer, and that the mucous layer could be modelled as a viscous Newtonian fluid, two assumptions they recognised might not be valid. However, their work was a forerunner of later 'cilia sublayer' models, and they calculated realistic flow rates of around $110\ \mu\mathrm{m/s}$, based on a beat frequency of $100\ \mathrm{rad/s}$. Their characterisation of the cilium as a

rigid rod is exploited in §2.3.

An alternative approach was pursued independently by Ross (1971) and Blake (1971), the latter modelling fluid transport by water-propelling organisms. The cilia tips were modelled as an impermeable 'wavy wall'. These 'envelope models' were extensions of work by Taylor (1951) on the swimming of micro-organisms with propulsive tails, such as spermatozoa, and work by Lighthill (1952) on the motion of squirming near-spherical organisms. The envelope was modelled as a flexible sheet along which propagated sinusoidal waves. The study of Ross (1971) took into account the non-Newtonian nature of the upper mucous layer. He modelled the mucus as a nonlinear Maxwell fluid, and solved the resulting system of equations analytically using Fourier series and asymptotic expansions, assuming that the amplitude of the metachronal wave in the sheet was small compared with the mucus depth. He calculated mucus flow rates which were of the correct order of magnitude ($25\ \mu\mathrm{m/s}$), but because of the design of his model, could not touch on issues such as tip penetration or flow in the PCL. It also seems clear that the envelope model is not suitable for lung cilia: it has been noted (Blake, 1972) that at velocities found in nature, the envelope model is not adequate for systems exhibiting antiplectic metachronism, since the tips of the cilia may be widely-spaced during the effective stroke. In implementing the model it is necessary to enforce a no-slip condition on the envelope, which does not agree with experimental observations (Blake and Sleigh, 1974).

The 'cilia sublayer' approach was developed by Blake (1972), initially for ciliated micro-organisms, especially to model systems where the no-slip condition on the envelope is violated. The epithelium was taken to be a flat, doubly-infinite plane, and the metachronal wavefront to be a straight line in the y direction, moving in the negative x direction. Exploiting slenderness, the cilia were modelled by distributions of point force singularities or 'Stokeslets' along their centre-lines. Given the force distribution along a cilium, the flow field could be found by integrating the force with the appropriate Green's function G_{jk} over the length of the cilium and

summing over all of the cilia:

$$u_j = \sum_{m=-\infty}^{\infty} \sum_{n=-\infty}^{\infty} \int_0^L G_{jk}(\mathbf{x}, \boldsymbol{\xi}_{mn}(s,t)) f_k(\boldsymbol{\xi}_{mn}(s,t)) \, \mathrm{d}s, \tag{1.1}$$

where $\boldsymbol{\xi}_{mn}(s,t)$ is the position vector of the point on a cilium of arc-length s from the base, situated at $x = ma$, $y = nb$, at time t.

In order to find the force distributions, the 'resistive force theory' of Gray and Hancock (1955) was used, which approximates the normal and tangential components of the force distribution as being proportional to the relative velocity of the cilium and the fluid. The constants of proportionality must be derived using slender body analysis, see for example Chwang and Wu (1975). In the original study, Blake averaged the integrands over time and in the x and y directions—in Figure 1.2, the direction of mucus transport and the direction into the paper respectively. This simplified the mathematics significantly, so that a mean field velocity could be obtained. He also used a form of Poisson's summation formula to convert the doubly-infinite sum of Green's functions into an exponentially decreasing Fourier-transformed version, so that a good approximation to the sum could be found from the leading order term.

These techniques were then extended to muco-ciliary transport in the lung (Blake, 1973b). The same discrete sublayer analysis was used, together with the beat cycle of *Paramecium* since data were not available for lung cilia. The effect of gravity on a thickened mucous layer was also included in the model, showing that angle of inclination would have a very significant effect in diseased lungs where the mucous layer was an order of magnitude thicker than the PCL. In this initial study, the ASL was assumed to have constant viscosity, and the Green's function for a semi-infinite fluid was used.

This approach to modelling cilia has certain other limitations—in particular it only takes account of the interaction between the cilium and the mean flow (Liron and Mochon, 1976a)—this is not necessarily a good approximation below the top of the cilia layer, where the oscil-

lations in fluid velocity may be large. Blake also noted that the ciliary beat of *Paramecium* is three-dimensional, and the metachronism exhibited is not simply antiplectic—although some recent research has suggested that the ciliary beat in the lung may indeed be planar (Chilvers and O'Callaghan, 2000). In modelling micro-organism propulsion, Liron and Mochon (1976a) only averaged in the y direction and exploited simplifying periodicity arguments to reduce the doubly-infinite sum of forces and singularities to a finite sum of forces over one beat cycle and an infinite sum of singularities that could be calculated analytically. They avoided the need to use Gray and Hancock theory by requiring only that the velocity at a point on a cilium is equal to that of the fluid flow. Once the velocity of the cilium is calculated from beat cycle data, this gives an integral equation for the force distribution, which can be solved numerically using a quadrature procedure. The calculation of the flow field over the rest of the fluid is then straightforward. This approach is extended and applied to the muco-ciliary system in chapter 3.

For a genuinely accurate model, the ASL needs to be considered as at least two separate layers, the lower being watery and nearly Newtonian, the upper being viscous and non-Newtonian. As a first step towards this analysis, Blake (1975b) applied the earlier discrete sublayer model together with a two-layer Newtonian model including the effects of gravity and interaction with the airflow. The model differed from most in this field in that the cilia were assumed to be synchronised rather than forming a metachronal wave, based on the fact that the cilia in the lung are very closely packed, at least on an individual cell. Mean and oscillatory velocity profiles were calculated, of maximum magnitude around $0.05\sigma L$, and $0.3\sigma L$, corresponding to $18\ \mu\mathrm{m/s}$ and $108\ \mu\mathrm{m/s}$ for our parameter set respectively. With the aim of modelling a non-Newtonian mucous layer, a discussion was given of how Fourier analysis could be used with a linear Maxwell model in order to produce a linear consitutive equation, as exploited in this study in chapter 2. Penetration into the mucous layer was not modelled, and there was no experimental data available for the cilia beat cycle shape. These limitations were addressed in Blake (1984), Blake and Fulford (1984) and Fulford and Blake (1986), where the cilia beat cycles found by Sleigh

(1977) and Sanderson and Sleigh (1981) were used, together with Gray and Hancock-type resistance coefficients for a slender body 'straddling' the interface between two Newtonian fluids of differing viscosity. These coefficients were calculated based on continuity of normal stress at the boundary between the fluids, neglecting surface tension. As a second order correction they then calculated the interface shape subject to surface tension. They modelled the effects of having a large number of inactive cilia, as in a diseased lung, and determined an optimum penetration depth. A typical velocity profile is given in Figure 1.3, profile A.

A different approach to modelling the cilia sublayer was developed by Keller (1975). Known as the 'continuum sublayer' or 'traction layer' model, the action of the cilia is modelled as a spatially continuous volume force distribution. Keller applied this technique to ciliated microorganisms such as *Paramecium* and *Opalina* where the mucous layer does not have to be considered. Exploiting the periodicity of the ciliary beat, he first found the stream function for Stokes flow in terms of the force distribution with Fourier series analysis. He then used the resistive force theory of Gray and Hancock together with expressions for the resistance coefficients derived by Chwang and Wu (1975) for a very slender ellipsoid. Since the force exerted by the cilium depends on the velocity of the surrounding fluid, and vice-versa, it was necessary to use an iterative algorithm, starting with zero fluid velocity, calculating the force over the ciliary beat cycle, calculating the resulting velocity and continuing until convergence was achieved. This method, which discretised the cilium as a finite number of segments, is known as a 'pigeon-hole algorithm'. The averaging technique has been criticised (Fulford and Blake, 1986) because it apparently does not adequately discriminate between the effective and recovery strokes, resulting in excessive oscillatory velocities in the upper layer. However, replacing the cilia with a volume force is a very useful simplification, and this idea is used in chapter 2.

Blake and Winet (1980) applied the traction layer approach to muco-ciliary transport in the lung, with the idealised beat pattern of Barton and Raynor (1967) and modelling the mucous layer as a Newtonian fluid. They took into account the resistance of the ciliary sublayer by

modelling it as an ‘active porous medium’, building on the earlier paper of Blake (1977). Their results suggested that slight penetration into the mucous layer by the cilia substantially enhanced transport.

Liron and Rozenson (1983) examined tip penetration in a different way. They modelled mucus as a non-Newtonian fluid with the linearised Oldroyd equations, valid for small rates of shear. They assumed that the only forces driving the fluids were a constant pressure gradient and a series of impulses, represented by Dirac delta functions, produced by the cilium tips. After solving the resulting equations by Fourier transforms they concluded that penetration was necessary for transport. However, their approach did not take into account the resistance of the ciliary sublayer (Fulford and Blake, 1986).

Raptis and Perkidis (1973) formulated a mathematical model of the pharyngeal epithelium of the frog, modelling each cilium as a collection of infinitesimal cylinders, the cilium being straight, shortening during the recovery stroke, with the effective stroke taking up $1/4$ of the ciliary beat cycle. Summing the contributions from all the cylinders making up each cilium and using a resistance coefficient, they found the total force exerted on the mucus ‘blanket’ per cilium. By setting this equal to the gravitational force on the mucus, they calculated a transport velocity which differed with experimentally observed values by only about 4%. However, issues such as tip penetration, PCL velocity and mucus viscoelasticity were not addressed, and the limitations of the similar work of Barton and Raynor (1967) also apply. In addition, it is difficult to extend their analysis to the bronchioles of the lung, since balancing the propulsive force with gravity is no longer appropriate - as discussed above, gravitational force is not significant in healthy epithelia.

In a more recent paper, King et al. (1993) formulated a simple analytical model of the muco-ciliary system designed to test the effect of mucus viscoelasticity. They established, amongst other things, that mucus transport increases as the shear modulus of elasticity decreases. However, their model is limited in a number of ways—they assumed that there was no net transport

of PCL in the cilia sublayer, something which our models are designed to test, they only took into account steady motion of the PCL, whereas oscillatory motion may prove important for mixing effects (Matsui et al., 1998b), and that there was a layer of PCL between the top of the cilia sublayer and the mucous layer, ruling out the effect of tip penetration.

A more fundamental approach to ciliary modelling has been developed in the 1990s (Gueron and Liron, 1992, 1993). They model the internal action of the cilium that causes it to bend, as attempted by Sleigh (1962) and others, together with a hydrodynamic analysis based on that suggested by Lighthill (1975). These 'internal' models differ from the discrete sublayer models described above in that they actually predict the existence of coordination and metachronism between several cilia, rather than simply assume it exists.

Their approach to the hydrodynamics is far more accurate than Gray and Hancock theory, and an error estimate can be derived rigorously. This work is a significant step in proving that ciliary coordination can result from fluid mechanical effects alone, although the computational cost limited the number of cilia that could be simulated at once. We suggest that their approach may be very valuable if extended to problem of the nodal flow in the embryo, where there are a small number of rotating primary cilia, and their possible coordination is less well understood. Applying their techniques to the muco-ciliary system, with vast arrays of cilia and interactions with the mucous layer may be more challenging.

1.4 Salt/fluid controversy, cystic fibrosis and mean transport of PCL

Accurate modelling of muco-ciliary clearance is important in that it may help to improve the understanding of the pathogenesis and treatment of respiratory disease—in particular cystic fibrosis lung disease. CF is a genetic disorder which causes, *inter alia,* chronic bacterial infections of the lung.

The symptoms of CF result from an abnormality in the protein CFTR (cystic fibrosis trans-

membrane regulator) but it is not known exactly how this abnormality results in lung infections. The muco-ciliary system protects the lungs from infection in several different ways (Salathe et al., 1997)—it provides a mechanical barrier to pathogens, trapping and transporting foreign material out of the lung. It provides a biological barrier, as glycoconjugates bind to bacteria and prevent them from adhering to the epithelium. It also provides a chemical barrier, exhibiting antioxidant properties which protect against free radicals.

Various explanations have been advanced for the pathogenesis of CF: it could be due to the way CFTR affects airway cells, preventing them from ingesting and killing bacteria. It could also be a result of abnormal ion transport by CFTR. An understanding of this requires knowledge of how the ASL is regulated by the epithelium.

One theory, the 'hypotonic ASL/defensin' hypothesis, described by Smith et al. (1996), postulates that normal epithelia are covered by an ASL with sufficiently low salt concentration (hypotonicity) to activate defensins and create an antimicrobial 'shield' on airway surfaces. The epithelium extracts salt, but not water, from the PCL. In CF patients, salt is not extracted due to a defect in Cl^- conductance, rendering defensins inactive. Implicit in this hypothesis (Quinton, 1994) is that PCL is not transported along with the mucus out of the lungs. This must be the case because the surface area of the lungs decreases greatly moving from the bronchioles to the bronchia and finally the trachea, but the ASL depth does not greatly increase.

Another theory, the 'isotonic volume transport/mucus clearance' hypothesis (Boucher, 1994) predicts that airway epithelia regulate the height of the ASL by isotonic ion and water transport to optimise mucus clearance. In CF the rate of ion and water transport is abnormally high, reducing PCL volume, concentrating and dehydrating mucus, resulting in plugging of the airways and infection. This is consistent with the idea that PCL is being transported axially out of normal lungs. If this hypothesis is true, novel treatments for CF should focus on restoring ASL volume (Matsui et al., 1998b) rather than changing ASL tonicity. The question of whether CF lung disease is caused by salt concentration or excessive fluid absorption has been called the

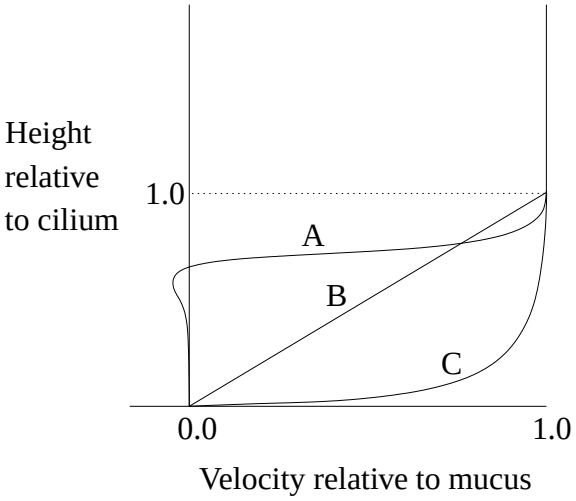

Figure 1.3: Comparing the velocity profiles predicted by theory (typified by A), shear-driven flow (B) and those apparently found by experiment (C)—redrawn from Matsui et al. (1998b).

'salt/fluid controversy' (Guggino, 2001).

By studying the transport of fluorescent tracer particles in cultures of human tracheobronchial cells, Matsui et al. (1998b) apparently demonstrated that PCL and mucus were transported at approximately the same rate, with the velocity profile in the PCL increasing very rapidly from the epithelium. Further experimental evidence for this hypothesis can be found in Matsui et al. (1998a).

However, most of the relevant theoretical work predicts small velocities throughout most of the PCL and hence relatively low transport of PCL out of the lungs. The PCL should be almost stationary. It must be that either the theoretical work of Fulford and Blake omits some phenomena, or that either the experimental results need to be reinterpreted.

Further investigation of *in vivo* ASL has been conducted by Tarran et al. (2001) and Jayaraman et al. (2001). Both groups found that normal ASL is isotonic, but found conflicting results concerning ASL thickness in murine models of CF. The pathogenesis of CF may be still more complex than suggested above (Landry and Eidelman, 2001).

1.5 Towards a resolution of the paradox

1.5.1 Previous work

In an initial investigation of the conflicting experimental and theoretical results, Blake and Gaffney (2001) began to model tracer dispersion in ASL. Using a steady velocity profile typical of those found in Fulford and Blake (1986), they solved a two dimensional advection-diffusion equation numerically using an alternating direction implicit method. They found that the results were not consistent with the experimental results of Matsui et al., giving differential transport in the two layers. They repeated the simulation with a large *ad hoc* oscillatory component, which did not satisfy the continuity equation, but nevertheless provided insight into whether oscillatory effects could produce cotransport. They found less difference in transport between the two layers, but the discrepancy was still significant. It may be that the velocity profiles are not correct, and they suggested various additional physical effects that might have to be included in the model, such as mechanical or osmotic pressure gradients. It is possible that the experimental setup may introduce additional physical effects—the cultures exhibited circular transport of mucus, not uni-directional transport. It is necessary to simulate tracer dispersion using velocity fields which satisfy the continuity equation. It may also be that the length scales used in their simulation may have affected the results—the initial 'column' of tracer was about $600\ \mu\mathrm{m}$ in width, rather than the $400\ \mu\mathrm{m}$ in the relevant experiments. Finally, it is possible that continuum modelling of the muco-ciliary system is inappropriate, and that molecular level effects associated with the interaction of cilia and mucus may be present.

Barlow (2000) developed a simple traction-layer model of muco-ciliary transport that forms the basis for the far more detailed system presented in chapter 2. Barlow's model produced different velocity profiles from those of Fulford and Blake, with nearly a shear-driven flow in the PCL, as depicted in Figure 1.3 profile (B), due to the fact that sublayer resistance was not modelled. These profiles were also significantly different from those suggested by Matsui

et al. (1998b), as illustrated in Figure 1.3. The profiles were used in an advection-diffusion simulation similar to those described above. With a steady velocity field only, there was a significant difference in transport between the two layers. With an oscillatory profile, however, almost identical transport was achieved, suggesting that much smaller PCL transport than that suggested by Matsui et al. (1998b) could result in cotransport. However, the author noted that this may have been due to the fact that unrealistically large diffusion coefficients had to be used to avoid numerical errors.

1.5.2 Outline of thesis

In chapter 2 we greatly extend Barlow's original model by incorporating mucus viscoelasticity, the viscous coupling between the cilia and fluid in the PCL, pressure gradients in the mucus and PCL caused by surface and interface tension, and a model of the cilia beat cycle that allows for the time asymmetry of the effective and recovery strokes. By modelling the force exerted on the mucus using a resistance coefficient, we can calculate the fluid velocity in a consistent way. Our model sheds light on the important physical effects involved in efficient mucus transport, and shows some interesting parallels with experimental and clinical results.

In chapter 3 we outline a new discrete-cilia model based on the work of Liron (1978) and Chwang and Wu (1975) which models flow in the PCL with greater temporal and spatial detail than the traction layer analysis. Our model improves the convergence and accuracy of the solution in the near field around the cilium, while still allowing efficient numerical solution. Although calculating the volume flux remains difficult, some insight into the limitations of previous analyses is given.

In chapter 4 we apply the tracer dispersion model of Blake and Gaffney (2001) to the new velocity profiles found in chapter 2. Based on the findings of chapter 3 we also investigate tracer dispersion where the PCL flux is greater than that predicted by the traction layer model, and where the effective diffusion of tracer is increased due to mixing by the cilia between the

mucus and PCL. We then suggest ways in which the paradox may be resolved.

Finally chapter 5 contains a summary and discussion of the significance of our results, suggesting directions of future research.

CHAPTER 2

TRACTION LAYER MODEL—A PHYSICALLY-BASED PHENOMENOLOGICAL MODEL OF MUCUS TRANSPORT

2.1 Introduction

In this section we describe a 'traction layer' model of muco-ciliary transport. The model considers the ASL as three fluid layers, the lower layer being Newtonian, the remaining two being linearly viscoelastic. The propulsive force produced by the cilia is modelled by a volume force which acts in the region—the traction layer—where the cilia penetrate the mucus, varying spatially and temporally with the metachronal wave. The effect of the beating cilia on the flow in the PCL is modelled using the 'active porous medium' ideas first presented in Blake (1975a). A possible shear-thinning effect in the traction layer is included. By using Fourier series analysis we exploit periodicity and convert the system of PDEs to a system of ODEs. Under the assumptions of lubrication theory, this system is decoupled and solved analytically. The full system is then solved numerically, and the two approaches are compared.

This model will provide insight into the different possible ASL velocity profiles discussed in chapter 1 and shown in Figure 1.3. It will also provide more qualitative information than

has previously been available into the nature of the spatial and temporal variations in the muco-ciliary flow, which will be useful in the tracer dispersion simulations described in chapter 4. Finally, the model allows investigation of how different physical parameters, such as viscosity, and different physical effects, such as pressure gradients and surface tension, affect transport, particularly in diseased states.

2.2 Fluid flow equations

We treat the ASL as three fluid layers separated by flat interfaces at $z = h$ and $z = L$ as shown in Figure 2.1. This assumption seems reasonable if we examine the micrographs of Sanderson and Sleigh (1981), in which the mucus–PCL interface is shown to be remarkably flat, even when there are large undulations in the epithelium—which are not present in the experiments of Matsui et al. (1998b). The parameter h is the depth of the PCL, L is the length of the cilia, H is the depth of the ASL. In this chapter we consider a two dimensional model of the ASL, as shown in Figure 2.1. We refer to the direction of transport, the x_1 direction, as the x or 'horizontal' direction. We refer to the direction normal to the epithelium, the x_3 direction, as the z or 'vertical' direction.

The lower layer $0 < z < h$, representing the PCL, is modelled by a Newtonian fluid of viscosity μ^P. We take $\mu^P = 0.001 \text{ N m}^{-2} \text{ s}$, as for water. The traction layer region $h < z < L$, representing the region in which the cilia penetrate the mucus, is modelled by a Maxwell viscoelastic fluid with viscosity μ^{M1} and relaxation time λ_1. The upper layer $L < z < H$, representing the mucus above the penetration region, is modelled by a Maxwell fluid of viscosity μ^{M2} and the same relaxation time λ_1. In general $\mu^{M1} < \mu^{M2}$ because mucus is shear-thinning (Puchelle et al., 1985) and the shear rates in the traction layer will be far larger than above the traction layer. Due to lack of data regarding the possible variation of elasticity with shear rate, we assume that the relaxation time in both mucous regions is the same, however if experimental data becomes available showing that in general the elasticity will be different, it will

be straightforward to repeat our calculations with different values. It may also be noticed that adding a strain relaxation time as in the Oldroyd model (see, for example Joseph, 1990) would be very mathematically straightforward, however the present lack of experimental data makes it difficult to determine the value of such a parameter, so at this stage we shall not study this effect. We will discuss the values of the remaining parameters in §2.4.

As discussed in §1.2, the parameter h will be approximately $5.4\ \mu\mathrm{m}$, L will be about $6\ \mu\mathrm{m}$, and $H - L$ depending on the thickness of the upper mucous layer may vary from just $0 - 2\ \mu\mathrm{m}$, corresponding to the terminal bronchi, up to an average of $15\ \mu\mathrm{m}$, or more in pathological conditions, in the trachea. The mucous layer is still thicker in the pharynx and nasal passage, but we will not be concerned with these regions.

All published mathematical modelling work to date has represented mucus transport as taking place on a flat infinite plane, whereas mucous transport actually takes place on the inside of a tube. International Commission on Radiological Protection and Measurements (1994) state that all of the bronchi, the second to eleventh generations of the bronchial tree, will have diameter greater than approximately $1\ \mathrm{mm}$, whereas the ASL will not normally be more than $25\ \mu\mathrm{m}$ thick. The planar approximation is therefore very acceptable even quite deep into the bronchial tree, hence we shall use it in this study.

Through momentum balance, one can derive the following form of the Navier–Stokes momentum equations:

$$\frac{\partial \sigma_{jk}}{\partial x_k} + f_j = \rho \frac{\mathrm{D}u_j}{\mathrm{D}t}, \tag{2.1}$$

where σ_{jk} is the stress tensor, f_j the body force (force per unit volume) on the fluid representing the action of the cilia, ρ the density and u_j the fluid velocity, with summation over repeated indices. $\mathrm{D}/\mathrm{D}t$ represents the convective derivative $\partial/\partial t + u_i \partial/\partial x_i$.

From the parameters given in Matsui et al. (1998b), we use the scaling $U = 40 \times 10^{-6}\ \mathrm{m/s}$ for velocity. Based on the cilium dimensions, we use the length scale $L = 6 \times 10^{-6}\ \mathrm{m}$. For the density and viscosity of the ASL we use the density and viscosity of water, $\rho = 1000\ \mathrm{kg/m^3}$

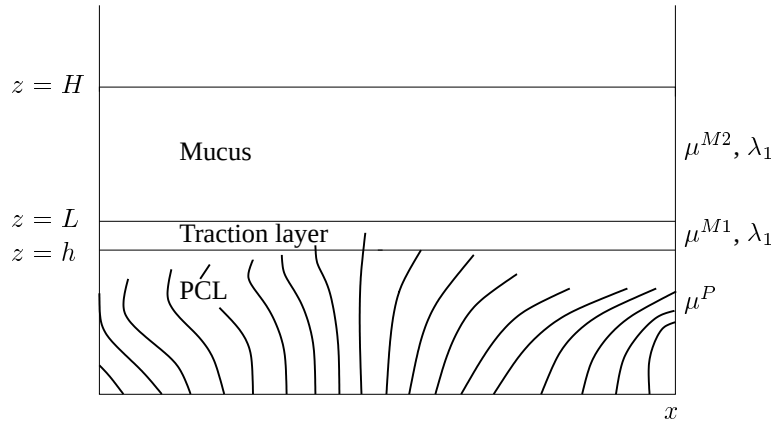

Figure 2.1: Diagram of the 3 layer model. Newtonian PCL, viscosity μ^P, depth h. Traction layer, viscosity μ^{M1}, elasticity λ_1, depth $L - h$. Mucus layer, viscosity μ^{M2}, elasticity λ_1, depth $H - L$.

and $\mu = \mu^P = 0.001$ Pa s. Hence the Reynolds number $\rho UL/\mu$ is 0.00024, so we neglect the convective term. The nondimensional parameter $\sigma\rho L^2/\mu$ will be small since the frequency σ will be of the order of 60 rad/s, so we neglect the time-dependent term $\partial u_j/\partial t$ and obtain

$$\frac{\partial \sigma_{jk}}{\partial x_k} + f_j = 0, \tag{2.2}$$

in dimensional variables. In addition to this we require the equation of mass conservation. For an incompressible fluid this is

$$\frac{\partial u_j}{\partial x_j} = 0. \tag{2.3}$$

Given appropriate boundary conditions, we will solve equations (2.2) and (2.3) in the three fluid layers.

2.3 Modelling the volume force exerted by the cilia

As discussed above, we write the force on the fluid as the sum of a propulsive force in the traction layer and a resistive force in the PCL, $\mathbf{f} = \mathbf{f}_{\text{prop}} + \mathbf{f}_{\text{res}}$.

Gravity is neglected in this model, as in previous models, based on the analysis of Blake

(1973b). Due to the very strong viscous coupling between the cilia and PCL, we neglect the effect of gravity in the PCL—this can be seen by observing the size of the resistance coefficients γ_x^P and γ_z^P in §2.3.1. In the mucous layer, we apply Blake's analysis and observe that in the 'worst case' of a vertical epithelium, the flow of $4\ \mu\mathrm{m}$ thick, 0.05 Pa s viscosity mucus will be $\rho g(H-L)^2/(4\mu^M) = 1000 \times 10 \times (4 \times 10^{-6})^2/(4 \times 0.05)$, or $0.8\ \mu\mathrm{m/s}$. As observed by Blake (1973b), this value is proportional to the square of the mucus depth and so deeper mucus, particularly in the case of disease, may be signficantly affected by gravity. In the experiments of Matsui et al. (1998b), the mucous layer was significantly thicker than $4\ \mu\mathrm{m}$, but the cultures were kept flat.

Our model incorporates the main features of the system—metachronism, the periodicity of the ciliary beat and the spatial variations in the propulsive force. It may be argued that the cilia will have a propulsive effect due to beat cycle asymmetry, as in micro-organism movement. However, the beat cycle asymmetry is far less pronounced in the muco-ciliary system (Sanderson and Sleigh, 1981) and the propulsive effect due to the the cilia engaging with the highly viscous mucous layer will be an order of magnitude greater than that in the PCL. Hence in this chapter, we do not model any propulsive effect due to beat cycle asymmetry.

We make the assumption that the mucus–PCL interface is flat throughout the beat cycle. The reasons for this are discussed in detail in §2.7.4 and §2.7.5. A consequence of this assumption is that for there to be positive propulsion, there must be penetration of the mucous layer by the cilia tips. In reality it may be possible for cilia to exert force on the mucus by 'pushing up' the mucous layer and producing a 'sprocket and chain' effect, without actually penetrating it. For all results shown in this paper, however, we must assume that 'penetration' takes place. Certainly the micrographs of Sanderson and Sleigh appear to show a nearly flat mucus–PCL interface. In addition, micrographs taken by Puchelle et al. (1998) show cilia penetrating the mucous layer.

2.3.1 Active porous medium model of the mat of cilia in the PCL

The dense mat of cilia will resist the flow of fluid, somewhat like a porous medium. In addition, the cilia oscillate, so that the fluid close to the surface of a cilium will move with similar velocity to the cilium. The combined effect is that the mat of cilia will reduce the transport of PCL, but cause significant oscillations throughout the layer. The resistive force will be assumed to act only in the PCL. This is because the cilia only penetrate the mucus for a very short portion of the cycle—at any one time, most of the volume of the mucus in the thin penetration layer will contain no cilia.

In modelling a porous medium, one can write the resistive force as being proportional to the fluid velocity, i.e. $\mathbf{f}_{\rm res}(x,z,t) = -\gamma\mathbf{u}$, where γ is a coefficient of resistance. Of course the cilia are in motion, so we actually consider the relative motion of the fluid and the field of cilia at each point in space, so the resistive force will be given by

$$\mathbf{f}_{\rm res}(x,z,t) = -\gamma(\mathbf{u}-\mathbf{u}_{\rm cilia}), \quad 0<z<h, \tag{2.4}$$

following Blake (1975a).

The cilia will have both a horizontal and vertical component to their motion, and in addition the porous medium will be anisotropic—the array of cilia will have a different resistance coefficient in the x and z directions. For this problem, we use

$$\begin{aligned} \gamma_x &= \frac{4\pi\mu}{(\log(d/r_0) - (1/2)(d^4-r_0^4)/(d^4+r_0^4))\,d^2}, \\ \gamma_z &= \frac{8\pi\mu}{4r_0^2 - r_0^4/d^2 - 3d^2 + 4d^2\log(d/r_0)}, \end{aligned} \tag{2.5}$$

which are the coefficients for a concentrated array of circular cylinders aligned respectively perpendicular and parallel to the flow. The parameter d is the spacing of the cilia, r_0 the radius of a cilium, $\log$ denotes the natural logarithm. This was derived in Happel (1959), and was

found by Happel to compare well to experimental data.

The resistance coefficients are proportional to the fluid viscosity. We use γ_x^P, γ_z^P to denote the resistance coefficients in the PCL, determined from μ^P, and γ_x^{M1}, γ_z^{M1} to denote the resistance coefficient in the traction layer—which we exploit in order to model the propulsive effect of cilia penetration—determined from μ^{M1}.

The parameter γ_x^P is approximately $90^2 \times \mu^P/L^2$, while γ_z^P is approximately $75^2 \times \mu^P/L^2$. One might anticipate that the precise values will not be be particularly important, since throughout most of the PCL, γ_x^P and γ_z^P may be large enough so that asymptotically, $u \sim u_{\text{cilia}}$. This approximation was exploited in Blake (1975a) and Blake (1977), in which the motion of the cilia was more accurately represented so that propulsion due to beat cycle asymmetry, as is observed in micro-organisms, could be modelled. However, the existence of large pressure gradients in the muco-ciliary system may mean that the assumption $u \sim u_{\text{cilia}}$ is violated. We shall see later that this is the case.

We require $\mathbf{u}_{\text{cilia}}$ as a function of (x, z, t)—we suggest a simplified Fourier series model that captures all of the important aspects of the beat cycle—periodicity, an effective stroke only 20% of the duration of the total period and velocity increasing linearly with distance from the epithelium. Of course we require $\int_0^T u_{\text{cilia}}\, \mathrm{d}t = 0$, i.e. there is no net movement of any point of the cilium over a beat cycle. Hence, we use the following representation for the horizontal and vertical components of the cilium velocity:

$$\begin{aligned} u_{\text{cilia}}(x,z,t) &= \nu z\sigma C(\kappa x + \sigma t) = \nu z\sigma \left(\textstyle\sum_{n=1}^{N_0} c_n \cos[(\kappa x + \sigma t)n] \right), \\ v_{\text{cilia}}(x,z,t) &= \nu z\sigma D(\kappa x + \sigma t) = \nu z\sigma \left(\textstyle\sum_{n=1}^{N_0} d_n \sin[(\kappa x + \sigma t)n] \right). \end{aligned} \tag{2.6}$$

The parameter κ is the wavenumber $2\pi/\lambda$, where λ is the wavelength, σ is the cilia beat frequency in radians per second, ν is the duration of the cilia beat as a fraction of the duration of the effective stroke. To obtain the Fourier series coefficients, we Fourier analysed the functions C and D shown in Figure 2.2, which provide a reasonable model of the velocity of the

cilium, using the idea that it is approximately a pendulum moving through an arc of $\pi/3$ radians, with the effective stroke five times faster than the recovery stroke. The period denoted 1 represents the cilium beating forwards during the first half of the effective stroke, the cilium tip moving upwards into the mucus. Hence the horizontal velocity is positive, the vertical velocity is positive, although it falls to zero as the cilium tip approaches its apex. The period denoted 2 represents the cilium tip during the second half of the effective stroke, during which the cilium tip continues to beat forward, but now has negative vertical velocity until it reaches the end of the effective stroke and stops. A satisfactory representation of this approximate characterisation is given by taking the first 4 and 7 terms of the Fourier series respectively, as shown in Figure 2.3. In this study we shall calculate the first $N_0 = 15$ terms of the solution, since we require 15 terms in order to represent the propulsive force, described in §2.3.2, accurately. Hence we shall set $c_5 = \ldots = c_{15} = 0 = d_8 = \ldots = d_{15}$. The values of the Fourier coefficients are given in appendix A.

The cilium moves through an angle of about $\pi/3$ rad in one fifth of the beat cycle, its tip covering a distance of $L\pi/3$. Assuming an angular frequency of $60\ \mathrm{rad/s}$, the duration of the effective stroke is $2\pi/(60 \times 5)$. The velocity of the cilium tip during the effective stroke is therefore approximately

$$\nu L\sigma \quad = \quad \frac{L\pi/3}{2\pi/(60 \times 5)} \quad = \quad \frac{5\sigma L}{6}, \tag{2.7}$$

so that $\nu = 5/6$ is chosen in all of the results presented below. We assume that the vertical component of the velocity varies between zero and one half—$\sin(\pi/6)$—of that of the horizontal velocity. The peak in the Fourier representation of the horizontal component is larger than twice the peak in the vertical component, as shown in Figure 2.3, however the mean of the horizontal velocity is nevertheless still twice the peak in the vertical component, as required.

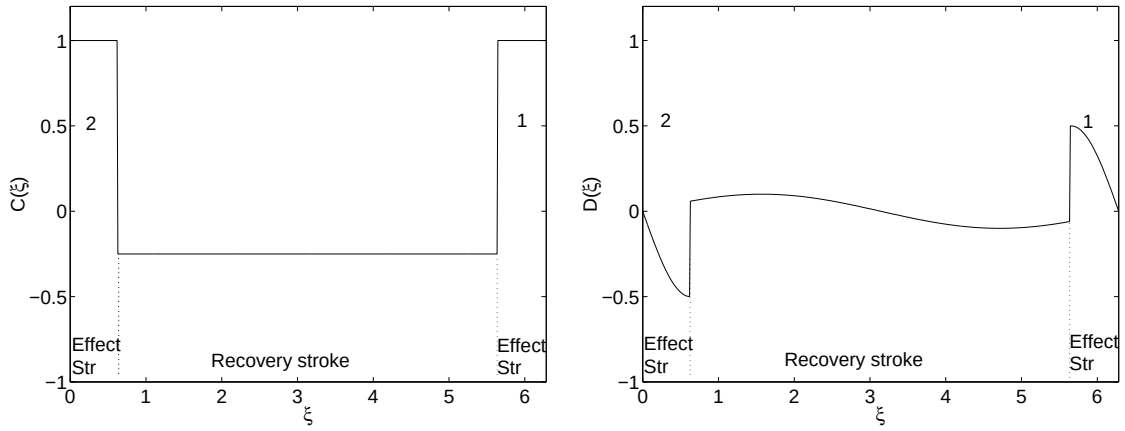

Figure 2.2: Horizontal and vertical cilium tip velocity—idealised representation, showing the variation with $\xi = \kappa x + \sigma t$. See text for further details.

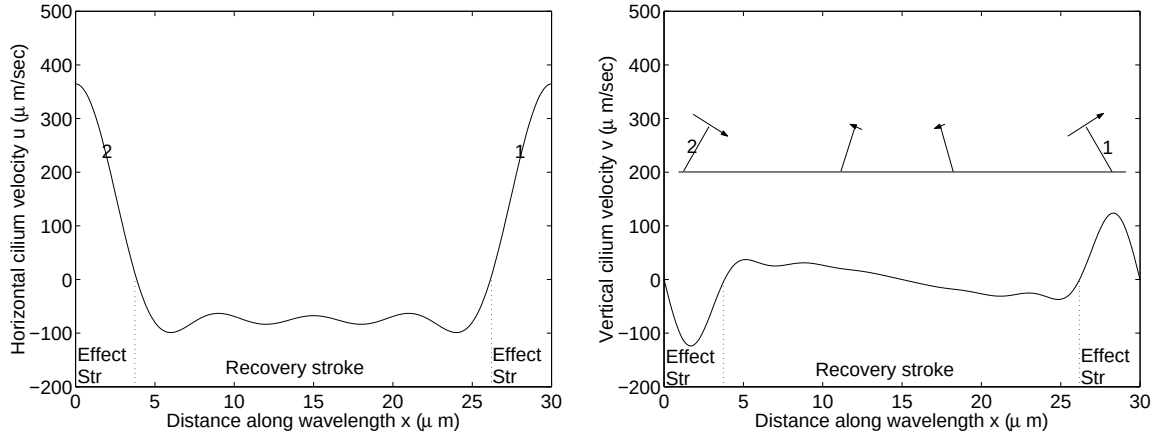

Figure 2.3: Horizontal and vertical cilium tip velocity—dimensional Fourier series, with parameters $L = 6\ \mu\mathrm{m}$, $\kappa = 2\pi/30\ \mu\mathrm{m}^{-1}$, $\sigma = 60\ \mathrm{rad/s}$, using 4 and 7 terms respectively in the Fourier expansion as discussed in text.

2.3.2 Traction layer force due to penetration by cilia

In this section we again make use of the active porous medium approach, now using the 'resistance coefficients' γ_x^{M1} and γ_z^{M1} to model the propulsive force exerted by the cilia as they penetrate the mucous layer and push it forward. At the level of the interface, where there will be many cilia bodies in the mucous layer, we apply the porous medium model and write the force as $\mathbf{f}_{\text{prop}} = (f_{\text{prop}}, 0, g_{\text{prop}})$, where $\mathbf{f}_{\text{prop}} = (f_{\text{prop}}, 0, g_{\text{prop}})$, where

$$\begin{aligned} f_{\text{prop}}(x, z = h, t) &= \left(\tfrac{1}{2} f_0 + \textstyle\sum_{n=1}^{N_1} f_n \cos[(\kappa x + \sigma t)n]\right) \gamma_x^{M1}(u - u_{\text{cilia}}), \\ g_{\text{prop}}(x, z = h, t) &= \left(\tfrac{1}{2} g_0 + \textstyle\sum_{n=1}^{N_1} g_n \sin[(\kappa x + \sigma t)n]\right) \gamma_z^{M1}(v - v_{\text{cilia}}). \end{aligned} \tag{2.8}$$

γ_x^{M1} and γ_z^{M1} are resistance coefficients such as those chosen in the last section, and we choose $N_1 = 15$.

For mathematical simplicity, we approximate the interaction velocities $(u - u_{\text{cilia}})$ and $(v - v_{\text{cilia}})$ by the constants $-U_{\text{int}}$ and $-V_{\text{int}}$, and calculate the values at $z = h$ at the midpoint of the beat cycle $x = 0$ and $t = 0$. We then assume that the force profile will decay monotonically to zero moving towards the beginning or end of the beat cycle, as represented by the profile in Figure 2.4. Furthermore, at any point in time, fewer cilia will reach $z > h$ than $z = h$, since the cilium tip only reaches the top of the traction layer for a brief fraction of the cycle. Above $z = L$, there will be no cilia at all, so that the viscous coupling between the cilia and the mucus will therefore be much weaker. Hence we assume that the force exerted by the cilia on the mucus falls monotonically to zero between $z = h$ and $z = L$. Modelling this variation by the function $\sin(\pi z/L)/\sin(\pi h/L)$ we have

$$\begin{aligned} f_{\text{prop}}(x, z, t) &= -\left(\tfrac{1}{2} f_0 + \textstyle\sum_{n=1}^{N_1} f_n \cos[(\kappa x + \sigma t)n]\right) \gamma_x^{M1} U_{\text{int}} \dfrac{\sin(\pi z/L)}{\sin(\pi h/L)}, \\ g_{\text{prop}}(x, z, t) &= -\left(\tfrac{1}{2} g_0 + \textstyle\sum_{n=1}^{N_1} g_n \sin[(\kappa x + \sigma t)n]\right) \gamma_z^{M1} V_{\text{int}} \dfrac{\sin(\pi z/L)}{\sin(\pi h/L)}. \end{aligned} \tag{2.9}$$

Replacing the function $\sin(\pi z/L)/\sin(\pi h/L)$ with a linear function leads to qualitatively very similar results. The constants $-U_{\text{int}}$ and $-V_{\text{int}}$ are determined as explained in §2.9.2.

This approach to modelling the force is not ideal, since in reality there will be complex interactions between the tips of the penetrating cilia and the mucus–PCL interface. The interface will not be a smooth, flat surface: it will deform in response to the penetration of the cilia. There may be surface forces caused by the cilia deforming the interface, and there may be molecular level interactions between the nanoscale 'crown' on the tip of the cilium (Foliguet and Puchelle, 1986) and the mucus polymer network. We essentially model the interface as moving closely with the cilia at $y = h$, then make a reasonable estimate for the force in the rest of the traction layer. It is in this respect that the model is 'phenomenological'.

The Fourier coefficients f_n, g_n are chosen by Fourier-analysing the functions F and G as depicted in Figure 2.4. The function F represents positive propulsion for $1/5$th of the beat cycle—based on the data of Sanderson and Sleigh (1981)—rising linearly to a maximum value, then falling linearly back to zero. The function G represents the vertical velocity of the cilium. Visualising the cilium beat as a simple pendular motion, we see that at the apex of the stroke, the vertical velocity is zero. In front of this point, the velocity is positive, as the cilium tip is moving up, behind this point, the velocity is negative, as the cilium tip is moving downwards. The values of the coefficients are given in appendix A. We shall see that the final results also exhibit this sharp oscillation.

We have assumed the force to be constant in the direction perpendicular to the effective stroke (in Figure 2.1 this is the direction *into* the page), which is not strictly true—in fact we have averaged over the row of cilia which we assume to be in phase. This removes information

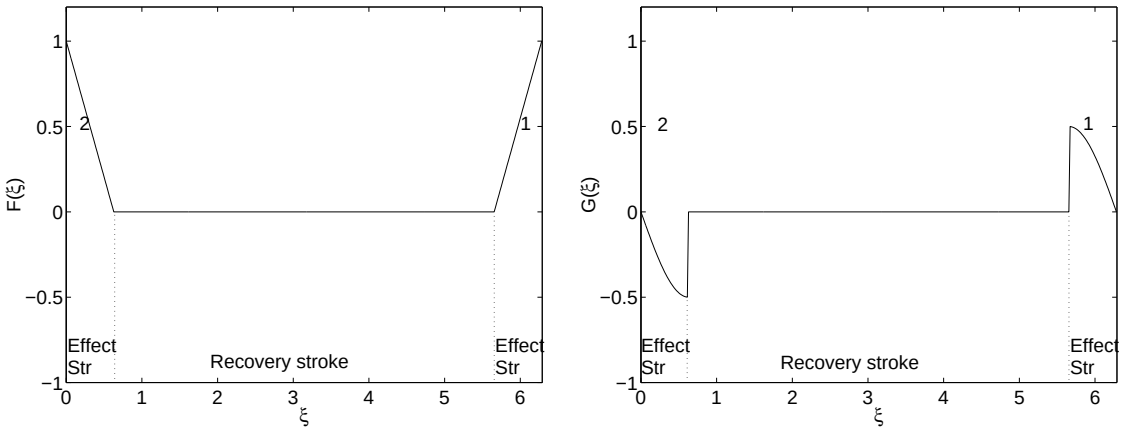

Figure 2.4: Plots of the functions F and G, the idealised representations of the variations of the horizontal and vertical propulsive force in $\xi = \kappa x + \sigma t$.

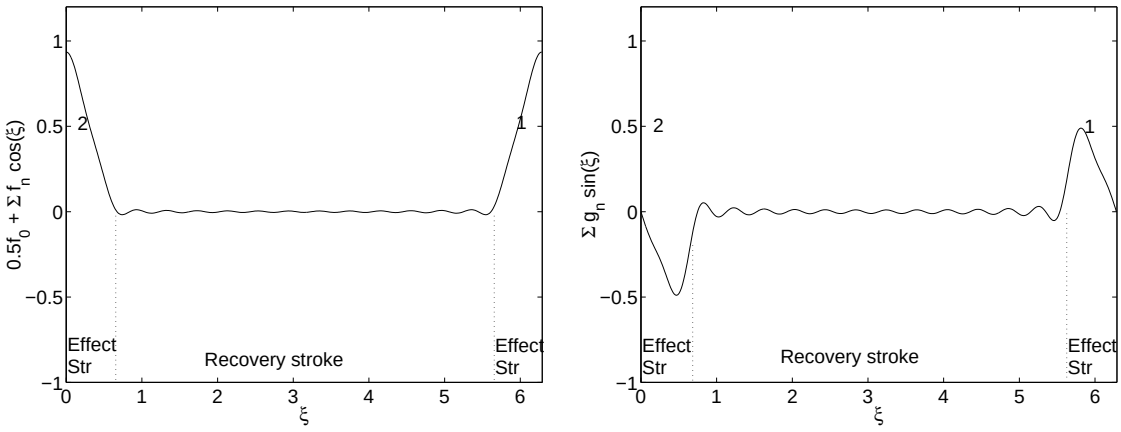

Figure 2.5: Horizontal and vertical cilium force—Fourier series representations $0.5f_0 + \sum f_n \cos(\xi), \sum g_n \sin(\xi), 0 < \xi < 2\pi$.

about the variation of velocity in this direction. A three dimensional model of PCL flow is developed in chapter 3.

2.4 Constitutive relations

The next step in solving (2.2) and (2.3) is to determine relations between stress and strain. We will consider the Newtonian PCL and non-Newtonian mucous layer separately.

2.4.1 Periciliary layer

Modelling the PCL as a Newtonian fluid, the constitutive equation is

$$\tau_{jk} \;=\; 2\mu^P d_{jk}. \tag{2.10}$$

τ_{jk} is the deviatoric part of the stress tensor, so that $\sigma_{jk} = -p\delta_{jk} + \tau_{jk}$. The quantity d_{jk} is the rate of strain tensor $(1/2)(u_{j,k} + u_{k,j})$. In this chapter we shall use the convention that subscript commas denote differentiation, so that $u_{j,k} = \partial u_j / \partial x_k$.

2.4.2 Mucous layer

Mucus is a highly complex polymer gel which exhibits, amongst other behaviours, shear-thinning, viscoelasticity, spinnability and adhesiveness (Puchelle et al., 1987). A detailed review of the composition, molecular structure and rheologic properties of mucus may be found in Sleigh et al. (1988). There exists a plethora of experimental results, with varying applicability to the *in vivo* system, due to differing experimental methods, mucus collection and storage techniques and variation within and between individuals. Mucin concentration and hydration of the layer, which are likely to vary throughout the lungs and with ambient conditions, and health will affect mucus rheology. It is also difficult to obtain uncontaminated and undisturbed mucus from the respiratory tract. Nor is it straightforward to determine how experiments should be interpreted, since only a rather complex rheological model—like that in Quemada (1984)—

could be fitted to a whole spectrum of experimental results. It also seems likely that, due to the varying strain rates, the rheological properties throughout the volume of the mucus are non uniform with, for instance, lower viscosity near the zone of ciliary penetration.

Previous experimental studies have concluded that viscoelasticity is one of the most crucial elements of the system for effective transport to occur. Meyer and Silberberg (1980) observed that in experiments on the transport of various mucus samples and mucus analogues on the excised frog palate, the loss modulus (associated with viscosity) was much less important to determining efficient transport than the storage modulus (associated with elasticity). They speculated that '...during the very brief period of the power stroke... the mucous layer must react elastically, i.e. with minimum relative slip. Then, over the beginning of the recovery stroke, a period of sufficient length must again be granted for the cilium to release itself from the contact of the mucus...' Hence we model mucus with an elastic component which allows it to deform and then recoil in response to penetration. For analytic simplicity we choose the Maxwell constitutive equation

$$\lambda_1 \frac{\delta \tau_{jk}}{\delta t} + \tau_{jk} \quad = \quad 2\mu^M d_{jk}, \tag{2.11}$$

with a single relaxation time λ_1 and a steady flow viscosity μ^M which will be equal to μ^{M1} or μ^{M2} depending on whether we are considering the traction layer or the force-free mucous layer. The operator $\delta/\delta t$ is a time derivative which is invariant under change of coordinates. It simplifies our analysis considerably if $\delta/\delta t$ can be approximated by the partial derivative $\partial/\partial t$. One example of an invariant rate is the co-rotational derivative

$$\frac{\delta \tau_{jk}}{\delta t} \quad = \quad \frac{\partial \tau_{jk}}{\partial t} + u_i \tau_{jk,i} - \frac{1}{2}(u_{j,i} - u_{i,j})\tau_{ik} + \frac{\tau_{ji}}{2}(u_{i,k} - u_{k,i}) \tag{2.12}$$

(Joseph, 1990), which translates and rotates with material points of the fluid. If we make the assumption that throughout most of the volume of mucus, the advective (second) term and

rotational (third and fourth) terms will be small, we recover the derivative $\partial/\partial t$, although in the region of penetration $h < z < L$, the penetration of the cilia will entail large velocity values, so that this approximation may not be justified. The linearised model will however provide more insight into the time-dependent nature of the flow than has previously been available—investigating the effect of non-linearity will be the subject of future work. Ross (1971) examined a Maxwell model of mucus with the co-rotational time derivative. He found that, subject to the amplitude of the ciliary tips being small, the non-linear terms did not enter the leading three terms of his asymptotic solution. With the linearisation, we have

$$\lambda_1 \frac{\partial \tau_{jk}}{\partial t} + \tau_{jk} \quad = \quad 2\mu^M d_{jk}. \tag{2.13}$$

In fact (Silberberg, 1983) mucus will possess a spectrum of relaxation mechanisms up to maybe $60\ \mathrm{s}$, due to varying lengths of polymer chains and different mechanisms by which the molecular network can deform. A more complete model would involve a number of Maxwell elements, but since we will restrict our attention to very short-lived deformations, we argue that one mechanism will provide a good representation. This model does not entail behaviours such as shear-thinning and so we will have to choose viscosity values appropriate to the shear rates observed in the muco-ciliary system.

Three different classes of experiments have been performed on mucus samples: steady shearing tests, creep tests and oscillatory tests. Steady shearing tests do not represent the dynamic conditions found in the lung, and apparently permanently destroy the structure of the mucus sample (Reid, 1973; Davis and Dippy, 1969). Creep tests give information on the time-dependent response of mucus, but are less suitable for short timescale behaviour (Fung, 1993). Oscillatory testing provides the most useful information. The techniques used have developed from the cone-and-plate rheometer used by Davis and Dippy (1969) to less destructive microrheometer techniques, as used by for example King and Macklem (1977). In the

cone-and-plate rheometer, the sample is subjected to a small amplitude oscillatory straining motion; in the microrheometer a small steel ball is oscillated under a magnetic field. Two constants are found: G', the storage modulus (associated with elasticity) and G'', the loss modulus (associated with viscosity). Fung (1993) describes how these constants can be related to our constitutive equation. The strain on the mucus will be of the form $\gamma = \gamma_0 \mathrm{e}^{i\omega t}$. For small oscillations the stress will respond sinusiodally, with a phase difference δ: $\tau = \tau_0 \mathrm{e}^{i(\omega t+\delta)}$. Then $G^* = G' + iG'' := \tau/\gamma$. Noting that $\dot{\tau} = i\omega\tau$ and $\dot{\gamma} = i\omega\gamma$ we can substitute into Maxwell's constitutive equation to show that

$$G' = \frac{\mu^M \omega^2 \lambda_1}{1+\omega^2\lambda_1^2}, \qquad G'' = \frac{\mu^M \omega}{1+\omega^2\lambda_1^2}. \tag{2.14}$$

As discussed above, a set of values for G' and G'' measured over a wide range of ω will lead to a widely varying set of values for μ^M and λ_1. We cannot fit the simple Maxwell model to a range of real experimental results. However if we choose a characteristic frequency of the system, 5–10 Hz, we can find appropriate values for μ^M and λ_1. In this study, we use the results published by Lutz et al. (1973) for canine tracheal mucus. At the frequency of 7.2497 Hz they reported values of $G' = 1$ Pa and $G'' = 0.64491$ Pa, which correspond to the parameters $\lambda_1 = 0.034$ s^{-1} and $\mu^M = 0.0482$ N m^{-2} s. Since $\mu^P \approx \mu^{\text{water}} \approx 0.001$ N m^{-2} s, we have $\mu^M/\mu^{\text{water}} = 48.2$.

2.5 Fourier series solution

Due to the periodicity of the ciliary beat, the force terms that drive the system are periodic. In addition, since we are testing the hypotonic defensin (impermeable epithelium) hypothesis, we take the boundary conditions on the epithelium to be constant, $\mathbf{u} = \mathbf{0}$. Neglecting airflows, the boundary conditions on the surface will also be homogeneous. Finally, we neglect any steady pressure gradient, because in the circular transport experiments of Matsui et al. (1998b), no

such pressure gradients could have been present, due to the fact that any such pressure must be continuous moving around one complete circle. Hence we assume that the solution $\mathbf{u}, p$ is periodic.

Writing all variables as Fourier series we have for example,

$$\tau_{jk} \quad = \quad \frac{(\tau_{jk})_0}{2} + \sum_{n=1}^{N} (\tau_{jk})_n, \tag{2.15}$$

where for $n \geq 1$, $(\tau_{jk})_n = a_n(z)\cos[n(\kappa x + \sigma t)] + b_n(z)\sin[n(\kappa x + \sigma t)]$, so that each $(\tau_{jk})_n$ is $2\pi/\kappa n$-periodic in $x + \sigma t/2\pi$. The term $(\tau_{jk})_0$ is independent of both x and t. It is then possible to equate terms with periodicity in $2\pi/\kappa n$ (and the terms constant in x and t). By writing

$$(\tau_{jk})_n \quad = \quad \mathrm{Rl}\{(\hat{\tau}_{jk})_n \mathrm{e}^{in\sigma t}\}, \tag{2.16}$$

hats being used with other variables analogously, Rl denoting real part, we convert from the 'time domain' to the 'frequency domain', in which the independent variable t is replaced by the frequency $n\sigma$. This results in a linear constitutive equation:

$$\mathrm{Rl}\{\lambda_1 in\sigma(\hat{\tau}_{jk})_n \mathrm{e}^{in\sigma t}\} + \mathrm{Rl}\{(\hat{\tau}_{jk})_n \mathrm{e}^{in\sigma t}\} \quad = \quad 2\mu^M \mathrm{Rl}\{(\hat{d}_{jk})_n \mathrm{e}^{in\sigma t}\}, \tag{2.17}$$

which leads to

$$(\hat{\tau}_{jk})_n \quad = \quad 2\mu^M \frac{1}{1 + in\sigma\lambda_1}(\hat{d}_{jk})_n, \quad = \quad \frac{2\mu^M}{\phi_n + i\psi_n}(\hat{d}_{jk})_n, \tag{2.18}$$

where $\phi_n = 1$, $\psi_n = n\sigma\lambda_1$.

For the steady term $(n = 0)$, we have the Newtonian constitutive equation

$$(\hat{\tau}_{jk})_0 \quad = \quad 2\mu^M (\hat{d}_{jk})_0. \tag{2.19}$$

2.6 Fluid flow equations

The subscripts are omitted in what follows, so that for instance $\mathbf{u}_n$ is written as $\mathbf{u}$.

2.6.1 Steady terms $(n = 0)$

In all three layers we have the Newtonian constitutive equations $\hat{\tau}_{jk} = 2\mu\hat{d}_{jk}$, for μ^P, μ^{M1}, μ^{M2}. This leads, with equation (2.2), to the familiar Stokes flow equations

$$\boldsymbol{\nabla}\hat{p} \;=\; \mu\nabla^2\hat{\mathbf{u}} + \hat{\mathbf{f}}. \tag{2.20}$$

Using the fact that $\hat{p}, \hat{\mathbf{u}}$ are constant in x_1, we have

$$\begin{aligned} 0 &= \mu\hat{u}_{1,33} + \hat{f}_1, \\ \hat{p}_{,3} &= \mu\hat{u}_{3,33} + \hat{f}_3. \end{aligned} \tag{2.21}$$

We shall see later that the vertical pressure gradient will also be zero.

2.6.2 Unsteady terms $(n \geqslant 1)$

In this section we show how in the frequency domain the momentum equations for the mucous layer are a complex form of the familiar Stokes flow momentum equations for each term in the Fourier series expansions of the velocity.

The transformed momentum equations are

$$\begin{aligned} \hat{\sigma}_{11,1} + \hat{\sigma}_{13,3} + \hat{f}_1 &= 0, \\ \hat{\sigma}_{31,1} + \hat{\sigma}_{33,3} + \hat{f}_3 &= 0. \end{aligned} \tag{2.22}$$

which are equivalent to

$$\begin{aligned} -\hat{p}_{,1} + \hat{\tau}_{11,1} + \hat{\tau}_{13,3} + \hat{f}_1 &= 0, \\ \hat{\tau}_{31,1} + \hat{\tau}_{33,3} - \hat{p}_{,3} + \hat{f}_3 &= 0. \end{aligned} \tag{2.23}$$

In the mucous layers, the stress is given by equation (2.18), so that

$$\begin{aligned} -\hat{p}_{,1} + 2\mu^M(\phi + i\psi)^{-1}(\hat{d}_{11,1} + \hat{d}_{13,3}) + \hat{f}_1 &= 0, \\ 2\mu^M(\phi + i\psi)^{-1}(\hat{d}_{31,1} + \hat{d}_{33,3}) - \hat{p}_{,3} + \hat{f}_3 &= 0, \end{aligned} \tag{2.24}$$

which can be rewritten as

$$\begin{aligned} -\hat{p}_{,1} + \mu^M(\phi + i\psi)^{-1}(2\hat{u}_{1,11} + \hat{u}_{1,33} + \hat{u}_{3,13}) + \hat{f}_1 &= 0, \\ \mu^M(\phi + i\psi)^{-1}(\hat{u}_{3,11} + \hat{u}_{1,31} + 2\hat{u}_{3,33}) - \hat{p}_{,3} + \hat{f}_3 &= 0. \end{aligned} \tag{2.25}$$

Using the continuity equation this simplifies to

$$\begin{aligned} -\hat{p}_{,1} + \mu^M(\phi + i\psi)^{-1}(\hat{u}_{1,11} + \hat{u}_{1,33}) + \hat{f}_1 &= 0, \\ \mu^M(\phi + i\psi)^{-1}(\hat{u}_{3,11} + \hat{u}_{3,33}) - \hat{p}_{,3} + \hat{f}_3 &= 0, \end{aligned} \tag{2.26}$$

or, in vector notation

$$\boldsymbol{\nabla}\hat{p} = \frac{\mu^M}{\phi + i\psi}\nabla^2\hat{\mathbf{u}} + \hat{\mathbf{f}}, \tag{2.27}$$

which can be recognised as the Stokes flow momentum equation with complex viscosity

$\mu^M/(\phi + i\psi)$. Similarly, in the PCL we have

$$\boldsymbol{\nabla}\hat{p} \;=\; \mu^P \nabla^2 \hat{\mathbf{u}} + \hat{\mathbf{f}}. \tag{2.28}$$

2.6.3 Force terms

In order to simplify the notation we replace u_1, u_3, x_1, x_3, f_1 and f_3 with u, v, x, z, f and g respectively. As before, we omit subscripts to denote the term in the Fourier series for the force, velocity and pressure. In the PCL the force terms are, for $n \geqslant 0$,

$$\begin{aligned} f &= -\gamma_x^P(u - \nu z\sigma c_n \cos((\kappa x + \sigma t)n), \\ g &= -\gamma_z^P(v - \nu z\sigma d_n \sin((\kappa x + \sigma t)n). \end{aligned} \tag{2.29}$$

Writing $u = \mathrm{Rl}\{(\breve{u}^r + i\breve{u}^i)\mathrm{e}^{in(\kappa x+\sigma t)}\}$, and similarly for other variables we have

$$\begin{aligned} \breve{f}^r &= -\gamma_x^P(\breve{u}^r - \nu z\sigma c_n), \qquad \breve{f}^i = -\gamma_x^P\breve{u}^i, \\ \breve{g}^i &= -\gamma_z^P(\breve{v}^i + \nu z\sigma d_n), \qquad \breve{g}^r = -\gamma_z^P\breve{v}^r \qquad \text{for} \quad 0 < z < h. \end{aligned} \tag{2.30}$$

In the traction layer the force terms are

$$\begin{aligned} f &= -U_{\mathrm{int}}\gamma_x^{M1} f_n \cos((\kappa x + \sigma t)n)\frac{\sin(\pi z/L)}{\sin(\pi h/L)}, \\ g &= -V_{\mathrm{int}}\gamma_z^{M1} g_n \sin((\kappa x + \sigma t)n)\frac{\sin(\pi z/L)}{\sin(\pi h/L)}. \end{aligned} \tag{2.31}$$

Writing out real and imaginary parts as above we have

$$\begin{aligned} \breve{f}^r &= -U_{\mathrm{int}}\gamma_x^{M1} f_n \frac{\sin(\pi z/L)}{\sin(\pi h/L)}, \qquad \breve{f}^i = 0, \\ \breve{g}^i &= V_{\mathrm{int}}\gamma_z^{M1} g_n \frac{\sin(\pi z/L)}{\sin(\pi h/L)}, \qquad \breve{g}^r = 0 \qquad \text{for} \quad h < z < L. \end{aligned}$$

2.7 Field equations and boundary conditions

2.7.1 Nondimensional field equations in the PCL

We nondimensionalise as follows: $x = \lambda x'$, $z = Lz'$, $u = \sigma L u'$, $v = (\sigma L^2/\lambda)v'$, $p = \mathcal{P}^P p'$, $f = (\mu^P \sigma/L) f'$. The scaling for v ensures that the continuity equation is balanced. For convenience we omit the primes. We shall also use h and H to represent the nondimensional parameters h/L and H/L. The terms $\hat{\mathbf{u}}$, $\hat{p}$ are now $1/n$-periodic in $2\pi x$.

For $n = 0$,

$$\begin{aligned} 0 &= \frac{\mu^P \sigma}{L} \frac{\mathrm{d}^2 \hat{u}}{\mathrm{d}z^2} + \frac{\mu^P \sigma}{L} \hat{f}, \\ \frac{\mathcal{P}^P}{L} \frac{\mathrm{d}\hat{p}}{\mathrm{d}z} &= \frac{\mu^P \sigma}{\lambda} \frac{\mathrm{d}^2 \hat{v}}{\mathrm{d}z^2} + \frac{\mu^P \sigma}{L} \hat{g}, \end{aligned} \tag{2.32}$$

and for $n \geqslant 1$,

$$\begin{aligned} \frac{\mathcal{P}^P}{\lambda} \frac{\partial \hat{p}}{\partial x} &= \mu^P \sigma L \left(\frac{1}{\lambda^2} \frac{\partial^2 \hat{u}}{\partial x^2} + \frac{1}{L^2} \frac{\partial^2 \hat{u}}{\partial z^2} \right) + \frac{\mu^P \sigma}{L} \hat{f}, \\ \frac{\mathcal{P}^P}{L} \frac{\partial \hat{p}}{\partial z} &= \frac{\mu^P \sigma L^2}{\lambda} \left(\frac{1}{\lambda^2} \frac{\partial^2 \hat{v}}{\partial x^2} + \frac{1}{L^2} \frac{\partial^2 \hat{v}}{\partial z^2} \right) + \frac{\mu^P \sigma}{L} \hat{g}. \end{aligned} \tag{2.33}$$

For $n = 0$, we have simply $\partial \hat{u}/\partial x = 0$, so by the continuity equation $\partial \hat{v}/\partial z = 0$. As discussed above, $\hat{v} = 0$ on $z = 0$ so $\hat{v} \equiv 0$ for all z. Since the zeroth term of the vertical force $\hat{g} = 0$, the second equation is then simply $\partial \hat{p}/\partial z = 0$, and so the pressure is constant. Hence

$$0 = \frac{\mathrm{d}^2 \hat{u}}{\mathrm{d}z^2} + \hat{f}. \tag{2.34}$$

For $n \geqslant 1$, in order to balance the first equation we choose the pressure scaling $\mathcal{P}^P = \mu^P \sigma \lambda / L$.

Hence

$$\begin{aligned}\frac{\partial \hat{p}}{\partial x} &= \frac{L^2}{\lambda^2}\frac{\partial^2 \hat{u}}{\partial x^2} + \frac{\partial^2 \hat{u}}{\partial z^2} + \hat{f}, \\ \frac{\partial \hat{p}}{\partial z} &= \frac{L^4}{\lambda^4}\frac{\partial^2 \hat{v}}{\partial x^2} + \frac{L^2}{\lambda^2}\frac{\partial^2 \hat{v}}{\partial z^2} + \frac{L}{\lambda}\hat{g}.\end{aligned} \tag{2.35}$$

It may appear that it is possible to apply lubrication theory, by noting that $L^2/\lambda^2 \ll 1$. However, the Fourier series representation of u means that $\hat{u} = (\check{u}^r + i\check{u}^i)\mathrm{e}^{2\pi n x i}$, so that $\partial^2\hat{u}/\partial x^2 = -4\pi^2 n^2 \hat{u}$. Using this representation, we can rewrite the real and imaginary parts of the $n \geqslant 1$ equations as

$$\begin{aligned}-2\pi n \check{p}^i &= -\chi^2 \check{u}^r + \frac{\mathrm{d}^2 \check{u}^r}{\mathrm{d}z^2} + \check{f}^r, \\ 2\pi n \check{p}^r &= -\chi^2 \check{u}^i + \frac{\mathrm{d}^2 \check{u}^i}{\mathrm{d}z^2} + \check{f}^i, \\ \frac{\mathrm{d}\check{p}^r}{\mathrm{d}z} &= -\chi^2\epsilon^2 \check{v}^r + \epsilon^2\frac{\mathrm{d}^2 \check{v}^r}{\mathrm{d}z^2} + \epsilon\check{g}^r, \\ \frac{\mathrm{d}\check{p}^i}{\mathrm{d}z} &= -\chi^2\epsilon^2 \check{v}^i + \epsilon^2\frac{\mathrm{d}^2 \check{v}^i}{\mathrm{d}z^2} + \epsilon\check{g}^i,\end{aligned} \tag{2.36}$$

where $\epsilon = L/\lambda$ and $\chi = 2\pi n\epsilon$. In general we do not have $\chi^2\epsilon^2 \ll 1$. Using the scaling $\mu^P\sigma/L$ for the force terms and using equation (2.30), we have for $n = 0$,

$$0 = \frac{\mathrm{d}^2 \check{u}^{r,i}}{\mathrm{d}z^2} - \alpha_x^2 \check{u}^{r,i}, \tag{2.37}$$

and for $n \geqslant 1$,

$$\begin{aligned} -2\pi n\check{p}^i &= -\beta_x^2\check{u}^r + \frac{\mathrm{d}^2\check{u}^r}{\mathrm{d}z^2} + \nu y c_n \alpha_x^2, \\ 2\pi n\check{p}^r &= -\beta_x^2\check{u}^i + \frac{\mathrm{d}^2\check{u}^i}{\mathrm{d}z^2}, \\ \frac{\mathrm{d}\check{p}^r}{\mathrm{d}z} &= -\beta_z^2\epsilon^2\check{v}^r + \epsilon^2\frac{\mathrm{d}^2\check{v}^r}{\mathrm{d}z^2}, \\ \frac{\mathrm{d}\check{p}^i}{\mathrm{d}z} &= -\beta_z^2\epsilon^2\check{v}^i + \epsilon^2\frac{\mathrm{d}^2\check{v}^i}{\mathrm{d}z^2} - \epsilon\nu z d_n \alpha_z^2, \end{aligned} \tag{2.38}$$

where the resistance parameters are defined as $\alpha_x^2 = \gamma_x^P L^2/\mu^P$, $\alpha_z^2 = \gamma_z^P L^2/\mu^P$, $\beta_x^2 = \chi^2 + \alpha_x^2$, $\beta_z^2 = \chi^2 + \alpha_z^2$. Note that α_x, α_z are independent of the value of the viscosity, and so also apply in the mucous layer.

2.7.2 Nondimensional field equations in the mucus

After nondimensionalising we have for $n = 0$,

$$\begin{aligned} 0 &= \frac{\mu^M\sigma}{L}\frac{\mathrm{d}^2\hat{u}}{\mathrm{d}z^2} + \frac{\mu^M\sigma}{L}\hat{f}, \\ \frac{\mathcal{P}^M}{L}\frac{\mathrm{d}\hat{p}}{\mathrm{d}z} &= \frac{\mu^M\sigma\mu^M}{\lambda}\frac{\mathrm{d}^2\hat{v}}{\mathrm{d}z^2} + \frac{\mu^M\sigma}{L}\hat{g}, \end{aligned} \tag{2.39}$$

and for $n \geqslant 1$,

$$\begin{aligned} \frac{\mathcal{P}^M}{\lambda}\frac{\partial\hat{p}}{\partial x} &= \frac{\mu^M\sigma L}{\phi + i\psi}\left(\frac{-4\pi^2n^2}{\lambda^2}\hat{u} + \frac{1}{L^2}\frac{\partial^2\hat{u}}{\partial z^2}\right) + \frac{\mu^M\sigma}{L}\hat{f}, \\ \frac{\mathcal{P}^M}{L}\frac{\partial\hat{p}}{\partial z} &= \frac{\mu^M\sigma L^2}{\lambda(\phi + i\psi)}\left(\frac{-4\pi^2n^2}{\lambda^2}\hat{v} + \frac{1}{L^2}\frac{\partial^2\hat{v}}{\partial z^2}\right) + \frac{\mu^M\sigma}{L}\hat{g}. \end{aligned} \tag{2.40}$$

This applies in both the traction layer, with viscosity μ^{M1}, and the force-free mucous layer μ^{M2}. As before, for $n = 0$, $\hat{v} \equiv 0$ so the velocity can be found from equation (2.34). For $n \geqslant 1$, in

order to balance the first equation we choose the pressure scaling $\mathcal{P}^M = \mu^M \sigma\lambda/(L[\phi + i\psi])$, so

$$\begin{aligned}
\frac{\partial \hat{p}}{\partial x} &= \left(\frac{-4\pi^2 n^2 L^2}{\lambda^2}\hat{u} + \frac{\partial^2 \hat{u}}{\partial z^2}\right) + (\phi + i\psi)\hat{f}, \\
\frac{\partial \hat{p}}{\partial z} &= \left(\frac{-4\pi^2 n^2 L^4}{\lambda^4}\hat{v} + \frac{L^2}{\lambda^2}\frac{\partial^2 \hat{v}}{\partial z^2}\right) + \frac{L(\phi + i\psi)}{\lambda}\hat{g}.
\end{aligned} \tag{2.41}$$

For $n = 0$, $\hat{p}$ is constant, which may be taken to be zero, so that the first equation is solved to give $\hat{u}$, then the continuity equation gives $\hat{v} \equiv 0$. Decomposing variables as previously we note that in terms of nondimensional variables,

$$\begin{aligned}
\check{f}^r &= -\frac{L}{\mu^{M1}\sigma}\sigma L U_{\rm int} f_n \gamma_x^{M1} \frac{\sin(\pi z)}{\sin(\pi h)}, \quad \check{f}^i = 0, \\
\check{g}^i &= \frac{L}{\mu^{M1}\sigma}\frac{\sigma L^2}{\lambda} V_{\rm int} g_n \gamma_z^{M1} \frac{\sin(\pi z)}{\sin(\pi h)}, \quad \check{g}^r = 0.
\end{aligned} \tag{2.42}$$

Hence we have, in the traction layer $h < z < 1$,

$$0 = \frac{\mathrm{d}^2 \check{u}^r}{\mathrm{d}z^2} - f_0 \alpha_x^2 U_{\rm int}\frac{\sin(\pi z)}{\sin(\pi h)}, \quad 0 = \frac{\mathrm{d}^2 \check{u}^i}{\mathrm{d}z^2} \quad \text{for} \quad n = 0, \tag{2.43}$$

and

$$\begin{aligned}
-2\pi n \check{p}^i &= -\chi^2 \check{u}^r + \frac{\mathrm{d}^2 \check{u}^r}{\mathrm{d}z^2} - \phi f_n \alpha_x^2 U_{\rm int}\frac{\sin(\pi z)}{\sin(\pi h)}, \\
2\pi n \check{p}^r &= -\chi^2 \check{u}^i + \frac{\mathrm{d}^2 \check{u}^i}{\mathrm{d}z^2} - \psi f_n \alpha_x^2 U_{\rm int}\frac{\sin(\pi z)}{\sin(\pi h)}, \\
\frac{\mathrm{d}\check{p}^r}{\mathrm{d}z} &= -\chi^2\epsilon^2 \check{v}^r + \epsilon^2\frac{\mathrm{d}^2 \check{v}^r}{\mathrm{d}z^2} - \epsilon\psi g_n \alpha_z^2 V_{\rm int}\frac{\sin(\pi z)}{\sin(\pi h)}, \\
\frac{\mathrm{d}\check{p}^i}{\mathrm{d}z} &= -\chi^2\epsilon^2 \check{v}^i + \epsilon^2\frac{\mathrm{d}^2 \check{v}^i}{\mathrm{d}z^2} + \epsilon\phi g_n \alpha_z^2 V_{\rm int}\frac{\sin(\pi z)}{\sin(\pi h)} \quad \text{for} \quad n \geqslant 1.
\end{aligned} \tag{2.44}$$

In the force-free mucous layer $1 < z < H$, the fluid flow equations are given by replacing f_n, g_n with zero in equations (2.43) and (2.44).

2.7.3 Continuity equation

The continuity equation (2.3) takes the same form in all three layers. As discussed above, for $n = 0$, $\partial u/\partial x = 0$, so $v \equiv 0$. For $n \geqslant 1$ we have

$$\begin{aligned} -2\pi n \check{u}^i + \frac{\mathrm{d}\check{v}^r}{\mathrm{d}z} &= 0, \\ 2\pi n \check{u}^r + \frac{\mathrm{d}\check{v}^i}{\mathrm{d}z} &= 0. \end{aligned} \tag{2.45}$$

In order to solve the system it will be convenient to differentiate these equations with respect to z,

$$\begin{aligned} -2\pi n \frac{\mathrm{d}\check{u}^i}{\mathrm{d}z} + \frac{\mathrm{d}^2\check{v}^r}{\mathrm{d}z^2} &= 0, \\ 2\pi n \frac{\mathrm{d}\check{u}^r}{\mathrm{d}z} + \frac{\mathrm{d}^2\check{v}^i}{\mathrm{d}z^2} &= 0. \end{aligned} \tag{2.46}$$

If we impose these conditions in each layer, along with the original mass conservation equation on one boundary and both interfaces, mass conservation will hold throughout the fluid.

2.7.4 Surface and interface tension

Surface tension forces will act on the mucus-air interface, and possibly at the interface between the mucus and PCL. By considering the surface as $\eta = H + \varepsilon\cos(\kappa x + \sigma t)$ and approximating the curvature as $|\eta_{xx}| = O(4\pi^2\varepsilon/\lambda^2)$, and by approximating the surface stress as $|\mu^{M2}\eta_t/L| = O(\mu^{M2}\varepsilon\sigma/L)$, we have the following estimate for the capillary number, the ratio of the magnitudes of surface tension to viscous forces,

$$\mathcal{C} = O\left(\frac{\lambda^2\mu^{M2}\sigma}{4\pi^2\mathcal{T}L}\right). \tag{2.47}$$

This is similar to the dimensionless number found by Ross (1971), only with an additional factor of $4\pi^2$. The parameter $\mathcal{T}$ denotes surface tension, while σ denotes radian frequency of the ciliary beat.

Albers et al. (1996) determined values of surface tension of sputum for patients with cystic fibrosis and chronic bronchitis, comparing two different experimental methods. The mean values for each condition and each method lay between 72 dyne$/$cm and 93 dyne$/$cm, so we estimate mucus surface tension by 80 dyne$/$cm, or 0.08 N$/$m in S. I. units. Using equation (2.47), and parameters in S. I. units, $\mathcal{T} = 0.08$, $L = 6 \times 10^{-6}$, $\lambda = 3 \times 10^{-5}$, $\mu^{M2} = 0.0482$ and $\sigma = 60$ we find that $\mathcal{C} = 1/7300$. This shows that surface tension forces will flatten the surface on a timescale much shorter than the ciliary beat duration, and explains why in the micrographs of Sanderson and Sleigh (1981), the mucus surface is remarkably flat, despite the rapid oscillations in velocity below. It is therefore reasonable to assume that surface tension flattens both the mucus surface and the mucus–PCL interface on a timescale much faster than the ciliary beat. We shall take the mucus–PCL interface to be a flat surface given by $z = h$ and the mucus surface to be given by $z = H$. The system will be solved with boundary conditions of zero normal velocity. This is discussed briefly in sections 2.12.6 and 2.12.8.

2.7.5 Traction layer mucus–PCL interface

Because we do not explicitly model the action of interface tension, it is not possible to calculate the normal stress balance on the interface. Instead we use the boundary condition of zero vertical velocity. Together with continuity of tangential stress we have, in tensor notation

$$\tau_{13}^{P} = \tau_{13}^{M1}, \qquad u_3^{M1} = 0. \tag{2.48}$$

Making the transformation to the frequency domain this becomes

$$\begin{aligned}
\mu^P(\hat{u}^P_{1,3}+\hat{u}^P_{3,1}) &= \mu^{M1}(\hat{u}^M_{1,3}+\hat{u}^M_{3,1}), & \hat{u}^{M1}_3 &= 0 \quad \text{for} \quad n=0,\\
\mu^P(\hat{u}^P_{1,3}+\hat{u}^P_{3,1}) &= \mu^{M1}(\phi_n+i\psi_n)^{-1}(\hat{u}^M_{1,3}+\hat{u}^M_{3,1}), & \hat{u}^{M1}_3 &= 0 \quad \text{for} \quad n\geqslant 1.
\end{aligned} \tag{2.49}$$

Nondimensionalising we have

$$\begin{aligned}
\left(\hat{u}^P_{1,3}+\epsilon^2\hat{u}^P_{3,1}\right) &= \theta_1(\hat{u}^{M1}_{1,3}+\epsilon^2\hat{u}^{M1}_{3,1}), & \hat{u}^{M1}_3 &= 0 \quad \text{for} \quad n=0,\\
(\phi+i\psi)\left(\hat{u}^P_{1,3}+\epsilon^2\hat{u}^P_{3,1}\right) &= \theta_1(\hat{u}^{M1}_{1,3}+\epsilon^2\hat{u}^{M1}_{3,1}), & \hat{u}^{M1}_3 &= 0 \quad \text{for} \quad n\geqslant 1.
\end{aligned}$$

As discussed above, for $n=0$, $\hat{u}_3=0$ and $\hat{p}=0$. Noting that $\partial\hat{u}_3/\partial x$=$2\pi n i\hat{u}_3$, and writing $u_1=u$, $u_3=v$ as above,

$$\frac{\partial\hat{u}^P}{\partial z} = \theta_1\frac{\partial\hat{u}^{M1}}{\partial z}, \tag{2.50}$$

where we define the viscosity ratios θ_1 and θ_2 for μ^{M1}/μ^P and μ^{M2}/μ^{M1} respectively. For $n\geqslant 1$,

$$(\phi+i\psi)\left(\frac{\partial\hat{u}^P}{\partial z}+2\pi n i\epsilon^2\hat{v}^P\right) = \theta_1\left(\frac{\partial\hat{u}^{M1}}{\partial z}+2\pi n i\epsilon^2\hat{v}^{M1}\right), \qquad \hat{v}^{M1} = 0. \tag{2.51}$$

There is now only one matching condition for $n=0$, which is appropriate since the vertical component of the momentum equation is trivially satisfied. By taking real and imaginary parts,

$$\frac{\mathrm{d}\breve{u}^{r,i\,P}}{\mathrm{d}z} = \theta_1\frac{\mathrm{d}\breve{u}^{r,i\,M1}}{\mathrm{d}z}, \tag{2.52}$$

and for $n \geqslant 1$,

$$\begin{aligned}
\frac{\phi}{\theta_1}\frac{\mathrm{d}\check{u}^{r\,P}}{\mathrm{d}z} - \frac{\psi}{\theta_1}\frac{\mathrm{d}\check{u}^{i\,P}}{\mathrm{d}z} - \frac{2\pi n\epsilon^2}{\theta_1}\left(\phi\check{v}^{i\,P} + \psi\check{v}^{r\,P}\right) &= \frac{\mathrm{d}\check{u}^{r\,M1}}{\mathrm{d}z} - 2\pi n\epsilon^2\check{v}^{i\,M1}, \\
\frac{\phi}{\theta_1}\frac{\mathrm{d}\check{u}^{i\,P}}{\mathrm{d}z} + \frac{\psi}{\theta_1}\frac{\mathrm{d}\check{u}^{r\,P}}{\mathrm{d}z} + \frac{2\pi n\epsilon^2}{\theta_1}\left(\phi\check{v}^{r\,P} - \psi\check{v}^{i\,P}\right) &= \frac{\mathrm{d}\check{u}^{i\,M1}}{\mathrm{d}z} + 2\pi n\epsilon^2\check{v}^{r\,M1}, \\
\check{v}^{r\,M1} &= 0, \\
\check{v}^{i\,M1} &= 0. \qquad (2.53)
\end{aligned}$$

2.7.6 Upper mucous–traction layer interface

At $z = 1$ there is an 'interface' between the shear-thinned traction layer subject to the propulsive force of the cilia, and the upper mucous layer free from volume forces. We assume that there is no interface tension acting since the mucus is essentially one fluid. This leaves us to consider continuity of both tangential and normal stress,

$$\tau_{13}^{M1} = \tau_{13}^{M2}, \quad -p^{M1} + \tau_{33}^{M1} = -p^{M2} + \tau_{33}^{M2}. \qquad (2.54)$$

We nondimensionalise with pressure scalings $\mathcal{P}^{M1,\,M2} = \mu^{M1,\,M2}\sigma\lambda/([\phi + i\psi]L)$. Taking real and imaginary parts for $n = 0$,

$$\frac{\mathrm{d}\check{u}^{r\,M1}}{\mathrm{d}z} = \theta_2\frac{\mathrm{d}\check{u}^{r\,M2}}{\mathrm{d}z}, \qquad \frac{\mathrm{d}\check{u}^{i\,M1}}{\mathrm{d}z} = \theta_2\frac{\mathrm{d}\check{u}^{i\,M2}}{\mathrm{d}z}, \qquad (2.55)$$

and for $n \geqslant 1$,

$$\begin{aligned}
\frac{\mathrm{d}\check{u}^{r\,M1}}{\mathrm{d}z} - 2\pi n\epsilon^2 \check{v}^{i\,M1} &= \theta_2\left(\frac{\mathrm{d}\check{u}^{r\,M2}}{\mathrm{d}z} - 2\pi n\epsilon^2\check{v}^{i\,M2}\right), \\
\frac{\mathrm{d}\check{u}^{i\,M1}}{\mathrm{d}z} + 2\pi n\epsilon^2 \check{v}^{r\,M1} &= \theta_2\left(\frac{\mathrm{d}\check{u}^{i\,M2}}{\mathrm{d}z} + 2\pi n\epsilon^2\check{v}^{r\,M2}\right), \qquad (2.56) \\
-\check{p}^{r\,M1} + 2\epsilon^2\frac{\mathrm{d}\check{v}^{r\,M1}}{\mathrm{d}z} &= -\theta_2\check{p}^{r\,M2} + 2\theta_2\epsilon^2\frac{\mathrm{d}\check{v}^{r\,M2}}{\mathrm{d}z}, \\
-\check{p}^{i\,M1} + 2\epsilon^2\frac{\mathrm{d}\check{v}^{i\,M1}}{\mathrm{d}z} &= -\theta_2\check{p}^{i\,M2} + 2\theta_2\epsilon^2\frac{\mathrm{d}\check{v}^{i\,M2}}{\mathrm{d}z}. \qquad (2.57)
\end{aligned}$$

2.7.7 Mucus free surface

Neglecting the viscosity of air, supposing that the air pressure is constant, and making the assumption that the mucus surface is flat, we have for the tangential stress $\sigma_{1k}n_k = 0$ where $\mathbf{n} = (0, 0, 1)$. As for the mucus–PCL interface we replace the normal stress balance with the condition that the vertical velocity is zero. The conditions are therefore

$$\tau_{13}^{M2} = 0, \qquad \hat{u}_3^{M2} = 0. \qquad (2.58)$$

These are transformed into, for $n = 0$,

$$\mu^{M2}(\hat{u}_{1,3}^{M2} + \hat{u}_{3,1}^{M2}) = 0, \qquad \hat{u}_3^{M2} = 0, \qquad (2.59)$$

and for $n \geqslant 1$,

$$\frac{\mu^{M2}}{\phi + i\psi}(\hat{u}_{1,3}^{M2} + \hat{u}_{3,1}^{M2}) = 0, \qquad \hat{u}_3^{M2} = 0. \qquad (2.60)$$

Nondimensionalising as above and taking real and imaginary parts, for $n = 0$,

$$\frac{\mathrm{d}\check{u}^{r\,M2}}{\mathrm{d}z} = 0, \qquad \frac{\mathrm{d}\check{u}^{i\,M2}}{\mathrm{d}z} = 0, \qquad (2.61)$$

and for $n \geqslant 1$,

$$\begin{aligned} \frac{\mathrm{d}\check{u}^{r\,M2}}{\mathrm{d}z} - 2\pi n\epsilon^2 \check{v}^{i\,M2} &= 0, & \frac{\mathrm{d}\check{u}^{i\,M2}}{\mathrm{d}z} + 2\pi n\epsilon^2 \check{v}^{r\,M2} &= 0, \\ \check{v}^{r\,M2} &= 0, & \check{v}^{i\,M2} &= 0. \end{aligned} \tag{2.62}$$

2.7.8 No-slip conditions

As discussed above, we assume that there is no flow through the epithelium, so that $v = 0$ on $z = 0$ for all n. For viscous flow we have the no-slip boundary condition $u = 0$ on the solid interface at $z = 0$. Finally, the fluid velocity will be continuous across the boundaries, so that $u^P = u^{M1}$, $v^P = v^{M1}$ on $z = h$ and $u^{M1} = u^{M2}$, $v^{M1} = v^{M2}$ on $z = 1$.

For $n = 0$ we have six variables, $\check{u}^{r\,P}$, $\check{u}^{i\,P}$, $\check{u}^{r\,M1}$, $\check{u}^{i\,M1}$, $\check{u}^{r\,M2}$, $\check{u}^{i\,M2}$, 6 second order ODEs from the u component of the momentum equations, and 12 boundary and matching conditions. The ODEs are linear with constant coefficients and so can be solved analytically.

For $n \geqslant 1$ we have additionally $\check{v}^{r\,P}$, $\check{v}^{i\,P}$, $\check{v}^{r\,M1}$, $\check{v}^{i\,M1}$, $\check{v}^{r\,M2}$, $\check{v}^{i\,M2}$, $\check{p}^{r\,P}$, $\check{p}^{i\,P}$, $\check{p}^{r\,M1}$, $\check{p}^{i\,M1}$, $\check{p}^{r\,M2}$, $\check{p}^{i\,M2}$, a total of 18 variables. By counting the first derivatives of the velocity terms as variables, we have a total of 30. There are 12 momentum equations, given in sections 2.7.1 and 2.7.2, and 6 equations following from mass conservation, given in 2.7.3. Using the first derivatives of the velocity terms, the second order momentum equations can be rewritten as 24 first order ODEs, giving a total of 30. There are 4 no-slip boundary conditions, 8 conditions for continuity of velocity, 12 conditions for continuity of stress, given in sections 2.7.5, 2.7.6 and 2.7.7, and 6 conditions to enforce conservation of mass, as discussed in section 2.7.3. This gives a total of 30 boundary and matching conditions in total, closing the system.

2.8 Steady flow solution for $n = 0$

It is now possible to solve for the steady term of the fluid velocity analytically. It is easily seen that $\check{u}^i = 0$ is the solution for the imaginary part of the momentum equations. Hence $u = \check{u}^r$.

We have the momentum equations

$$\begin{aligned} -\alpha_x^2 u^P + \frac{\mathrm{d}^2 u^P}{\mathrm{d}z^2} &= 0, \\ \frac{\mathrm{d}^2 u^{M1}}{\mathrm{d}z^2} &= \alpha_x^2 U_{\mathrm{int}} f_0 \frac{\sin(\pi z)}{\sin(\pi h)}, \\ \frac{\mathrm{d}^2 u^{M2}}{\mathrm{d}z^2} &= 0, \end{aligned} \tag{2.63}$$

boundary conditions,

$$u^P = 0 \quad \text{at} \quad z = 0, \qquad \frac{\mathrm{d}u^{M2}}{\mathrm{d}z} = 0 \quad \text{at} \quad z = H, \tag{2.64}$$

and matching conditions,

$$\begin{aligned} u^P &= u^{M1}, & \frac{\mathrm{d}u^P}{\mathrm{d}z} &= \theta_1 \frac{\mathrm{d}u^{M1}}{\mathrm{d}z} & \text{at} \quad z = h, \\ u^{M1} &= u^{M2}, & \frac{\mathrm{d}u^{M1}}{\mathrm{d}z} &= \theta_2 \frac{\mathrm{d}u^{M2}}{\mathrm{d}z} & \text{at} \quad z = 1. \end{aligned} \tag{2.65}$$

The parameters $\theta_1 := \mu^{M1}/\mu^P$ and $\theta_2 := \mu^{M2}/\mu^{M1}$ are the viscosity ratios between neighbouring layers. These are integrated to give the solution

$$\begin{aligned} u^P &= -\frac{U_{\mathrm{int}} f_0 \alpha_x \theta_1 (1 + \cos(\pi h)) \sinh(\alpha_x z)}{\pi \sin(\pi h) \cosh(\alpha_x h)}, \\ u^{M1} &= -\frac{U_{\mathrm{int}} f_0 \alpha_x^2}{\pi \sin(\pi h)} \left\{ \frac{\theta_1}{\alpha_x} \tanh(\alpha_x h)(1 + \cos(\pi h)) + z + \frac{\sin(\pi z)}{\pi} - h - \frac{\sin(\pi h)}{\pi} \right\}, \\ u^{M2} &= -\frac{U_{\mathrm{int}} f_0 \alpha_x^2}{\pi \sin(\pi h)} \left\{ \frac{\theta_1}{\alpha_x} \tanh(\alpha_x h)(1 + \cos(\pi h)) + 1 - h - \frac{\sin(\pi h)}{\pi} \right\}. \end{aligned} \tag{2.66}$$

The constant U_{int} is determined in section 2.9.2, and through this the mean transport depends additionally on λ_1 and θ_2. The solution is very simple in form—throughout the region $z > 1$, the velocity is constant. In the penetration region $h < z < 1$ the velocity is approximately linear. In the region $z < h$, the solution is approximately proportional to the exponential

$\mathrm{e}^{\alpha_x(z-h)}$ in a region of size $O(1/\alpha_x)$ near the interface, and very close to zero elsewhere, for $\alpha_x \gg 1$. Solutions are shown in Figures 2.6(D) to 2.10(D), and 2.12(D) to 2.16(D). Immediately we notice some similarity between our mean profiles and that of Fulford and Blake (1986), as shown in Figure 1.3, although it should be noted that Fulford and Blake (1986) predicted significant transport of PCL above $z = 0.6L$, whereas we predict significant transport above $z = 0.85L$.

Recalling that $u = (1/2)u_0 + \sum_{n=1}^{N} u_n$ where the u_n terms average to zero in time, for $\alpha_x \gg 1$ we have PCL flux

$$\int_0^h u \, \mathrm{d}z \quad \sim \quad \frac{-U_{\mathrm{int}} f_0 \theta_1 (1 + \cos(\pi h))}{2\pi \sin(\pi h)} + O\left(\mathrm{e}^{-\alpha_x h}\right), \tag{2.67}$$

and mucus flux

$$\begin{aligned} \int_h^H u \, \mathrm{d}z \quad \sim \quad & \frac{-U_{\mathrm{int}} f_0}{2\pi \sin(\pi h)} \left\{ \frac{1}{2}(1-h)(2H-h-1) + \frac{1+\cos(\pi h)}{\pi^2} - \frac{\sin(\pi h)}{\pi}(H-h) \right\} \\ & + O\left(\alpha_x^{-1}\right). \end{aligned} \tag{2.68}$$

Numerical values for the flux are given in sections 2.10.4 and 2.12.7

2.9 Analytical solution for $n \geqslant 1$

2.9.1 Analysis

By neglecting surface tension at $z = H$ and making certain simplifying assumptions, we may reduce the system to one which can be solved analytically. In section 2.12 we present numerical results without this simplification, which will provide insight into the importance of surface tension, and the resulting pressure gradients, in the mucous layer.

If surface tension is neglected, the correct normal stress boundary condition at the free

surface is

$$-\hat{p}^{M2} + \hat{\tau}_{33}^{M2} = 0, \tag{2.69}$$

where we assume that the air pressure above the mucus is constant. Without loss of generality, we may take this constant to be zero. Proceeding as for equation 2.44 and making the assumption that $2\epsilon^2 \check{v}^{r\,\prime}$, $2\epsilon^2 \check{v}^{i\,\prime}$ are small on the mucus free surface, using equation (2.57) we have $p^{M2} = 0$ on $z = H$. By neglecting terms of order ϵ^2 and setting $V_{\text{int}} = 0$ (justified in section 2.9.2) in the field equations, it follows that $\mathrm{d}p/\mathrm{d}z = 0$ and so the pressure is constant and equal to zero across the force-free mucous layer $1 < z < H$. By proceeding similarly, and neglecting the vertical force component in the traction layer, we deduce that p^{M1} is also zero across the traction layer $h < z < 1$. On the mucus–PCL interface, the presence of the ϕ and ψ terms makes it more difficult to justify setting the pressure to zero. However, by neglecting terms of order ϵ in the field equations (2.38), we can show that p^P is constant. This analysis removes six equations—the real and imaginary parts of the z components of the momentum equations in each of the three layers, and four variables—the real and imaginary parts of the pressure $\check{p}^r$ and $\check{p}^i$ in the two mucous layers. In order to implement our initial analytical model, we neglect the $2\pi n\epsilon^2 \check{v}^r$ and $2\pi n\epsilon^2 \check{v}^i$ terms from the stress matching conditions and free surface boundary conditions, which results in the decoupling of u and v. For the numerical solution this simplification will not be necessary. In order that the system is fully determined we require some additional conditions for the pressure. The approach we take is to require that the mucus–PCL interface is flat, as discussed above. Then by considering conservation of mass in the form

$$\frac{\partial u}{\partial x} + \frac{\partial v}{\partial z} \;=\; 0, \tag{2.70}$$

we require that $\int_0^h \hat{u}\,\mathrm{d}z$ is constant. This condition allows us to determine the pressure.

The system then consists of 6 momentum equations for the horizontal velocity and pressure,

and 6 continuity equations which relate the horizontal and vertical velocity. Rewriting $\hat{u} = (\check{u}^r + i\check{u}^i)\mathrm{e}^{2\pi nxi}$ for simplicity we have, for $n \geqslant 1$, the ODEs

$$\begin{aligned}
\Pi &= -\beta_x^2 \hat{u}^P + \frac{\mathrm{d}^2 \hat{u}^P}{\mathrm{d}z^2} + \nu z c_n \alpha_x^2, \\
0 &= -\chi^2 \hat{u}^{M1} + \frac{\mathrm{d}^2 \hat{u}^{M1}}{\mathrm{d}z^2} + U_{\mathrm{int}} f_n(\phi + i\psi) \frac{\sin(\pi z)}{\sin(\pi h)} \mathrm{e}^{2\pi nxi}, \\
0 &= -\chi^2 \hat{u}^{M2} + \frac{\mathrm{d}^2 \hat{u}^{M2}}{\mathrm{d}z^2},
\end{aligned} \tag{2.71}$$

where Π is the (nth component of the) pressure gradient $\mathrm{d}p/\mathrm{d}x$. The boundary conditions are now

$$\hat{u} = 0 \quad \text{at} \quad z = 0, \qquad \frac{\mathrm{d}\hat{u}}{\mathrm{d}z} = 0 \quad \text{at} \quad z = H, \tag{2.72}$$

and the matching conditions are

$$\begin{aligned}
(\phi + \psi)\frac{\mathrm{d}\hat{u}^P}{\mathrm{d}z} &= \theta_1 \frac{\mathrm{d}\hat{u}^{M1}}{\mathrm{d}z}, \qquad \hat{u}^P = \hat{u}^{M1} \qquad \text{at} \quad z = h, \\
\frac{\mathrm{d}\hat{u}^{M1}}{\mathrm{d}z} &= \theta_2 \frac{\mathrm{d}\hat{u}^{M2}}{\mathrm{d}z}, \qquad \hat{u}^{M1} = \hat{u}^{M2} \qquad \text{at} \quad z = 1.
\end{aligned} \tag{2.73}$$

The momentum equations can be solved to give $\hat{u}$ in terms of the pressure, the vertical velocity $\hat{v}$ can then be found from the continuity equations and finally the pressure can be determined from the assumption that the mucus–PCL interface does not move vertically. In order to simplify the analysis, we first find a solution $\hat{u}^\Pi$ of the porous medium equation with a constant pressure gradient Π

$$-\beta_x^2 + \frac{\mathrm{d}^2 \hat{u}^\Pi}{\mathrm{d}z^2} = \Pi \quad \text{for} \quad n \geqslant 1, \tag{2.74}$$

with boundary conditions $\hat{u} = 0$ on $z = 0, h$. Once $\hat{u}^\Pi$ is found, we then define $\hat{u}^C = \hat{u}^P - \hat{u}^\Pi$

and solve the ODE

$$-\beta_x^2 + \frac{\mathrm{d}^2\hat{u}^C}{\mathrm{d}z^2} = -\nu c_n \alpha_x^2 z \mathrm{e}^{2\pi n x i}, \tag{2.75}$$

coupled with the equations for layers 2 and 3, with an altered stress matching condition at $z = h$. We find that

$$\hat{u}^\Pi = \frac{\Pi \mathrm{e}^{2\pi n x i}}{\beta_x^2}\left(\cosh(\beta_x z) - 1 - \frac{\sinh(\beta_x z)}{\sinh(\beta_x h)}(\cosh(\beta_x h) - 1)\right). \tag{2.76}$$

The stress matching condition at $z = h$ then becomes

$$(\phi + i\psi)\left(\frac{\mathrm{d}\hat{u}^C}{\mathrm{d}z} + \frac{\mathrm{d}\hat{u}^\Pi}{\mathrm{d}z}\right) = \theta_2 \frac{\mathrm{d}\hat{u}^{M1}}{\mathrm{d}z}, \tag{2.77}$$

the remaining conditions for $\hat{u}^C$ are the same as for $\hat{u}^P$. For $n \geqslant 1$ we have the following equations to solve, for each term in the Fourier series for u

$$\begin{aligned} -\beta_x^2\hat{u}^\Pi + \frac{\mathrm{d}^2\hat{u}^\Pi}{\mathrm{d}z^2} &= -\nu c_n \alpha_x^2 z \mathrm{e}^{2\pi n x i}, \\ -\chi^2\hat{u}^{M1} + \frac{\mathrm{d}^2\hat{u}^{M1}}{\mathrm{d}z^2} &= -U_{\mathrm{int}} f_n \alpha_x^2 (\phi + i\psi)\frac{\sin(\pi z)}{\sin(\pi h)}\mathrm{e}^{2\pi n x i}, \\ -\chi^2\hat{u}^{M2} + \frac{\mathrm{d}^2\hat{u}^{M2}}{\mathrm{d}z^2} &= 0. \end{aligned} \tag{2.78}$$

Solving these equations for the hatted variables, and then transforming back to the time domain we obtain the x-components of the velocity. The solutions are given in appendix B.

2.9.2 Determining the interaction velocity U_{int}

The constant U_{int} is undetermined in equation (2.78). We do this by the following rationale: in order for the solution to be self-consistent, U_{int} should be equal to $u - u_{\mathrm{cilia}}$ evaluated at $z = h$. We impose the condition at the midpoint of the effective stroke, $2\pi x + \sigma t = 0$. By starting

with an initial estimate of U_{int}, together with upper and lower bounds, we calculate the velocity terms for $n = 0$ from equation (2.8) and the terms for $n = 1, \ldots, 15$ from equation (B.4), which are then summed to give the horizontal velocity u at the point $x = 0$, $z = h$, $t = 0$. We evaluate $u - u_{\text{cilia}}$, and adjust U_{int} using interval bisection. The solution is then recalculated and the process is continued until convergence is achieved. For example, with our standard parameter set given in section 2.10.1, we obtained $U_{\text{int}} = -0.0246963$, $u - u_{\text{cilia}} = -0.0246979$. We choose the Fourier series representation, given in Figure 2.3, to determine u for this purpose. It may be argued that we should choose instead the 'ideal' value from Figure 2.2, however even the ideal value is an approximate representation of the real beat cycle, and our choice of the Fourier series value is fully consistent with the flow in the PCL which is governed by the Fourier series representation of u_{cilia}.

2.10 Analytical results and discussion

2.10.1 Standard parameter set

In Figure 2.6 we present some profiles of the solutions u and v for the following physiologically reasonable 'standard' parameter set: $L = 6\ \mu\text{m}$, $\lambda = 30\ \mu\text{m}$, $H = 10\ \mu\text{m}$, $h = 5.4\ \mu\text{m}$, $\sigma = 60\ \text{rad/s}$, $\lambda_1 = 0.03$ s, $\theta_1 = 6$, $\theta_2 = 8$, $\alpha_x = 90$, $\nu = 5/6$. The viscosity ratios θ_1 and θ_2 were chosen so that $\theta_1\theta_2 = 48$, corresponding to approximately the viscosity value $\mu^M = 0.0482\ \text{N m}^{-2}\ \text{s}$ found in section 2.4. The resistance coefficient α_x is defined as in equations (2.6) and (2.38), and determined from the parameters $d = 0.3\ \mu\text{m}$ for the cilia spacing and $r_0 = 0.1\ \mu\text{m}$ for the cilium radius.

Figure 2.6(A) shows the horizontal velocity profile at five different points along the wavelength. The trace furthest to the right corresponds to the effective stroke. There is a large forward flow of mucus close to the point of penetration, decaying exponentially to a value of over $100\ \mu\text{m/s}$ at the top of the mucous layer. In the PCL there is approximately equal forward and backward flow at the top and bottom of the layer, caused by the pressure gradient which

maintains the interface at a constant height. It may appear surprising that so close to the epithelium, the fluid velocity is relatively large. This is due to the effect of a large positive pressure gradient acting to maintain conservation of mass in the face of a large shearing motion in the active porous medium. If the fluid flowed with the cilia, it would be propelled rapidly forwards at this point, leading to a large positive vertical velocity, deforming the interface. Since the cilia will be beating 'forwards' in this region, it should be realised that the backflow is a mean negative flow if we average in the y direction (into the paper). The fluid will flow backwards between the cilia, but very near to the cilium surface will be propelled forward. Due to the strong viscous coupling between the cilia, the pressure gradient is very large in magnitude, the term Π_1 having an absolute value of 1447 for the standard parameter set. Around the beginning and the end of the recovery stroke, there is a smaller forward flow of mucus throughout the layer, apparently due to the mucus being 'pulled' forward by the mucus further ahead and behind undergoing the effective stroke. During the middle of the recovery stroke the mucus moves forwards much more slowly or actually flows backwards. In the PCL, the profile is the reverse of that seen during the effective stroke, only with smaller magnitude due to the slower cilia movement.

Figure 2.6(B) shows the vertical velocity component v. Throughout the entire PCL, the velocity is very small relative to the velocities found in the mucous layer. It would be expected that in reality the vertical movement of the cilia would result in significant velocities in the PCL, but since this level of detail was not present in this simplified model, it is not borne out by the results. There are however large oscillations in the mucous layer, particularly around the effective stroke, where the vertical velocity of the mucus surface reaches $250\ \mu\mathrm{m/s}$. This would cause significant movement of the mucus surface, and hence our assumption that the mucus surface is flat is inconsistent. By constraining the mucus surface to be flat due to surface tension, as in the full numerical system, the model will be self-consistent. Figure 2.11 shows the velocity field for this parameter set in a different way, using arrows to represent the velocity vector at

various points in the fluid. This shows very clearly the differences between the analytical results, and the numerical results shown in Figure 2.17, which exhibit circulation patterns in the PCL during part of the recovery stroke.

Figure 2.6(C) shows that the mucus surface undergoes positive horizontal transport throughout the beat cycle, while the mucus around the traction layer undergoes both positive and negative flow, although we can see from the mean velocity trace on graph (D) that the entire mucous layer above $z = L$ undergoes the same mean transport. We also observe a small phase lag between the peak velocity at the mucus surface and mucus–PCL interface, due to the viscoelasticity of the mucus. Interestingly, this phase lag is much smaller for the full model shown in Figure 2.12(C).

Figure 2.6(D) shows that the mean transport throughout most of the PCL is very close to zero. This agrees somewhat with the work of Fulford and Blake (1986), as depicted in Figure 1.3, and is very different from the profiles suggested by Matsui et al. (1998b). We anticipate this because we have modelled the sublayer as a field of very strong viscous resistance, represented in our model by the coefficient $\alpha_x = 90$. The total flux of PCL is very much smaller than the total flux of mucus. Figure 2.6(D) also depicts the instantaneous peak horizontal velocity. We notice that in the traction layer region, the peak velocity is over ten times the size of the mean velocity. On the mucus surface, the ratio is closer to three times.

2.10.2 Mean mucus transport

Our results using the standard parameter set predict a mean mucus velocity of $36.3\ \mu\mathrm{m/s}$. Salathe et al. (1997) report a range of values of between $67\ \mu$m/s and $333\ \mu$m/s. The authors believed that the first figure, based on less invasive measuring techniques, is more accurate. Reviewing the results of similar studies, International Commission on Radiological Protection and Measurements (1994) reported a wide range of values depending upon disease, ambient conditions and other factors. For healthy subjects, values of $70\ \mu$m/s and $92\ \mu$m/s for tracheal

transport, and $40\ \mu$m/s for bronchial transport were reported. Finally, the hTBE cultures studied by Matsui et al. (1998b) showed a mean transport of $39.2\ \mu\mathrm{m/s}$, very close to our predicted value.

2.10.3 Different parameter sets

Figures 2.7 to 2.10 show corresponding results where one parameter at a time has been adjusted. In Figure 2.7, the viscosity ratios are adjusted to $\theta_1 = 12$, $\theta_2 = 4$, so that the absolute mucus viscosity in $1 < z < H$ is the same, but we are simulating a smaller shear-thinning effect in the traction layer. Since we do not appear to have any clear data on the shear-thinning effect, this parameter set is as plausible as the previous. The profiles are almost identical, the only significant difference being that the mucus transport is reduced to $30.9\ \mu\mathrm{m/s}$, and the vertical mucus velocity is around $50\ \mu\mathrm{m/s}$ smaller in magnitude. In section 2.12.6 we investigate the effect of the shear-thinning ratio on mean mucus velocity more systematically.

In Figure 2.8 we simulate slower ciliary beating with $\sigma = 36$. The graphs are very similar to the standard parameter set, only with smaller amplitude oscillations, and the transport speed reduced to $23.5\ \mu\mathrm{m/s}$. A 40% reduction in beat frequency leads to a 35.3% reduction in transport. We might expect a reduction in σ to reduce the mucus velocity proportionately due to the velocity scaling σL. The reduction is not quite so large since the viscoelastic interaction of the mucus and cilia is altered. This interaction is discussed in more detail in §2.12.5

In Figure 2.9 we reduce the time constant for relaxation of stress to $\lambda_1 = 0.01$ s. The effect is an increase in transport speed to $44.1\ \mu\mathrm{m/s}$, together with smaller peak values for the horizontal and vertical velocity. It is interesting that less elastic mucus leads to more rapid transport, and indeed if we set $\lambda_1 = 0$, we obtain a transport speed of $57.6\ \mu\mathrm{m/s}$. The price that has to be paid for this, however, is that the force on the cilia tips as they propel the mucus is proportionately higher—$f \propto U_{\mathrm{int}} \propto u$, all else being held constant. It might be anticipated that this would reduce the rate of ciliary beating. In addition, a non-Newtonian mucous layer,

by permitting larger oscillations than a Newtonian one, may produce better mixing and hence better transport of contaminants—this will be the subject of chapter 4. Larger oscillations may also help to create a continuous mucous layer in the first place, as mucus production in the lower reaches of the respiratory tree is patchy (International Commission on Radiological Protection and Measurements, 1994). It is also possible that an elastic mucous layer will interact differently with the penetrating cilia than a Newtonian one, although investigating this is beyond the scope of this model. The profiles shown are slightly different from the profiles for the standard parameter set, with the mucus surface velocity being positive throughout the beat cycle, the vertical oscillations being of smaller magnitude, and there being a much smaller lag between the velocity at the interface and at $z = 1$.

Figure 2.10 shows the effect of slightly thickening the mucous layer to $12\ \mu\mathrm{m}$. This does not have a significant effect beyond slightly increasing the transport speed to $36.8\ \mu\mathrm{m}$, and slightly increasing the vertical oscillations on the upper mucus surface. A full discussion of the way in which different physical parameters affect mucus tranport is given in §2.12.

2.10.4 PCL and mucus flux results

For the standard parameter set, $U_{\mathrm{int}} = -0.0247$. Using equation (2.67), we have a nondimensional PCL flux of 7.47×10^{-4}. This corresponds to a dimensional value of $1.61\ \mu\mathrm{m}^2/\mathrm{s}$. This compares with a mucus flux of 7.66×10^{-2}, corresponding to a dimensional value of $165\ \mu\mathrm{m}^2/\mathrm{s}$.

2.11 Numerical solution for $n \geqslant 1$

Rather than making the assumptions above, we may instead solve the full ODE system directly using the NAG routine D02GAF (NAG, 1993). This approach has the advantages that both the surface and interface may be constrained to be flat, pressure gradients in all three layers are retained, and vertical variations in the pressure are also permitted. The algorithm D02GAF starts with an initial approximation calculated from the boundary conditions and estimates of

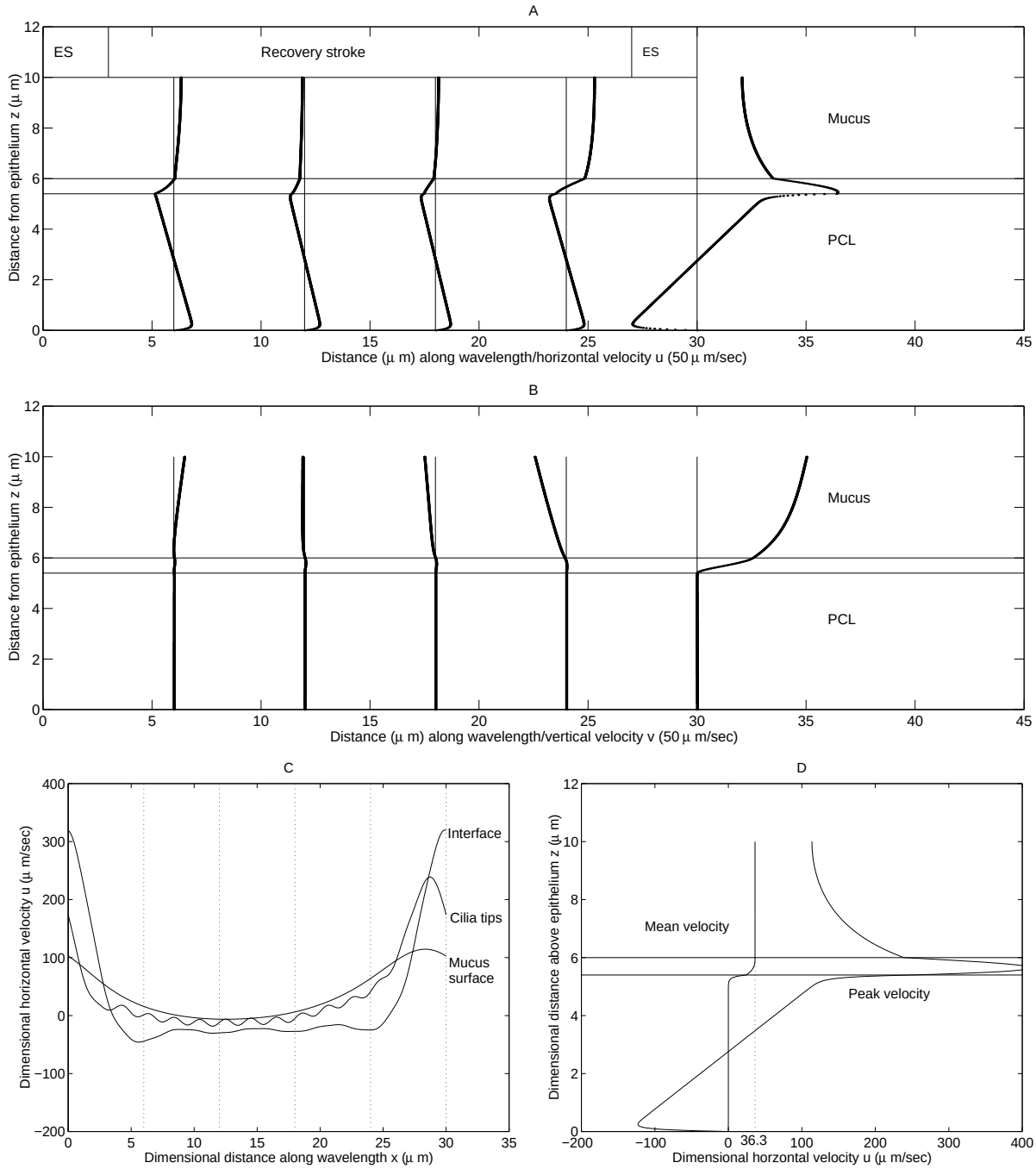

Figure 2.6: Traction layer analytical results. A—horizontal velocity profiles at five points along the wavelength versus distance from epithelium. B—vertical velocity profiles at five points along the wavelength versus distance from epithelium. C—horizontal velocity at three different levels in the ASL, the mucus–PCL interface, the cilia tips $z = L$ and the mucus surface $z = H$, versus distance along the wavelength. D—mean and peak horizontal velocity versus height above the epithelium. Dimensional parameter values: $L = 6\ \mu\mathrm{m}$, $\lambda = 30\ \mu\mathrm{m}$, $H = 10\ \mu\mathrm{m}$, $h = 5.4\ \mu\mathrm{m}$, $\sigma = 60\ \mathrm{rad/s}$, $\lambda_1 = 0.03$ s. Viscosity ratios $\theta_1 = 6$, $\theta_2 = 8$. Sublayer resistance coefficient $\alpha_x = 90$, sublayer velocity scaling $\nu = 5/6$.

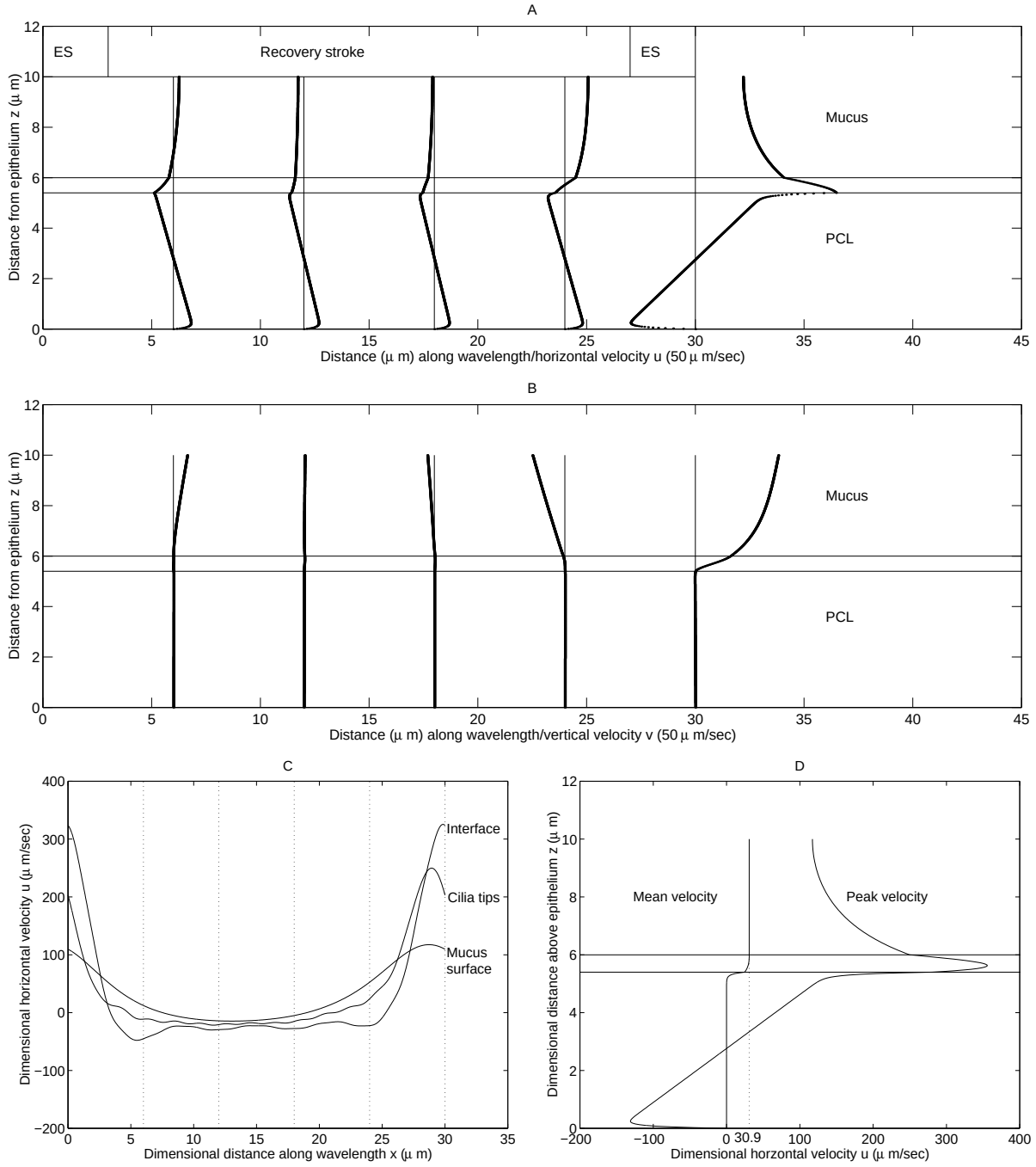

Figure 2.7: Traction layer analytical results—less shear-thinning. Dimensional parameter values: $L = 6\ \mu\mathrm{m}$, $\lambda = 30\ \mu\mathrm{m}$, $H = 10\ \mu\mathrm{m}$, $h = 5.4\ \mu\mathrm{m}$, $\sigma = 60\ \mathrm{rad/s}$, $\lambda_1 = 0.03$ s. Viscosity ratios $\theta_1 = 12$, $\theta_2 = 4$. Sublayer resistance coefficient $\alpha_x = 90$, sublayer velocity scaling $\nu = 5/6$.

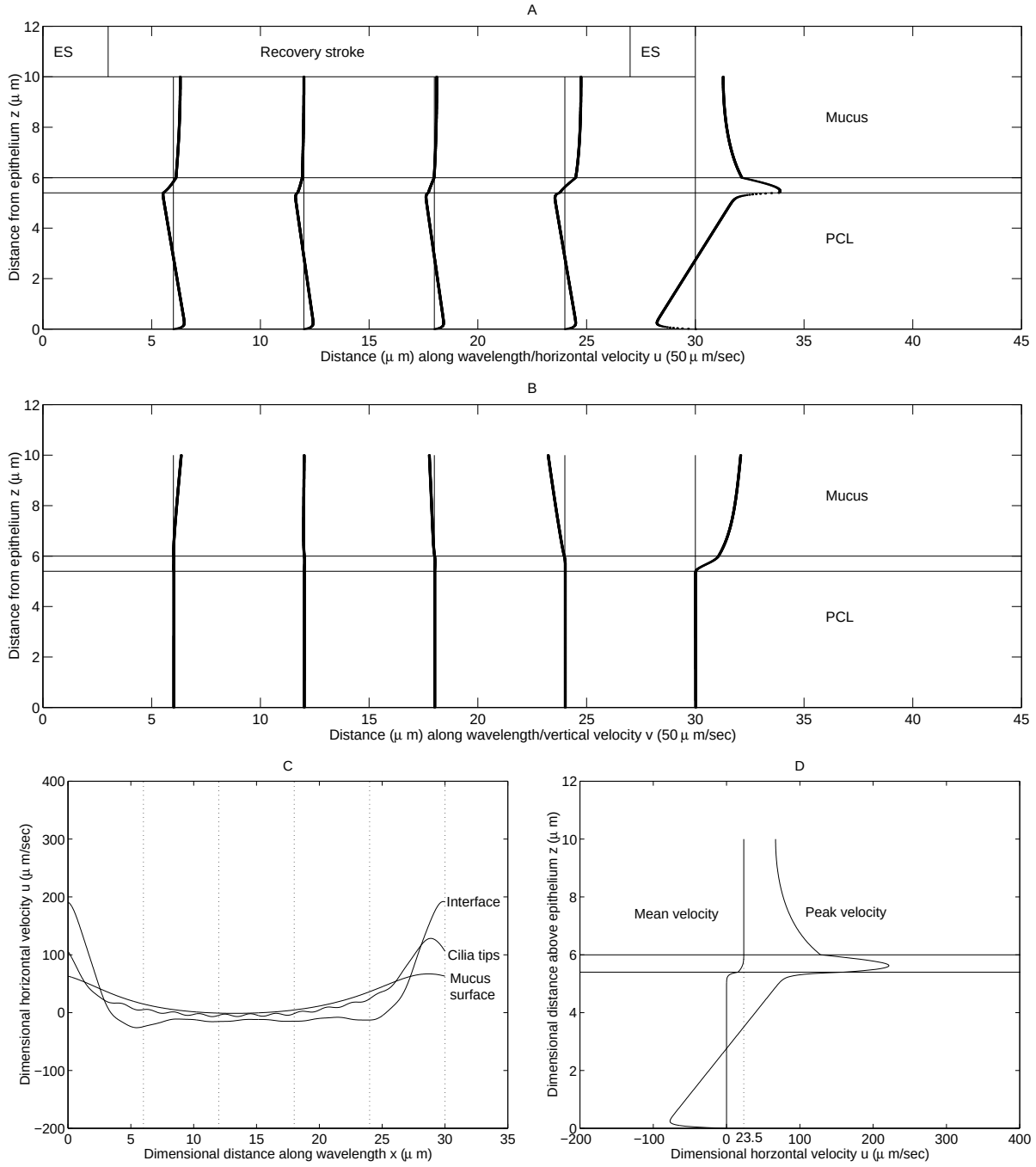

Figure 2.8: Traction layer analytical results—slower ciliary beating. Dimensional parameter values: $L = 6\ \mu\mathrm{m}$, $\lambda = 30\ \mu\mathrm{m}$, $H = 10\ \mu\mathrm{m}$, $h = 5.4\ \mu\mathrm{m}$, $\sigma = 36\ \mathrm{rad/s}$, $\lambda_1 = 0.03$ s. Viscosity ratios $\theta_1 = 6$, $\theta_2 = 8$. Sublayer resistance coefficient $\alpha_x = 90$, sublayer velocity scaling $\nu = 5/6$.

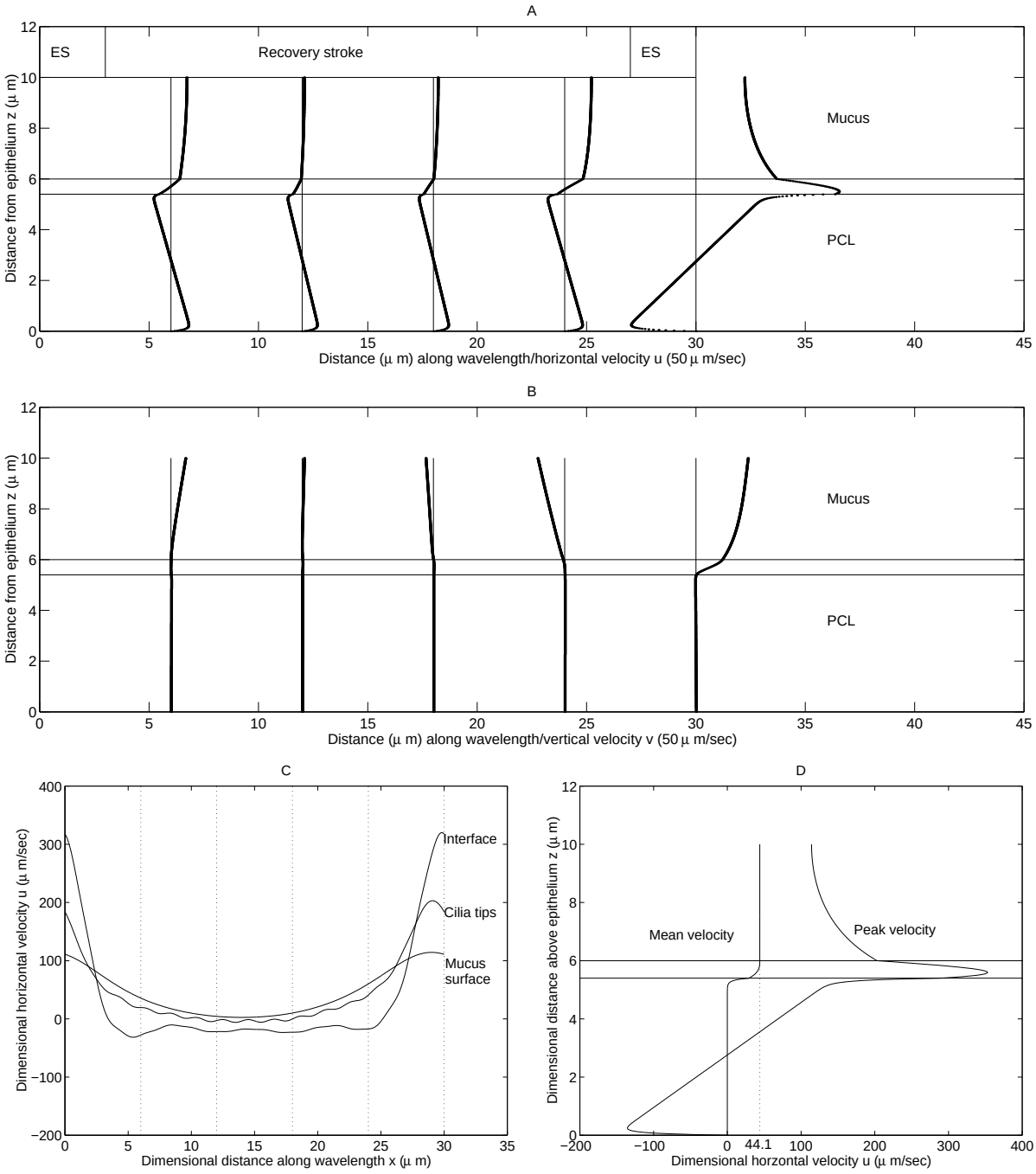

Figure 2.9: Traction layer analytical results—less elastic mucus. Dimensional parameter values: $L = 6\ \mu\text{m}$, $\lambda = 30\ \mu\text{m}$, $H = 10\ \mu\text{m}$, $h = 5.4\ \mu\text{m}$, $\sigma = 60\ \text{rad/s}$, $\lambda_1 = 0.01$ s. Viscosity ratios $\theta_1 = 6$, $\theta_2 = 8$. Sublayer resistance coefficient $\alpha = 90$, sublayer velocity scaling $\nu = 5/6$.

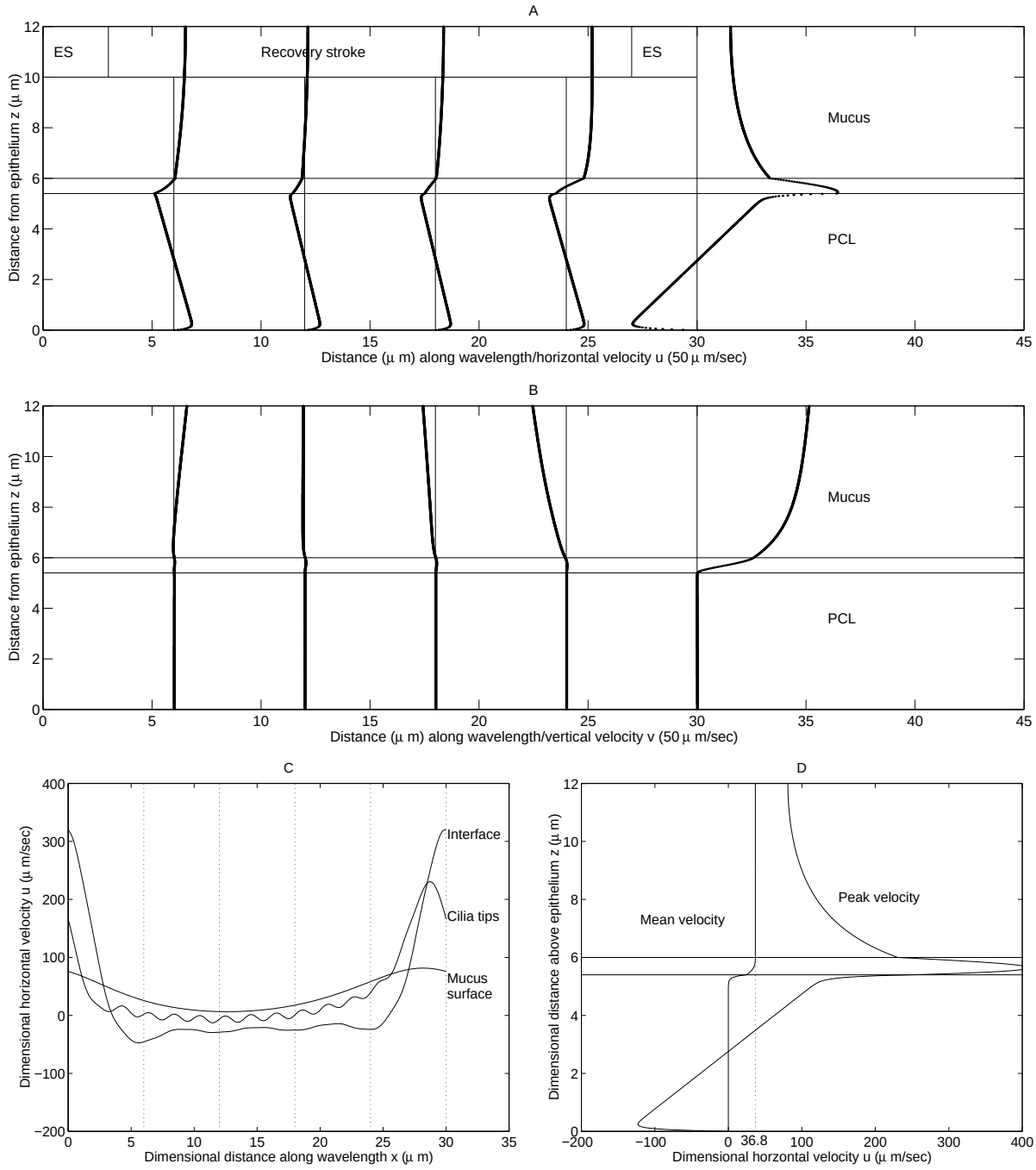

Figure 2.10: Traction layer analytical results—deeper mucus. Dimensional parameter values: $L = 6\ \mu\mathrm{m}$, $\lambda = 30\ \mu\mathrm{m}$, $H = 12\ \mu\mathrm{m}$, $h = 5.4\ \mu\mathrm{m}$, $\sigma = 60\ \mathrm{rad/s}$, $\lambda_1 = 0.03$ s. Viscosity ratios $\theta_1 = 6$, $\theta_2 = 8$. Sublayer resistance coefficient $\alpha = 90$, sublayer velocity scaling $\nu = 5/6$.

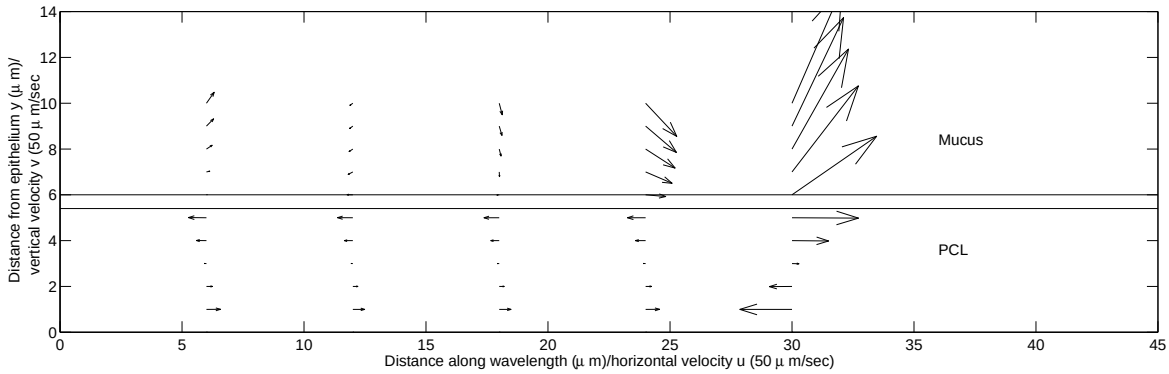

Figure 2.11: Traction layer analytical results—quiver plot of the velocity field for the 'standard' parameter set $L = 6\ \mu\mathrm{m}$, $\lambda = 30\ \mu\mathrm{m}$, $H = 10\ \mu\mathrm{m}$, $h = 5.4\ \mu\mathrm{m}$, $\sigma = 60\ \mathrm{rad/s}$, $\lambda_1 = 0.03$ s. Viscosity ratios $\theta_1 = 6$, $\theta_2 = 8$. Sublayer resistance coefficient $\alpha_x = 90$, sublayer velocity scaling $\nu = 5/6$.

the solution at boundary points for which there is no boundary condition. This is then improved using a finite difference technique with deferred correction.

2.11.1 Transforming the domain

In order to solve the system numerically it must be rewritten in the form

$$Y_i' \quad = \quad F_i(X, Y_1, \ldots, Y_{30}), \tag{2.79}$$

for $i = 1, \ldots, 30$, and solved on a domain $0 < X < 1$. We make the following transformations: In the PCL,

$$z \quad = \quad hX, \qquad \frac{\mathrm{d}}{\mathrm{d}z} \quad = \quad \frac{1}{h}\frac{\mathrm{d}}{\mathrm{d}X}, \qquad z = 0 \ldots h, \quad X = 0 \ldots 1. \tag{2.80}$$

In the traction layer,

$$z \quad = \quad 1 - (1-h)X, \qquad \frac{\mathrm{d}}{\mathrm{d}z} \quad = \quad \frac{-1}{1-h}\frac{\mathrm{d}}{\mathrm{d}X}, \qquad z = h \ldots 1, \quad X = 1 \ldots 0. \tag{2.81}$$

In the force-free mucous layer,

$$z = 1 + (H-1)X, \qquad \frac{\mathrm{d}}{\mathrm{d}z} = \frac{1}{H-1}\frac{\mathrm{d}}{\mathrm{d}X}, \qquad z = 1 \ldots H, \quad X = 0 \ldots 1. \tag{2.82}$$

2.11.2 Variables of the ODE system

We now define the variables $Y_1, \ldots, Y_{30}$ in order to write the boundary and matching conditions in the form $Y_i = 0$ at $X = 0$ or $X = 1$.

$$Y_1 = \check{u}^r_P \qquad Y_{11} = \check{u}^r_P - \check{u}^r_{M1}$$

$$Y_2 = \check{u}^i_P \qquad Y_{12} = \check{u}^i_P - \check{u}^i_{M1}$$

$$Y_3 = \check{v}^r_P \qquad Y_{13} = \check{v}^r_P - \check{v}^r_{M1}$$

$$Y_4 = \check{v}^i_P \qquad Y_{14} = \check{v}^i_P - \check{v}^i_{M1}$$

$$Y_5 = -2\pi n \check{u}^i_P + \check{v}^{r\prime}_P/h \qquad Y_{15} = -2\pi n \check{u}^i_{M1} - \check{v}^{r\prime}_{M1}/(1-h)$$

$$Y_6 = 2\pi n \check{u}^r_P + \check{v}^{i\prime}_P/h$$

$$Y_7 = \phi \check{u}^{r\prime}_P/h - \psi \check{u}^{i\prime}_P/h - 2\pi n \epsilon^2(\phi \check{v}^i_P + \psi \check{v}^{i\prime}_P - \theta_1 \check{v}^i_{M1}) + \theta_1 \check{u}^{r\prime}_{M1}/(1-h)$$

$$Y_8 = \phi \check{u}^{i\prime}_P/h + \psi \check{u}^{r\prime}_P/h - 2\pi n \epsilon^2(\psi \check{v}^i_P - \phi \check{v}^{i\prime}_P + \theta_1 \check{v}^r_{M1}) + \theta_1 \check{u}^{i\prime}_{M1}/(1-h)$$

$$Y_9 = \check{p}^r_P$$

$$Y_{10} = \check{p}^i_P$$

$$Y_{16} = 2\pi n \check{u}^r_{M1} - \check{v}^{i\prime}_{M1}/(1-h)$$

$$Y_{17} = -\check{u}^{r\prime}_{M1}/(1-h) - 2\pi n \epsilon^2 \check{v}^i_{M1} - \theta_2 \check{u}^{r\prime}_{M2}/(H-1) + 2\pi n \theta_2 \epsilon^2 \check{v}^i_{M2}$$

$$Y_{18} = -\check{u}^{i\prime}_{M1}/(1-h) + 2\pi n \epsilon^2 \check{v}^r_{M1} - \theta_2 \check{u}^{i\prime}_{M2}/(H-1) - 2\pi n \theta_2 \epsilon^2 \check{v}^r_{M2}$$

$$Y_{19} = -\check{p}^r_{M1} - 2\epsilon^2 \check{v}^{r\prime}_{M1}/(1-h) + \theta_2 \check{p}^r_{M2} - 2\theta_2 \epsilon^2 \check{v}^{r\prime}_{M2}/(H-1)$$

$$Y_{20} = -\check{p}^i_{M1} - 2\epsilon^2 \check{v}^{i\prime}_{M1}/(1-h) + \theta_2 \check{p}^i_{M2} - 2\theta_2 \epsilon^2 \check{v}^{i\prime}_{M2}/(H-1)$$

$$Y_{21} = \check{u}^r_{M1} - \check{u}^r_{M2} \qquad Y_{26} = 2\pi n\check{u}^r_{M2} + \check{v}^{i\prime}_{M2}/(H-1)$$
$$Y_{22} = \check{u}^i_{M1} - \check{u}^i_{M2} \qquad Y_{27} = \check{u}^{r\prime}_{M2}/(H-1) - 2\pi n\epsilon^2\check{v}^i_{M2}$$
$$Y_{23} = \check{v}^r_{M1} - \check{v}^r_{M2} \qquad Y_{28} = \check{u}^{i\prime}_{M2}/(H-1) + 2\pi n\epsilon^2\check{v}^r_{M2}$$
$$Y_{24} = \check{v}^i_{M1} - \check{v}^i_{M2} \qquad Y_{29} = \check{p}^r_{M2}$$
$$Y_{25} = -2\pi n\check{u}^i_{M2} + \check{v}^{r\prime}_{M2}/(H-1) \qquad Y_{30} = \check{p}^i_{M2}.$$

The boundary conditions take the form $Y_i = 0$ on $X = 0$ for $i = 1, ..., 6, 17, ..., 26$, and $Y_i = 0$ on $X = 1$ for $i = 3, 4$, $i = 7, 8$, $i = 11, ..., 16$, $i = 23, 24, 27, 28$. There are no boundary conditions for the pressure Y_9, Y_{10}, Y_{29} and Y_{30}, but two boundary conditions for Y_3, Y_4, Y_{23} and Y_{24}, so that there are 30 boundary conditions for 30 variables. Writing the system of 18 ODEs in terms of these variables we have

$$h(\phi^2+\psi^2)(-2\pi nY_{10} + (\beta_x^2+\chi^2)Y_1 - \nu X h c_n \alpha_x^2 - 2\pi n\epsilon^2 Y_6)$$
$$= \phi Y_7' + \psi Y_8' + \theta_1\phi Y_{17}' + \theta_1\theta_2\psi Y_{27}' + \theta_1\psi Y_{18}' + \theta_1\theta_2\psi Y_{28}'$$

$$h(\phi^2+\psi^2)(2\pi nY_9 + (\beta_x^2+\chi^2)Y_2 + 2\pi n\epsilon^2 Y_5)$$
$$= \phi Y_8' - \psi Y_7' - \theta_1\psi Y_{17}' - \theta_1\theta_2\phi Y_{27}' + \theta_1\phi Y_{18}' + \theta_1\theta_2\phi Y_{28}'$$

$$(\phi^2+\psi^2)(Y_9' + (\chi^2+\beta_z^2)\epsilon^2 h Y_3)$$
$$= 2\pi nh\epsilon^2[\phi Y_8 - \psi Y_7 - \theta_1\psi Y_{17} - \theta_1\theta_2\psi Y_{27} + \theta_1\phi Y_{18} + \theta_1\theta_2\phi Y_{28}]$$

$$(\phi^2+\psi^2)(Y_{10}' + (\chi^2+\beta_z^2)\epsilon^2 h Y_4)$$
$$= -2\pi nh\epsilon^2[\phi Y_7 + \psi Y_8 + \theta_1\phi Y_{17} + \theta_1\theta_2\phi Y_{27} + \theta_1\psi Y_{18} + \theta_1\theta_2\psi Y_{28}]$$
$$-\nu h^2 d_n \alpha_z^2 \epsilon(\phi^2+\psi^2)X$$

$$Y_5' = 0$$

$$Y_6' = 0$$

$$-2\pi n[-Y_{20}+2\epsilon^2 Y_{16}+\theta_2 Y_{30}]-2\chi^2\theta_2(Y_1-Y_{11}-Y_{21})+4\pi n\theta_2\epsilon^2 Y_{26}$$
$$=-4\chi^2(Y_1-Y_{11})-(Y'_{17}+\theta_2 Y'_{27})/(1-h)+2\pi n\epsilon^2 Y_{16}$$
$$-\phi f_n\alpha_x^2 U_{\rm int}\sin(\pi(1-(1-h)X))/\sin(\pi h)$$

$$2\pi n[-Y_{19}+2\epsilon^2 Y_{15}+\theta_2 Y_{29}]-2\chi^2\theta_2(Y_2-Y_{12}-Y_{22})-4\pi n\theta_2\epsilon^2 Y_{25}$$
$$=-4\chi^2(Y_2-Y_{12})-(Y'_{18}+\theta_2 Y'_{28})/(1-h)-2\pi n\epsilon^2 Y_{15}$$
$$-\psi f_n\alpha_x^2 U_{\rm int}\sin(\pi(1-(1-h)X))/\sin(\pi h)$$

$$Y'_{19}-4\pi n\epsilon^2(Y'_2-Y'_{12})-\theta_2 Y'_{29}-4\pi n\epsilon^2\theta_2(Y_2-Y_{12}-Y_{22})=(1-h)\cdot$$
$$(-2\chi^2\epsilon^2(Y_3-Y_{13})+2\pi n(Y_{18}+\theta_2 Y_{28})-\epsilon\psi g_n\alpha_z^2 V_{\rm int}\sin(\pi(1-(1-h)X))/\sin(\pi h))$$

$$Y'_{20}+4\pi n\epsilon^2(Y'_1-Y'_{11})-\theta_2 Y'_{30}+4\pi n\epsilon^2\theta_2(Y_1-Y_{11}-Y_{21})=(1-h)\cdot$$
$$(-2\chi^2\epsilon^2(Y_4-Y_{14})-2\pi n(Y_{17}+\theta_2 Y_{27})+\epsilon\phi g_n\alpha_z^2 V_{\rm int}\sin(\pi(1-(1-h)X))/\sin(\pi h))$$

$$Y'_{15}=0$$

$$Y'_{16}=0$$

$$Y'_{27}=(H-1)(2\chi^2(Y_1-Y_{11}-Y_{21})-2\pi n\epsilon^2 Y_{26}-2\pi n Y_{30})$$

$$Y'_{28}=(H-1)(2\chi^2(Y_2-Y_{12}-Y_{22})+2\pi n\epsilon^2 Y_{25}+2\pi n Y_{29})$$

$$Y'_{29}=(H-1)(-2\chi^2(Y_3-Y_{13}-Y_{23})+2\pi n\epsilon^2 Y_{28})$$

$$Y'_{30}=(H-1)(-2\chi^2(Y_4-Y_{14}-Y_{24})-2\pi n\epsilon^2 Y_{27})$$

$$Y'_{25}=0$$

$$Y'_{26}=0.$$

In addition we have 12 equations that follow from the definitions of the Y_is,

$$hY_5 = -2\pi n Y_2 h + Y_3'$$

$$hY_6 = 2\pi n Y_1 h + Y_4'$$

$$Y_7 = (\phi/h + \theta_1/(1-h))Y_1' - 2\pi n\epsilon^2\phi Y_4 - (\psi/h)Y_2' - 2\pi n\epsilon^2\psi Y_3$$
$$-\theta_1 Y_{11}'/(1-h) + 2\pi n\epsilon^2\theta_1(Y_4 - Y_{14})$$

$$Y_8 = (\phi/h + \theta_1/(1-h))Y_2' + 2\pi n\epsilon^2\phi Y_3 + (\psi/h)Y_1' - 2\pi n\epsilon^2\psi Y_4$$
$$-\theta_1 Y_{12}'/(1-h) - 2\pi n\epsilon^2\theta_1(Y_3 - Y_{13})$$

$$Y_{15}(1-h) = -2\pi n(Y_2 - Y_{12})(1-h) - (Y_3' - Y_{13}')$$

$$Y_{16}(1-h) = 2\pi n(Y_1 - Y_{11})(1-h) - (Y_4' - Y_{14}')$$

$$Y_{17}(1-h) = Y_{11}' - Y_1' - 2\pi n\epsilon^2(Y_4 - Y_{14})(1-h) - \theta_2(Y_1' - Y_{11}' - Y_{21}')(1-h)/(H-1)$$
$$+2\pi n\theta_2\epsilon^2(Y_4 - Y_{14} - Y_{24})(1-h)$$

$$Y_{18}(1-h) = Y_{12}' - Y_2' + 2\pi n\epsilon^2(Y_3 - Y_{13})(1-h) - \theta_2(Y_2' - Y_{12}' - Y_{22}')(1-h)/(H-1)$$
$$-2\pi n\theta_2\epsilon^2(Y_3 - Y_{13} - Y_{23})(1-h)$$

$$Y_{25} = -2\pi n(Y_2 - Y_{12} - Y_{22}) + (Y_3' - Y_{13}' - Y_{23}')/(H-1)$$

$$Y_{26} = 2\pi n(Y_1 - Y_{11} - Y_{21}) + (Y_4' - Y_{14}' - Y_{24}')/(H-1)$$

$$Y_{27} = -2\pi n\epsilon^2(Y_4 - Y_{14} - Y_{24}) + (Y_1' - Y_{11}' - Y_{21}')/(H-1)$$

$$Y_{28} = 2\pi n\epsilon^2(Y_3 - Y_{13} - Y_{23}) + (Y_2' - Y_{12}' - Y_{22}')/(H-1).$$

This can be rearranged to give a system of 30 first order equations that can be solved numerically, as given in appendix C.

2.12 Numerical results and discussion

2.12.1 Comparing the numerical and analytical profiles

In Figures 2.12–2.16, we present graphs of the numerical results, corresponding to the graphs given for the analytical results in Figures 2.6–2.10. Again, the 'standard' parameter set which we use for reference is $L = 6\ \mu$m, $\lambda = 30\ \mu$m, $H = 10\ \mu$m, $h = 5.4\ \mu$m, $\sigma = 60$ rad/s, $\lambda_1 = 0.03$ s, $\theta_1 = 6$, $\theta_2 = 8$, $\alpha_x = 90$ and for the numerical model only, $\alpha_z = 75$.

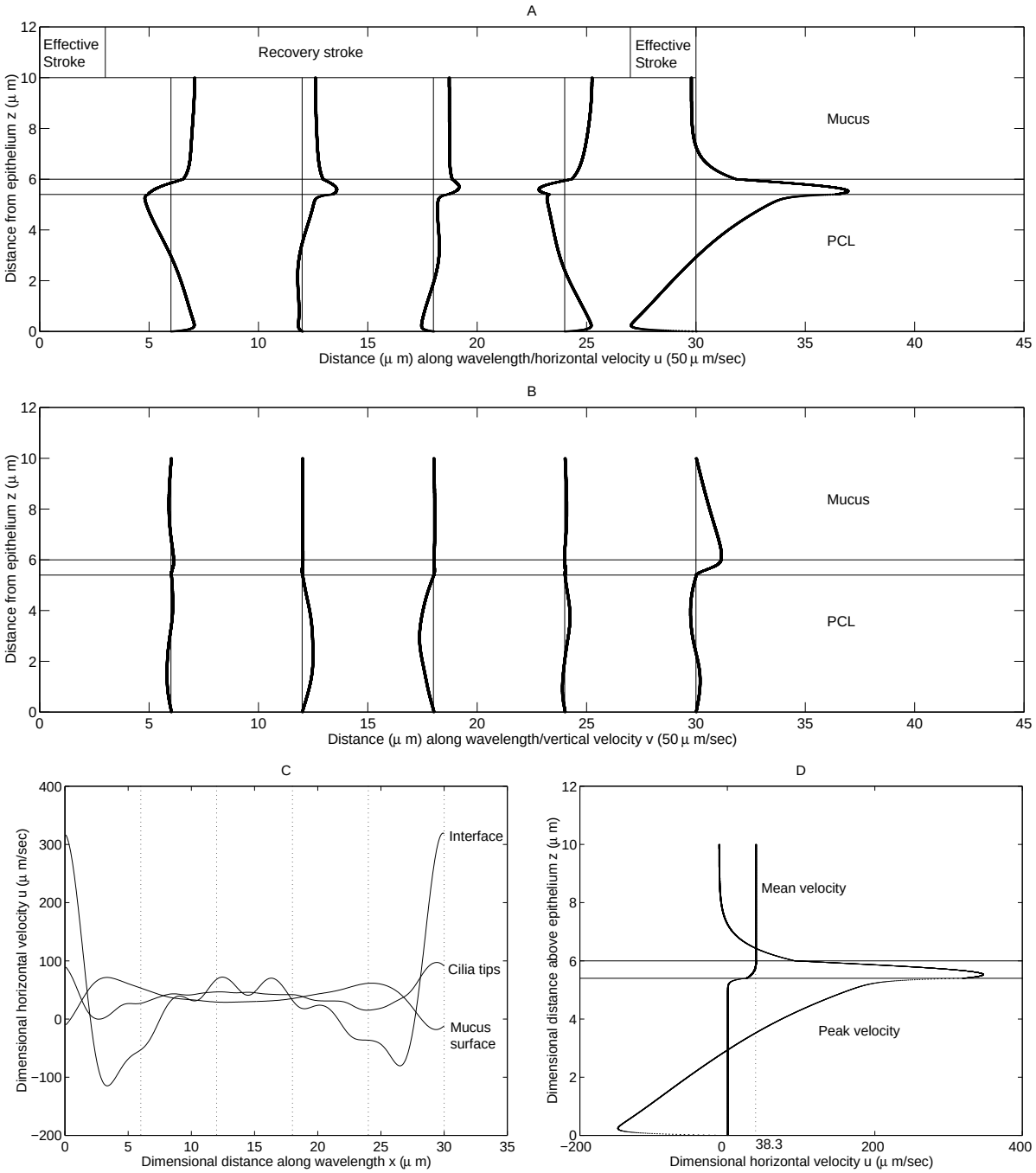

Figure 2.12: Traction layer numerical results. A—horizontal velocity profiles at five points along the wavelength versus distance from epithelium. B—vertical velocity profiles at five points along the wavelength versus distance from epithelium. C—horizontal velocity at three different levels in the ASL, the mucus–PCL interface, the cilia tips $z = L$ and the mucus surface $z = H$, versus distance along the wavelength. D—mean and peak horizontal velocity versus height above the epithelium. Dimensional parameter values: $L = 6\ \mu\mathrm{m}$, $\lambda = 30\ \mu\mathrm{m}$, $H = 10\ \mu\mathrm{m}$, $h = 5.4\ \mu\mathrm{m}$, $\nu = 5/6$, $\sigma = 60\ \mathrm{rad/s}$, $\lambda_1 = 0.03$ s. Viscosity ratios $\theta_1 = 6$, $\theta_2 = 8$. Sublayer resistance coefficients $\alpha_x = 90$, $\alpha_z = 75$.

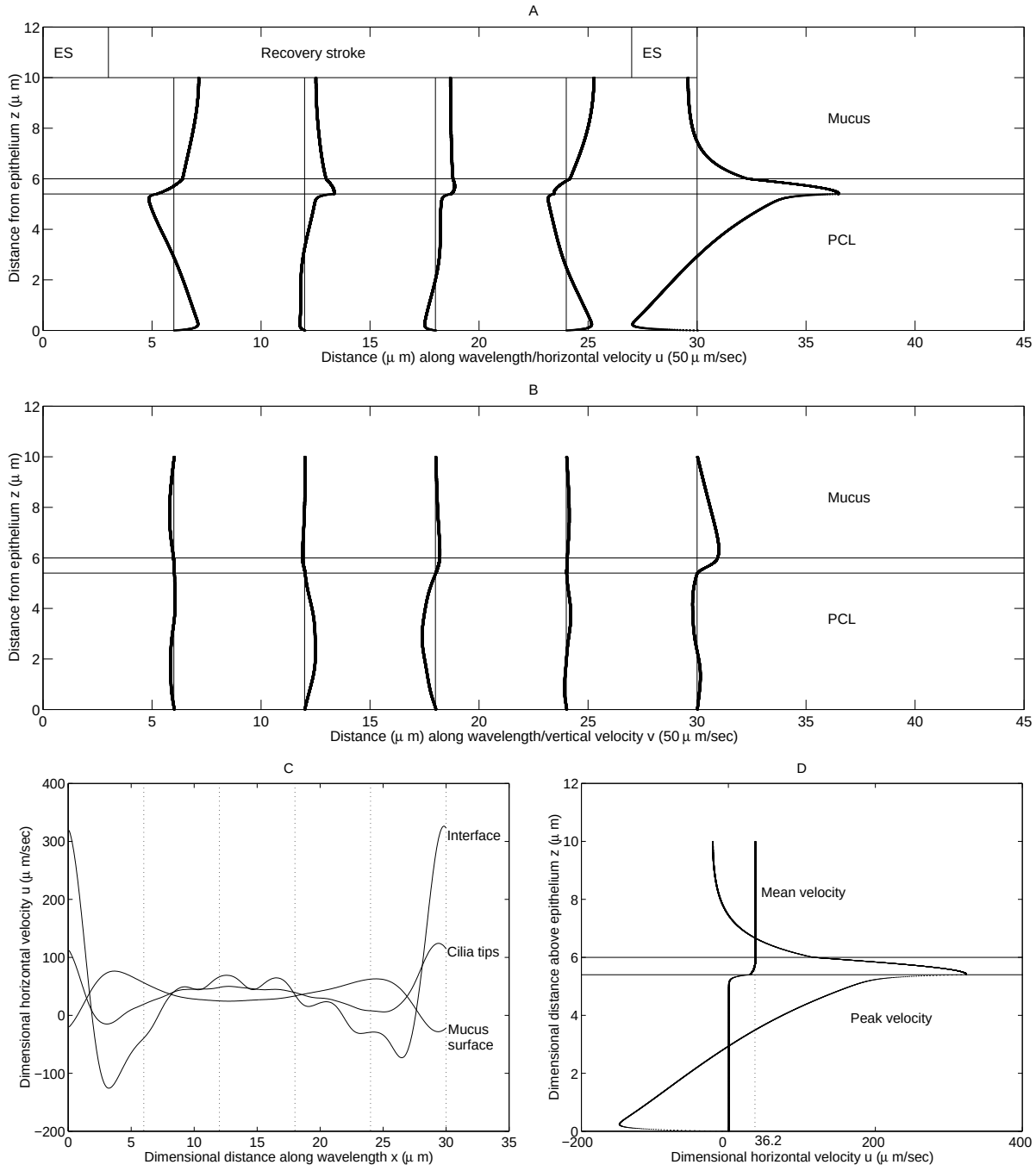

Figure 2.13: Traction layer numerical results—less shear-thinning. Dimensional parameter values: $L = 6\ \mu\mathrm{m}$, $\lambda = 30\ \mu\mathrm{m}$, $H = 10\ \mu\mathrm{m}$, $h = 5.4\ \mu\mathrm{m}$, $\nu = 5/6$, $\sigma = 60\ \mathrm{rad/s}$, $\lambda_1 = 0.03$ s. Viscosity ratios $\theta_1 = 12$, $\theta_2 = 4$. Sublayer resistance coefficient $\alpha_x = 90$, $\alpha_z = 75$.

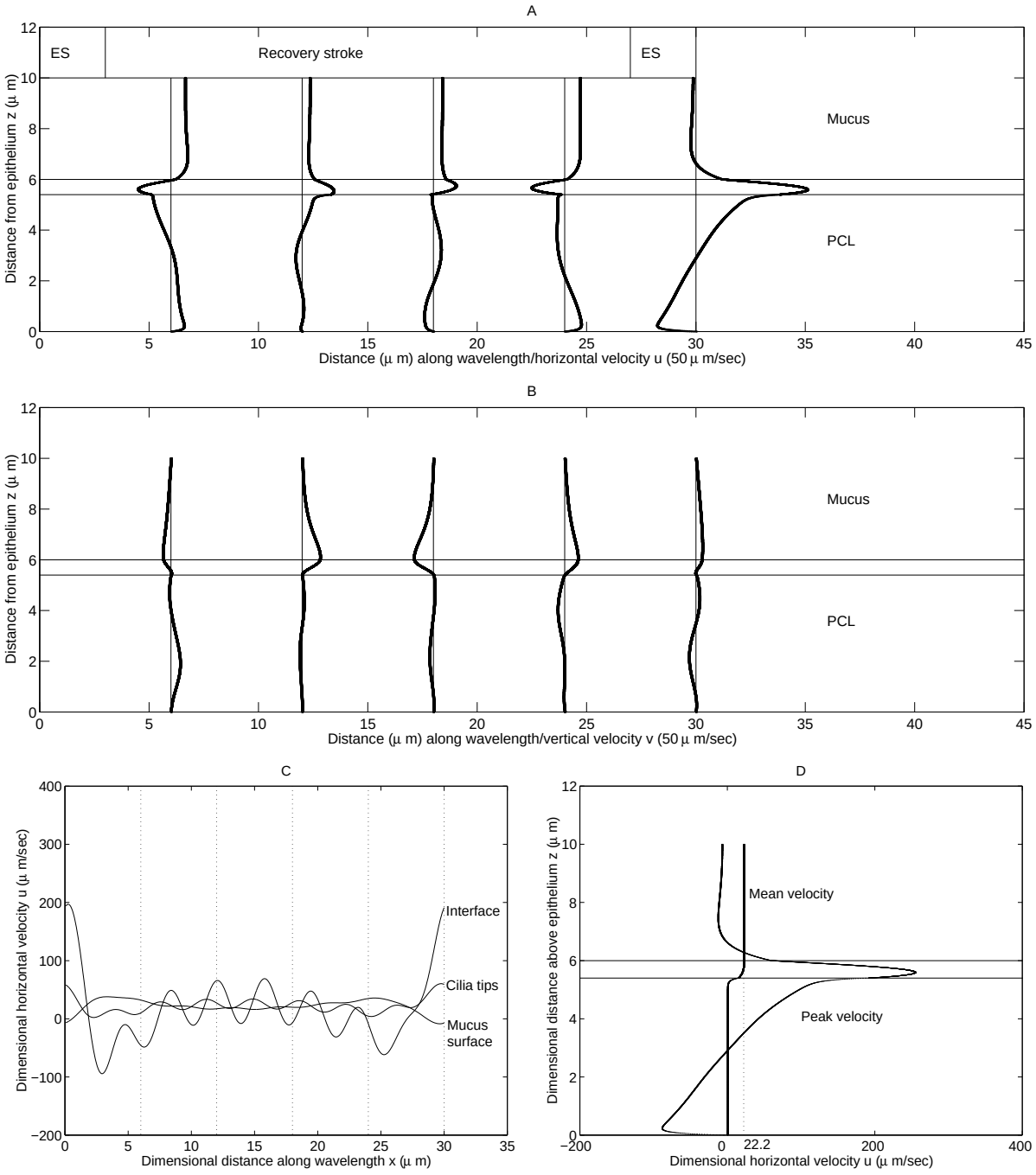

Figure 2.14: Traction layer numerical results—slower ciliary beating. Dimensional parameter values: $L = 6\ \mu\text{m}$, $\lambda = 30\ \mu\text{m}$, $H = 10\ \mu\text{m}$, $h = 5.4\ \mu\text{m}$, $\nu = 5/6$, $\sigma = 36\ \text{rad/s}$, $\lambda_1 = 0.03$ s. Viscosity ratios $\theta_1 = 6$, $\theta_2 = 8$. Sublayer resistance coefficient $\alpha_x = 90$, $\alpha_z = 75$.

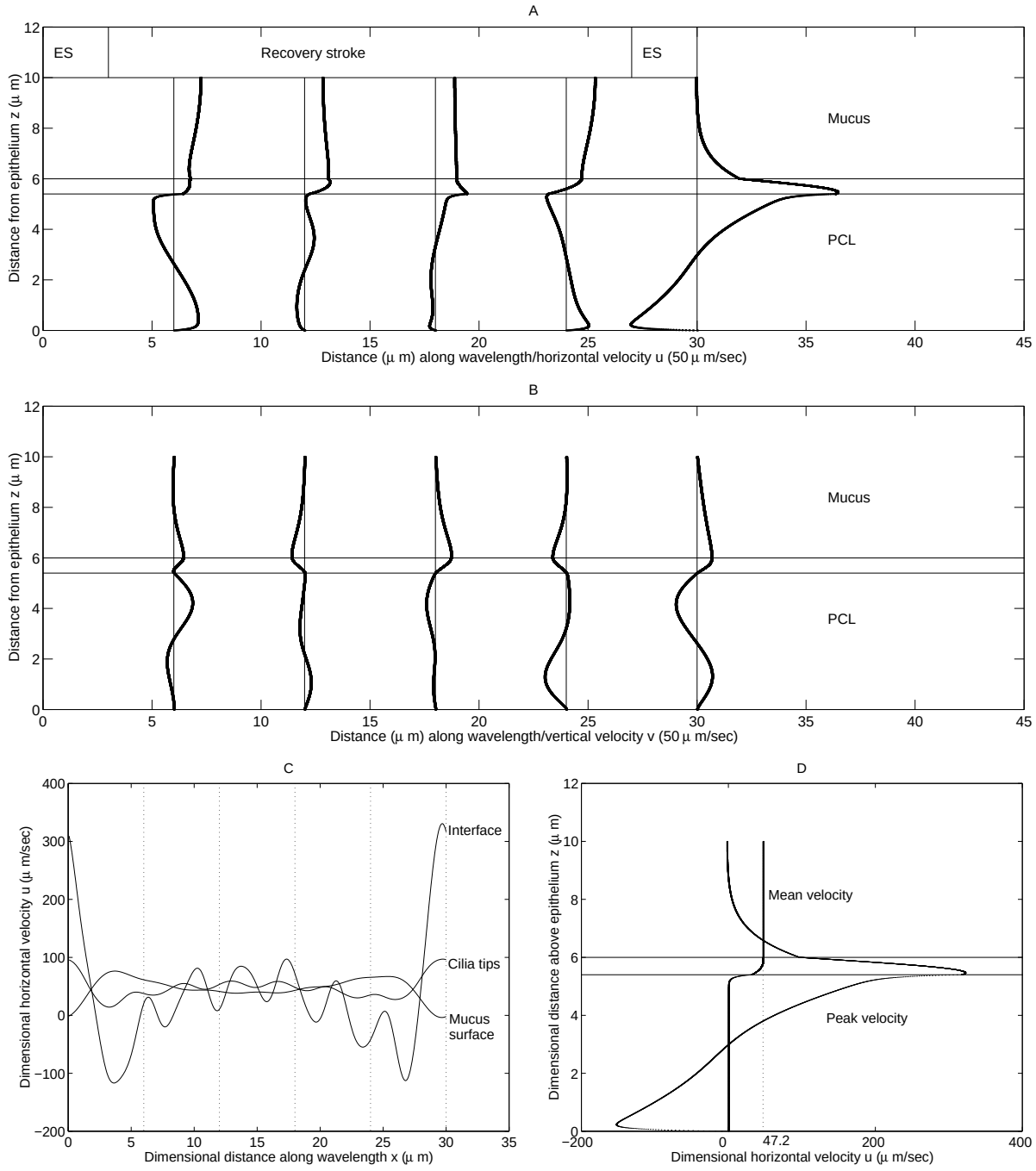

Figure 2.15: Traction layer numerical results—less elastic mucus. Dimensional parameter values: $L = 6\ \mu\mathrm{m}$, $\lambda = 30\ \mu\mathrm{m}$, $H = 10\ \mu\mathrm{m}$, $h = 5.4\ \mu\mathrm{m}$, $\nu = 5/6$, $\sigma = 60\ \mathrm{rad/s}$, $\lambda_1 = 0.01$ s. Viscosity ratios $\theta_1 = 6$, $\theta_2 = 8$. Sublayer resistance coefficient $\alpha = 90$, $\alpha_z = 75$.

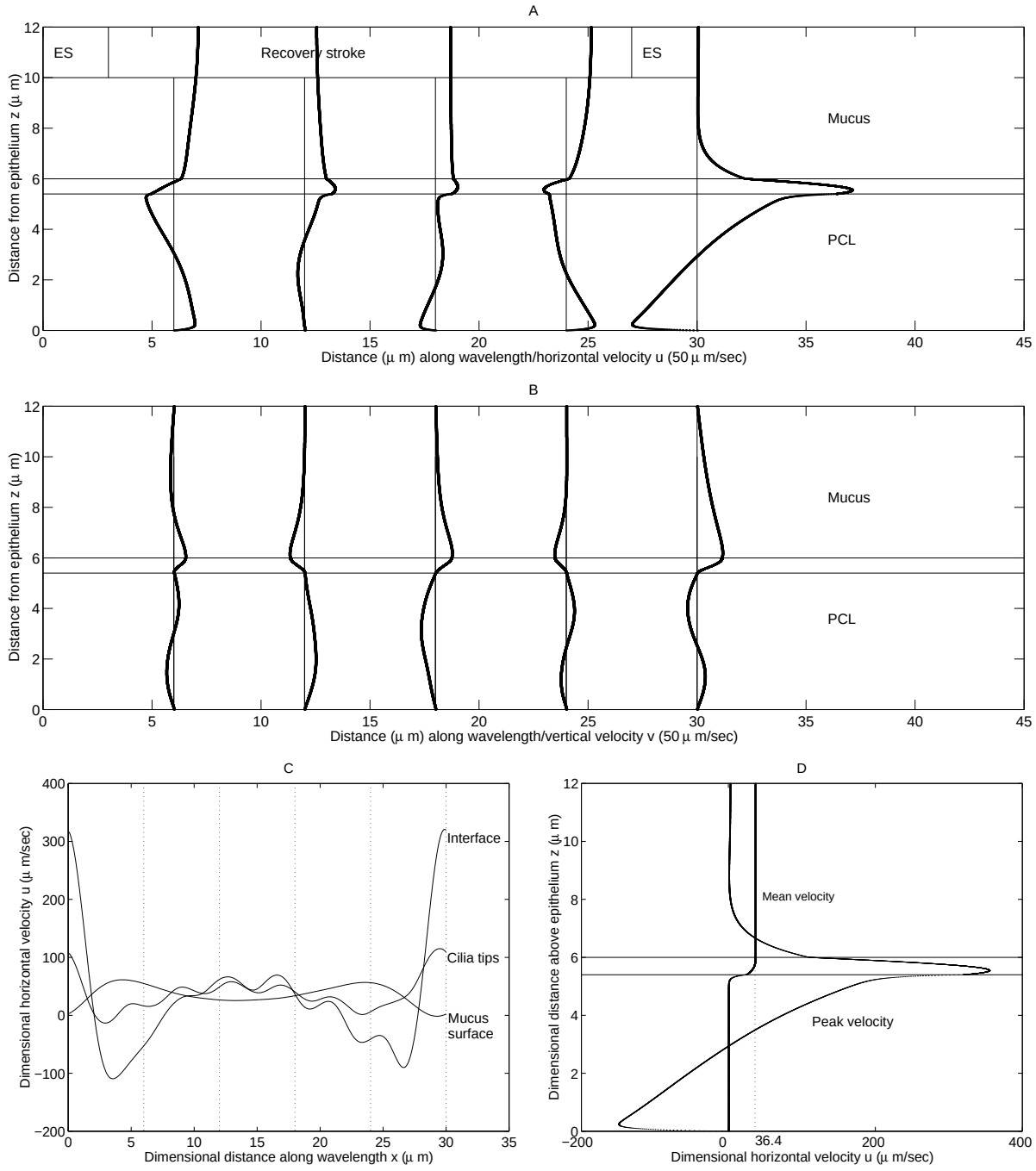

Figure 2.16: Traction layer results—deeper mucus. Dimensional parameter values: $L = 6\ \mu\mathrm{m}$, $\lambda = 30\ \mu\mathrm{m}$, $H = 12\ \mu\mathrm{m}$, $h = 5.4\ \mu\mathrm{m}$, $\nu = 5/6$, $\sigma = 60\ \mathrm{rad/s}$, $\lambda_1 = 0.03$ s. Viscosity ratios $\theta_1 = 6$, $\theta_2 = 8$. Sublayer resistance coefficient $\alpha = 90$, $\alpha_z = 75$.

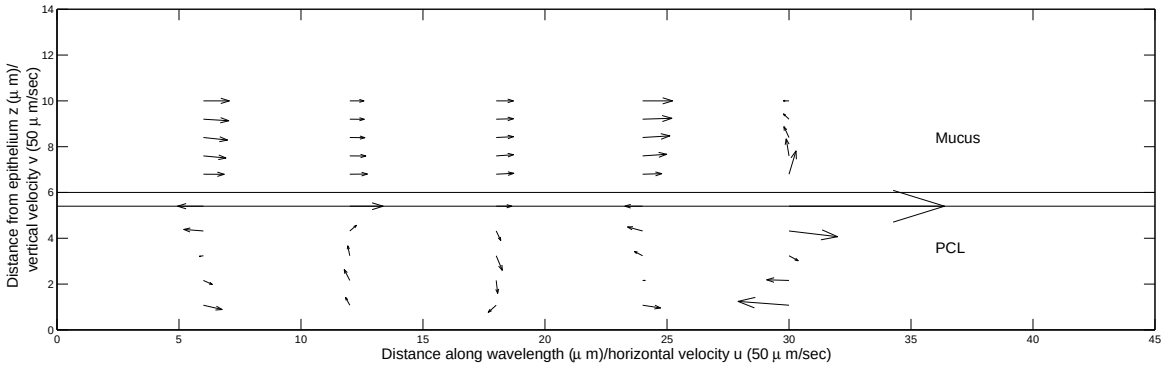

Figure 2.17: Traction layer numerical results—quiver plot of the velocity field for the 'standard' parameter set $L = 6\ \mu\mathrm{m}$, $\lambda = 30\ \mu\mathrm{m}$, $H = 10\ \mu\mathrm{m}$, $h = 5.4\ \mu\mathrm{m}$, $\sigma = 60\ \mathrm{rad/s}$, $\lambda_1 = 0.03$ s. Viscosity ratios $\theta_1 = 6$, $\theta_2 = 8$. Sublayer resistance coefficients $\alpha_x = 90$, $\alpha_z = 75$, sublayer velocity scaling $\nu = 5/6$.

Comparing Figure 2.12(A) to 2.6(A), certain features are shared by the solutions, particularly the shapes of the first, fourth and fifth profiles in the PCL, and the large peak flow at the point of penetration. It is certainly likely that there will be similarities given that the active porous medium, traction layer forces and interface boundary conditions are identical. However, the inclusion of pressure gradients in the mucous layer, and the constraint that the mucus surface is flat result in a number of significant differences. During the effective stroke, the numerical model predicts slightly larger forward and backward flow in the PCL, but a significantly smaller 'peak' in the traction layer. For the numerical model there is positive transport in the upper part of the mucous layer, except at the midpoint of the effective stroke where the mucus is actually flowing backwards. This is due to the pressure gradient enforcing mass conservation between $z = 1$ and $z = H$—any additional forward oscillation in the lower part of the layer must be balanced by a reduced forward flow in the upper part of the layer. Conversely, as the mucus is pulled back during the recovery stroke, the pressure gradient allows mucus to flow more rapidly in the upper part of the layer to counterbalance this. The numerical results also differ in that the pressure gradient in the PCL varies during the recovery stroke, so that the profiles for $x = 12$ and $x = 18$ differ from the analytical predictions, showing smaller magnitude flow in

the opposite directions.

Comparing Figures 2.12(B) and 2.6(B), it appears that the magnitude of the vertical oscillations is far smaller for the numerical model, due to the constraint that the vertical velocity is zero on both the interface and the surface. The peaks in the vertical velocity for the analytical model are of the order of $250\ \mu\mathrm{m}$/s, whereas in Figure 2.12(B) the vertical velocity is zero on the surface, as required by our boundary conditions.

Examining the rest of the beat cycle, there are other differences between the two models. The numerical model predicts rather complex variations in the flow field during the effective stroke, whereas the analytical model predicts that the profile will be rather more uniform. Unexpectedly, the numerical model predicts that for about half of the recovery stroke, when the cilia are moving backwards, there is nevertheless a large forward flux in the traction layer. The analytical model however predicts a negative velocity at the interface throughout the recovery stoke. Also since the numerical model includes the effect of the vertical component of the active porous medium term, there are some relatively small vertical oscillations in the PCL not present in the analytical model. As for the analytical model, we also present a 'quiver plot' of the velocity field, in Figure 2.17. This graph shows more clearly the prediction of the numerical model that the mucus above $z = L$ flows nearly uniformly and steadily throughout most of the beat cycle, except for the time of penetration, whereas the analytical model predicts slow moving mucus except just before, during and after the time of penetration, when it moves rapidly forwards. It is also clear from this graph that there are some circulation patterns present in both the PCL during the recovery stroke, and the mucous layer, during the recovery stroke. Possibly these patterns are responsible for a certain amount of mixing which can assist with the removal of foreign particles. In particular, any flow responsible for moving particles from the PCL, which does not exhibit significant mean transport, to the mucous layer may assist in their removal.

Figure 2.12(C) shows the variations in horizontal velocity along the beat cycle for the nu-

merical model. The mucus velocity at the level of the cilia tips is positive throughout most of the beat cycle, although of smaller magnitude than for the analytical model, and not showing the large phase lag. The fluid on the interface has a very similar peak velocity for the numerical model, is negative before and after the effective stroke, but unlike the analytical model also shows a forward velocity halfway during the recovery stroke. We also observe the brief period during which the mucus surface actually moves backwards, although for most of the beat cycle it has significant positive velocity.

Figure 2.12(D) shows the mean and peak velocity profile for the numerical model. The mean profile, which is given by equation (2.66) is of the same shape as for the analytical model, but with slightly greater mucus transport. The peak velocity is actually smaller for the numerical model halfway up the traction layer, and due to a slightly larger lag between the cilium velocity and the mucus velocity at the interface, where the constant U_{int} is calculated, there is slightly stronger propulsion of mucus by the cilium.

2.12.2 The relative importance of pressure gradients in the mucus and PCL

Together with the above we have investigated a similar model (not shown) with no pressure gradients anywhere in the fluid. We calculated only a very small mean mucus velocity—$1.63\ \mu\mathrm{m/s}$ for the standard parameter set. The analytical model with pressure in the PCL only predicted very similar mucus transport to the model presented here. This suggests that it is the action of pressure gradients in the PCL, rather than the mucous layer, that are essential to ensuring positive transport of mucus. This calls into question the earlier suggestion of Sleigh et al. (1988) that there is no significant interface tension between the PCL and mucus.

2.12.3 Profiles for different parameter sets

Figure 2.13 shows the profiles for the numerical model with a reduced shear-thinning effect. The total mucus viscosity $\theta_1\theta_2$ remains the same as for the standard parameter set, but the

shear-thinning ratio θ_2 is reduced to 4. The profiles are not greatly altered, with the exception of there being smaller oscillations in the traction layer due to the increased viscosity, a smaller peak velocity at the point of penetration, and smaller vertical oscillations throughout the PCL. It is apparent from examining the horizontal profiles at $x = 6$ and $x = 24$ that the larger value of θ_1 results in the cilia having less influence on the traction layer during the recovery stroke, and the smaller value of θ_2 resulting in the traction layer having more influence on the upper mucous layer. The mean transport speed is slightly reduced to $36.2\ \mu\mathrm{m/s}$—the complex interactions causing this are discussed in §2.12.5.

Figure 2.14 shows the results for slower ciliary beating ($\sigma = 36$). As for the analytical model, the mean transport and oscillations are of smaller magnitude, which is expected since velocity is scaled with respect to σL. However, unlike the analytical model, slowing the rate of ciliary beating results in profiles that look very different. Almost all of the mucous layer moves backwards during the effective stroke, and at the level of the cilia tips, $z = 1$, the flow oscillates rapidly during the recovery stroke, as shown in Figure 2.14(C). The smaller value for σ interacts with the viscoelastic timescale λ_1 to produce a rapidly oscillating pressure gradient and hence very different results.

Figure 2.15 shows the rather erratic profiles produced when the time constant is reduced to 0.01 s, reducing the elasticity of the mucus. Again, the interaction between the forcing frequency and the viscoelastic element results in rapidly oscillating pressure gradients. The mean mucus transport is increased, since the mucus does not deform locally as readily when penetration occurs, and so mucus is 'dragged along' more strongly.

Figure 2.16 shows the effect of increasing the ASL depth to $12\ \mu\mathrm{m}$. Since the mucus surface is further from the traction layer, it has a smaller influence on propulsion. The effect of the flat mucus surface, which assists with transport, is reduced and so the mean mucus velocity is slightly reduced rather than slightly increased for the analytic model. The size of this effect is, however, only around 5%.

Parameters	Analytical velocity (μm/s)	Numerical velocity (μm/s)
Standard	36.3	38.3
$\theta_1 = 12,\ \theta_2 = 4$	30.9 ($\downarrow$ 14.9%)	36.2 ($\downarrow$ 5.48%)
$\sigma = 36\ \text{sec}^{-1}$	23.5 ($\downarrow$ 35.3%)	22.2 ($\downarrow$ 42.0%)
$\lambda_1 = 0.01$ sec	44.1 ($\uparrow$ 21.5%)	47.2 ($\uparrow$ 23.2%)
$\lambda_1 = 0.04$ sec	35.4 ($\downarrow$ 2.48%)	44.9 ($\uparrow$ 23.7%)
$H = 12\ \mu$m	36.8 ($\uparrow$ 1.38%)	36.4 ($\downarrow$ 4.96%)

Table 2.1: Mucus transport values from the numerical model for various parameter sets.

2.12.4 Mean mucus transport

Our simulation using the standard parameter set predicts a mean mucus velocity of $38.3\ \mu\text{m/s}$, slightly greater than that predicted for the analytical model ($36.3\ \mu\text{m/s}$), and close to the value of $39.2\ \mu\text{m/s}$ found by Matsui et al. (1998b).

Table 2.1 summarises the effect on mucus transport of different parameter sets. Decreasing the rate of ciliary beating within the experimentally observed range (Salathe et al., 1997) by 40% to $36\ \text{rad/s}$ results in an approximately proportionate reduction in transport. Increasing the mucus 'stiffness' by reducing the relaxation time to $0.01\ \text{s}$ significantly increases mucus transport by 23%, and surprisingly increasing the relaxation time to $0.04\ \text{s}$ also results in an increase in transport of around 23%. Thicker (deeper) mucus ($H = 12\ \mu\text{m}$) leads to only slightly slower mucus transport, provided that such parameters as the ciliary beat frequency and the mucus viscosity remain the same. Due to the thickened layer, the cilia are actually propelling a considerably larger volume of mucus. This suggests that if a thicker mucous layer is observed in patients with impaired mucus transport, it may not be the thickness *per se* that causes the impairment, but rather it may simply be a consequence of reduced transport. Conversely, this provides insight into how the body adapts to a thickening mucous layer moving from the bronchioles to the trachea—the cilia do not need to beat significantly faster to transport a greater volume of mucus. A greatly depleted, but still continuous, mucous layer represented by $H = 6.5\ \mu\text{m}$ shows transport increased significantly by 54.6%.

It is clear from Table 2.1 that the analytic model predicts certain qualitative responses of the system well, only failing to predict the effect of raising H and λ_1. It would be expected that moving the free surface would have a very different effect when surface tension is present at that surface. The effect of changing λ_1 is more subtle, it is due to the fact that a change in λ_1 results in a change to the pressure gradient in the mucus, which is not present in the analytical model. A more detailed discussion of the interaction between different parameters and physical effects is given in §2.12.5 and Figure 2.20.

2.12.5 Understanding the effects of different physical parameters on transport

Examining equation (2.66) we see that there are various ways in which mucus transport can be altered. The mucus velocity u^{M2} is proportional to the interaction velocity $-U_{\text{int}}$ and the first term in braces is proportional to the traction layer viscosity θ_1. Simply altering the value of the beat frequency σ, all else being equal, will have a proportionate effect on mucus transport. In addition, all of the parameters interact in a nonlinear way to affect $-U_{\text{int}}$, which we explore below.

For brevity we write the fluid velocity at the apex of the effective stroke as $u_{\text{pen}} = u(2\pi x + \sigma t = 0, z = h)$. Since $-U_{\text{int}} = u_{\text{cilia}} - u_{\text{pen}}$ it is clear that reducing the value of u_{pen} will increase $-U_{\text{int}}$ and hence the mean mucus velocity. In general, physical effects that resist the sharp forward flow of mucus in response to penetration will tend to decrease u_{pen} and hence increase transport. The effect of a positive instantaneous pressure gradient $\partial p/\partial x$ is to act as a resistance force to the forward flow of liquid, as can be seen from equation (2.35). At the point of penetration, this results in a reduction in u_{pen} and hence an increase in $-U_{\text{int}}$ and hence the mean transport.

Hence, the results in Table 2.1 can be understood physically. Reducing the relaxation time of the mucus to 0.01 s effectively reduces how readily the mucus will deform elastically in

response to penetration. The value of u_{pen} is hence smaller and so $-U_{\mathrm{int}}$ is increased, and hence the mean transport. Increasing the relaxation time to $0.04\ \mathrm{s}$ increases the elasticity of the mucus, and at the same time increases the positive pressure gradient in the upper part of the PCL from approximately $53\ \mathrm{Pa}/\mu\mathrm{m}$ to $65\ \mathrm{Pa}/\mu\mathrm{m}$. This has the overall effect of reducing u_{pen} and hence increasing the mucus transport. Decreasing the depth of the mucous layer greatly increases the effect of the mucus free surface and hence increases the pressure gradient by about 50%, decreasing u_{pen} and hence increasing transport. A schematic diagram showing the effects on transport speed of the various physical parameters is given in Figure 2.20.

2.12.6 Shear-thinning ratio

We were not able to determine parameters for the shear-thinning ratio, so we have produced results for a spectrum of values of θ_1 and θ_2 corresponding to a fixed free mucus viscosity of $\mu^{M2} = \theta_1\theta_2 = 48$. The effect on mean mucus transport is shown in Figure 2.18. For the numerical system, for values of θ_1 close to 3, a sharp spike occurs (not shown). This is due to the fact that the pressure gradient in the PCL enforcing $v(z = h) = 0$ becomes large and negative, forcing u to be far too large for the interation to converge. In reality, the interface would simply deform under this pressure gradient, and our model assumptions would break down. Since the interface does not appear to deform significantly in the micrographs of Sanderson and Sleigh (1981), it is likely that the viscosity of the traction layer does not approach this value, at least in the conditions they observed. For the standard parameter set, the jump in normal stress at the mucus–PCL interface is no larger than $100\ \mathrm{N\ m^{-2}}$. For $\theta_1 = 2.995$, the jump in normal stress reaches $1000\ \mathrm{N\ m^{-2}}$. In order to balance this, the surface tension force must be ten times larger, which corresponds to the curvature of the interface being ten times larger. Again estimating the surface tension to be $0.08\ \mathrm{Nm^{-1}}$, the curvature must increase from $1250\ \mathrm{m^{-1}}$ to $12500\ \mathrm{m^{-1}}$. If we make the simple assumption that the interface has the form $\eta = \eta_0 + \varepsilon\cos(\kappa x + \sigma t)$, for some small perturbation ε, the curvature can be approximated by $|\eta_{xx}| = \varepsilon\kappa^2$. If the wavenumber

$\kappa = 2\pi/3.0 \times 10^{-5}$ m^{-1}, then ε must increase from 2.8×10^{-2} μm to 0.28 μm, a significant disturbance on the scale of the muco-ciliary system.

Even ignoring this point, the relationship between transport and θ_1 is still nonlinear, with transport being greatest at $\theta_1 = 1$, and also being greater at $\theta_1 = 48$ than $\theta_1 = 6$. We can understand this by noting that at the point of penetration, the pressure gradients in the PCL and the force free mucous layer act to 'pull back' the forward flow of fluid, and hence increase the relative velocity U_{int} of the mucus and cilium and hence the mean flow. Examining boundary condition (2.53), we note that when $\theta_1 = 1$, we see that, ignoring the vertical velocity component which will be zero, the gradient $\mathrm{d}u/\mathrm{d}z$ must be the same above and below the interface. In general, the gradient is greater in the PCL than the traction layer, and so this corresponds to the flow in the PCL 'pulling back' the fluid in the traction layer, and can be seen by comparing figures 2.12(A) and 2.13(A). This results in reduced traction layer mucus velocity and hence an increased value of U_{int}, and increased mean transport. Conversely, for $\theta_1 = 48$ we have $\theta_2 = 1$. Examining boundary condition (2.56) we see that, ignoring the vertical component of the velocity, the gradient $\mathrm{d}u/\mathrm{d}z$ must now be the same above and below the interface at $y = 1$. Since the gradient is in general less in $y > 1$ than $h < y < 1$ this means that the flow in the force free mucous layer will now 'pull back' the traction layer mucus more effectively, hence increasing U_{int} and hence the mean transport. For the analytical model, transport does not significantly increase as θ_1 is increased towards 48. This is due to the fact that the force free mucous layer is not subject to any adverse pressure gradient and so will not act to resist the forward flow of the traction layer, regardless of the values of θ_1 and θ_2.

2.12.7 PCL and mucus flux results

For the standard parameter set, $U_{\text{int}} = -0.026017$. From equation (2.67), the nondimensional PCL flux is 7.87×10^{-4}, corresponding to a dimensional value of 1.70 $\mu\mathrm{m}^2/\mathrm{s}$. This compares with a mucus flux of 8.07×10^{-2}, corresponding to a dimensional value of 174 $\mu\mathrm{m}^2/\mathrm{s}$. The flux

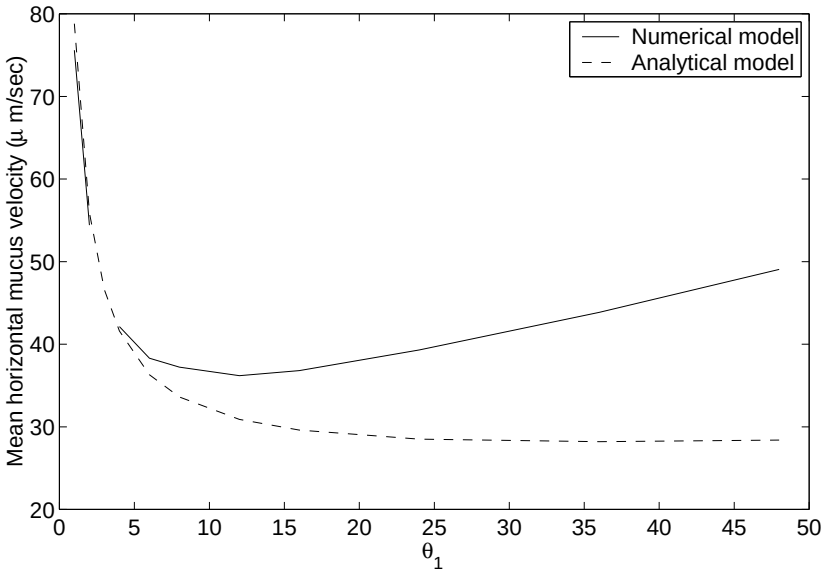

Figure 2.18: Mean mucus transport against traction layer viscosity θ_1 for fixed mucus viscosity $\theta_1\theta_2 = 48$, for numerical and analytical model. Sublayer resistance coefficients $\alpha_x = 90$, $\alpha_z = 75$, sublayer velocity scaling $\nu = 5/6$. Numerical model assumptions were not justified for $\theta_1 \sim 3$, in this region no results are given.

of mucus is over 100 times greater than that of PCL, due to the viscous resistance of the cilia.

2.12.8 Modelling diseased states

Our model is more suitable for comparison with diseases such as chronic obstructive pulmonary disease (COPD) or asthma, in which the distinct PCL and mucous layers and interface are more clearly preserved, than diseases such as cystic fibrosis, in which mucins may be found in the PCL, and in which the PCL may be significantly depleted. Detailed comparisons of these conditions may be found in Rogers (2004) and Boucher et al. (2000). In Table 2.2 we present some results providing a tentative simulation of various 'diseased' states of the muco-ciliary system. As one might expect, our model predicts that if the ciliary beat frequency is greatly reduced from $60\ \mathrm{rad/s}$ by 83% to $10\ \mathrm{rad/s}$, mucus transport is reduced almost proportionately. Hence one likely cause of impaired clearance is reduced ciliary beating. Surprisingly, altered rheological parameters such as much more viscous ($\theta_1 = \theta_2 = 30$), or much more 'watery'

mucus ($\lambda_1 = 0$, $\theta_1 = \theta_2 = 1$), or more elastic or Newtonian mucus ($\lambda_1 = 0.04$, $\lambda_1 = 0$), do not seem to significantly impair mucus clearance when compared with our initial parameter set. It is possible, however, that more viscous or less elastic mucus may have a more subtle effect by impairing ciliary beating.

The results appear to show that mucus is important to transport by producing an interface which supports pressure gradients in the PCL. The pressure gradients need have no mean effect, but they nevertheless allow the cilia to interact with the upper layer efficiently. The viscoelastic interaction of mucus and cilia itself appears not to be the important mechanism. Nevertheless, it is also possible that mucus elasticity is important in the interaction of the cilium tip and the mucous layer. Experimental observation and mathematical modelling of this interaction will provide further insight.

To simulate the effect of excessive fluid secretion, we chose the parameters $H = 40\ \mu\mathrm{m}$, $\theta_1 = 8$, $\theta_2 = 1$, representing a deep, less viscous mucous layer. The effect was to reduce velocity to $26.6\ \mu\mathrm{m/s}$, which although significantly less than the standard parameters, was not the virtual cessation of transport one might expect. However, as found by Blake (1973b), a very deep mucous layer will be subject to significant gravitational force, which was not included in our model. In addition, deeper mucus may result in 'plugging' of airways, and disruption of the normal surface and interface properties. It should also be noted that for a deep mucous layer or a very narrow airway, curvature in the y direction, as depicted in Figure 2.19 will no longer be negligible (Rogers, 2004), and may lead to important pressure gradients caused by surface tension.

In summary, nothing short of a cessation of normal ciliary beating appears sufficient to interupt muco-ciliary functioning in our model. However, the fact that transport is so impaired by the lack of a pressure gradient in the PCL caused by interface tension suggests strongly that mucus–PCL interaction is important for maintaining efficient transport. For instance, excessive surfactant may, by lowering interface tension, impair the system. Our 'interface' is an idealisa-

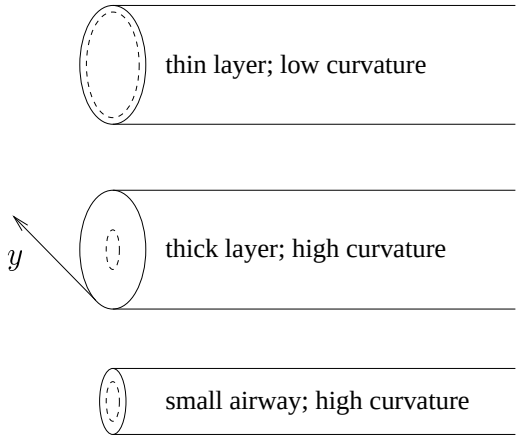

Figure 2.19: As the mucous layer thickens or in narrower airways, curvature in the y direction becomes important.

Parameters	Mean mucus velocity$(\mu\mathrm{m/s})$	
	Analytical	Numerical
Standard	36.3	38.3
Very slow ciliary beating $\sigma = 10\ \mathrm{rad/sec}$	$8.43\ (\downarrow 76.8\%)$	$7.33\ (\downarrow 80.9\%)$
Very viscous mucus $\theta_1 = 30,\ \theta_2 = 30$	$53.3(\uparrow 46.8\%)$	$56.8\ (\uparrow 48.3\%)$
'Watery' mucus $\lambda_1 = 0,\ \theta_1 = 1,\ \theta_2 = 1$	$68.8(\uparrow 89.5\%)$	$58.8\ (\uparrow 53.5\%)$
Elastic, 'watery' mucus $\lambda_1 = 0.03\ \mathrm{s},\ \theta_1 = 1,\ \theta_2 = 1$	$65.5\ (\uparrow 80.4\%)$	$58.6\ (\uparrow 53.0\%)$
Deeper, less viscous mucus $H = 40\ \mu\mathrm{m},\ \theta_1 = 8,\ \theta_2 = 1$	$28.5\ (\downarrow 21.5\%)$	$26.6\ (\downarrow 30.5\%)$
Double viscosity $\theta_1 = 12,\ \theta_2 = 8$	$34.1\ (\downarrow 6.06\%)$	$39.1\ (\uparrow 2.08\%)$

Table 2.2: Mucus transport values from the numerical model for various possible 'diseased' states.

tion of the real system, which is known to deform in order to allow ciliary penetration (Puchelle et al., 1998). Future modelling work should investigate the role of this region further.

2.12.9 Comparision with experimental studies

Our simulations of disease states, which suggest that low mucus viscosity and elasticity do not harm, and indeed benefit transport, and that ciliary beat frequency is the most important determinant of normal functioning, show some interesting parallels with experimental studies, though these must be qualified by the fact that we have currently only considered an imperme-

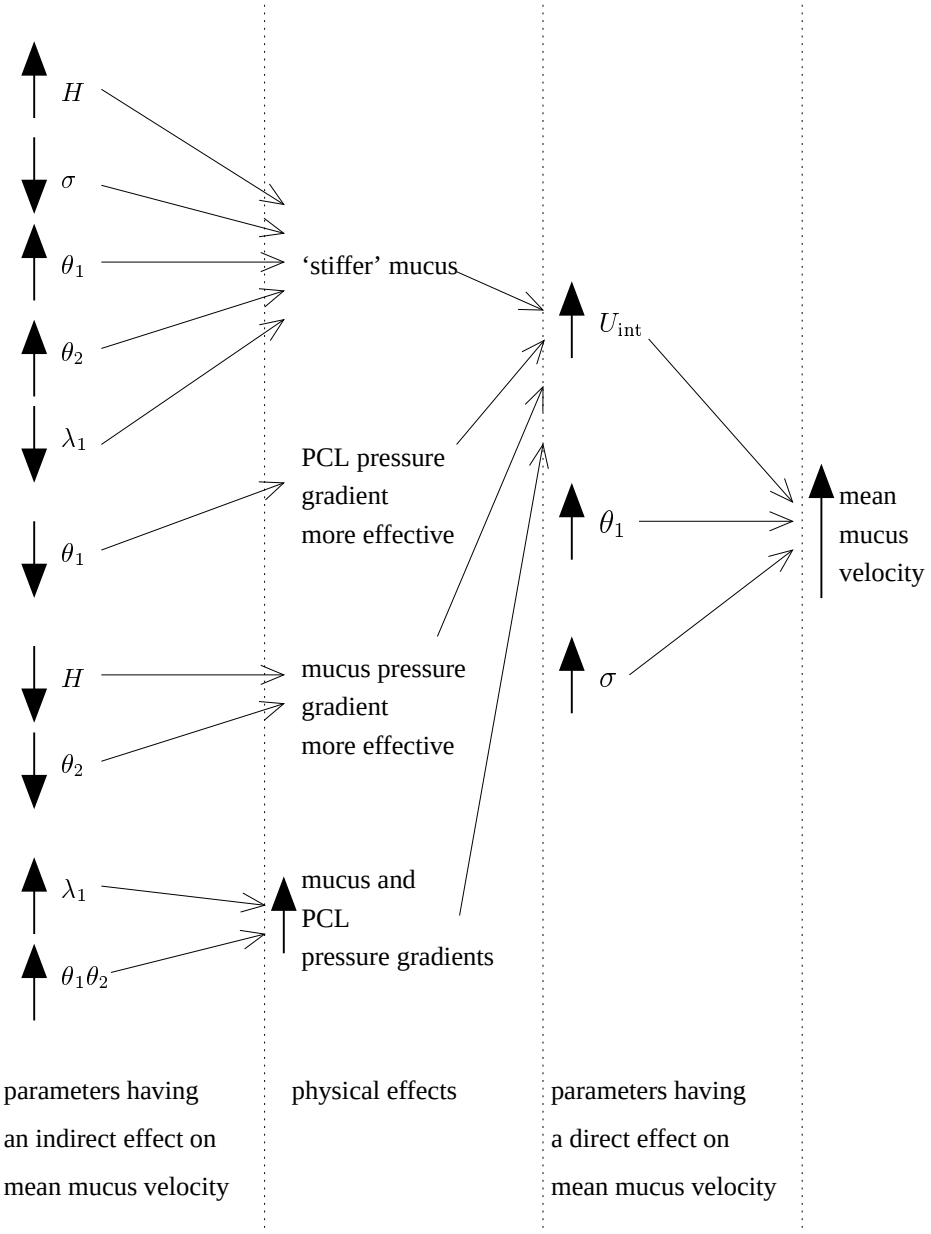

Figure 2.20: Schematic of the influence of physical parameters on mean mucus velocity. Working from the right, increases in interaction velocity U_{int}, traction layer viscosity θ_1 and beat frequency σ all directly increase mean mucus velocity, as shown in equation (2.66). Interaction velocity U_{int} may be increased by 'stiffer' mucus, by increasing PCL and mucus pressure gradients, and by increasing the effect of those pressure gradients. These effects are in turn caused by various changes to the parameters, for instance increases in relaxation time λ_1 and mucous layer viscosity $\theta_1\theta_2$ both cause an increase in mucus and PCL pressure gradients. Most parameters do not have a simple effect; for instance increasing the depth of the ASL H leads to 'stiffer' mucus, increasing U_{int}, hence tending to increase mean mucus velocity. However, increasing H will also render the pressure gradient in the mucous layer less effective, which tends to have the opposite effect. The overall effect of increasing H from $10\ \mu\text{m}$ to $40\ \mu\text{m}$ is shown in Table 2.2, a 30.5% decrease.

able epithelium.

A study of patients with pseudohypoaldosteronism (PHA) (Kerem et al., 1999) showed that no liquid is absorbed from the ASL by the epithelium, and consequent greatly enhanced mucus transport. They suggested that excess fluid is absorbed by the mucous layer, ensuring that the mucus does not 'float off' the cilia tips, and that the rheological properties of mucus are improved by the increased water content. Our results showing enhanced transport for 'watery mucus' support the hypothesis that increased water content of ASL, even beyond the normal level, is beneficial to transport. Shibuya et al. (2003) used a bovine trachea model to test the effect of both osmolality and liquid depletion on viscosity and transport. Adding sodium caused a highly significant increase in transport, whereas iso-osmolal removal of liquid resulted in approximately a doubling of 'viscoelasticity', and a nonsignificant increase in transport. This is qualitatively similar to our results predicting a very modest increase in transport of 2% for doubled mucus viscosity.

Mucolytic drugs, designed to reduce mucus viscosity, have been studied in an attempt to improve muco-ciliary transport and hence alleviate muco-ciliary disfunction. However, (Salathe et al., 1996; Rogers, 2005) mucolytics have tended to be ineffective for improving muco-ciliary transport *in vivo*. Symptoms of chronic bronchitis and chronic obstructive pulmonary disease have been slightly improved by the use of oral mucolytics (Poole and Black, 2001), but this modest benefit may be due to mechanisms other than improving muco-ciliary transport, such as antioxidant properties (Ekberg-Jansson et al., 2001), anti-inflammatory properties (Gibbs et al., 1999) or through increasing the water content of the ASL (Rochat et al., 2004). Our results showing that mucus viscosity does not have any clear effect on transport, and indeed that very viscous mucus may be transported more efficiently, are consistent with these findings.

Finally, β_2-adrenergic agents such as salbutamol and salmeterol have been shown to enhance ciliary beat frequency (Devalia et al., 1992) and salmeterol has been shown to slightly enhance muco-ciliary clearance in patients with asthma (Hasani et al., 2003). Conversely the β-blocking

drug propanolol depresses muco-ciliary clearance significantly (Pavia et al., 1986), consistent with our findings.

2.13 Conclusions and future work

In this chapter we presented a model of mucus transport which represented the propulsive and resistive forces of the cilia by physically-based phenomenological volume forces, and represented mucus as a linearised Maxwell fluid. Our model incorporated the main features of the system—metachronism, the periodicity of the ciliary beat, resistance of the cilia sublayer, spatial variations in the propulsive force, viscoelasticity of the mucous layer and surface and interface tension. By exploiting the periodicity of the beat cycle, we converted the fluid flow equations into a system of coupled ordinary differential equations. By neglecting surface tension and pressure gradients in the mucous layer, we were able to decouple the equations and find an analytical solution. We then calculated numerical solutions, with no such simplifying assumptions, beyond assuming that the surface and interface were flat. The numerical and analytical solutions showed some superficial resemblence, but differed significantly in the shape of the horizontal profiles, the magnitude of the vertical profiles, and the responses to changed parameters. The analytical solution did however provide insight into the relative importance of the surface and interface in ensuring efficient transport, and assisted with identifying and understanding which physical effects caused certain responses.

Subject to the assumption of no-flux through the epithelium and consistent with the hypotonic defensin hypothesis, the time-averaged horizontal profile is qualitatively similar to the results of Fulford and Blake (1986), and the earlier work of Blake and Winet (1980), although with positive transport of PCL only occurring very close to the interface. Our results are very different from those predicted by Matsui et al. (1998b). This demonstrates that a detailed model consistent with the hypotonic defensin hypothesis produces PCL flux inconsistent with the conclusions of Matsui et al. (1998b), even with the novel incorporation of mucus viscoelasticity,

surface tension and pressure gradients. Clearly, it will be of considerable interest to determine whether models incorporating osmotic flow, and thus consistent with the isotonic volume hypothesis, produce significantly different results. In addition we observed large oscillations in the PCL relative to the net mucus transport, and circulation patterns in the PCL that may assist in the mixing and removal of tracer particles or contaminants.

Our models predicted physiologically reasonable values for mucus transport, from physiologically justified parameter sets. Our numerical results predicted several interesting properties of the muco-ciliary system. The dependence of transport on the choice of physical parameters was nonlinear. It emerged that transport was only significantly disrupted by a reduction in σ. The system was remarkably robust to changes in other parameters, although this is notwithstanding the assumption that the mucus–PCL interface and mucus surface remain flat, and that the ASL does not become so thick that gravity is important. It might be expected that the muco-ciliary system has evolved to function efficiently even when subjected to various changes in physical properties. Pressure gradients with zero mean, brought about by the interface and surface tension were crucial to ensuring efficient interaction between the mucus and cilia. Consistent with recent experimental findings, ciliary beat frequency was a crucial determinant of efficient transport, and 'watery' mucus was transported more efficiently than normal mucus.

There are a number of ways that the model could be developed. The cilium-mucus interaction is difficult to represent in a simple way. There are many cilium bodies penetrating the mucus, at different angles, in the presence of surface forces, with possible molecular level interactions taking place. The role of surfactant in allowing cilia tips to deform and penetrate the mucus may be very interesting to investigate. In order to model further the way in which different physical parameters interact, it would be necessary to model the internal mechanics and energy consumption of the cilia, as has been done by Gueron and Liron (1992), so that for instance we could test whether increasing viscosity would affect beat frequency; however extending their model to the two layer system with large numbers of cilia would be very chal-

lenging. It is also known that the presence of mucus provides a stimulus for ciliary beating (Sleigh et al., 1988)—investigating possible mechanisms for this coupling may be illuminating. It might also be useful to model small deformations of the surface and interface, and the surface tension forces this would produce. Integration of more detailed models of mucus rheology, such as that of Quemada (1984) with the fluid flow equations may provide still more insight, as would considering possible non-Newtonian effects in the PCL (Boucher, 2003). Integrating a Maxwell element for the PCL into this model would be very straightforward.

As discussed above, our results make for an interesting parallel with the study of PHA patients by Kerem et al. (1999), which concludes that the greater mucus transport observed indicates that the thickness of the PCL is maintained so that the cilia can continue to penetrate the mucus. An extension of this model would be to consider how the cilia can propel mucus in the case where the PCL is greatly thickened so that penetration is not possible, and to test whether such a system results in efficient transport. However, in light of our findings that 'watery' mucus is propelled very efficiently, their explanation seems most likely. It may also be interesting to use the framework presented here to investigate roles of beat cycle asymmetry and metachronal coordination, and to examine how viscoelasticity may assist with transporting fluid over non-ciliated regions.

Finally, our model of the behaviour of the 'active porous medium' is only an approximation of the beating cilia. In particular, there is a gap between the tips of the cilia and the mucus interface throughout the recovery stroke, which was not a feature of our model. In chapter 3 we develop a singularity model of the field of cilia in order to model the flow in the PCL more accurately.

CHAPTER 3

A NEW DISCRETE-CILIA MODEL FOR THE FLOW IN THE PERICILIARY LAYER

3.1 Introduction

In chapter 2 we modelled the action of the cilia by spatially continuous volume forces. In this chapter we model the cilia as discrete slender bodies. This is in order to gain more information regarding the detail of the three dimensional flow of periciliary liquid around the cilia, and to make progress towards calculating more accurate data regarding the flux in this layer, although due to computational considerations we do not yet have definitive results for the cilium spacing found in the lung. We begin by discussing how a slender body in Stokes flow conditions may be modelled by line distributions of singularity solutions. A single cilium moving in an infinite fluid is modelled using techniques developed by Hancock (1953), Lighthill (1975) and Chwang and Wu (1975). Techniques for modelling large fields of cilia are reviewed, including those first presented by Blake (1972) and Liron and Mochon (1976a). We then present a model for the cilia sublayer in the lung, which uses the Stokeslet for a point force in a fluid between two no-slip boundaries given by Liron and Mochon (1976b) and the dipole distribution for a slender ellipsoid from Chwang and Wu (1975). The lower boundary represents the epithelium, the upper

boundary represents the highly viscous mucus interface, moving horizontally according to the traction layer model of chapter 2. An extension of the techniques of Liron and Mochon, using the ideas developed for a single cilium, is presented. The resulting integral equations are solved using a simple quadrature formula, as used by Liron and Mochon (1976a), but with additional refinement points to improve convergence and ensure that the solution is correct in both the near and far-fields. Our approach is particularly useful since it does not involve extending the discrete-cilia model to multiple non-Newtonian layers.

3.2 Representing a single cilium

As in the work of Blake, Liron and Mochon we begin by defining $\boldsymbol{\xi}$, the curve describing the time-dependent shape of the centre line of a cilium whose base is fixed at the origin.

$$\boldsymbol{\xi} \quad = \quad (\xi_1(s,t), \xi_2(s,t), \xi_3(s,t)), \tag{3.1}$$

where s is the arc length along the cilium, varying between 0 and L, and t is time. The cilium shape will be periodic in time, so that $\boldsymbol{\xi}(s,t) = \boldsymbol{\xi}(s,t+T)$, where T is the period of the ciliary beat cycle. Due to the small size of the ASL compared with the size of the culture or bronchial tube, the epithelium is modelled as a doubly-infinite flat plane given by $x_3 = 0$.

One could attempt to model the internal mechanics of the cilia, and for simpler systems this has been done (Gueron and Liron, 1992, 1993) but, due to the computational cost that would result from modelling individual cilia in the complex liquid medium of the lung, this would be rather difficult to apply to our problem. In this study we will be concerned with calculating the fluid flow for a specified beat pattern. We follow Blake (1972) and represent the ciliary beat by a finite Fourier series:

$$\boldsymbol{\xi}(s,t) \quad = \quad \sum_{n=1}^{m_1} [\mathbf{a}_n(s)\cos(n\sigma t) + \mathbf{b}_n(s)\sin(n\sigma t)],$$

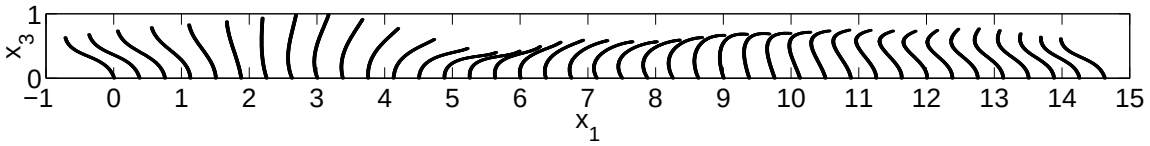

Figure 3.1: Computer reconstruction of the beat cycle from Sanderson and Sleigh (1981). Wavenumber $\kappa = 0.42$. Axes scaled with respect to cilium length.

$$\mathbf{a}_n(s) = \sum_{m=1}^{m_2} \mathbf{A}_{nm} s^m, \qquad \mathbf{b}_n(s) = \sum_{m=1}^{m_2} \mathbf{B}_{nm} s^m, \tag{3.2}$$

where σ is the angular frequency in $\mathrm{rad/s}$. For this simulation we use the coefficients $\mathbf{A}_{mn}$ and $\mathbf{B}_{mn}$ given by Fulford and Blake (1986), which produces the beat cycle depicted in Figure 3.1. The values for m_1 and m_2 are 6 and 3 respectively. These coefficients were obtained by least squares fitting to photographic images of cultures of cilia produced by Sanderson and Sleigh (1981).

3.3 Singularity solutions

The Stokeslet $S_{jk}(\mathbf{x}, \mathbf{y})$ for the velocity at $\mathbf{x}$ due to a point force at $\mathbf{y}$ is given by the solution $\mathbf{S}_k = (S_{1k}, S_{2k}, S_{3k})$ of the Stokes flow equations

$$\begin{aligned} -\boldsymbol{\nabla} p_k + \mu \nabla^2 \mathbf{S}_k + \mathbf{e}_k \delta(\mathbf{x} - \mathbf{y}) &= 0, \\ \boldsymbol{\nabla} \cdot \mathbf{S}_k &= 0. \end{aligned} \tag{3.3}$$

δ denotes the three dimensional Dirac delta distribution. $\mathbf{e}_k$ denotes the cartesian unit vector in the k direction. The velocity field resulting from a force $\mathbf{f}$ is then given by $u_j = S_{jk} f_k$. Here and in what follows we use the summation convention.

In an infinite fluid, the Stokeslet is given by $S^{\infty}_{jk} = (\delta_{jk}/r + r_j r_k / r^3)/(8\pi\mu)$. The potential source dipole, or doublet, is a higher order singularity given by $K_{jk} = (\delta_{jk}/r^3 - 3 r_j r_k / r^5)/(4\pi)$. This singularity decays much more rapidly, and will have a far less significant effect on the far-

field when compared with the Stokeslet. However, in the near-field it may be important.

For our new sublayer model, we will use the Stokeslet derived by Liron and Mochon (1976b) for a point force in the domain $-\infty < x_1 < \infty$, $-\infty < x_2 < \infty$ and $0 < x_3 < L$, as shown in Figure 3.6, and denoted by S_{jk}^C, and the summed and averaged form of this, denoted D_{jk}^C. In summary have

$$
\begin{aligned}
S_{jk}^{\infty} \quad & \text{Stokeslet for point force in infinite domain,} \\
S_{jk}^{\infty/2} \quad & \text{Stokeslet for point force in semi-infinite domain } x_3 \geqslant 0, \\
S_{jk}^{C} \quad & \text{Stokeslet for point force in confined domain } 0 \leqslant x_3 \leqslant L, \\
D_{jk}^{C} \quad := \quad & \sum_{q=-\infty}^{\infty} \int_{-\infty}^{\infty} S_{jk}^{C}(x_1, x_2, x_3, \xi_1 + q m_0 a, 0, \xi_3) \, \mathrm{d}x_2, \\
K_{jk} \quad & \text{potential source dipole in infinite domain,}
\end{aligned}
$$

and the symbol S_{jk} for a generic Stokeslet. The term D_{jk}^C results from considering a rectangular array of point forces with spacing $m_0 a$ in the x_1 direction, where $m_0 a$ is the metachronal wavelength, and spacing b in the x_2 direction. The expression is found from averaging (integrating) over $nb < x_2 < (n+1)b$, then summing over the double array. This is explained in more detail in §3.6.1.

3.4 Using singularity solutions to represent the cilium

The singularity approach exploits the linearity of the Stokes flow equations by summing singularity solutions of the field equations in order to satisfy the boundary conditions. Since the cilium is a slender body, we require that there will be a constant velocity on any circle around the surface. In addition, we require that for any given motion of the cilium $\partial\boldsymbol{\xi}/\partial t$, there exists a distribution of singularities that will give rise to a fluid flow $\mathbf{u}$ that is equal to $\partial\boldsymbol{\xi}/\partial t$ on the whole of the surface of the cilium.

A boundary integral formulation would typically involve distributing Stokeslets and Stress-

lets over the entire boundary surface, which in this case would be the surface of the cilium. This would be very computationally expensive, due to the large number of node points required. Instead we pursue a solution based on distributions of singularities along the axes of the cilia. This approach was first pursued by Hancock (1953), for the modelling of organisms such as nematode worms and spermatozoa.

We compare three different distributions of singularities, to determine which gives the most satisfactory representation. To begin with, we will work in the infinite domain.

3.4.1 Stokeslet distribution

The simplest way to represent the moving cilium is with a line distribution of Stokeslets $S_{jk}^{\infty}(\mathbf{x}, \boldsymbol{\xi}(s,t))$, of strength $f_k(\boldsymbol{\xi}(s,t))$ for $0 < s < L$, the approach used by Hancock (1953). At any time $t > 0$, the velocity field is then given by

$$u_j(\mathbf{x},t) \;=\; \int_0^L S_{jk}^{\infty}(\mathbf{x}, \boldsymbol{\xi}(s,t)) f_k(\boldsymbol{\xi}(s,t))\, \mathrm{d}s. \tag{3.4}$$

Here and in what follows, we use the summation convention for the directional index k. Applying this equation on the cilium, $u_j(\boldsymbol{\xi}(s,t)) = \partial \xi_j(s,t)/\partial t$ and so

$$\frac{\partial \xi_j}{\partial t}(s^*,t) \;=\; \int_0^L S_{jk}^{\infty}(\boldsymbol{\xi}(s^*,t), \boldsymbol{\xi}(s,t)) f_k(\boldsymbol{\xi}(s,t))\, \mathrm{d}s. \tag{3.5}$$

Hence we have a Fredholm integral equation of the first kind for the force distribution $f_k(\boldsymbol{\xi}(s,t))$. In what follows, we nondimensionalise with L as the length scale, σL at the velocity scale, σ^{-1} as the time scale and $\mu\sigma L^2$ as the force scale (so that the scaling for f_k is $\mu\sigma L$).

A simple way to solve this equation would be to replace the integral with a quadrature formula, such as the midpoint rule, and solve the resulting integral equation, as used by Liron and Mochon (1976a). However, S_{jk}^{∞} varies very rapidly close to the singularity, causing unacceptable oscillations in the solution between meshpoints. A more satisfactory approach is to divide

the cilium into the segments $((i-1)/N, i/N)$ with midpoints $s_i = (i-0.5)/N$, and assume that the force distribution $f_k(\boldsymbol{\xi}(s,t))$ can be approximated by the midpoint value $f_k(\boldsymbol{\xi}(s_i,t))$. This leads to

$$\begin{aligned}\frac{\partial \xi_j}{\partial t}(s_q,t) &= \sum_{i=1,i\neq q}^{N} f_k(\boldsymbol{\xi}(s_i,t)) \int_{(i-1)/N}^{i/N} \mu S_{jk}^{\infty}(\boldsymbol{\xi}(s_q,t),\boldsymbol{\xi}(s,t))\,\mathrm{d}s \\ &\quad + f_k(\boldsymbol{\xi}(s_q,t)) \int_{(q-1)/N}^{q/N} \mu S_{jk}^{\infty}(\boldsymbol{\xi}(s_q,t)+r_0\mathbf{n},\boldsymbol{\xi}(s,t))\,\mathrm{d}s, \end{aligned} \tag{3.6}$$

where $\mathbf{n} = (n_1, 0, n_3)$ is the normal to the cilium axis in the plane in which the cilia beat. We can then apply the midpoint rule with Q points to each integral, using the midpoints $s_{il} = (i-1)/N + (l-0.5)/(QN)$. Hence we have

$$\begin{aligned}\frac{\partial \xi_j}{\partial t}(s_q,t) &= \frac{1}{QN} \sum_{i=1,i\neq q}^{N} \sum_{l=1}^{Q} \mu S_{jk}^{\infty}(\boldsymbol{\xi}(s_q,t),\boldsymbol{\xi}(s_{il},t)) f_k(\boldsymbol{\xi}(s_i,t)) \\ &\quad + \frac{1}{QN} \sum_{l=1}^{Q} \mu S_{jk}^{\infty}(\boldsymbol{\xi}(s_q,t)+r_0\mathbf{n},\boldsymbol{\xi}(s_{ql},t)) f_k(\boldsymbol{\xi}(s_q,t)). \end{aligned} \tag{3.7}$$

The $+r_0\mathbf{n}$ term moves the point of evaluation off the cilium axis and onto a point on its surface to ensure that the Stokeslet is large, but finite. Equation (3.7) can be rearranged into a matrix equation

$$\frac{\partial \xi_j}{\partial t}(s_q,t) = \sum_{i=1}^{N} \mathcal{A}_{qj}^{ik} f_k(\boldsymbol{\xi}(s_i,t)), \quad 1 \leqslant j \leqslant 3, \quad 1 \leqslant q \leqslant N, \tag{3.8}$$

where $\mathcal{A}_{qj}^{ik}$ is given by

$$\mathcal{A}_{qj}^{ik} = \begin{cases} \dfrac{1}{QN} \displaystyle\sum_{l=1}^{Q} \mu S_{jk}^{\infty}(\boldsymbol{\xi}(s_q,t),\boldsymbol{\xi}(s_{il},t)) & \text{if} \quad i \neq q, \\ \dfrac{1}{QN} \displaystyle\sum_{l=1}^{Q} \mu S_{jk}^{\infty}(\boldsymbol{\xi}(s_q,t)+r_0\mathbf{n},\boldsymbol{\xi}(s_{ql},t)) & \text{if} \quad i = q. \end{cases} \tag{3.9}$$

This presents a system of $3N$ equations for $3N$ unknowns, the $f_k(\boldsymbol{\xi}(s_i,t))$ for $i = 1,\ldots,N$ and $k = 1,2,3$, which can be solved numerically with the F04AAF NAG library routine. The solution for the velocity field can then be calculated using the discretised version of equation (3.4),

$$u_j(\mathbf{x},t) = \frac{1}{QN}\sum_{i=1}^{N}\sum_{l=1}^{Q}\mu S_{jk}^{\infty}(\mathbf{x},\boldsymbol{\xi}(s_{il},t))f_k(\boldsymbol{\xi}(s_i,t))\,\mathrm{d}s. \tag{3.10}$$

When solving integral equations of the first kind various difficulties may be encountered. One such problem is the existence of non-trivial solutions f to the homogeneous equation $0 = \int_0^1 f(s)S(s)\,\mathrm{d}s$ when the kernel S is not everywhere positive—this means that the inhomogeneous problem will not have a unique solution and numerical results may be incorrect. We have tested the algorithm with $\partial\boldsymbol{\xi}/\partial t$ set to zero, but the only solution obtained for f was the zero solution. It is important for this type of integral equation that the matrix $\mathcal{A}$ is not singular or severely ill-conditioned, otherwise the solution is likely to be wildly oscillating. The kernel S_{jk}^{∞} is large at points where $i = q$ and $j = k$, which is useful because it ensures the diagonal elements of the matrix $\mathcal{A}$ are relatively large compared with the other elements, so that the solution is stable.

Once the force distribution is found, the algorithm can be checked for consistency by evaluating the velocity on the cilium surface. Using $\mathbf{n} = (n_1, 0, n_3)$ and $\mathbf{b} = (0,1,0)$ to denote the unit normal and binormal to the cilium centre line, we apply two tests: is the velocity on the line $\boldsymbol{\xi}(s,t) + r_0\mathbf{n}$ on the cilium surface equal to the cilium velocity $\partial\boldsymbol{\xi}/\partial t$, and is the velocity constant on the circle $\boldsymbol{\xi}(s,t) + r_0\cos\theta\mathbf{n} + r_0\sin\theta\mathbf{b}$, on the cilium surface for $0 < \theta < 2\pi$?

Some results are shown in Figure 3.2. In graph (A), there is an excellent fit to the boundary conditions except for near the cilium tip, where the calculated velocity diverges significantly from the cilium velocity, and near the base, where there is a small divergence from the expected zero velocity. Graph (B) shows a variation of around 10% in the velocity moving around the cylinder. We now consider refined approaches in order to represent the cilium more accurately.

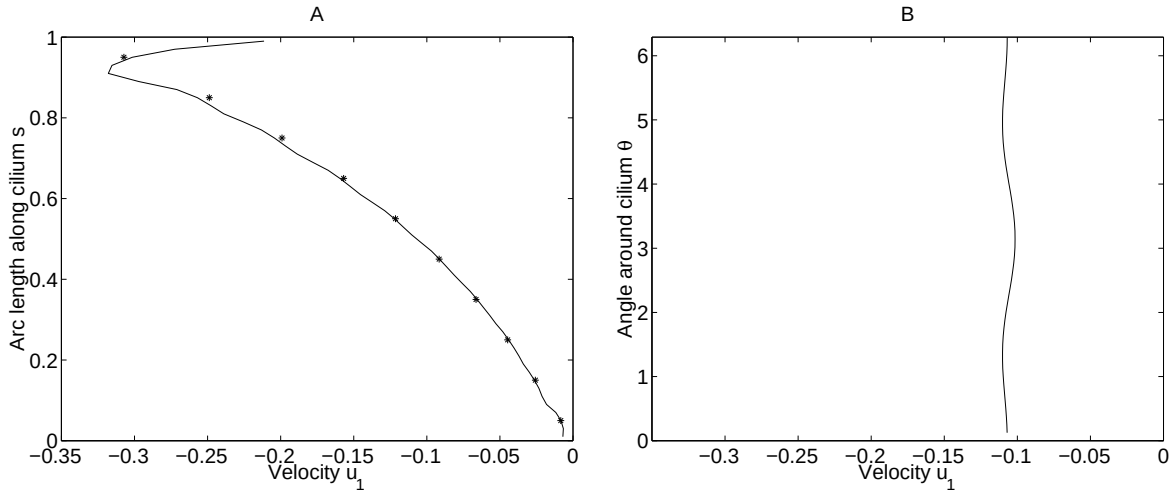

Figure 3.2: A—Profile along cilium for Stokeslet code, true cilium velocity at node points given by $*$. Parameters $N = 10$, $Q = 11$, $r_0 = 0.1/6$. B—Profile around cilium at $s = 0.5$.

3.4.2 Stokeslet and dipole distribution—the cylinder

Following on from the ideas of Hancock, Lighthill (1975) suggested that cilia and flagella could better be modelled by considering the combined action of Stokeslets and dipoles distributed on their axes. In Childress (1981) it is shown how the flow at $x = 0$ around a straight circular cylinder of radius A, lying on the x–axis between $x = -B$ and $x = C$ ($A, B, C > 0$, $A \ll B, C$) is given by a distribution of Stokeslets of strength $\mathbf{f}$ and dipoles of strength $A^2\mathbf{f}^n/4\mu$, where $\mathbf{f}^n$ is the component of $\mathbf{f}$ normal to the cilium axis. Since it is necessary to assume that $A \ll B, C$, this result may break down near the ends of the cilium. The cylindrical cilium shape is illustrated in Figure 3.4(A).

With $A = r_0$, this leads to the following integral equation:

$$\begin{aligned}\frac{\partial \xi_j}{\partial t}(s^*, t) &= \int_0^1 \mu S^{\infty}_{jk}(\boldsymbol{\xi}(s^*, t), \boldsymbol{\xi}(s, t)) f_k(\boldsymbol{\xi}(s, t))\, \mathrm{d}s \\ &\quad + \frac{r_0^2}{4} \int_0^1 K_{jk}(\boldsymbol{\xi}(s^*, t), \boldsymbol{\xi}(s, t)) f^n_k(\boldsymbol{\xi}(s, t))\, \mathrm{d}s, \end{aligned} \tag{3.11}$$

The singularity K_{jk} is the potential source dipole defined above, $\mathbf{f}^n$ is the projection of the force

$\mathbf{f}$ onto the plane normal to the cilium at the point $\boldsymbol{\xi}(s,t)$. The normal component of the force is defined to be $\mathbf{f}^n = (\mathbf{f}\cdot\mathbf{n})\mathbf{n} + (\mathbf{f}\cdot\mathbf{b})\mathbf{b}$.

Using the same discretisation as in §3.4, we have

$$\begin{aligned}\frac{\partial \xi_j}{\partial t}(s_q,t) &= \frac{1}{QN}\sum_{i=1,i\neq q}^{N}\sum_{l=1}^{Q}\mu S^{\infty}_{jk}(\boldsymbol{\xi}(s_q,t),\boldsymbol{\xi}(s_{il},t))f_k(\boldsymbol{\xi}(s_i,t))\\ &\quad+\frac{r_0^2}{4QN}\sum_{i=1,i\neq q}^{N}\sum_{l=1}^{Q}K_{jk}(\boldsymbol{\xi}(s_q,t),\boldsymbol{\xi}(s_{il},t))f^n_k(\boldsymbol{\xi}(s_i,t))\\ &\quad+\frac{1}{QN}\sum_{l=1}^{Q}\mu S^{\infty}_{jk}(\boldsymbol{\xi}(s_q,t)+r_0\mathbf{n},\boldsymbol{\xi}(s_{ql},t))f_k(\boldsymbol{\xi}(s_q,t))\\ &\quad+\frac{r_0^2}{4QN}\sum_{l=1}^{Q}K_{jk}(\boldsymbol{\xi}(s_q,t)+r_0\mathbf{n},\boldsymbol{\xi}(s_{ql},t))f^n_k(\boldsymbol{\xi}(s_q,t)).\end{aligned} \tag{3.12}$$

This can again be rearranged into the form (3.8) where $\mathcal{A}^{ik}_{qj}$ is given by

$$\mathcal{A}^{ik}_{qj} = \begin{cases}\dfrac{1}{QN}\displaystyle\sum_{l=1}^{Q}\Big[\frac{r_0^2}{4}K_{jp}(\boldsymbol{\xi}(s_q,t),\boldsymbol{\xi}(s_{il},t))\,(n_pn_k+\delta_{p2}\delta_{k2})\\ \qquad\qquad+\mu S^{\infty}_{jk}(\boldsymbol{\xi}(s_q,t),\boldsymbol{\xi}(s_{il},t))\Big] & \text{if}\quad i\neq q,\\ \dfrac{1}{QN}\displaystyle\sum_{l=1}^{Q}\Big[\frac{r_0^2}{4}K_{jp}(\boldsymbol{\xi}(s_q,t)+r_0\mathbf{n},\boldsymbol{\xi}(s_{il},t))\,(n_pn_k+\delta_{p2}\delta_{k2})\\ \qquad\qquad+\mu S^{\infty}_{jk}(\boldsymbol{\xi}(s_q,t)+r_0\mathbf{n},\boldsymbol{\xi}(s_{il},t))\Big] & \text{if}\quad i=q,\end{cases} \tag{3.13}$$

where $p=1,2,3$ is a summation index. The velocity field can then be computed from

$$u_j(\mathbf{x},t) = \int_0^1 \mu S^{\infty}_{jk}(\mathbf{x},\boldsymbol{\xi}(s,t))f_k(\boldsymbol{\xi}(s,t))\,\mathrm{d}s + \frac{r_0^2}{4}\int_0^1 K_{jk}(\mathbf{x},\boldsymbol{\xi}(s,t))f^n_k(\boldsymbol{\xi}(s,t))\,\mathrm{d}s, \tag{3.14}$$

and the solution $f_k(\boldsymbol{\xi}(s_i,t))$ can be tested as before by replacing $\mathbf{x}$ with $\boldsymbol{\xi}(s_q,t)+r_0\mathbf{n}$ and $u_j(\mathbf{x},t)$ with $\partial\xi_j/\partial t$.

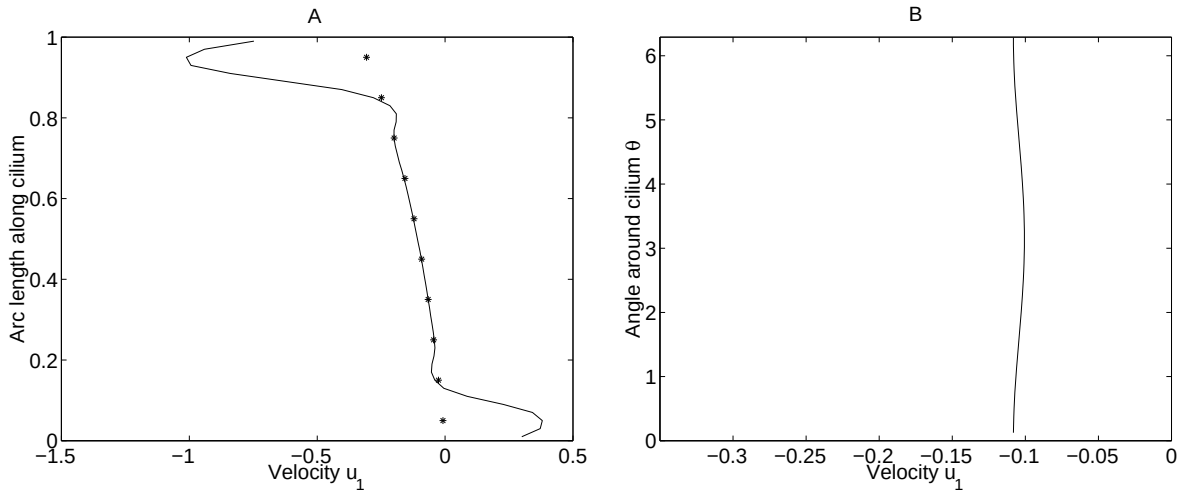

Figure 3.3: A—Profile along cilium for cylinder algorithm with $N = 10$, $Q = 11$, $r_0 = 0.1/6$. B—Profile around cilium at $s = 0.5$.

In Figure 3.3 we present some calculations for the cylinder algorithm. Graph (A) is significantly worse than Figure 3.2(A), since near the ends of the cilium, the dipole correction is not valid. Graph (B), however, shows a rather more satisfactory profile moving around the cilium. In §3.4.3 we use a refinement to the dipole distribution which gives more satisfactory results.

3.4.3 Stokeslet and dipole distribution—the ellipsoid

Another approach is to model the cilium as a slender ellipsoid. Chwang and Wu (1975) showed that the flow around a prolate spheroid $x^2/\beta^2 + (y^2 + z^2)/r_0^2 = 1$, $\beta \geq r_0$ is given by a distribution of Stokeslets with strength $\mathbf{f}$ and dipoles with strength $(l^2 - x^2)r_0^2/2\beta^2\mathbf{f}$. The focal length is $2l$, so that $l = (\beta^2 - r_0^2)^{1/2}$. In nondimensional units, where the cilium length is 1, we choose $l = 1/2$, $r_0 = 0.1/6$, so $\beta^2 = l^2 + r_0^2 = 0.2503$. The arc length parameter is given by $s = x + 1/2$ and so the singularity strength is $s(1 - s)r_0^2/0.5006$.

This leads to the expression

$$\begin{aligned}\frac{\partial \xi_j}{\partial t}(s^*, t) &= \int_0^1 \mu S_{jk}^{\infty}(\boldsymbol{\xi}(s^*, t), \boldsymbol{\xi}(s, t)) f_k(\boldsymbol{\xi}(s, t))\, \mathrm{d}s \\ &\quad + \frac{r_0^2}{1/2 + 2r_0^2} \int_0^1 s(1 - s) K_{jk}(\boldsymbol{\xi}(s^*, t), \boldsymbol{\xi}(s, t)) f_k(\boldsymbol{\xi}(s, t))\, \mathrm{d}s, \qquad (3.15)\end{aligned}$$

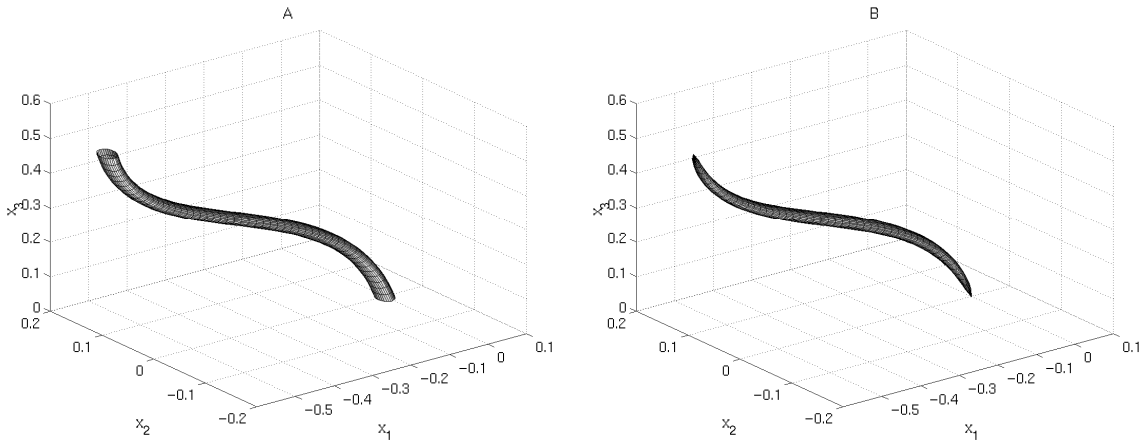

Figure 3.4: Notional cilium shapes for the ‘cylindrical’ and ‘ellipsoidal’ models. A—cylindrical cilium. B—ellipsoidal cilium.

which differs from equation (3.11) in that the dipole strength is calculated from f_k rather than the normal component f_k^n. This is then discretised,

$$\begin{aligned}\frac{\partial \xi_j}{\partial t}(s_q,t) &= \frac{1}{QN}\sum_{i=1,i\neq q}^{N}\sum_{l=1}^{Q}\mu S^{\infty}_{jk}(\boldsymbol{\xi}(s_q,t),\boldsymbol{\xi}(s_{il},t))f_k(\boldsymbol{\xi}(s_i,t))\\ &+\frac{r_0^2}{QN(1/2+2r_0^2)}\sum_{i=1,i\neq q}^{N}\sum_{l=1}^{Q}s_i(1-s_i)K_{jk}(\boldsymbol{\xi}(s_q,t),\boldsymbol{\xi}(s_{il},t))f_k(\boldsymbol{\xi}(s_i,t))\\ &+\frac{1}{QN}\sum_{l=1}^{Q}\mu S^{\infty}_{jk}(\boldsymbol{\xi}(s_q,t)+r_0\mathbf{n},\boldsymbol{\xi}(s_{ql},t))f_k(\boldsymbol{\xi}(s_q,t))\\ &+\frac{r_0^2}{QN(1/2+2r_0^2)}\sum_{l=1}^{Q}s_q(1-s_q)K_{jk}(\boldsymbol{\xi}(s_q,t)+r_0\mathbf{n},\boldsymbol{\xi}(s_{ql},t))f_k(\boldsymbol{\xi}(s_q,t)),\end{aligned} \tag{3.16}$$

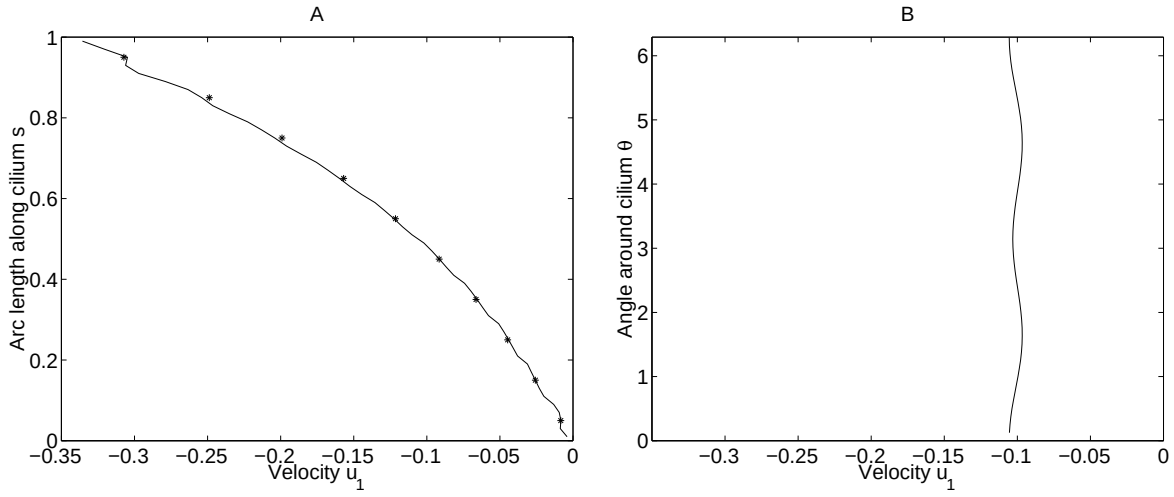

Figure 3.5: A—Profile along cilium for slender ellipsoid algorithm. Parameters $N = 10$, $Q = 11$, $r_0 = 0.1/6$. B—Profile around cilium at $s = 0.5$.

again leading to a matrix equation of the form (3.8),

$$\mathcal{A}_{qj}^{ik} = \begin{cases} \dfrac{1}{QN}\displaystyle\sum_{l=1}^{Q}\Bigg[\mu S_{jk}^{\infty}(\boldsymbol{\xi}(s_q,t),\boldsymbol{\xi}(s_{il},t)) \\ \quad + \dfrac{r_0^2}{1/2+2r_0^2}s_i(1-s_i)K_{jk}(\boldsymbol{\xi}(s_q,t),\boldsymbol{\xi}(s_{il},t))\Bigg] & \text{if} \quad i \neq q, \\ \dfrac{1}{QN}\displaystyle\sum_{l=1}^{Q}\Bigg[\mu S_{jk}^{\infty}(\boldsymbol{\xi}(s_q,t)+r_0\mathbf{n},\boldsymbol{\xi}(s_{ql},t)) \\ \quad + \dfrac{r_0^2}{1/2+2r_0^2}s_q(1-s_q)K_{jk}(\boldsymbol{\xi}(s_q,t)+r_0\mathbf{n},\boldsymbol{\xi}(s_{ql},t))\Bigg] & \text{if} \quad i = q. \end{cases} \tag{3.17}$$

In Figure 3.5(A) there is a very significant improvement in the fit between the cilium velocity and the calculated velocity at the cilium tip and base. Figure 3.5(B) shows that the variations in velocity around the cilium are still small, comparable with the results for the other algorithms.

3.5 Singularity distributions for the confined domain

Since we wish to model a cilium beating in a confined domain, we now repeat the above calculations with the confined domain Stokeslet, S_{jk}^C, which satisfies $S_{jk}^C(x_3 = 0) = 0 = S_{jk}^C(x_3 = 1)$,

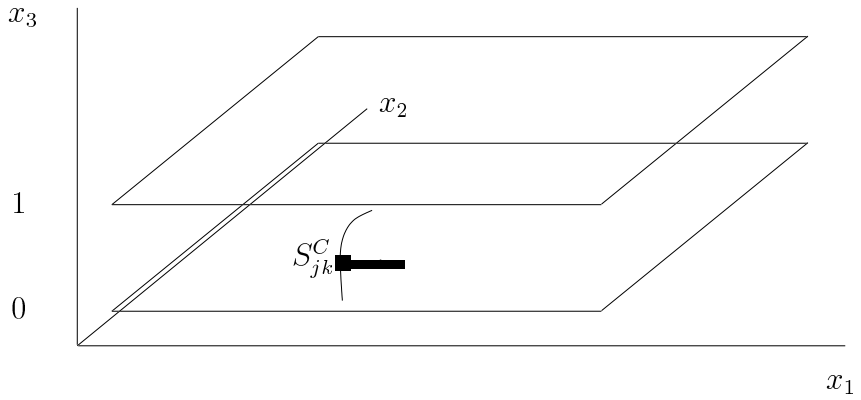

Figure 3.6: Confined domain $0 < x_3 < 1$.

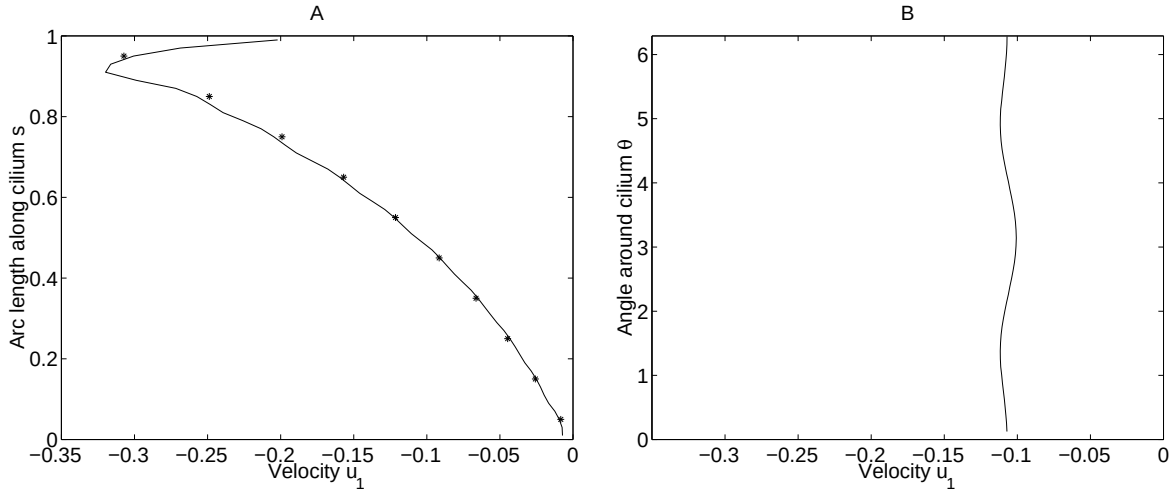

Figure 3.7: A—Profile along cilium for Stokeslet code, confined domain. Parameters $N = 10$, $Q = 11$, $r_0 = 0.1/6$. B—Profile around cilium at $s = 0.5$.

as depicted in Figure 3.6. We shall not modify the dipole, due to its higher-order decay.

In Figure 3.7 for the Stokeslet only, there is again significant divergence between the expected cilium tip velocity and the calculated velocity. The results moving around the cilium are similar to the infinite domain results, with a range of approximately 0.011. In Figure 3.8 for the ellipsoidal representation, the profile along the length of the cilium is again very satisfactory. The variations in velocity moving around the cilium are approximately 0.007, which is an improvement on the Stokeslet only results. Based on the calculations presented here, we conclude that the slender ellipsoid is the best representation for the cilium, and will use this for our model

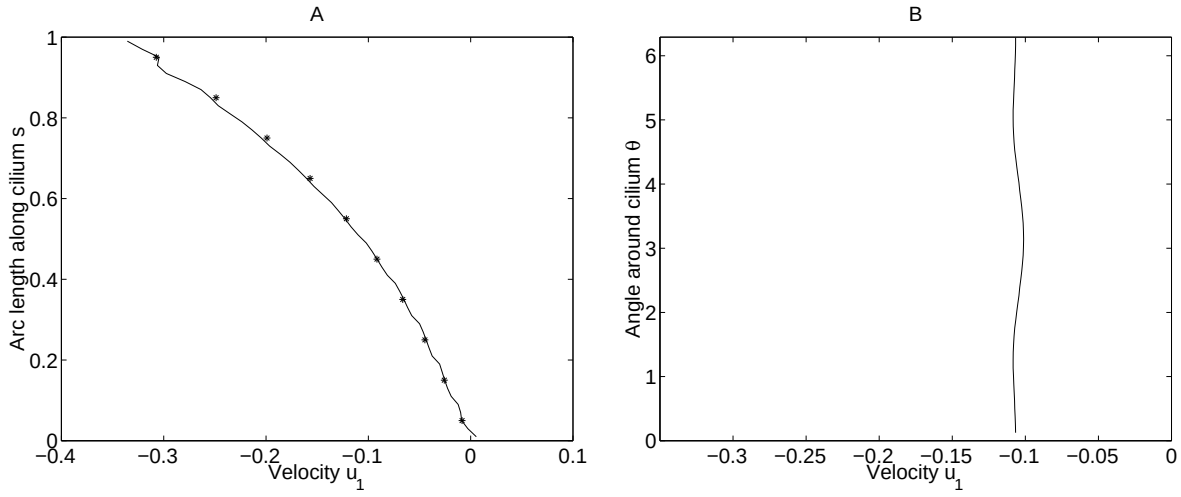

Figure 3.8: A—Profile along cilium for slender ellipsoid code, confined domain. Parameters $N = 10$, $Q = 11$, $r_0 = 0.1/6$. B—Profile around cilium at $s = 0.5$.

in §3.7.

3.6 Representing infinite arrays of cilia

The next step in modelling the sublayer is to take into account the large number of cilia. The approach taken by Blake (1973b) was to consider an evenly spaced doubly-infinite array of cilia, and to make the simplifying assumption that the metachronal wave extends throughout the cilia in the x_1 direction, and that the cilia are in phase in the x_2 direction. The periodicity of the wave and the symmetry in the x_2 direction can then be exploited. This setup is depicted in Figure 3.9.

3.6.1 Metachronal wave

We assume antiplectic metachronism, that is the metachronal wavefront propagates in the negative x_1 direction, the mucus being transported in the positive x_1 direction. With this assumption, a cilium whose base is fixed at $x_1 = x$ will be described by $(x, 0, 0) + \boldsymbol{\xi}(s, \kappa x/\sigma + t)$, $0 < s < 1$, where κ is the wavenumber $2\pi/\lambda$, $\sigma/2\pi$ is the frequency and $c = \sigma/\kappa$ is the wavespeed. The plus sign before the σ indicates antiplectic metachronism. If we assume that the cilia have a

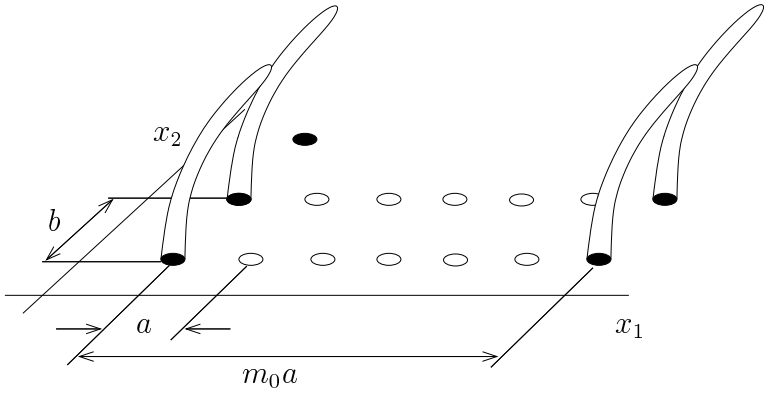

Figure 3.9: The doubly-infinite array of cilia, with spacing a in the x_1 direction and b in the x_2 direction. In the x_1 direction, every m_0th cilium is in phase due to periodicity. In the x_2 direction, every cilium is assumed to be in phase.

spacing a in the x_1 direction and b in the x_2 direction then the cilium at $(ma, nb, 0)$ is described by

$$\boldsymbol{\xi}_{mn}(s,t) = (ma + \xi_1(s,\tau_m), nb + \xi_2(s,\tau_m), \xi_3(s,\tau_m)), \tag{3.18}$$

where

$$\tau_m = \kappa m a/\sigma + t, \quad m, n = 0, \pm 1, \pm 2, \ldots \tag{3.19}$$

Blake, (1972; 1973b; 1975b; 1984), Fulford and Blake (1986), Liron and Mochon (1976a) and Liron (1978) all modelled the cilia as line distributions of Stokeslets S_{jk} only. Summing over the doubly-infinite array we have

$$u_j(\mathbf{x},t) = \sum_{n=-\infty}^{\infty} \sum_{m=-\infty}^{\infty} \int_0^1 f_k(\boldsymbol{\xi}_{mn}(s,t)) \mu S_{jk}(\mathbf{x}, \boldsymbol{\xi}_{mn}(s,t)) \, \mathrm{d}s, \tag{3.20}$$

where $j = 1, 2, 3$. It is not possible to solve this integral equation immediately but there are various ways to rearrange it into a more tractable form. Suppose there are m_0 cilia in one wavelength, so that for all integers m we can write $m = qm_0 + r$, where $0 \leq r \leq m_0 - 1$ and

$q = 0, \pm 1, \pm 2, \ldots$. By definition,

$$\begin{aligned} \boldsymbol{\xi}(s, \tau_m) &= \boldsymbol{\xi}(s, m_0 \kappa a q/\sigma + \kappa a r/\sigma + t), \\ &= \boldsymbol{\xi}(s, 2\pi q/\sigma + \kappa a r/\sigma + t), \\ &= \boldsymbol{\xi}(s, \kappa a r/\sigma + t), \end{aligned} \tag{3.21}$$

the last line following by periodicity of $\boldsymbol{\xi}$. We write $\boldsymbol{\xi}(s, \kappa a r/\sigma + t)$ as $\boldsymbol{\xi}^r(s,t)$. By making some further periodicity assumptions on f_k, given in equation (3.26) we can show that $f_k(\boldsymbol{\xi}^r(s,t)) = f_k(\boldsymbol{\xi}_{mn}(s,t))$. Hence we can rewrite the above as

$$u_j(\mathbf{x}, t) = \sum_{r=0}^{m_0 - 1} \int_0^1 f_k(\boldsymbol{\xi}^r(s,t)) \sum_{q=-\infty}^{\infty} \sum_{n=-\infty}^{\infty} \mu S_{jk}(\mathbf{x}, \boldsymbol{\xi}_{qm_0+r,n}(s,t)) \, \mathrm{d}s, \tag{3.22}$$

as given in Sleigh and Blake (1975), Liron and Mochon (1976a). In the following sections we review the approaches developed by Blake, Fulford, Liron and coworkers to solving equation 3.22. In §3.7 we then present an improved model which is an extension of the work of Liron and Mochon.

3.6.2 Poisson summation formula

It would be useful if the doubly-infinite sum could be approximated by the first few terms, however it is not clear that this would be very accurate. Blake (1972) used a form of the Poisson summation formula (Lighthill, 1958) to convert this sum into an exponentially decreasing series involving the Fourier-transformed Stokeslet. This is especially useful since finding the solution for a particular domain will involve first finding the Fourier-transformed version. Indeed, it may not in practice be possible to invert the transform.

For the semi-infinite Stokeslet $S_{jk}^{\infty/2}$, taking only the zeroth term of the double series, Blake

found that

$$\sum_{q=-\infty}^{\infty}\sum_{n=-\infty}^{\infty} S_{jk}^{\infty/2} = \frac{\delta_{j1}\delta_{k1}+\delta_{j2}\delta_{k2}}{m_0\mu ab}K(x_3,\xi_3) + O\left(\frac{m_0 ab}{L^2}\right), \tag{3.23}$$

where the kernel K is defined by

$$K(x_3,\xi_3) \;=\; \begin{cases} x_3 & \text{if} \quad x_3 < \xi_3, \\ \xi_3 & \text{if} \quad \xi_3 < x_3, \end{cases} \tag{3.24}$$

as given in Blake (1972), and with the error estimate in Blake (1999). An average was then taken in the x_1 and x_2 directions and in time, so that the mean velocity profile $\mathbf{U}(x_3)$ could be found. In order to solve for the forces, a Gray and Hancock (1955) type approximation was used. The tangential component of the force on a cilium was assumed to be proportional to the tangential component of the interaction velocity of the cilium with the mean flow, so that $\delta\mathbf{F}_T = C_T[(\partial\boldsymbol{\xi}/\partial t - \mathbf{U} + \mathbf{V})\cdot\mathbf{t}]\mathbf{t}\delta s$, where $\mathbf{U}$ is the mean velocity of the fluid, $\mathbf{V}$ is the mean velocity due to the cilium in question and $\mathbf{t}$ is the unit tangent. The normal component was defined similarly, with constant of proportionality C_N. The values for C_T, C_N were determined from slender body analyses. For the 1972 study, Blake used

$$C_T \;=\; \frac{2\pi\mu}{\log(L/r_0)+k_1}, \qquad C_N \;=\; \gamma C_T, \tag{3.25}$$

where γ is defined in terms of an asymptotic expansion in r_0/L and k_1 is a constant of $O(1)$. Choosing appropriate values for C_N and C_T depends on the particular shape of the slender body. For example, Chwang and Wu (1975) gave values based on a slender ellipsoid model. This led to a pair of coupled integral equations for $\mathbf{U}$ and $\mathbf{V}$, which were solved iteratively. The resulting velocity profiles can be found in Blake (1972).

This approach was extended further in a series of papers (Blake, 1984; Blake and Fulford, 1984; Fulford and Blake, 1986) which presented a far more detailed model of the cilia beating

in a two layer fluid. By taking the mucus–PCL interface to be flat, to a first approximation, and assuming that the correct boundary conditions were continuity of normal and tangential stress together with velocity, Green's functions could be derived for point forces in both the mucus and PCL. The rearrangement (3.22) was used, together with the first order approximation to the array of Green's functions. The force due to a slender body 'straddling' the interface was calculated as an asympotic expansion, and mean velocity profiles were calculated for the cases where the cilia do or do not penetrate the mucous layer. Surface tension was considered to be a second order effect, and approximate shapes of the interface were calculated. Their numerical results suggested that penetration was not necessary for positive propulsion in normal lungs, although this may be a consequence of the way the interfacial boundary was modelled.

3.6.3 Exploiting periodicity

At present we are concerned with obtaining more detail regarding the flow in the PCL. Liron and Mochon (1976a) and Liron (1978) avoided the need to use time averaging and Gray and Hancock type approximations and produced an integral equation for the force distribution as follows: they assumed that there was no variation of f_k with x_2, and that f_k varied with the metachronal wave, so that

$$\begin{aligned} f_k(\boldsymbol{\xi}_{mn}(s,t)) &= f_k(\boldsymbol{\xi}_{m0}(s,t)), \\ f_k(\boldsymbol{\xi}_{mn}(s,t)) &= f_k(\boldsymbol{\xi}_{m+1,n}(s,t-\kappa a/\sigma)). \end{aligned} \tag{3.26}$$

From this it follows that $f_k(\boldsymbol{\xi}_{mn}(s,t)) = f_k(\boldsymbol{\xi}_{00}(s,t+\kappa m a/\sigma)) = f_k(\boldsymbol{\xi}(s,\tau_m))$.

They argued that, because there was no phase difference in the x_2 direction, it was legitimate to average out the velocity in this direction. Using the symbol S_{jk} for a generic Stokeslet, this

gave the mean velocity

$$\begin{aligned}\bar{u}_j(x_1, x_3, t) &= \frac{1}{b}\int_0^b \mathrm{d}x_2 \sum_{m=-\infty}^{\infty}\sum_{n=-\infty}^{\infty}\int_0^1 f_k(\boldsymbol{\xi}(s,\tau_m))\mu S_{jk}(\mathbf{x}, \boldsymbol{\xi}_{mn}(s,t))\,\mathrm{d}s, \\ &= \frac{1}{b}\sum_{m=-\infty}^{\infty}\int_0^1 f_k(\boldsymbol{\xi}(s,\tau_m))\left(\int_{-\infty}^{\infty}\mu S_{jk}(\mathbf{x}, \boldsymbol{\xi}_{m0}(s,t))\,\mathrm{d}x_2\right)\,\mathrm{d}s, \quad (3.27)\end{aligned}$$

the last line following since $S_{jk}(\mathbf{x}, \boldsymbol{\xi})$ depends on x_2 and ξ_2 only through their difference. Applying the periodicity assumption above this reduced to

$$\begin{aligned}\bar{u}_j(x_1, x_3, t) &= \frac{1}{b}\sum_{r=0}^{m_0-1}\int_0^1 f_k(\boldsymbol{\xi}^r(s,t))\left(\sum_{q=-\infty}^{\infty}\int_{-\infty}^{\infty}\mu S_{jk}(\mathbf{x}, \boldsymbol{\xi}_{qm_0+r,0}(s,t))\,\mathrm{d}x_2\right)\,\mathrm{d}s, \\ &= \frac{1}{b}\sum_{r=0}^{m_0-1}\int_0^1 f_k(\boldsymbol{\xi}^r(s,t))\mu D_{jk}(x_1 - ra, x_3, \boldsymbol{\xi}^r(s,t))\,\mathrm{d}s, \quad (3.28)\end{aligned}$$

where the kernel D_{jk} must be calculated for the appropriate domain from S_{jk}, as in Liron and Mochon (1976a) and Liron (1978).

3.6.4 Pressure gradient

Liron (1978) observed that, due to the periodic boundary conditions resulting from the above analysis, the solution was non-unique—an arbitrary constant pressure gradient could be added. In the circular transport experiments of Matsui et al. (1998b), no pressure gradient could have been present, due to the fact that any such pressure must be continuous as we move around the culture. For now, we shall not consider the effect of a pressure gradient, although it is certainly possible that *in vivo* one may be present.

3.7 Improved discrete cilia model

3.7.1 Improving the near field resolution

Liron (1996) argued that taking an average in the x_2 direction is by no means accurate, since the

variations of $S_{jk}(\mathbf{x}, \boldsymbol{\xi}_{m0}(s,t))$ in x_2 for $\mathbf{x}$ close to $\boldsymbol{\xi}_{m0}(s,t)$ are significant. The doubly-infinite sums of the Stokeslets were calculated analytically as a remedy for this, however the expressions are very lengthy and computationally expensive. Instead we will proceed by performing the averaging in the far-field only, using the exact form of the Stokeslet in the near-field. By not averaging in the near-field we also can check that the boundary condition discussed in §3.4.1 is satisfied by the solution. We shall work in the confined domain, using the Stokeslet S^C_{jk}. As before we start with the doubly-infinite field of cilia:

$$u_j(\mathbf{x},t) = \sum_{n=-\infty}^{\infty} \sum_{m=-\infty}^{\infty} \int_0^1 f_k(\boldsymbol{\xi}_{mn}(s,t)) \mu S^C_{jk}(\mathbf{x}, \boldsymbol{\xi}_{mn}(s,t)) \, \mathrm{d}s, \tag{3.29}$$

and assume without loss of generality that the point $\mathbf{x}$ lies close to the cilium with base at $(m^*a, 0)$, given by $\boldsymbol{\xi}_{m^*0}(s,t)$. Adding a field of dipoles to represent the nearest cilium as a slender ellipsoid and separating out near and far-field contributions, we have

$$\begin{aligned} u_j(\mathbf{x},t) \;=\; & \sum_{n=-\infty}^{\infty} \sum_{m=-\infty}^{\infty} \int_0^1 f_k(\boldsymbol{\xi}_{mn}(s,t)) \mu S^C_{jk}(\mathbf{x}, \boldsymbol{\xi}_{mn}(s,t)) \, \mathrm{d}s \\ & - \int_0^1 f_k(\boldsymbol{\xi}_{m^*0}(s,t)) \mu S^C_{jk}(\mathbf{x}, \boldsymbol{\xi}_{m^*0}(s,t)) \, \mathrm{d}s \\ & + \int_0^1 f_k(\boldsymbol{\xi}_{m^*0}(s,t)) \mu S^C_{jk}(\mathbf{x}, \boldsymbol{\xi}_{m^*0}(s,t)) \, \mathrm{d}s \\ & + \int_0^1 \frac{r_0^2}{1/2 + 2r_0^2} s(1-s) f_k(\boldsymbol{\xi}_{m^*0}(s,t)) K_{jk}(\mathbf{x}, \boldsymbol{\xi}_{m^*0}(s,t)) \, \mathrm{d}s, \end{aligned} \tag{3.30}$$

where the sum of the first two terms will not vary rapidly with x_2. Using the periodicity argu-

ment as for (3.22) we have

$$\begin{aligned} u_j(\mathbf{x},t) &= \sum_{r=0}^{m_0-1}\int_0^1 f_k(\boldsymbol{\xi}^r(s,t))\sum_{q=-\infty}^{\infty}\sum_{n=-\infty}^{\infty}\mu S^C_{jk}(\mathbf{x},\boldsymbol{\xi}_{qm_0+r,n}(s,t))\,\mathrm{d}s \\ &\quad -\int_0^1 f_k(\boldsymbol{\xi}_{m^*0}(s,t))\mu S^C_{jk}(\mathbf{x},\boldsymbol{\xi}_{m^*0}(s,t))\,\mathrm{d}s \\ &\quad +\int_0^1 f_k(\boldsymbol{\xi}_{m^*0}(s,t))\mu S^C_{jk}(\mathbf{x},\boldsymbol{\xi}_{m^*0}(s,t))\,\mathrm{d}s \\ &\quad +\int_0^1 \frac{r_0^2}{1/2+2r_0^2}s(1-s)f_k(\boldsymbol{\xi}_{m^*0}(s,t))K_{jk}(\mathbf{x},\boldsymbol{\xi}_{m^*0}(s,t))\,\mathrm{d}s. \end{aligned} \tag{3.31}$$

We then average the first two terms in the x_2 direction:

$$\begin{aligned} u_j(\mathbf{x},t) &= \frac{1}{b}\int_{-b/2}^{b/2}\mathrm{d}x_2\sum_{r=0}^{m_0-1}\int_0^1 f_k(\boldsymbol{\xi}^r(s,t))\sum_{q=-\infty}^{\infty}\sum_{n=-\infty}^{\infty}\mu S^C_{jk}(\mathbf{x},\boldsymbol{\xi}_{qm_0+r,n}(s,t))\,\mathrm{d}s \\ &\quad -\frac{1}{b}\int_{-b/2}^{b/2}\mathrm{d}x_2\int_0^1 f_k(\boldsymbol{\xi}_{m^*0}(s,t))\mu S^C_{jk}(\mathbf{x},\boldsymbol{\xi}_{m^*0}(s,t))\,\mathrm{d}s \\ &\quad +\int_0^1 f_k(\boldsymbol{\xi}_{m^*0}(s,t))\mu S^C_{jk}(\mathbf{x},\boldsymbol{\xi}_{m^*0}(s,t))\,\mathrm{d}s \\ &\quad +\int_0^1 \frac{r_0^2}{1/2+2r_0^2}s(1-s)f_k(\boldsymbol{\xi}_{m^*0}(s,t))K_{jk}(\mathbf{x},\boldsymbol{\xi}_{m^*0}(s,t))\,\mathrm{d}s, \end{aligned} \tag{3.32}$$

and again, since μS^C_{jk} depends on x_2 and ξ_2 only through their difference, we have

$$\begin{aligned} u_j(\mathbf{x},t) &= \frac{1}{b}\sum_{r=0}^{m_0-1}\int_0^1 f_k(\boldsymbol{\xi}_{mn}(s,t))\left(\sum_{q=-\infty}^{\infty}\int_{-\infty}^{\infty}\mu S^C_{jk}(\mathbf{x},\boldsymbol{\xi}_{qm_0+r,0}(s,t))\,\mathrm{d}x_2\right)\mathrm{d}s \\ &\quad -\frac{1}{b}\int_0^1 f_k(\boldsymbol{\xi}_{m^*0}(s,t))\left(\int_{-b/2}^{b/2}\mu S^C_{jk}(\mathbf{x},\boldsymbol{\xi}_{m^*0}(s,t))\,\mathrm{d}x_2\right)\mathrm{d}s \\ &\quad +\int_0^1 f_k(\boldsymbol{\xi}_{m^*0}(s,t))\mu S^C_{jk}(\mathbf{x},\boldsymbol{\xi}_{m^*0}(s,t))\,\mathrm{d}s \\ &\quad +\int_0^1 \frac{r_0^2}{1/2+2r_0^2}s(1-s)f_k(\boldsymbol{\xi}_{m^*0}(s,t))K_{jk}(\mathbf{x},\boldsymbol{\xi}_{m^*0}(s,t))\,\mathrm{d}s. \end{aligned} \tag{3.33}$$

The Stokeslet averaged between $x_2=-b/2$ and $x_2=b/2$ is denoted $\bar{S}^C_{jk}$. For computation, this

may be calculated numerically, for example with an efficient adaptive grid method. By using the definitions of $\boldsymbol{\xi}_{qm_0+r,0}(s,t)$, τ_{qm_0+r}, the fact that the singularities only depend on x_1, ξ_1 and x_2, ξ_2 through their respective differences, and the definition of the kernel D^C_{jk}, one can rewrite the summed and averaged Stokeslet as follows

$$\begin{aligned}
&\sum_{q=-\infty}^{\infty} \int_{-\infty}^{\infty} \mu S^C_{jk}(\mathbf{x}, \boldsymbol{\xi}_{qm_0+r,0}(s,t))\, \mathrm{d}x_2 \\
= &\sum_{q=-\infty}^{\infty} \int_{-\infty}^{\infty} \mu S^C_{jk}(x_1, x_2, x_3, (qm_0+r)a + \xi_1(s, \tau_{qm_0+r}), \xi_2(s, \tau_{qm_0+r}), \xi_3(s, \tau_{qm_0+r}))\, \mathrm{d}x_2 \\
= &\sum_{q=-\infty}^{\infty} \int_{-\infty}^{\infty} \mu S^C_{jk}(x_1 - ra, x_2, x_3, qm_0 a + \xi_1(s, t + kra/\sigma), \xi_2, \xi_3)\, \mathrm{d}x_2 \\
= &\sum_{q=-\infty}^{\infty} \int_{-\infty}^{\infty} \mu S^C_{jk}(x_1 - ra, x_2, x_3, qm_0 a + \xi^r_1(s,t), \xi^r_2(s,t), \xi^r_3(s,t))\, \mathrm{d}x_2 \\
= &\ \mu D^C_{jk}(x_1 - ra, x_3, \xi^r_1(s,t), \xi^r_3(s,t)).
\end{aligned} \tag{3.34}$$

The last line following by definition of D^C_{jk}. By periodicity,

$$S^C_{jk}(\mathbf{x}, \boldsymbol{\xi}_{m^*0}(s,t)) = S^C_{jk}(x_1 - m^* a, x_2, x_3, \xi^{m^*}_1(s,t), \xi^{m^*}_2(s,t), \xi^{m^*}_3(s,t)) \tag{3.35}$$

and we have already shown that $f_k(\boldsymbol{\xi}_{m^*0}(s,t)) = f_k(\boldsymbol{\xi}^{m^*}(s,t))$. Hence we have

$$\begin{aligned}
u_j(\mathbf{x},t) = &\ \frac{1}{b} \sum_{r=0}^{m_0-1} \int_0^1 f_k(\boldsymbol{\xi}^r(s,t)) \mu D^C_{jk}(x_1 - ra, x_3, \xi^r_1(s,t), \xi^r_3(s,t))\, \mathrm{d}s \\
&- \frac{1}{b} \int_0^1 f_k(\boldsymbol{\xi}^{m^*}(s,t)) \mu \bar{S}^C_{jk}(x_1 - m^* a, x_3, \xi^{m^*}_1(s,t), \xi^{m^*}_3(s,t))\, \mathrm{d}s \\
&+ \int_0^1 f_k(\boldsymbol{\xi}^{m^*}(s,t)) \mu S^C_{jk}(x_1 - m^* a, x_2, x_3, \xi^{m^*}_1(s,t), \xi^{m^*}_2(s,t), \xi^{m^*}_3(s,t))\, \mathrm{d}s \\
&+ \int_0^1 \frac{r_0^2}{1/2 + 2r_0^2} s(1-s) f_k(\boldsymbol{\xi}^{m^*}(s,t)) \\
&\cdot K_{jk}(x_1 - m^* a, x_2, x_3, \xi^{m^*}_1(s,t), \xi^{m^*}_2(s,t), \xi^{m^*}_3(s,t))\, \mathrm{d}s.
\end{aligned} \tag{3.36}$$

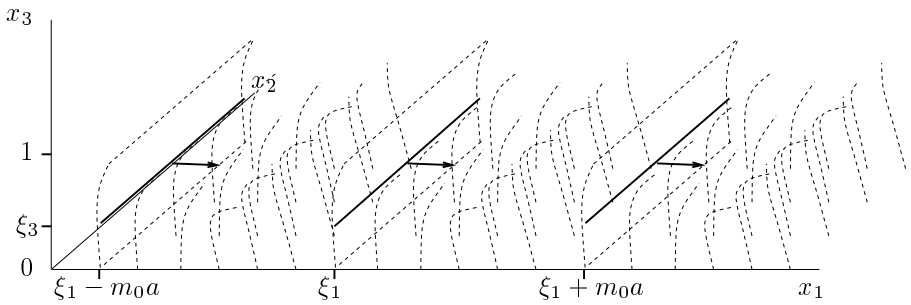

Figure 3.10: A representation of the summed and averaged singularity D^C_{jk}. Each singularity is equivalent to a line of point forces in the x_2 direction, repeated every $m_0 a$ units in the x_1 direction.

Applying this on the cilium so that $\mathbf{x} = (\xi_1^{m^*} + m^* a, \xi_2^{m^*}, \xi_3^{m^*})$ we have

$$\begin{aligned}
\frac{\partial \xi_j^{m^*}}{\partial t}(s^*,t) &= \frac{1}{b}\sum_{r=0}^{m_0-1}\int_0^1 f_k(\boldsymbol{\xi}^r(s,t)) \\
&\quad \cdot \mu D^C_{jk}(\xi_1^{m^*}(s^*,t) + (m^*-r)a, \xi_3^{m^*}(s^*,t), \xi_1^r(s,t), \xi_3^r(s,t))\,\mathrm{d}s \\
&\quad -\frac{1}{b}\int_0^1 f_k(\boldsymbol{\xi}^{m^*}(s,t))\mu \bar{S}^C_{jk}(\boldsymbol{\xi}^{m^*}(s^*,t), \boldsymbol{\xi}^{m^*}(s,t))\,\mathrm{d}s \\
&\quad + \int_0^1 f_k(\boldsymbol{\xi}^{m^*}(s,t))\mu S^C_{jk}(\boldsymbol{\xi}^{m^*}(s^*,t), \boldsymbol{\xi}^{m^*}(s,t))\,\mathrm{d}s \\
&\quad + \int_0^1 \frac{r_0^2 s(1-s)}{1/2 + 2r_0^2} f_k(\boldsymbol{\xi}^{m^*}(s,t)) K_{jk}(\boldsymbol{\xi}^{m^*}(s^*,t), \boldsymbol{\xi}^{m^*}(s,t))\,\mathrm{d}s. \qquad (3.37)
\end{aligned}$$

The kernels D^C_{jk} and $D^C_{jk} - \bar{S}^C_{jk}$ are depicted in Figures 3.10 and 3.11. The above equation can be solved as before to give the force distribution $f_k(\boldsymbol{\xi}^m(s_i,t))$, on every node point of every one of the m_0 cilia, at a fixed time t. By periodicity, we have $f_k(\boldsymbol{\xi}^m(s_i, t + \kappa n a/\sigma)) = f_k(\boldsymbol{\xi}^{m+n}(s_i,t))$, so if we calculate the force distribution at time $t = 0$, then we have the force distribution at the discrete points in time kna/σ, $n = 0, 1, \ldots, m_0 - 1, \ldots$ If there are sufficiently many cilia so that a is small, then by calculating the force distribution at $t = 0$ we have a significant amount of information about the progress of the force distribution, and hence the velocity field.

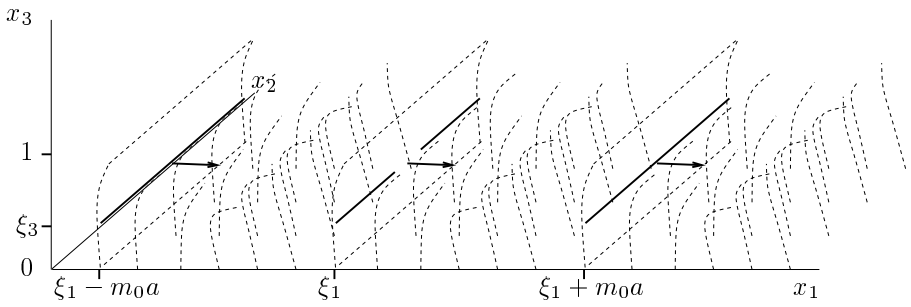

Figure 3.11: A representation of the kernel $D^C_{jk} - \bar{S}^C_{jk}$. This is the summed and averaged singularity D^C_{jk} with the near-field contribution $\bar{S}^C_{jk}$ removed.

3.7.2 Cilia between two flat plates

Various forms of the Stokeslet have been employed for modelling lung cilia. As discussed above, Blake (1973b) began with the semi-infinite Stokeslet, and after some manipulation found the representation $K(x_3, \xi_3)$ defined in equation (3.24) for the doubly-infinite field. Blake (1975b) used a finite sequence of image singularities to approximate the Stokeslet for a finite depth fluid above a plane no-slip boundary, which is appropriate if the ASL is considered as a fluid of constant viscosity, as may be the case in the distal airways and near the alveoli, where the mucous layer is not yet established. Fulford and Blake (1986) used the leading order term for the rather more complex Stokeslet in a two layer Newtonian system. We shall proceed differently, using the concept of a fluid between two parallel plates to represent the PCL. The mucus boundary, which remains relatively flat and is almost solid compared to the PCL is hence modelled as a flat no-slip boundary. We argue that this is legitimate because '...cilia encounter mucus as a solid...' (Salathe et al., 1997) and '...the response of the mucous layer lying on top of the bed of beating cilia is that of a semi-solid sheet...' (Meyer and Silberberg, 1980). In order to accommodate the movement of the mucous layer we again exploit the linearity of the Stokes flow equation by adding a time-dependent shear-driven flow given by the traction layer model. Our discrete cilia model can be considered a higher order correction to the two-dimensional phenomenological model of chapter 2, to gain more detail regarding the three-dimensional flow

patterns in the PCL.

The ciliated plate, representing the epithelium, is at $x_3 = 0$, the moving plate, representing the mucous layer, is at $x_3 = 1$. We split the total velocity u_j into two parts, $u_j = u_j^{\rm shear} + u_j^{\rm discrete}$, where $u_j^{\rm shear}$ is the solution of the Stokes flow equations with a moving boundary, discussed in §3.7.3, and $u_j^{\rm discrete}$ is the flow due to the discrete array of cilia.

To calculate the flow due to cilia beating in a domain bounded by two flat plates, as a model for flow in the ductus efferentes of the male reproductive tract, Blake (1973a) proposed taking the single plate solution he had developed in Blake (1972) near each plate, then connecting the solutions with a flat or parabolic profile. Liron and Mochon (1976b) derived the exact form for a Stokeslet in such a domain using the technique of double Fourier transforms. They did not give a simple closed-form solution, but instead gave solutions in terms of both Hankel transforms and exponentially decreasing infinite series, the latter being especially suitable for numerical computation. Liron (1978) found the summed and averaged form D_{jk}^C, given in appendix D, and used this together with the integral equation approach described in §3.6.3 to calculate instantaneous flow fields, averaged in the x_2 direction, for a field of 7 cilia per wavelength.

At present we assume that the epithelium is impermeable, consistent with the hypotonic defensin hypothesis. This corresponds to the boundary condition that $u = v = 0$ on $x_3 = 0$.

3.7.3 Shear-driven flow

We now need to derive the shear-driven component $u_j^{\rm shear}$, representing Stokes flow in the absence of resistance forces due to the moving boundary at $z = 1$. For simplicity we use the notation u, v for the x_1 and x_3 components of the velocity $u_1^{\rm shear}$ and $u_3^{\rm shear}$, and x, z for x_1, x_3. Following chapter 2 we write the solution as a finite Fourier series $u = \sum_{n=0}^{15} u_n$, make the transformation $u_n = \mathrm{Rl}\{(\check{u}_n^r + i\check{u}_n^i)\mathrm{e}^{in(\kappa x + \sigma t)}\}$, and nondimensionalise u, v, x, z, p with scalings σL, $\sigma L^2/\lambda$, λ, L, $\mu\sigma\lambda/L$ respectively. In what follows we omit the subscripts.

For $n = 0$ we have

$$\frac{\mathrm{d}^2 u}{\mathrm{d}z^2} = 0, \tag{3.38}$$

and for $n \geq 1$

$$\begin{aligned} -2\pi n \check{p}^i &= -\chi^2 \check{u}^r + \frac{\mathrm{d}^2 \check{u}^r}{\mathrm{d}z^2}, & 2\pi n \check{p}^r &= -\chi^2 \check{u}^i + \frac{\mathrm{d}^2 \check{u}^i}{\mathrm{d}z^2}, \\ \frac{\mathrm{d}\check{p}^r}{\mathrm{d}z} &= -\chi^2 \epsilon^2 \check{v}^r + \epsilon^2 \frac{\mathrm{d}^2 \check{v}^r}{\mathrm{d}z^2}, & \frac{\mathrm{d}\check{p}^i}{\mathrm{d}z} &= -\chi^2 \epsilon^2 \check{v}^i + \epsilon^2 \frac{\mathrm{d}^2 \check{v}^i}{\mathrm{d}z^2}, \end{aligned} \tag{3.39}$$

along with the differentiated continuity equations

$$-2\pi n \frac{\mathrm{d}\check{u}^i}{\mathrm{d}z} + \frac{\mathrm{d}^2 \check{v}^r}{\mathrm{d}z^2} = 0, \qquad 2\pi n \frac{\mathrm{d}\check{u}^r}{\mathrm{d}z} + \frac{\mathrm{d}^2 \check{v}^i}{\mathrm{d}z^2} = 0, \tag{3.40}$$

where $\epsilon = L/\lambda$ and $\chi = 2\pi n L/\lambda$.

The flow is determined by the boundary conditions on $z = 0$ and $z = 1$. On $z = 0$, assuming the epithelium is impermeable we have $u = v = 0$. On $z = 1$ we use the interface velocity calculated from the numerical model in chapter 2, with horizontal and vertical components $u_{\mathrm{tl}}(x,t) = \sum_{n=0}^{15} \{(\check{u}^r_{\mathrm{tl}\,n} + i\check{u}^i_{\mathrm{tl}\,n})\mathrm{e}^{in(\kappa x + \sigma t)}\}$ and $v_{\mathrm{tl}}(x,t) = \sum_{n=0}^{15} \{(\check{v}^r_{\mathrm{tl}\,n} + i\check{v}^i_{\mathrm{tl}\,n})\mathrm{e}^{in(\kappa x + \sigma t)}\}$.

For $n = 0$ assuming no steady pressure gradient as in chapter 2, we have the shear-driven flow solution

$$u(z) = u_{\mathrm{tl}\,0} z. \tag{3.41}$$

For $n \geq 1$, we rewrite this as a system of 10 first order ODEs —from the six equations above and four definition equations—in 10 variables. Primes denote differentiation with respect to z.

$$
\begin{aligned}
Z_1 &= \check{u}^r & Z_6 &= \check{p}^i \\
Z_2 &= \check{u}^i & Z_7 &= -2\pi n \check{u}^i + \check{v}^{r\prime} \\
Z_3 &= \check{v}^r & Z_8 &= -2\pi n \check{u}^i + \check{v}^{r\prime} \\
Z_4 &= \check{v}^i & Z_9 &= \check{u}^{r\prime} \\
Z_5 &= \check{p}^{r\prime} & Z_{10} &= \check{u}^{i\prime}.
\end{aligned}
$$

The field equations are then written as

$$
\begin{aligned}
Z_1' &= Z_9 & Z_6' &= -\chi^2\epsilon^2 Z_4 - 2\pi n \epsilon^2 Z_9 \\
Z_2' &= Z_{10} & Z_7' &= 0 \\
Z_3' &= 2\pi n Z_2 + Z_7 & Z_8' &= 0 \\
Z_4' &= -2\pi n Z_1 + Z_8 & Z_9' &= \chi^2 Z_1 - 2\pi n Z_6 \\
Z_5' &= -\chi^2\epsilon^2 Z_3 + 2\pi n \epsilon^2 Z_{10} & Z_{10}' &= \chi^2 Z_2 + 2\pi n Z_5.
\end{aligned}
$$

The boundary conditions are written as

$$
\begin{aligned}
& & Z_1 &= 0 \\
Z_1 &= \check{u}^r_{\mathrm{tl}\,n} & Z_2 &= 0 \\
Z_2 &= \check{u}^i_{\mathrm{tl}\,n} & Z_3 &= 0 \\
Z_3 &= \check{v}^r_{\mathrm{tl}\,n} & Z_4 &= 0 \\
Z_4 &= \check{v}^i_{\mathrm{tl}\,n} \quad \text{at} \quad z = 1, & Z_7 &= 0 \\
& & Z_8 &= 0 \quad \text{at} \quad z = 0.
\end{aligned}
$$

As in chapter 2, the equations $Z_7' = 0 = Z_8'$ together with the boundary conditions $Z_7 = 0 = Z_8$ ensure that $Z_7 \equiv 0 \equiv Z_8$, so that the continuity equation holds throughout the fluid. This system is solved numerically using the NAG routine D02GBF.

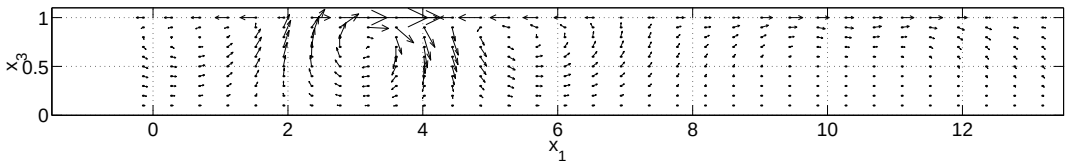

Figure 3.12: Fluid velocity vectors for the shear-driven flow only. Position scaled with respect to cilium length L, velocity scaled with respect to σL.

3.7.4 Modelling the flow in the periciliary layer

Combining the shear-driven flow and the flow due to the cilia and using the analysis from §3.7 we have

$$\begin{aligned} u_j(\mathbf{x},t) &= \frac{1}{b}\sum_{r=0}^{m_0-1}\int_0^1 f_k(\boldsymbol{\xi}^r(s,t))\mu D^C_{jk}(x_1-ra,x_3,\xi_1^r(s,t),\xi_3^r(s,t))\,\mathrm{d}s \\ &\quad -\frac{1}{b}\int_0^1 f_k(\boldsymbol{\xi}^{m^*}(s,t))\mu \bar{S}^C_{jk}(x_1-m^*a,x_3,\xi_1^{m^*}(s,t),\xi_3^{m^*}(s,t))\,\mathrm{d}s \\ &\quad +\int_0^1 f_k(\boldsymbol{\xi}^{m^*}(s,t))\mu S^C_{jk}(x_1-m^*a,x_2,x_3,\xi_1^{m^*}(s,t),\xi_2^{m^*}(s,t),\xi_3^{m^*}(s,t))\,\mathrm{d}s \\ &\quad +\int_0^1 \frac{r_0^2}{1/2+2r_0^2}s(1-s)f_k(\boldsymbol{\xi}^{m^*}(s,t)) \\ &\quad \cdot K_{jk}(x_1-m^*a,x_2,x_3,\xi_1^{m^*}(s,t),\xi_2^{m^*}(s,t),\xi_3^{m^*}(s,t))\,\mathrm{d}s \\ &\quad +u_j^{\mathrm{shear}}(\mathbf{x},t), \end{aligned} \tag{3.42}$$

for the velocity near the m^*th cilium. Discretising, we have

$$\begin{aligned}
\frac{\partial \xi_j^{m^*}}{\partial t}(s_q,t) &= \frac{1}{bN}\sum_{r=0,r\neq m^*}^{m_0-1}\sum_{i=1}^{N} f_k(\boldsymbol{\xi}^r(s_i,t)) \\
&\cdot\mu D_{jk}^C(\xi_1^{m^*}(s_q,t)+(m^*-r)a,\xi_3^{m^*}(s_q,t),\xi_1^r(s_i,t),\xi_3^r(s_i,t)) \\
&+\frac{1}{bQN}\sum_{i=1}^{N}\sum_{l=1}^{Q} f_k(\boldsymbol{\xi}^{m^*}(s_i,t)) \\
&\cdot\mu D_{jk}^C(\xi_1^{m^*}(s_q,t),\xi_3^{m^*}(s_q,t),\xi_1^{m^*}(s_{il},t),\xi_3^{m^*}(s_{il},t)) \\
&-\frac{1}{bQN}\sum_{i=1}^{N}\sum_{l=1}^{Q} f_k(\boldsymbol{\xi}^{m^*}(s_i,t))\mu \bar{S}_{jk}^C(\boldsymbol{\xi}^{m^*}(s_q,t),\boldsymbol{\xi}^{m^*}(s_{il},t)) \\
&+\frac{1}{QN}\sum_{i=1}^{N}\sum_{l=1}^{Q}\Bigg[f_k(\boldsymbol{\xi}^{m^*}(s_i,t))\mu S_{jk}^C(\boldsymbol{\xi}^{m^*}(s_q,t),\boldsymbol{\xi}^{m^*}(s_{il},t)) \\
&+\frac{r_0^2}{1/2+2r_0^2}s_q(1-s_q)f_k(\boldsymbol{\xi}^{m^*}(s_i,t))K_{jk}(\boldsymbol{\xi}^{m^*}(s_q,t),\boldsymbol{\xi}^{m^*}(s_{il},t))\Bigg] \\
&+u_j^{\text{shear}}(\boldsymbol{\xi}(s_q,t),t). \qquad (3.43)
\end{aligned}$$

Note that for the cilia $r \neq m^*$, we do not perform the refinement in the integral in order to reduce computational time. This leads to the matrix equation

$$\frac{\partial \xi_j^m}{\partial t}(s_q,t) - u_j^{\text{shear}}(\boldsymbol{\xi}^m(s_q,t),t) = \sum_{r=0}^{m_0-1}\sum_{i=1}^{N}\mathcal{A}_{qjm}^{ikr} f_k(\boldsymbol{\xi}^m(s_i,t)), \qquad (3.44)$$

where the coefficients $\mathcal{A}^{ikr}_{qjm}$ are given by

$$\mathcal{A}^{ikr}_{qjm} = \begin{cases} \dfrac{\mu}{bN} D^C_{jk}(\xi^m_1(s_q,t)+(m-r)a, \xi^m_3(s_q,t), \xi^r_1(s_i,t), \xi^r_3(s_i,t)) & \text{if} \quad m \neq r, \\ \dfrac{1}{QN}\displaystyle\sum_{l=1}^{Q}\Big[\dfrac{\mu}{b} D^C_{jk}(\xi^m_1(s_q,t), \xi^m_3(s_q,t), \xi^r_1(s_i,t), \xi^r_3(s_i,t)) \\ \quad +\mu S^C_{jk}(\boldsymbol{\xi}^m(s_q,t), \boldsymbol{\xi}^r(s_{ql},t)) - \dfrac{\mu}{b}\bar{S}^C_{jk}(\boldsymbol{\xi}^m(s_q,t), \boldsymbol{\xi}^r(s_{ql},t)) \\ \quad +\dfrac{r_0^2 s_q(1-s_q)}{1/2+2r_0^2} K_{jk}(\boldsymbol{\xi}^m(s_q,t), \boldsymbol{\xi}^r(s_{ql},t))\Big] & \text{if} \quad m = r, \quad i \neq q, \\ \dfrac{1}{QN}\displaystyle\sum_{l=1}^{Q}\Big[\dfrac{\mu}{b} D^C_{jk}(\xi^m_1(s_q,t)+r_0 n_1, \xi^m_3(s_q,t)+r_0 n_3, \xi^r_1(s_i,t), \xi^r_3(s_i,t)) \\ \quad +\mu S^C_{jk}(\boldsymbol{\xi}^m(s_q,t)+r_0\mathbf{n}, \boldsymbol{\xi}^r(s_{ql},t)) - \dfrac{\mu}{b}\bar{S}^C_{jk}(\boldsymbol{\xi}^m(s_q,t)+r_0\mathbf{n}, \boldsymbol{\xi}^r(s_{ql},t)) \\ \quad +\dfrac{r_0^2 s_i(1-s_i)}{1/2+2r_0^2} K_{jk}(\boldsymbol{\xi}^m(s_q,t)+r_0\mathbf{n}, \boldsymbol{\xi}^r(s_{ql},t))\Big] & \text{if} \quad m = r, \quad i = q. \end{cases}$$

Once the force distributions $f_k(\boldsymbol{\xi}^r(s_i,t))$ for $i = 1,\ldots,N$, $r = 0,\ldots,m_0-1$ and $k = 1,2,3$ have been found, the fluid velocity can be calculated as before. For a point $\mathbf{x}$ such that the nearest cilium is the m^*th, and without loss of generality $-b/2 < x_2 < b/2$, we have

$$\begin{aligned} u_j(\mathbf{x},t) &= \frac{1}{b}\sum_{r=0}^{m_0-1}\int_0^1 f_k(\boldsymbol{\xi}^r(s,t))\mu D^C_{jk}(x_1-ra, x_3, \xi^r_1(s,t), \xi^r_3(s,t))\,\mathrm{d}s \\ &\quad -\frac{1}{b}\int_0^1 f_k(\boldsymbol{\xi}^{m^*}(s,t))\mu\bar{S}^C_{jk}(x_1-m^*a, x_3, \xi^{m^*}_1(s,t), \xi^{m^*}_3(s,t))\,\mathrm{d}s \\ &\quad +\int_0^1 f_k(\boldsymbol{\xi}^{m^*}(s,t))\mu S^C_{jk}(x_1-m^*a, x_2, x_3, \xi^{m^*}_1(s,t), \xi^{m^*}_2(s,t), \xi^{m^*}_3(s,t))\,\mathrm{d}s \\ &\quad +\int_0^1 \frac{r_0^2}{1/2+2r_0^2} s(1-s) f_k(\boldsymbol{\xi}^{m^*}(s,t)) \\ &\quad \cdot K_{jk}(x_1-m^*a, x_2, x_3, \xi^{m^*}_1(s,t), \xi^{m^*}_2(s,t), \xi^{m^*}_3(s,t))\,\mathrm{d}s \\ &\quad +u^{\mathrm{shear}}_j(\mathbf{x},t). \end{aligned} \tag{3.45}$$

3.8 Results

In Figures 3.13 and 3.14 we present velocity field solutions for our model at different points along the ciliary beat at time $t = 0$, for 50 cilia per wavelength. The beat cycle of Sanderson and Sleigh (1981) was used, as calculated by Fulford and Blake (1986) and depicted in Figure 3.1. It was necessary to choose the metachronal wavelength to be $m_0 a = 15L = 90\ \mu\mathrm{m}$, rather longer than the value of $30\ \mu\mathrm{m}$ quoted by Fulford and Blake (1986). This length was chosen to prevent the cilia from 'intersecting'. In reality, the cilia would be likely to slip past each other as can be observed in the micrographs of Sanderson and Sleigh (1981), however our slender body model is not designed for the situation in which the cilia actually approach. Figure 3.15 shows that the boundary conditions on the cilium with base at the origin are approximately satisfied, although due to the greater cilium density the results are not as accurate as the single cilium model shown in Figure 3.8. The spacing between cilium centres is $1.8\ \mu\mathrm{m}$, in the lungs the spacing will be of the order of $0.3\ \mu\mathrm{m}$, however our model provides a good indication of the flow fields likely to arise.

Figure 3.14 shows 'close up' graphs of each velocity profile, to reveal more detail. Comparing the results with Figure 3.12 it is notable that the cilia do not have a significant effect on the flow field except very near the cilium axis. The flow is dominated by shear-driven flow originating in the mucous layer. This is even more clear from the plot in Figure 3.16. It is possible that in a more biologically accurate model with a cilium spacing of around $0.3\ \mu\mathrm{m}$, the flow field will appear rather different.

Figure 3.17 shows the flow profile in the region between the cilia tips and the mucous layer. It is interesting to note that the backward movement of the cilia tips does not cause a backward flow of fluid, but rather the PCL flows forwards with the mucous layer. The gap between the cilia tips and the mucus interface was not modelled in chapter 2, which predicted very small transport of PCL. Our results here suggest that there could be substantial transport of PCL in

this gap. More detailed modelling of the PCL flux may help to resolve the controversy regarding the normal transport of PCL.

3.9 Discussion

The theory presented above represents a new, mathematically tractable model for the velocity profile in the PCL, providing a new level of detail about the flow. Our model is very acceptably consistent with the boundary conditions, and includes the effect of viscoelastic mucus movement, using the results of chapter 2. There is a significant forward flow of PCL in the gap between the cilium tips and the mucus interface. It was not possible to make definitive conclusions regarding the mean flux of PCL due to the fact that integrating the errors in the singularity distributions over the fluid volume would not be acceptably accurate. It will be necessary to carry out simulations with a decreased cilium spacing in order to make definitive conclusions regarding the flow in the PCL. In particular, it will be very interesting to find out whether the PCL flux for a very dense mat of cilia is indeed as small as was estimated in chapter 2. It would be interesting to extend this model to include the effect of osmotic flows through the epithelium, although this would likely be a substantial task.

This model suggests that the traction layer model of chapter 2 may be extended and improved by altering the active porous medium region $z < h$ to allow for a region between the cilia tips and the interface such that during the recovery stroke, fluid can flow forwards without the presence of the dense mat of cilia. This may lead to a more accurate estimation of the mean PCL transport. This would agree with the results of Fulford and Blake (1986), which showed significant transport of PCL in a thin layer close to the mucus interface.

The boundary conditions were not satisfied as accurately for the dense field of 50 cilia, compared with the single cilium case. Johnson (1980) used uniformly valid asymptotic expansions to represent a slender body with finite curvature in an infinite domain, finding a representation in terms of Stokeslets and higher order singularities. This was extended by Bartha and

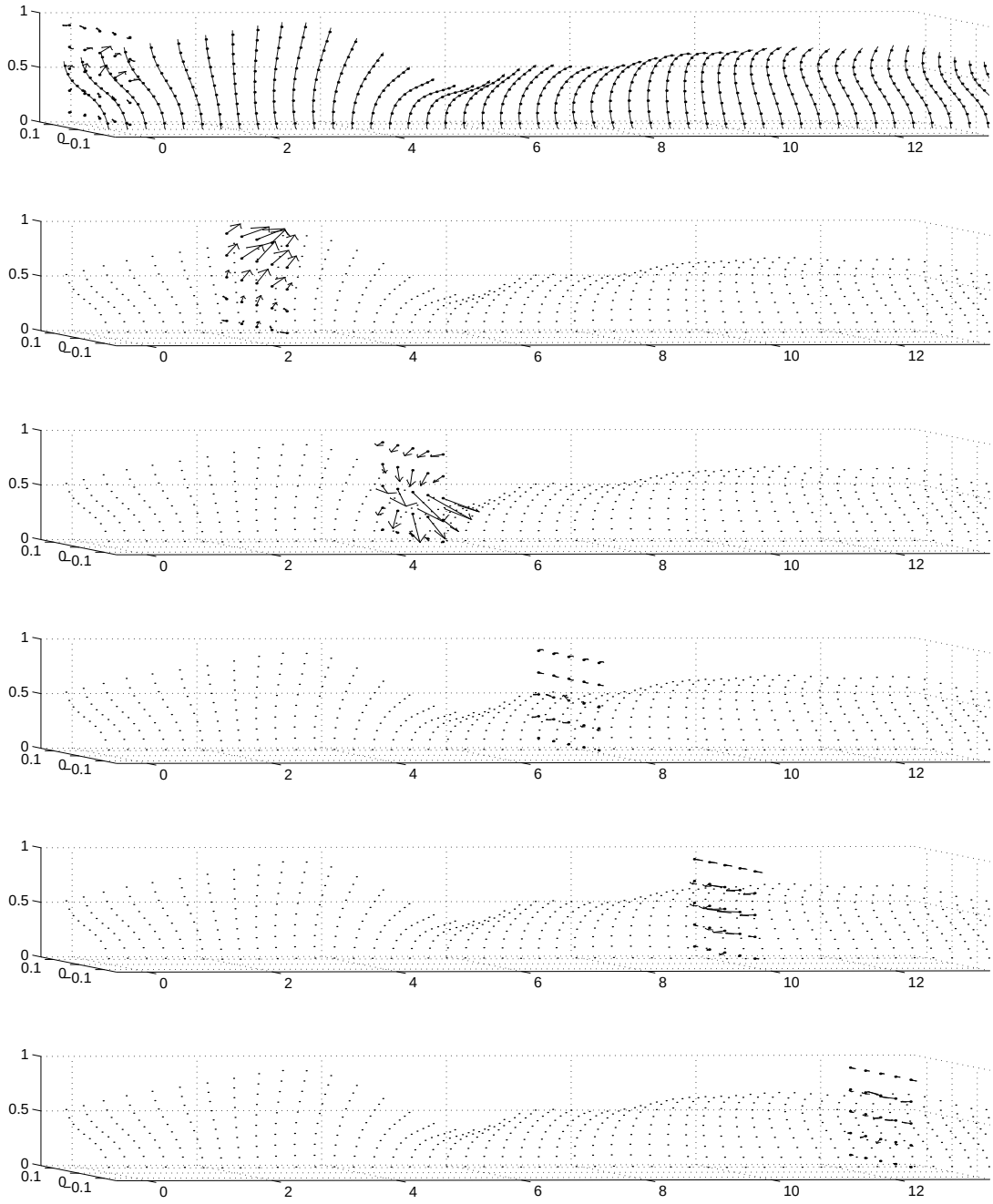

Figure 3.13: Plot of the fluid velocity vectors calculated on different grids in the fluid, or equivalently at different times during the beat cycle. $m_0 = 50$ cilia, $N = 10$ nodes, $Q = 11$ refinement points. Results calculated using equation (3.45). Close-up profiles are given in Figure 3.14.

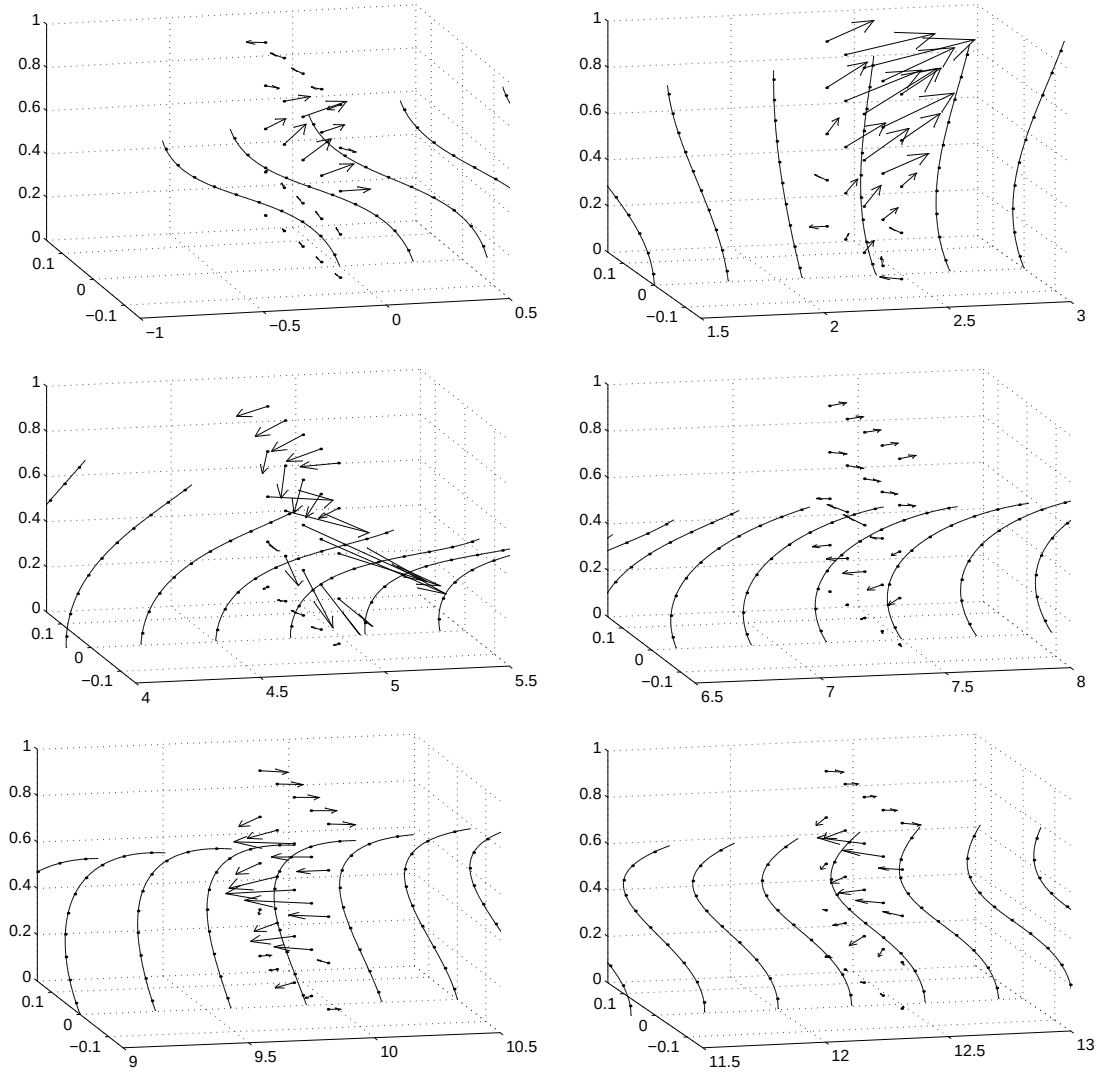

Figure 3.14: Close-up plots of the fluid velocity vectors from Figure 3.13. $m_0 = 50$ cilia, $N = 10$ nodes, $Q = 11$ refinement points. Results calculated using equation (3.45).

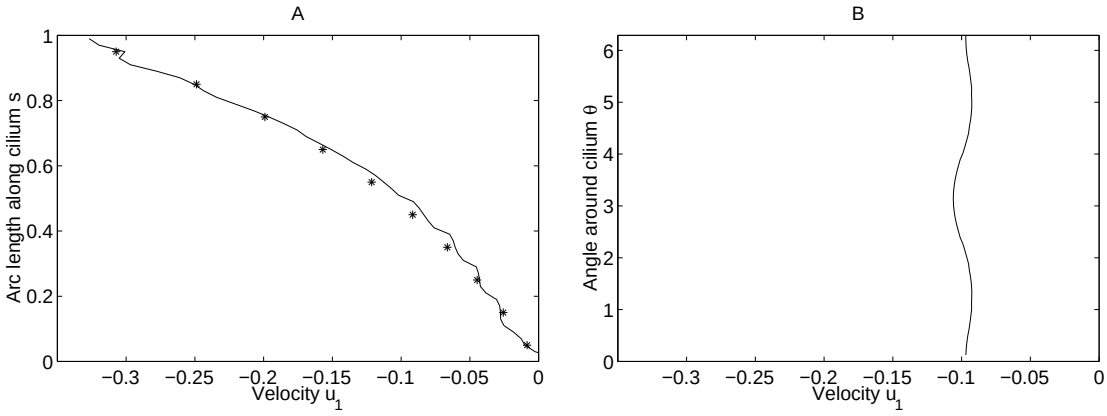

Figure 3.15: Checking the boundary conditions on the cilium at the origin for the results shown in Figure 3.13. A—Profile along cilium. $N = 10, Q = 11, r_0 = 0.1/6$. B—Profile around cilium at $s = 0.5$. Velocity scaled with respect to σL. Results calculated using equation (3.45).

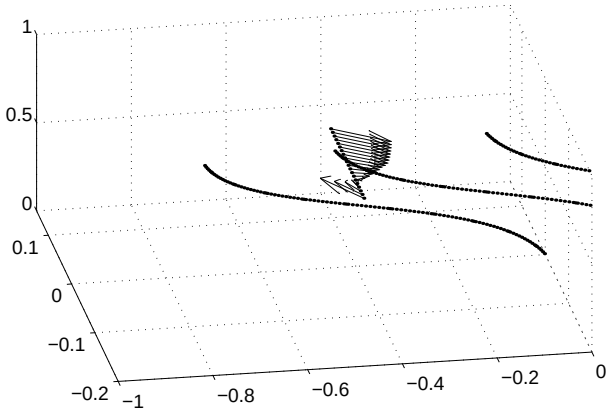

Figure 3.16: Fluid velocity vectors on the line $x_1 = \xi_1(0.5, 0)$, $0 < x_2 < b/2$, $x_3 = \xi_3(0.5, 0)$ during the recovery stroke. The cilium reverses the flow in a region of radius $0.18\ \mu\mathrm{m}$.

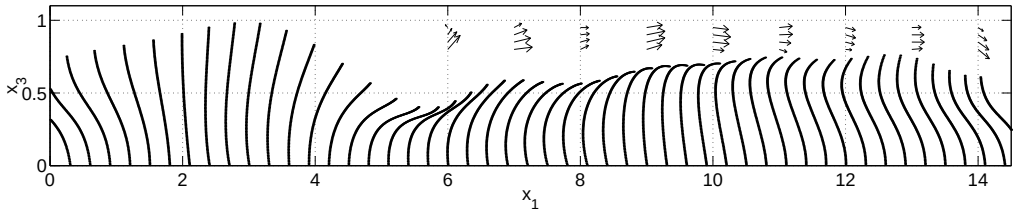

Figure 3.17: Positive fluid transport in the region between the cilia tips and the mucous layer during the recovery stroke. The forward component of the velocity u_1 has a peak value of over $110\ \mu\mathrm{m/s}$.

Liron (1988a) for a slender body in the presence of a no-slip boundary, and in Bartha and Liron (1988b) for two close slender bodies with or without a wall. One could extend the model described here by proceeding similarly, allowing for finite curvature, and for interactions with two or several adjacent cilia. This type of model would, however, require an iterative solution, and so would not be as computationally efficient.

In our model we evaluated the singularity at an arbitrarily chosen point on the surface of the cilium, $\boldsymbol{\xi} + r_0\mathbf{n}$. A more rigorous approach would be to derive an analogous version of the Lighthill–Gueron–Liron theorem (Liron, 2001) for the confined domain, which does not have this drawback. Alternatively, in order to determine the PCL flux accurately, one could pursue an exact boundary integral model (Pozrikidis, 1992), in which the centre line integral is replaced by integrals over the entire surface of the cilia. This would allow an accurate model of closely-spaced cilia interacting, and could provide a solution sufficiently accurate that the flux may be determined by performing an integral over the volume (or, using incompressibility, a surface) of the fluid, although this would be very computationally demanding at present.

CHAPTER 4

TRACER DISPERSION MODELLING

4.1 Introduction

To test the amount of axial PCL transport in the normal lung, Matsui et al. (1998b) carried out experiments with human tracheobronchial epithelial (hTBE) cultures. By tracking the movement of photoactivated tracer 'columns' they concluded that mean PCL velocity was close to that of the mucous layer, contrary to previous fluid mechanical modelling work, and hence there must be significant absorption of fluid by the ASL. In this chapter we extend the work of Blake and Gaffney (2001) and Barlow (2000) by applying a two dimensional advection diffusion model to the dispersion of tracer, using the velocity profiles from chapter 2, with the aim of reconciling fluid mechanical modelling with the observed results.

4.2 Tracer dispersion experiments of Matsui et al. (1998b)

In suitable media the cultures produced a mucous layer around 25 μm in depth and in around a quarter of cases the cultures exhibited spontaneous circular transport. The ASL was labelled with caged fluorescein-dextran, which was then photoactivated in 400 $\mu\mathrm{m}$ width columns. It was found that over periods of around 20 s, the photoactivated regions moved at the same speed in both the PCL and the mucus. Average circular transport speeds of 39.2 $\mu\mathrm{m}$/s were

reported, with higher values at the outer edge of the rotating mucus. Matsui et al. (1998b), Figure 3 shows a fluorescent region initially and after 20 s. There is no smearing between the two images, as might be expected if the PCL had not been transported with the same speed as the mucus (Matsui et al., 1998b), and the pulses are of similar size. Furthermore, using confocal microscopy, vertical sections of ASL were visualised. There was no difference in transport of fluorescent particles with height above the epithelium. Using this technique they found estimates for the diffusion coefficients of dextran in mucus and PCL: $3.6\ \mu\mathrm{m}^2\ \mathrm{s}^{-1}$ and $160\ \mu\mathrm{m}^2\ \mathrm{s}^{-1}$ respectively. The diffusion coeffcients were estimated from non cilio-active cultures, and so represent spreading of tracer due to diffusion only and not due to advective transport.

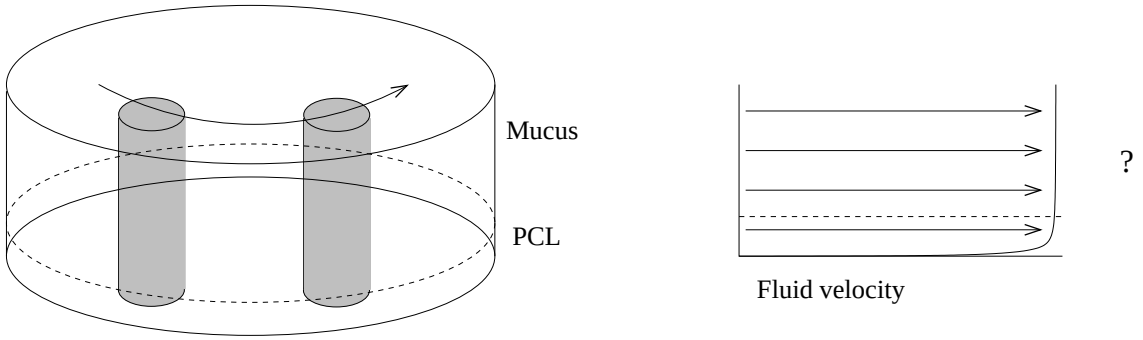

Figure 4.1: A simplified representation of the cotransport phenomenon found by Matsui et al. (1998b).

At first sight these results appear to show that tracer particles in the PCL are advected along at the same speed as tracer particles in the mucous layer, implying that the fluid velocity in both layers is approximately equal. However, diffusion is also present in the system, and vertical diffusion may be particularly important since the layer is so thin. To test this, Blake and Gaffney (2001) and Barlow (2000) formulated a continuum advection-diffusion model, as described in the introduction. Below we briefly describe the model and our implementation.

4.3 Two dimensional advection-diffusion model

Using $c(\mathbf{x}, t)$ to denote concentration of tracer, in the presence of a fluid flow field $\mathbf{u}$, the advective flux of tracer is $c\mathbf{u}$. Using Fick's law, the diffusive flux will be $-D\nabla^2 c$. Hence the total flux of tracer will be given by $\mathbf{J} = c\mathbf{u} - D\boldsymbol{\nabla} c$. It is possible that other effects besides advection and diffusion may be present in the system, such as adhesion of tracer particles to the mucus, but these are beyond the scope of this study. Using conservation of tracer and the divergence theorem, we can derive

$$\frac{\partial c}{\partial t} = \boldsymbol{\nabla} \cdot (D\boldsymbol{\nabla} c - c\mathbf{u}). \tag{4.1}$$

The diffusion coefficient D will depend only on the properties of the fluid. Since the PCL occupies $0 < z < h$ and the mucous layer $h < z < H$ we have $D = D(z)$. From incompressibility, the velocity field u satisfies $\boldsymbol{\nabla} \cdot \mathbf{u} = 0$, leading to the simpification

$$\frac{\partial c}{\partial t} = D\nabla^2 c + \frac{\mathrm{d}D}{\mathrm{d}z}\frac{\partial c}{\partial z} - \mathbf{u} \cdot \boldsymbol{\nabla} c. \tag{4.2}$$

The initial conditions must represent a pulse of photoactivated tracer of width about $400\ \mu\mathrm{m}$. We choose a rounded 'peak' for the tracer pulse of the form

$$c_{\mathrm{peak}}(x) = \exp\left(-\left[\frac{150 \times 4}{4000 \times 34}\,(x - 1173.3)\right]^2\right), \tag{4.3}$$

with a smooth transition to zero in a narrow region around the peak, so that

$$c(x,z,0) \;=\; \begin{cases} 0 & (x<960), \\ c_{\mathrm{peak}}(1066.7)\sin\left(\dfrac{\pi}{2}\left[1-\dfrac{3(1066.7-x)/4}{80}\right]\right) & (960<x<1066.7), \\ c_{\mathrm{peak}}(x) & (1066.7<x<1258.7), \\ c_{\mathrm{peak}}(1258.7)\sin\left(\dfrac{\pi}{2}\left[1-\dfrac{3(1066.7-x)/4}{80}\right]\right) & (1258.7<x<1365.3), \\ 0 & (x>1365.3). \end{cases} \tag{4.4}$$

where x is measured in $\mu\mathrm{m}$. This is illustrated in Figure 4.2, with white denoting zero concentration, black maximum concentration ($c=1$).

For boundary conditions, we assume that the flux of tracer is zero as $x \to \pm\infty$—solving numerically on a finite domain we must approximate this by $\partial c/\partial x = 0$ at the edges $x=0$ and $x=X$, using the notation of appendix E.1. We also assume that no tracer is absorbed by the epithelium, so that $\partial c/\partial z = 0$ on $z=0$, and that there is no flux through the free surface. For a flat free surface, this is simply $\partial c/\partial z = 0$ on $z=H$.

As discussed above, the diffusion coefficient in the PCL was found to be around $D_P = 160\ \mu\mathrm{m}^2/\mathrm{s}$, in the mucous layer to be $D_M = 3.6\ \mu\mathrm{m}^2/\mathrm{s}$. To begin with, we model the variation of $D(z)$ in the ASL by the function

$$D_1(z) \;=\; \frac{1}{2}\left((D_P-D_M)\tanh\left(40\left[\frac{h-z}{L}\right]\right)+D_P+D_M\right), \tag{4.5}$$

where $h=0.9\ \mu\mathrm{m}$, $L=6\ \mu\mathrm{m}$. This is equal to D_P throughout most of the region $0<z<h$ and to D_M throughout most of the region $h<z<H$, with a smooth transition in a region of width approximately $0.8\ \mu\mathrm{m}$. The smooth transition means that the term $\mathrm{d}D/\mathrm{d}z$ may be determined in equation (4.2). The diffusion profile is shown in Figure 4.3(A).

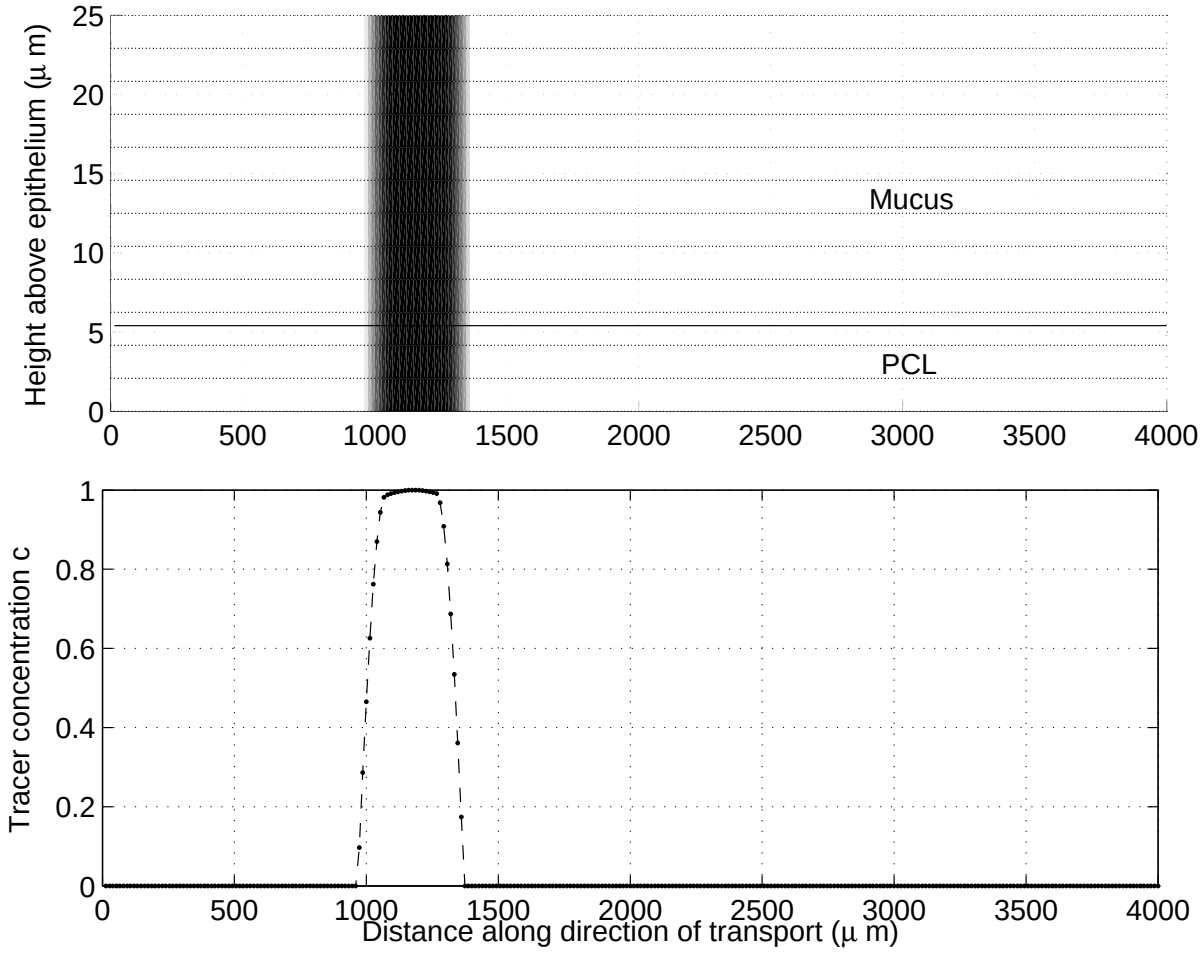

Figure 4.2: Initial conditions—a tracer pulse with width approximately $400\ \mu\mathrm{m}$.

4.3.1 Advective and diffusive timescales

In Barlow (2000) and Blake and Gaffney (2001) it was shown that the tracer transport in the PCL was far larger than might be predicted from considering advection only. This is essentially the phenomenon known as 'Taylor Disperson' (Taylor, 1953). Despite the fact that the fluid flux in the PCL is two orders of magnitude smaller than in the mucous layer, the difference in tracer transport may be less than a factor of 2. This occurs because the vertical diffusional timescale is no longer than the advective timescale, so that differences in tracer concentration may be 'smoothed out' by diffusion. The vertical component of the diffusive flux is $-D\partial c/\partial z$. As the pulses begin to separate over a very short vertical lengthscale, the gradient $\partial c/\partial z$ becomes large and hence the diffusive term may balance the advective horizontal flux cu.

Making estimates of $X = 400\ \mu\mathrm{m}$ (the width of the tracer pulse) and $U = 40\ \mu\mathrm{m/s}$, the horizontal advective timescale is $X/U = 10\ \mathrm{s}$. The vertical diffusive timescale may be estimated from the depth of the PCL $L = 6\ \mu\mathrm{m}$ and the diffusion coefficient D. Matters are rather complicated by the fact that D varies by two orders of magnitude across the ASL. Taking D to be the value in the PCL, $160\ \mu\mathrm{m}^2/\mathrm{s}$, we have a timescale of $6^2/160 = 0.225\ \mathrm{s}$, and hence diffusion would be dominant. Taking the value for the mucous layer, we have $6^2/3 = 12\ \mathrm{s}$. In this case, the timescales for advection and diffusion would be comparable, and the result unclear. Also, the effect of the large oscillations found in the traction layer model are not entirely clear. We are therefore motivated to seek a numerical solution. An initial investigation using an *ad hoc* oscillatory profile was presented by Blake and Gaffney (2001); we extend this by using the model results from chapter 2, and a more accurate advective scheme.

4.3.2 Numerical solution

An extension of the alternating direction implicit algorithm is used to solve equation (4.2), as first used for this problem by Blake and Gaffney (2001). The ADI algorithm is a relatively efficient method of solution, since each timestep involves only the solution of a set of tridi-

agonal or pentadiagonal matrix equations. A detailed description of the algorithm is given in appendix E.1. In order to discretise the advective terms, Blake and Gaffney (2001) used first order upwind discretisation. This method is more stable than central differencing, but has the disadvantages of being only first order accurate and introducing numerical diffusion. Since additional diffusion would have the effect of reducing the separation between the tracer pulses in the mucus and PCL, this could produce misleading results. Instead we shall use the QUICK scheme (Leonard, 1979). For 1D problems, QUICK is stable, formally third order accurate, conservative and does not introduce numerical diffusion. The scheme does not have these formal properties in 2D, but our results show greatly improved spatial convergence and very acceptably accurate conservation of c. Implementation is very straightforward, since at each timestep it is necessary to solve a system of pentadiagonal equations, which can be done with comparable efficiency to a tridiagonal system.

To compare and interpret the results of different simulations quantitatively, we calculate the distance moved by the centroid of the tracer pulse at different levels in the fluid:

$$d(z,t) := \frac{\int_{x=-\infty}^{\infty} xc(x,z,t)\,\mathrm{d}x}{\int_{x=-\infty}^{\infty} c(x,z,t)\,\mathrm{d}x}. \tag{4.6}$$

We then define the transport ratio $r(t) = d(H,t)/d(0,t)$, the ratio of the tracer transport at the top of the mucous layer to the bottom of the PCL. Due to the fact that vertical diffusion acts on a timescale of up to 12 s, it is expected that $r(t)$ will not 'converge' to a final value until a simulation has been performed for a similar time period. Unfortunately, this means that simulations will necessarily be computationally intensive, and three dimensional simulation is not feasible at this stage. Cotransport over the timescale of the experiment will be represented ideally by $r(t) \sim 1$ for $t = O(20)$ s.

t_{out}	δx	δz	δt	$d(0, t_{\text{out}})$	$d(25, t_{\text{out}})$	$r(t_{\text{out}})$
30	6.6667	0.1250	0.02	703.34	1068.7	1.5194
30	3.3333	0.1250	0.02	703.32	1068.6	1.5194
30	6.6667	0.0625	0.02	705.60	1068.9	1.5150
30	6.6667	0.1250	0.01	703.36	1068.7	1.5194

Table 4.1: Numerical simulation results for traction layer steady velocity profile and diffusion profile D_1, showing that convergence of r to 2 decimal places is achieved with $\delta x = 6.67\ \mu\text{m}$, $\delta z = 0.125\ \mu\text{m}$ and $\delta t = 0.02$ s. All times in seconds, distances in μm.

4.4 Steady transport results

4.4.1 Steady profile of chapter 2

We begin by presenting results for the steady velocity $\mathbf{u} = (u(z), 0)$ field given in equation (2.66), and with the diffusion profile $D_1(z)$. The diffusion and velocity profiles are shown together in Figure 4.3, for comparison. We used a domain of width $0 < x < 4000\ \mu\text{m}$ and height $0 < z < 25\ \mu\text{m}$. The ASL height was chosen to match the hTBE experiments, but does not appear to be critical to the results. To verify the mesh spacings and timestep chosen, we repeat the simulation with each of these parameters halved, as shown in Table 4.1. It is clear that convergence in x and t is very acceptably accurate, and convergence in z is also acceptable, with the choice of $\delta x = 6.67\ \mu\text{m}$, $\delta z = 0.125\ \mu\text{m}$ and $\delta t = 0.02$ s giving values of the transport ratio $r(t)$ that are accurate to 2 decimal places. We see that $r(30) \approx 1.52$, meaning that the tracer centroid in the mucous layer has been transported 52% farther than the tracer centroid in the PCL. In the hTBE experiments, this would mean that the tracer pulse would smear along, as viewed from above, which is not what was observed. As found by Blake and Gaffney (2001) and Barlow (2000), tracer transport in the PCL is still much larger than would be estimated from advection alone, due to vertical diffusion. By examining the results for 5–30 s in Table 4.2, it is clear that vertical diffusion takes at least 30 s in order to take full effect, since the distance between the peaks continues to increase every 10 s.

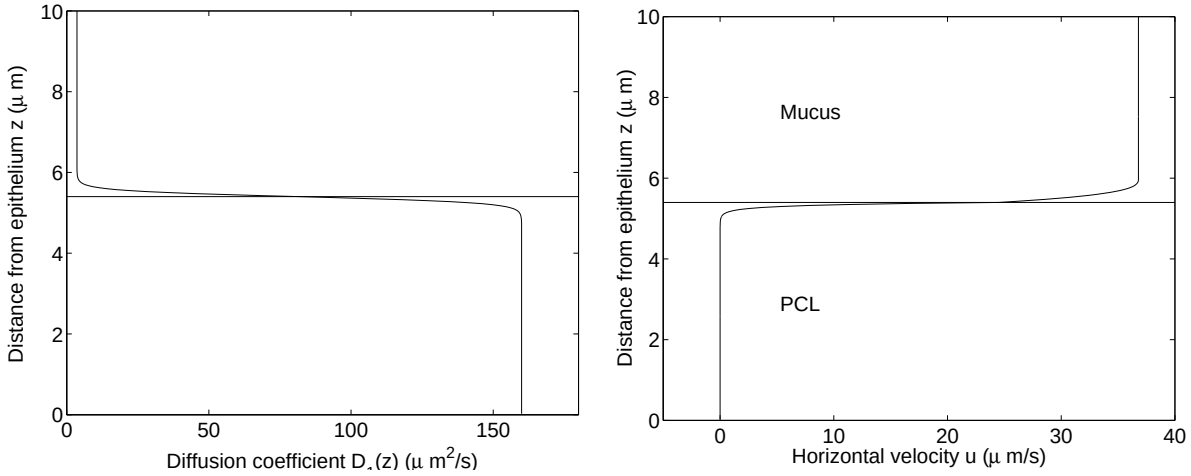

Figure 4.3: Diffusion profile $D_1(z)$. Mean horizontal velocity u versus height above epithelium for the results of chapter 2 with the standard parameter set.

t_{out}	$d(0, t_{\text{out}})$	$d(25, t_{\text{out}})$	$r(t_{\text{out}})$
5	74.920	191.28	2.5531
10	182.28	380.19	2.0858
20	431.19	736.86	1.7089
30	703.34	1068.7	1.5194

Table 4.2: Numerical simulation results for traction layer steady velocity profile (low mean PCL transport) and diffusion profile D_1. The separation between the pulses in the mucus and PCL continues to increase over the course of the simulation. Mesh spacings and timestep were $\delta x = 6.67\ \mu\text{m}$, $\delta z = 0.125\ \mu\text{m}$ and $\delta t = 0.02$ s. All times in seconds, distances in μm.

The shape of the tracer distribution is shown as a surface in three dimensions in Figure 4.4, and the profiles at $z = 0$ and $z = H$ are shown in the top graph of Figure 4.6. In what follows, we shall display the simulation results using the latter format, since it more clearly shows the difference between the tracer pulses at the top of the mucous layer and the bottom of the PCL.

4.4.2 Other steady velocity profiles

In Table 4.3, we give results for the other mean velocity profiles depicted in Figure 1.3. The 'plane Couette' flow, defined by $u(z) \propto z$ is the profile calculated from the mucous layer $L < z < H$ moving with constant velocity, with no sublayer resistance or pressure gradients, similar to the results of the simple model of Barlow (2000). The *ad hoc* 'boundary layer' flow,

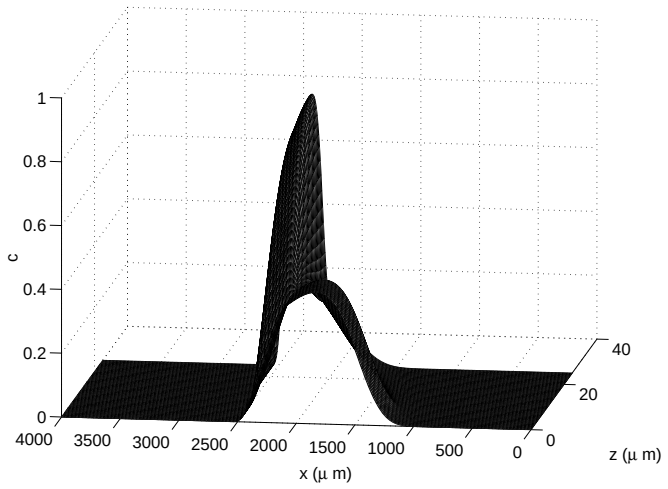

Figure 4.4: Tracer dispersion results—traction layer steady profile (low mean PCL transport), time duration 30 seconds. The surface represents c as a function of x, distance along the epithelium, and z height above the epithelium, measured in $\mu\mathrm{m}$. The upper peak shows the pulse in the mucous layer, the lower peak shows the more diffuse pulse in the PCL, which is transported more slowly.

which we represent by $u \propto 2z^{1/5} - z^{-2/5}$, is based on the profile suggested by Matsui et al. (1998b) in order to explain their experimental results. Plots of the exact profiles used are given in Figure 4.5. The simulation results are depicted in Figure 4.6. As might be expected, the plane Couette and boundary layer profiles cause successively greater transport of tracer in the PCL, with the boundary layer flow causing the pulses almost to match in size and position. It is interesting to note that for the low mean PCL transport results, the tracer in the mucous layer has an enlarged tail, showing the exchange of tracer between the two layers. The pulse in the PCL is very diffuse, due to the effect of vertical diffusion combined with shearing of the two layers. In the Couette and boundary layer graphs, the tracer pulse in the PCL is narrower, due to the fact that the pulses in the two layers are much more closely associated.

Quantitative measures of the results are shown in Table 4.3. Over the $30\ \mathrm{s}$ simulation period, only the 'boundary layer' flow provides a likely match with experimental results, the distance between the tracer centroids being only $23.7\ \mu\mathrm{m}$. This is very much at variance with the results

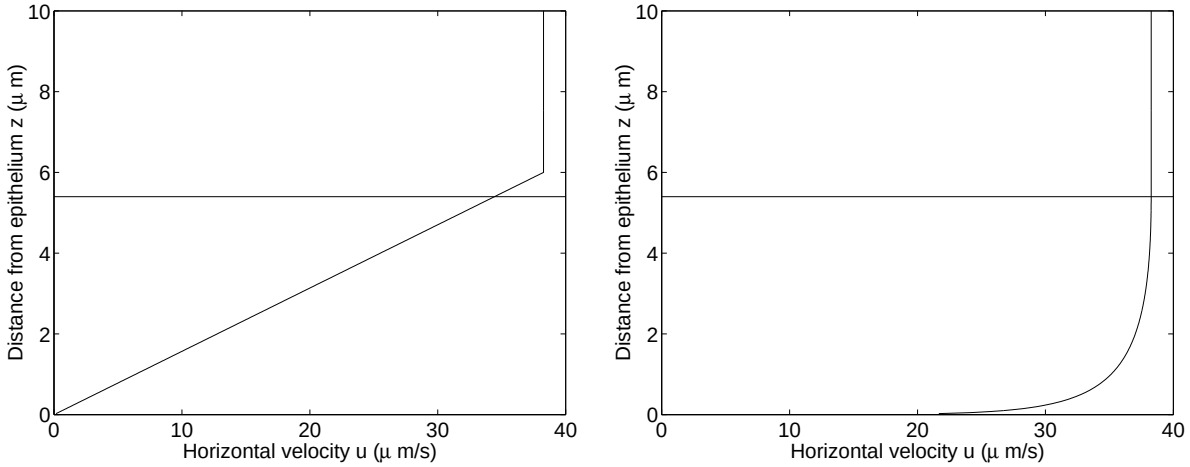

Figure 4.5: Mean velocity profiles for 'shear driven' or plane Couette flow, and the 'boundary layer' flow, used for simulation. Profiles were taken from Figure 1.3(B) and (C) respectively.

t_{out}	Profile type	$d(0, t_{\text{out}})$	$d(25, t_{\text{out}})$	$r(t_{\text{out}})$
30	Steady traction layer	703.34	1068.7	1.5194
30	Steady plane Couette	898.73	1103.6	1.2280
30	Steady Matsui et al.	1119.1	1142.8	1.0212

Table 4.3: Numerical simulation results for the steady velocity profiles depicted in Figures 4.3 and 4.5. Mesh spacings and timestep were $\delta x = 6.67\ \mu\text{m}$, $\delta z = 0.125\ \mu\text{m}$ and $\delta t = 0.02$ s. All times in seconds, distances in μm.

of our mechanical modelling—a considerable pressure gradient would be necessary to drive such a large flux of PCL through the dense field of cilia. In the next section, we examine the effects of introducing horizontal and vertical oscillation, and of altering the diffusion profile D.

4.5 Oscillatory transport results

4.5.1 Oscillatory numerical traction layer profile

Simulations using oscillatory profiles calculated numerically from the Fourier series in chapter 2 and depicted in Figure 2.12 are rather more computationally expensive, since a significant part of the algorithm involves calculating matrix coefficients from the series $\sum_{n=0}^{15} \mathbf{u}_n$. To obtain results more efficiently we restrict the domain to $0 < x < 1800\ \mu\text{m}$ and $0 < z < 10\ \mu\text{m}$,

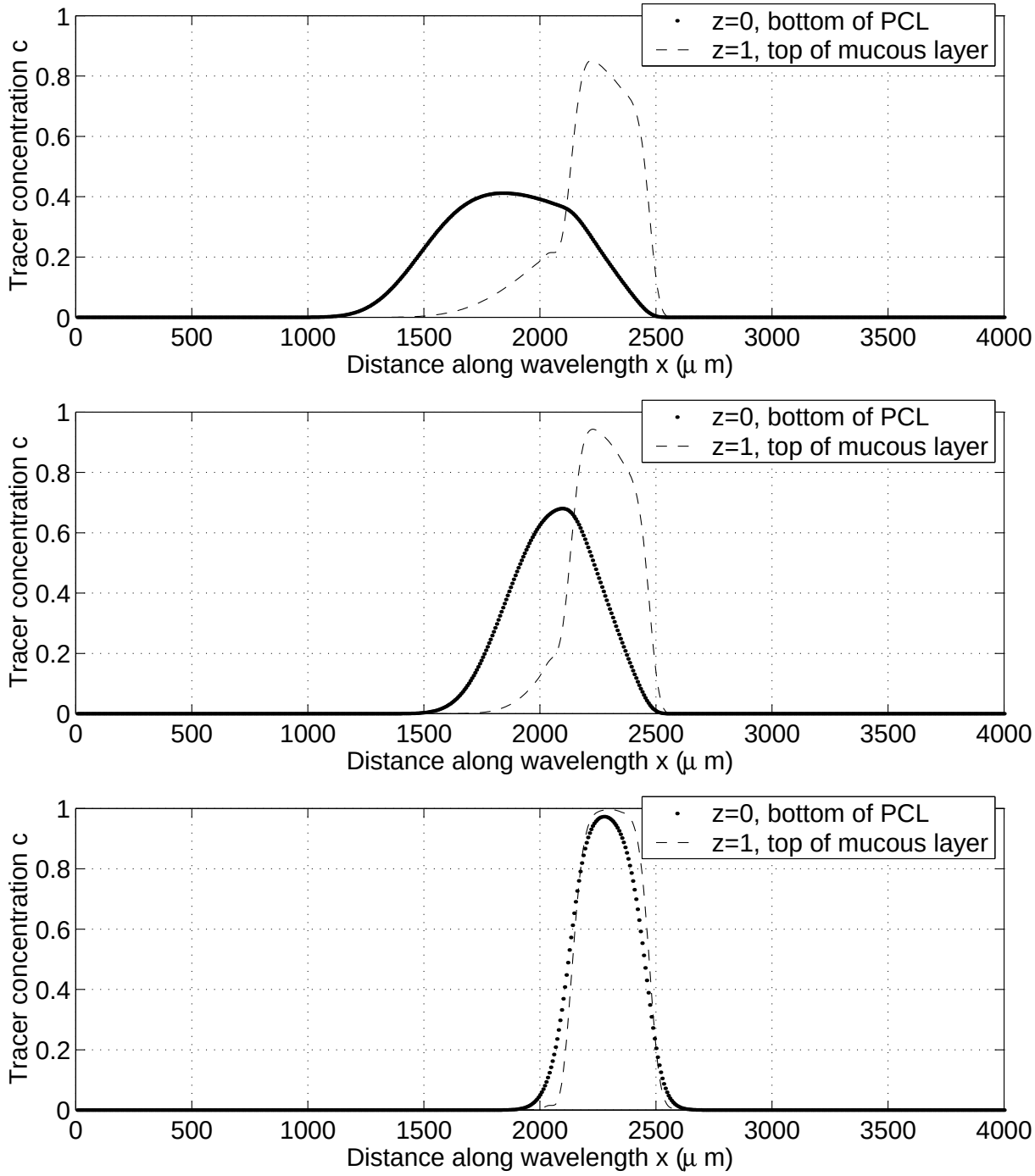

Figure 4.6: Tracer dispersion results—steady profiles with diffusion profile D_1. Top—steady traction layer velocity (low mean PCL transport), as shown in Figure 1.3(A). Middle—steady shear driven velocity (plane Couette flow), as shown in Figure 1.3(B). Bottom—steady 'boundary layer' profile as predicted by Matsui et al. (1998b) and shown in Figure 1.3(C) (high mean PCL transport). Time duration 30 seconds.

and simulate dispersion for a shorter time period. We have confirmed from simulations with the steady profile that the domain height does not have a significant effect. Efficiency is also greatly improved by employing an algorithm that exploits the periodicity of the ciliary beat, so that velocity values need only be calculated on a mesh covering one wavelength. For the oscillatory profiles the peak value of the velocity is of the order of 10 times that for the steady flow, so that the solution requires a finer spatial mesh. The timestep must also be reduced by a factor of ten in order to capture the detail of the ciliary beat cycle. As shown in Table 4.4, a good estimate of the transport ratio can be determined using $\delta x = 1.5\ \mu\mathrm{m}$, $\delta z = 0.0625\ \mu\mathrm{m}$ and $\delta t = 0.002\ \mathrm{s}$. As the simulation progresses, the size of $d(0,t)$ will increase relative to $d(10,t)$, and the accuracy of the estimate of $r(t) = d(10,t)/d(0,t)$ will improve.

In Blake and Gaffney (2001) it was shown that an *ad hoc* oscillatory component substantially increased tracer transport in the PCL, although by how much was not given quantitatively. Table 4.5 shows the transport ratios for $t = 5$, 10 and $20\ \mathrm{s}$ for our physically derived oscillatory profile. After 20 s, the transport ratio is only 1.18, whereas for the steady profile was 1.70. The addition of an oscillatory component hence makes a very significant difference. It was shown by Taylor (1953) that shearing in the velocity field $\partial u/\partial z$ effectively increased the diffusivity of c. The oscillatory terms introduce large transient values of $\partial u/\partial z$ in the region $h < z < L$, which greatly enhance diffusion between the mucous layer and PCL, hence reducing the timescale of diffusive mixing. The *ad hoc* oscillatory component used by Blake and Gaffney (2001) similarly possessed a sharp gradient for z close to h, being proportional to $\sqrt{4(z/h)(1-z/h)}$. It is interesting to note that the distance separating the peaks does not significantly increase between 5 and 10 s, increasing from $54.6\ \mu\mathrm{m}$ to $56.2\ \mu\mathrm{m}$. The presence of oscillatory mixing hence reduces the effective vertical diffusive timescale to less than 5 s, which is rather different from the steady transport results of Table 4.2. The inclusion of oscillations has brought us considerably closer to the experimentally observed results. In the following sections we examine other effects which increase mixing further.

t_{out}	δx	δz	δt	$d(0, t_{\text{out}})$	$d(10, t_{\text{out}})$
0.5	1.5	0.0625	0.002	2.8246	18.561
0.5	0.75	0.0625	0.002	2.7208	18.526
0.5	0.375	0.0625	0.002	2.7000	18.521
0.5	1.5	0.03125	0.002	2.8232	18.562
0.5	1.5	0.0625	0.001	2.8139	18.557

Table 4.4: Numerical simulation results for traction layer numerical oscillatory velocity profile and diffusion profile D_1, showing that satisfactory convergence is achieved for $d(0,t)$ and $d(H,t)$ with $\delta x = 1.5\ \mu\text{m}$, $\delta z = 0.0625\ \mu\text{m}$ and $\delta t = 0.002$ s. The transport ratio will become relatively more accurate as $d(0,t)$ increases with time. All times in seconds, distances in μm.

t_{out}	δx	δz	δt	$d(0, t_{\text{out}})$	$d(10, t_{\text{out}})$	$r(t_{\text{out}})$
5	1.5	0.0625	0.002	67.983	122.61	1.8035
10	1.5	0.0625	0.002	151.95	208.19	1.3702
20	1.5	0.0625	0.002	320.75	377.04	1.1755

Table 4.5: Numerical simulation results for traction layer numerical oscillatory velocity profile and diffusion profile D_1. The separation between the two pulses does not significantly increase after 5 s. All times in seconds, distances in μm.

4.5.2 Altering the diffusion profile

The diffusion profile D_1 chosen for the above simulations decreased abruptly from $160\ \mu\text{m}^2/\text{s}$ to $3.6\ \mu\text{m}^2/\text{s}$ at the mucus-PCL interface $y = h$. However, it is likely that vertical mixing due to penetration of the mucous layer by cilia, which was not a feature of the traction layer model, may substantially enhance vertical 'diffusion'. A simple phenomenological model of this advective mixing is to increase the diffusion coefficient in this region by moving the transition in $D(z)$ further up into the mucous layer, and smoothing the transition, so that

$$D_2(z) \;=\; \frac{1}{2}\left((D_P - D_M)\tanh\left(20\left[\frac{L-z}{L}\right]\right) + D_P + D_M\right). \tag{4.7}$$

The velocity profile and diffusion profile $D_2(z)$ are shown in Figure 4.7. The results of 20 s simulation are shown in Table 4.6 and Figure 4.9, middle graph. The pulses separate by just $35.9\ \mu\text{m}$ after 20 s, a 10.7% ratio compared with the 17.6% ratio observed for D_1.

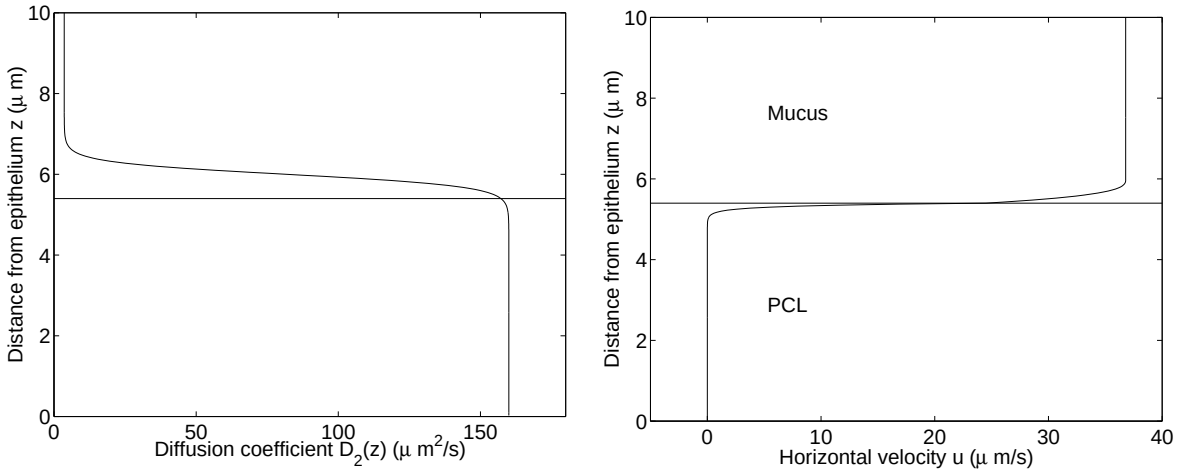

Figure 4.7: Adjusted diffusion profile $D_2(z)$. Mean horizontal velocity u versus height above epithelium for the results of chapter 2.

4.5.3 Mean profile of Fulford and Blake (1986) with oscillations

As discussed in chapter 2, although the traction layer model produces a mean profile superficially very similar to the results of Fulford and Blake (1986), they predicted significant fluid transport in the upper part of the PCL, likely due to the fact that the cilia bend closer to the epithelium during the recovery stroke and so do not resist the flow of fluid. Our discrete cilia results in chapter 3 confirm this—there is continuous positive fluid transport above the cilia tips during the recovery part of the beat cycle. A qualitative representation of this type of profile may be obtained by setting $h = 0.8L$ for the steady velocity component of the traction layer model. We then have the profile shown in Figure 4.8, with the standard traction layer profile for comparison.

Examining the numerical simulation results for this profile, shown in Table 4.6, the separation after 20 s is $51.6\ \mu\mathrm{m}$, a little less than the $56.3\ \mu\mathrm{m}$ observed for the standard profile, with $r(20) = 1.14$. Combining a Fulford and Blake (1986) type profile with the diffusion coefficient D_2 produces still less separation—$33.0\ \mu\mathrm{m}$, with $r(20) = 1.09$.

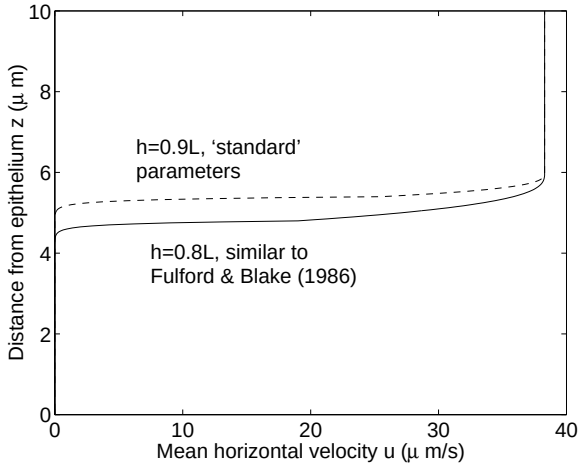

Figure 4.8: (Solid line) traction layer mean profile with $h = 0.8L$, representative of mean velocity from Fulford and Blake (1986), showing greater fluid transport in the upper part of the PCL. (Dotted line) mean velocity with $h = 0.9L$ for comparison.

4.5.4 *Ad hoc* 'plane Couette' oscillatory profile

In order to examine the effect of greater PCL transport with physically realistic oscillations, we combine the plane Couette profile shown in Figure 4.5 with the time-dependent terms $\mathbf{u}_1, \ldots, \mathbf{u}_{15}$ from the traction layer model. We simulated dispersion with the adjusted diffusion profile $D_2(z)$, again the results are shown in Table 4.6 and Figure 4.9, bottom graph. After 20 s, the separation between the two layers is just 3.9%. This is likely to be consistent with the results of Matsui et al. (1998b), since a 3.9% separation between the pulses is unlikely to be apparent in the images produced. Hence we see that the Matsui et al. profile 1.3(C) is not a necessary consequence of their observations—only 50% PCL transport is necessary to give apparent cotransport of tracer between the layers. It should be realised that this does not disprove the suggested profile of Matsui et al. (1998b), and indeed in the presence of osmotic pressure gradients, it has not been shown that such a flow could not occur.

The tracer pulses predicted by the traction layer and Couette simulations are shown in Figure 4.9. As for Figure 4.6, it is interesting to note that when the pulses separate by less, the

t_{out}	$D(z)$	Velocity field $\mathbf{u}$	$d(0, t_{\text{out}})$	$d(10, t_{\text{out}})$	$r(t_{\text{out}})$
20	$D_1(z)$	Traction layer	320.75	377.04	1.1755
20	$D_2(z)$	Traction layer	334.98	370.90	1.1072
20	$D_1(z)$	Oscillatory Fulford and Blake	359.76	411.37	1.1435
20	$D_2(z)$	Oscillatory Fulford and Blake	372.84	405.82	1.0885
20	$D_2(z)$	Oscillatory Couette	520.04	540.48	1.0393
20	$D_1(z)$	Oscillatory Matsui et al.	728.13	732.00	1.0053

Table 4.6: Numerical simulation results for various oscillatory profiles and diffusion coefficients $D_1(z)$ and $D_2(z)$. All times in seconds, distances in μm.

horizontal diffusion is reduced in both layers. The most striking comparision is between the top and middle graphs, which depict results differing only in the diffusion coefficient $D(z)$. The middle graph, corresponding to greater diffusion at the level of the interface, actually shows less horizontal spread than the top graph. This is due to the fact that increased separation of the tracer pulse in the D_1 simulation results in non-zero gradients $\partial c/\partial z$ over a wider region and hence greater vertical diffusion between the layers. This results in apparent greater horizontal diffusion, even though $D_1 \leqslant D_2$. We remark that the effect of vertical diffusion causing increased horizontal spreading is similar to the mechanism responsible for Taylor disperson. The fact that in experiments there was not significant horizontal spreading of the tracer pulses certainly argues for any separation between the two layers being small.

Finally, we note that for the suggested profile of Matsui et al., when combined with oscillations, leads to a separation of just 0.5%, as might be expected.

4.6 Conclusions

It is now easier to reconcile the experimental results of Matsui et al. (1998b) with theoretical modelling work, even without considering flow due to osmotic pressure gradients. By including the mechanically derived oscillatory flow of chapter 2, even with very low mean transport of PCL, we predicted results with relatively little 'smearing' of the tracer pulses. Adding a diffusive term to represent ciliary mixing at the interface leads to even closer tracer transport, with

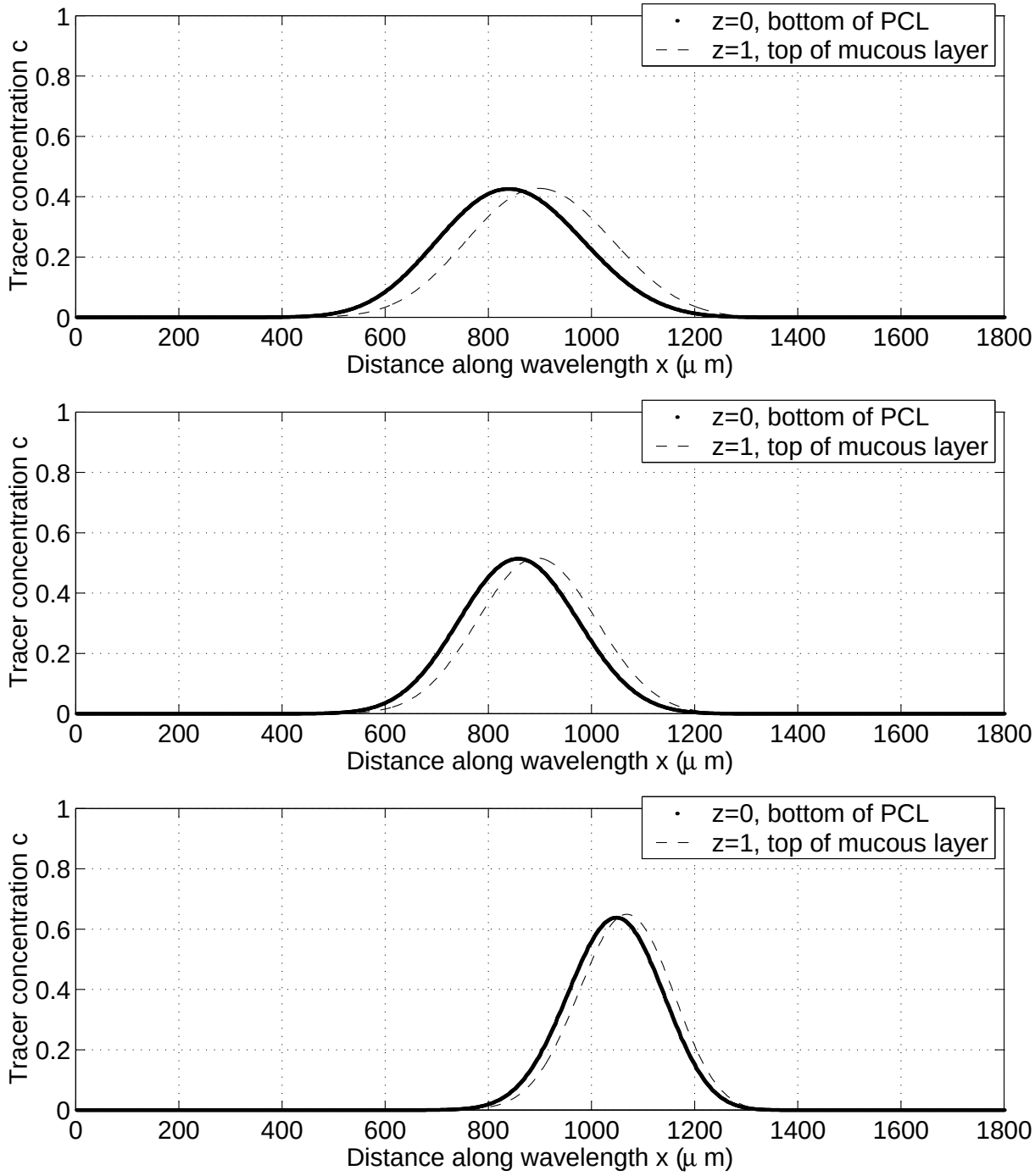

Figure 4.9: Numerical simulation results—oscillatory profiles. Top—oscillatory traction layer velocity (low mean PCL transport), with diffusion $D_1(z)$. Middle—oscillatory traction layer velocity (low mean PCL transport), with diffusion $D_2(z)$. Bottom—*ad hoc* oscillatory velocity with plane Couette steady flow (medium mean PCL transport) and diffusion $D_2(z)$. The bottom profile shows greater transport than the other two due to the greater fluid flux in the velocity term. When comparing the pulse size with Figure 4.6, note the altered x scaling. Time duration 20 seconds.

the tracer centroids separating by only 10.7% after 20 s. Increasing transport in the upper part of the PCL reduces the separation further to 8.85%, and refining our fluid dynamical model of the PCL in order to quantify this effect should be a subject for future research.

However, we noted from our simulations that even a very small separation between the pulses would result in considerably increased horizontal diffusion, unlike that which was observed by Matsui et al. (1998b). We can deduce from this that the tracer pulses in the experiment must have been very closely associated. Hence it appears likely that there is both greater fluid transport than predicted by the traction layer model, and additional effects such as vertical mixing near the interface. Future work should address both of these issues, for instance by extending the traction layer model.

Finally, it is clear that the mean fluid transport in the PCL need not be anywhere near as large as suggested by Matsui et al. (1998b). The simulation with the plane Couette mean profile together with oscillations predicted only 3.9% separation between the pulses, hence we concluded that PCL transport need not be any larger than 50% of that of mucus. It remains to be determined whether osmotic flows could produce such large PCL transport, and this too should be a subject for future work.

CHAPTER 5

SUMMARY AND FUTURE WORK

5.1 Summary

In chapter 1 we described the biology of the muco-ciliary system, previous modelling work related to cilia and mucus, and then discussed the salt/fluid controversy and the experiments of Matsui et al., which provided the main motivation for carrying out our research. In chapter 2 we extended and developed a two dimensional traction layer model of muco-ciliary transport to include sublayer resistance, linear viscoelasticity, the spatial and temporal variations in the beat cycle, a possible shear-thinning effect at the interface and the effect of very strong surface and interface tension. We solved these models analytically and numerically, producing profiles that were qualitatively similar to the mean profiles obtained by Fulford and Blake (1986), subject to the assumption of no-flux through the epithelium. Our results provided novel insight into the importance of interface tension in ensuring efficient transport, and we were able to provide explanations of the physical mechanisms that ensure efficient transport in a wide variety of conditions, in particular parallelling the experimental result that a dilute mucous layer may be transported more efficiently than a 'normal' one. In chapter 3 we formulated a new discrete sublayer model for the flow in the PCL based on Liron's 1978 analysis together with the representation of the mucus movement from chapter 2. We obtained more accurate velocity profiles

on the cilia than have previously been possible, together with three dimensional flow patterns for a field of 50 cilia per wavelength. It was interesting to note that in the region between the cilia tips during the recovery stroke and the mucus-PCL interface, there was significant forward flux of PCL. This strongly suggests that the PCL transport is greater than that predicted by chapter 2, and closer to that predicted by Fulford and Blake (1986), pointing to an area in which the traction layer model could be developed further. In chapter 4 we described the tracer dispersion simulations of Barlow (2000) and Blake and Gaffney (2001), and by using the same alternating direction implicit algorithm were able to test the profiles obtained in chapter 2, as well as profiles exhibiting greater PCL transport. We also modelled the effect of vertical mixing at the mucus-PCL interface by increased diffusion. We found that even a small separation between the tracer centroids in the two layers lead to significant horizontal diffusion, which was not observed in experiment, so that the tracer centroids must be very closely associated. We confirmed that the presence of oscillations significantly increased tracer transport in the PCL, as did increased diffusion at the mucus-PCL interface. It emerged that combining a 'plane Couette' mean profile with an oscillatory flow lead to results that were consistent with the experiments of Matsui et al. (1998b), and that their suggested flow profile, shown in Figure 1.3(C) was not a necessary consequence of their results. We also concluded that including vertical mixing at the interface, and modelling increased PCL transport in the upper part of the PCL will be necessary to improve the traction layer model.

5.2 Future work

There are many ways in which this research may be extended to gain more understanding. These are briefly summarised below.

- The traction layer model of chapter 2 provides a suitable framework for examining many more physical effects. Adding further Maxwell elements in order better to describe experimental results may be useful, and would be relatively straightforward to implement.

It would also be straightforward to introduce PCL viscoelasticity, once data is available. By altering the form of the active porous medium velocity, the problem of transport over regions with inactive cilia could be investigated. The model could easily be extended to consider several wavelengths, so that active, inactive and non-ciliated regions could be modelled. In particular the role of viscoelasticity in assisting with flow over such regions may be elucidated. One might also very the form of the propulsive force used, so that the role of the temporal asymmetry of the ciliary beat cycle may be investigated. As discussed above, perhaps the most illuminating improvement to the model would be to model the sublayer resistance effect more precisely, by introducing an additional thin layer in the PCL, modelling the region above the cilia tips during the recovery stroke, where the fluid may slip past. Vertical mixing effects due to the cilia penetrating and leaving the mucous layer should also be modelled.

- A more ambitious project would be to extend the spectral analysis to the case of non-linear viscoelasticity, investigating the effect of some or all of the non-linear terms resulting from an invariant time derivative. The non-Newtonian behaviour of mucous would also be better represented by the more physically based model of Quemada (1984). This would likely require direct numerical solution of the full PDE system. One might also model the surface and interface movement and consequent tension forces explicitly, although data regarding the interface tension may be difficult to obtain. Asymptotic analysis in the surface and interface height, similar to that pursued by Ross (1971) may be the best approach.

- According to the isotonic volume hypothesis explained in chapter 1, there will be absorption of fluid by the epithelium. It is therefore important to model possible osmotic flows, in order to determine whether they can lead to greater axial transport of PCL. A useful study in determining the parameters and timescales that may be relevant is the *in vitro*

and *in vivo* studies of Jayaraman et al. (2001). They determined normal concentrations of Na^+ and Cl^-, and determined the time course of responses to additions of both salt and saline. By adding the sodium channel blocker amiloride, they were able to test how much of the transepithelial flow was due to sodium transport alone.

- The discrete sublayer model of chapter 3 used the two dimensional results of the mucous layer flow from chapter 2 together with a more refined three dimensional model for the flow around the cilia. This may be improved further by taking the force distribution on the cilia calculated from chapter 3, converting to a spatially continuous but still fully three dimensional representation and hence formulating a more accurate traction layer model. Such a hybrid model would have the advantage that interactions between physical parameters could be tested, as for the traction layer model, but using more accurate data for the volume force.

- It would be very illuminating to model the two-way interaction between ciliary beating and mucus. In the study of chapter 2, we assumed the form and frequency of the ciliary beat, and modelled the effect on mucus flow. However, it is likely that some representation of the effect of the mucus properties on the ciliary beat will be necessary to understand the importance of mucus elasticity, and to test the theory of Meyer and Silberberg (1980) quoted in §2.4.2. One could attempt to combine a finite element representation of the mucus and PCL, a model of the moving contact line caused by the penetrating cilium, and a model of the internal mechanics of the cilium. This would be very computationally expensive, and it may only be possible to model one or several cilia, possibly in the presence of a background flow. One might even attempt to couple this with the nanoscale interaction between glycoprotein chains and the cilium 'crown'. The role of a possible surfactant lipid layer in allowing penetration might also be explained.

- For the discrete cilia model in chapter 3 one can calculate the volume flux without needing

to perform any simulations—once the dipole is neglected, Liron (1978) showed that the volume flux due to a Stokeslet between two no-slip boundaries is zero. Our 'centre line' representation of the cilia is satisfactory for calculating flow fields, but upon integrating over a surface in the flow, the error becomes significant. It follows that the precise boundary integral formulation is necessary to determine the correct flux, although this would be likely to be very computationally expensive for a field of 50–100 cilia. Calculating the flow due to one or several densely packed cilia may provide useful insight.

- The model of chapter 3 required that the cilia should not be placed too closely together, since the cilia might approach very closely. The case of cilia actually sliding past each other is rather difficult to model, and is an avenue for further research, possibly using the boundary integral representation for two or several cilia.

- It was only possible to perform a two dimensional simulation of tracer dispersion, whereas we have shown in chapter 3 that the flow field in the PCL shows significant variation in the x_2 direction, which may be responsible for additional mixing. Implementing a three dimensional simulation would require parallel processing, and the ADI algorithm extended to three dimensions would be a natural choice. Neglecting the effect of the edges of the tracer pulse by assuming periodicity in the x_2 direction, the number of grid points need not be excessive. The accuracy of the algorithm may also be improved by using a higher-order discretisation for the advective terms such as that given by Leonard (1979), although the oscillatory profiles necessitate a relatively fine grid due to the inherent small scale of the variations in the flow. Investigating an analytic or semi-analytic approach that would reduce the amount of computation necessary may also be valuable, and would be a useful technique for investigating chemical gradients in the related problem of symmetry-breaking in the embryonic node, see for example Cartwright et al. (2004).

In summary, we have elucidated certain aspects of the muco-ciliary system, particularly the oscillatory nature of the fluid flow and the physical interactions taking place that ensure efficient transport. In addition to this we have provided a framework for future investigation, in that both fluid dynamical models are very suitable for introducing further refinements and physical effects. The tracer dispersion study of chapter 4 has provided insight into how the experimental work in Matsui et al. (1998b) may be interpreted, and provided stimulus for improvements to the fluid dynamical modelling. Further work, likely involving osmotic modelling, is necessary before all of the details of the muco-ciliary flow are fully understood, but we hope that this thesis has provided a significant step forward.

APPENDIX A

FOURIER COEFFICIENTS

A.1 Force coefficients f_n, g_n

The coefficients f_n and g_n defining the propulsive force for the traction layer model of chapter 2:

$$f_0 = 0.2 \quad f_1 = 0.19351 \quad f_2 = 0.17503 \quad f_3 = 0.14737$$
$$f_4 = 0.11456 \quad f_5 = 0.08106 \quad f_6 = 0.05091 \quad f_7 = 0.02707$$
$$f_8 = 0.01094 \quad f_9 = 0.00239 \quad f_{10} = 0.0 \quad f_{11} = 0.00160$$
$$f_{12} = 0.00486 \quad f_{13} = 0.00785 \quad f_{14} = 0.00935 \quad f_{15} = 0.00901$$

$$g_0 = 0.0 \quad g_1 = -0.04905 \quad g_2 = -0.08745 \quad g_3 = -0.10731$$
$$g_4 = -0.10565 \quad g_5 = -0.08488 \quad g_6 = -0.05195 \quad g_7 = -0.01611$$
$$g_8 = 0.01363 \quad g_9 = 0.03101 \quad g_{10} = 0.03396 \quad g_{11} = 0.02469$$
$$g_{12} = 0.00855 \quad g_{13} = -0.00785 \quad g_{14} = -0.01900 \quad g_{15} = -0.02183$$

A.2 Active porous medium motion coefficients c_n, d_n

The active porous medium coefficients c_n, d_n defining u_{cil} and v_{cil}:

$c_0 = 0$ $c_1 = 0.46775$ $c_2 = 0.37843$ $c_3 = 0.25228$

$c_4 = 0.1169$ $c_n = 0.0 \quad (n \geq 5)$

$d_0 = 0$ $d_1 = 0.09217$ $d_2 = -0.19211$ $d_3 = -0.23553$

$d_4 = -0.23148$ $d_5 = -0.18536$ $d_6 = -0.11252$ $d_7 = -0.03354$

$d_n = 0 \quad (n \geq 8)$

APPENDIX B

TRACTION LAYER ANALYTICAL SOLUTION

B.1 Horizontal velocity profiles

In order to write the solutions down succinctly, we define the following constants and functions:

$$
\begin{aligned}
\chi_n &= 2\pi n L/\lambda \\
\beta_n^2 &= \alpha_x^2 + \chi_n^2 \\
V_1 &= \cosh(\chi_n)\sinh(\chi_n)(1-\theta_2) \\
&\quad + \tanh(\chi_n H)(\theta_2 \cosh^2(\chi_n) - \sinh^2(\chi_n))) \\
V_2 &= 1 + (1-\theta_2)\sinh^2(\chi_n) - \sinh(\chi_n)\tanh(\chi_n H)\cosh(\chi_n)(1-\theta_2)
\end{aligned}
\tag{B.1}
$$

$$
\begin{aligned}
\Theta_1(z) &= \cosh(\chi_n z) - \tanh(\chi_n H)\sinh(\chi_n z) \\
\Theta_2(z) &= \cosh(\chi_n z) - (V_1/V_2)\sinh(\chi_n z) \\
P_n &= \pi(\phi_n\theta_1\tanh(\beta_n h)\chi_n\cosh(\chi_n h)/V_2 - (\phi_n^2-\psi_n^2)\beta_n\sinh(\chi_n h))\Theta_1(1) \\
&\quad +\chi_n(\phi_n\pi\theta_1\tanh(\beta_n h)\cos(\pi h) - (\phi_n^2-\psi_n^2)\beta_n\sin(\pi h)) \\
Q_n &= \pi(-2\phi_n\psi_n\beta_n\sinh(\chi_n h) + \psi_n\theta_1\tanh(\beta_n h)\chi_n\cosh(\chi_n h)/V_2)\Theta_1(1) \\
&\quad +\chi_n(\psi_n\pi\theta_1\tanh(\beta_n h)\cos(\pi h) - 2\phi_n\psi_n\beta_n\sin(\pi h)) \\
S_n &= \phi_n\beta_n(\cosh(\chi_n h) - (V_1/V_2)\sinh(\chi_n h)) - \theta_1\tanh(\beta_n H)\Theta_2'(h) \\
T_n &= \psi_n\theta_1\tanh(\beta_n h)\Theta_2'(h) \\
F_n &= S_n^2 + T_n^2 \\
R_n &= P_n S_n + Q_n T_n \\
I_n &= Q_n S_n - P_n T_n \\
W_n &= \phi_n S_n + \psi_n T_n \\
Y_n &= \psi_n S_n - \phi_n T_n \\
J_n &= \frac{-W_n(\cosh(\beta_n h)-1)^2\Theta_2(h)}{F_n\beta_n^2\sinh(\beta_n h)\cosh(\beta_n h)} + \frac{1}{\beta_n^2}\left(\frac{2(\cosh(\beta_n h)-1)}{\beta_n\sinh(\beta_n h)} - h\right) \\
K_n &= \frac{Y_n(\cosh(\beta_n h)-1)^2\Theta_2(h)}{F_n\beta_n^2\sinh(\beta_n h)\cosh(\beta_n h)} \\
L_n &= \frac{(\cosh(\beta_n h)-1)}{\beta_n\sinh(\beta_n h)}\left\{\frac{-U_{\rm int}f_n\alpha_x^2\Phi_n(h)}{\chi_n(\chi_n^2+\pi^2)}\right. \\
&\quad \left. +\frac{\nu c_n\alpha_x^2}{\beta_n}\left(h - \frac{\tanh(\beta_n h)}{\beta_n}\right)\frac{W_n}{F_n}\Theta_2(h) - \frac{\nu c_n\alpha_x^2}{\beta_n^2}\left(h + h^2/2\right)\right\} \\
O_n &= \frac{(\cosh(\beta_n h)-1)}{\beta_n\sinh(\beta_n h)}\left\{\frac{-U_{\rm int}f_n\alpha_x^2\Psi_n(h)}{\chi_n(\chi_n^2+\pi^2)}\right. \\
&\quad \left. -\frac{\nu c_n\alpha_x^2}{\beta_n}\left(h - \frac{\tanh(\beta_n h)}{\beta_n}\right)\frac{Y_n}{F_n}\Theta_2(h)\right\}
\end{aligned}
\tag{B.2}
$$

$$
\begin{aligned}
\Phi_n(z) &= \pi\phi_n \sinh(\chi_n z)\Theta_1(1)/V_2 + \phi_n\chi_n \sin(\pi z) + \Theta_2(z)R_n/F_n \\
\Psi_n(z) &= \pi\psi_n \sinh(\chi_n z)\Theta_1(1)/V_2 + \psi_n\chi_n \sin(\pi z) + \Theta_2(z)I_n/F_n \\
\Omega_n &= \pi\phi_n \sinh(\chi_n)\Theta_1(1)/(\Theta_2(1)V_2) + R_n/F_n \\
\Lambda_n &= \pi\psi_n \sinh(\chi_n)\Theta_1(1)/(\Theta_2(1)V_2) + I_n/F_n \\
\Pi_n^r &= -(K_n O_n + L_n J_n)/(J_n^2 + K_n^2) \\
\Pi_n^i &= (J_n O_n - L_n K_n)/(J_n^2 + K_n^2).
\end{aligned} \tag{B.3}
$$

The solutions only depend on x and t through $\xi = 2\pi x + \sigma t$, so we can write

$$
\begin{aligned}
u^P = {} & \frac{\sinh(\beta_n z)}{\sinh(\beta_n h)} \\
& \cdot \left\{ \frac{-U_{\text{int}} f_n \alpha_x^2}{\chi_n(\chi_n^2 + \pi^2)\sin(\pi h)} \left(\Phi_n(h)\cos(\xi n) - \Psi_n(h)\sin(\xi n)\right) \right. \\
& + \frac{\nu c_n \alpha_x^2}{\beta_n} \left(h - \frac{\tanh(\beta_n h)}{\beta_n}\right) \left(\frac{W_n}{F_n}\cos(\xi n) - \frac{Y_n}{F_n}\sin(\xi n)\right) \Theta_2(h) \\
& - \frac{\left((\Pi_n^r W_n - \Pi_n^i Y_n)\cos(\xi n) - (\Pi_n^r Y_n + \Pi_n^i W_n)\sin(\xi n)\right)}{F_n} \\
& \left. \cdot \left(\frac{\cosh(\beta_n h) - 1}{\beta_n \cosh(\beta_n h)}\right) \Theta_2(h) - \frac{\nu c_n \alpha_x^2 h}{\beta_n^2}\cos(\xi n) \right\} \\
& + \frac{\Pi_n^r \cos(\xi n) - \Pi_n^i \sin(\xi n)}{\beta_n^2} \left(\frac{\sinh(\beta_n z) + \sinh(\beta_n(h - z))}{\sinh(\beta_n h)} - 1\right) \\
& + \frac{\nu c_n \alpha_x^2 z}{\beta_n^2}\cos(\xi n)
\end{aligned} \tag{B.4}
$$

$$
\begin{aligned}
u^{M1} = {} & \frac{-U_{\text{int}} f_n \alpha_x^2}{\chi_n(\chi_n^2 + \pi^2)\sin(\pi h)} \left\{\Phi_n(z)\cos(\xi n) - \Psi_n(z)\sin(\xi n)\right\} \\
& + \frac{\nu c_n \alpha_x^2}{\beta_n} \left(h - \frac{\tanh(\beta_n h)}{\beta_n}\right) \left(\frac{W_n}{F_n}\cos(\xi n) - \frac{Y_n}{F_n}\sin(\xi n)\right) \Theta_2(z) \\
& - \left((\Pi_n^r W_n - \Pi_n^i Y_n)\cos(\xi n) - (\Pi_n^r Y_n + \Pi_n^i W_n)\sin(\xi n)\right) \\
& \cdot \frac{(\cosh(\beta_n h) - 1)}{F_n \beta_n \cosh(\beta_n h)} \Theta_2(z)
\end{aligned} \tag{B.5}
$$

$$
\begin{aligned}
u^{M2} &= \left(\frac{-U_{\text{int}} f_n \alpha_x^2}{\chi_n(\chi_n^2+\pi^2)\sin(\pi h)} \left\{ \Omega_n \cos(\xi n) - \Lambda_n \sin(\xi n) \right\} \right. \\
&\quad \left. + \frac{\nu c_n \alpha_x^2}{\beta_n} \left(h - \frac{\tanh(\beta_n h)}{\beta_n} \right) \left\{ \frac{W_n}{F_n} \cos(\xi n) - \frac{Y_n}{F_n} \sin(\xi n) \right\} \right) \\
&\quad \cdot \frac{\Theta_1(z)\Theta_2(1)}{\Theta_1(1)}. \qquad \text{(B.6)}
\end{aligned}
$$

B.2 Vertical velocity components

Here we give the corresponding terms v^P, v^{M1}, v^{M2} for the Fourier series representations of the velocity component in the vertical (z) direction. Starting with the continuity equation (2.70), we can differentiate the expressions (B.4), (B.5) and (B.6) with respect to x to find $\partial v/\partial z$, then integrate with respect to z to find v. We again use the boundary condition that $v = 0$ on $z = 0$, and match the vertical velocities at the interfaces between the three regions.

For $n = 0$, the velocities u are independent of x, so that $\partial u/\partial x = \partial v/\partial z = 0$, and hence $v = 0$. For $n \geqslant 1$ we have the following:

$$
\begin{aligned}
v^P &= \frac{2n\pi(\cosh(\beta_n z) - 1)}{\beta_n \sinh(\beta_n h)} \\
&\quad \cdot \left\{ \frac{-U_{\text{int}} f_n \alpha_x^2}{\chi_n(\chi_n^2+\pi^2)} \left(\frac{\Phi_n(h)\sin(\xi n) + \Psi_n(h)\cos(\xi n)}{\sin(\pi h)} \right) \right. \\
&\quad + \frac{\nu c_n \alpha_x^2}{\beta_n} \left(h - \frac{\tanh(\beta_n h)}{\beta_n} \right) \\
&\quad \cdot \left(\frac{W_n}{F_n} \sin(\xi n) + \frac{Y_n}{F_n} \cos(\xi n) \right) \Theta_2(h) \\
&\quad - \frac{((\Pi_n^r W_n - \Pi_n^i Y_n)\sin(\xi n) + (\Pi_n^r Y_n + \Pi_n^i W_n)\cos(\xi n))}{F_n} \\
&\quad \left. \cdot \left(\frac{\cosh(\beta_n h) - 1}{\beta_n \cosh(\beta_n h)} \right) \Theta_2(h) - \frac{\nu c_n \alpha_x^2 h}{\beta_n^2} \sin(\xi n) \right\} \\
&\quad + 2\pi n \frac{\Pi_n^r \sin(\xi n) + \Pi_n^i \cos(\xi n)}{\beta_n^2} \\
&\quad \cdot \left(\frac{\cosh(\beta_n z) - 1 + \cosh(\beta_n(h-z)) - \cosh(\beta_n h)}{\beta_n \sinh(\beta_n h)} - z \right) \\
&\quad + \frac{\nu \pi n c_n \alpha_x^2 z^2}{\beta_n^2} \sin(\xi n) \qquad \text{(B.7)}
\end{aligned}
$$

$$
\begin{aligned}
v^{M1} \;=\;& \frac{-2U_{\rm int}\pi n f_n \alpha_x^2}{\chi_n(\chi_n^2+\pi^2)\sin(\pi h)} \\
& \cdot\left(\sin(\xi n)U_{\rm int}h^z\Phi_n(z^*)\;dz^* + \cos(\xi n)U_{\rm int}h^z\Psi_n(z^*)\;dz^*\right) \\
& +\frac{-10U_{\rm int}\pi n c_n\alpha_x^2}{\chi_n\beta_n}\left(h-\frac{\tanh(\beta_n h)}{\beta_n}\right)\left(\frac{W_n}{F_n}\sin(\xi n)+\frac{Y_n}{F_n}\cos(\xi n)\right) \\
& \cdot{\rm int}_h^z\Theta_2(z^*)\;dz^* \\
& -2\pi n\{(\Pi_n^r W_n-\Pi_n^i Y_n)\sin(\xi n)+(\Pi_n^r Y_n+\Pi_n^i W_n)\cos(\xi n)\} \\
& \cdot\frac{(\cosh(\beta_n h)-1)}{F_n\beta_n\cosh(\beta_n h)}U_{\rm int}h^z\Theta_2(z^*)\;dz^* + v^{(1)}(z=h)
\end{aligned}
\tag{B.8}
$$

$$
\begin{aligned}
v^{M2} \;=\;& 2\pi n\frac{\Theta_2(1)}{\Theta_1(1)}\left\{\frac{-U_{\rm int}f_n\alpha_x^2}{\chi_n^2(\chi_n^2+\pi^2)\sin(\pi h)}\left(\Omega_n\sin(\xi n)+\Lambda_n\cos(\xi n)\right)\right. \\
& +\frac{\nu c_n\alpha_x^2}{\beta_n}\left(h-\frac{\tanh(\beta_n h)}{\beta_n}\right)\left(\frac{W_n}{F_n}\cos(\xi n)+\frac{Y_n}{F_n}\sin(\xi n)\right) \\
& -\{(\Pi_n^r W_n-\Pi_n^i Y_n)\sin(\xi n)+(\Pi_n^r Y_n+\Pi_n^i W_n)\cos(\xi n)\} \\
& \left.\cdot\frac{(\cosh(\beta_n h)-1)}{F_n\beta_n\cosh(\beta_n h)}\right\}U_{\rm int}h^z\Theta_1(z^*)\;dz^* + v^{(2)}(z=1)
\end{aligned}
\tag{B.9}
$$

APPENDIX C

TRACTION LAYER NUMERICAL ODE SYSTEM

The system of 30 ODEs in the form $Y_i' = f(X, Y_1, ..., Y_{30})$ is as follows:

$$Y_1' = (h/(\phi^2+\psi^2))(\phi Y_7 + \psi Y_8 + \theta_1\theta_2\phi Y_{27} + \theta_1\phi Y_{17} + \theta_1\theta_2\psi Y_{28} + \theta_1\psi Y_{18})$$
$$+2\pi n\epsilon^2 h Y_4$$

$$Y_2' = (h/(\phi^2+\psi^2))(\phi Y_8 - \psi Y_7 - \theta_1\theta_2\psi Y_{27} - \theta_1\psi Y_{17} + \theta_1\theta_2\phi Y_{28} + \theta_1\phi Y_{18})$$
$$-2\pi n\epsilon^2 h Y_3$$

$$Y_3' = hY_5 + 2\pi n h Y_2$$

$$Y_4' = hY_6 - 2\pi n h Y_1$$

$$Y_5' = 0$$

$$Y_6' = 0$$

$$Y_7' = -2\pi n h\phi Y_{10} - 2\pi n h\psi Y_9 + (\beta_x^2+\chi^2)(\phi Y_1 - \psi Y_2)h - \nu X h^2 c_n \phi \alpha_x^2$$
$$-\theta_1(1-h)\Big(2\pi n(-Y_{20} + 2\epsilon^2 Y_{16} + \theta_2 Y_{30}) + 2\chi^2\theta_2(Y_1 - Y_{11} - Y_{21})$$
$$-4\pi n\theta_2\epsilon^2 Y_{26} - 4\chi^2(Y_1 - Y_{11}) + 2\pi n\epsilon^2 Y_{16}$$
$$-\phi f_n \alpha_x^2 U_{\text{int}} \sin(\pi(1-(1-h)X))/\sin(\pi h)\Big) - 2\pi n\epsilon^2(\phi Y_6 + \psi Y_5)h$$

$$Y_8' = 2\pi n h\phi Y_9 - 2\pi n h\psi Y_{10} + (\beta_x^2 + \chi^2)(\phi Y_2 + \psi Y_1)h - \nu X h^2 c_n \psi \alpha_x^2$$
$$-\theta_1(1-h)\Big(-2\pi n(-Y_{19} + 2\epsilon^2 Y_{15} + \theta_2 Y_{29}) + 2\chi^2\theta_2(Y_2 - Y_{12} - Y_{22})$$
$$-4\pi n\theta_2\epsilon^2 Y_{25} - 4\chi^2(Y_2 - Y_{12}) - 2\pi n\epsilon^2 Y_{15}$$
$$-\psi f_n \alpha_x^2 U_{\rm int}\sin(\pi(1-(1-h)X))/\sin(\pi h)\Big) + 2\pi n\epsilon^2(\phi Y_5 - \psi Y_6)h$$

$$Y_9' = 2\pi n\epsilon^2 h(\phi Y_8 - \psi Y_7 - \theta_1\psi Y_{17} - \theta_1\theta_2\psi Y_{27} + \theta_1\phi Y_{18} + \theta_1\phi\theta_2 Y_{28}) + (\beta_y^2 + \chi^2)h\epsilon^2 Y_3$$

$$Y_{10}' = -2\pi n\epsilon^2 h(\phi Y_7 + \psi Y_8 + \theta_1\phi Y_{17} + \theta_1\theta_2\phi Y_{27} + \theta_1\psi Y_{18} + \theta_1\theta_2\psi Y_{28})$$
$$-(\beta_y^2 + \chi^2)h\epsilon^2 Y_4 - \nu\epsilon h d_n \alpha_y^2 X$$

$$Y_{11}' = (h/(\phi^2+\psi^2))(\phi Y_7 + \psi Y_8 + \theta_1\theta_2\phi Y_{27} + \theta_1\phi Y_{17} + \theta_1\theta_2\psi Y_{28} + \theta_1\psi Y_{18})$$
$$+(1-h)(\theta_2 Y_{27} + Y_{17}) + 2\pi n h\epsilon^2 Y_4 + 2\pi n\epsilon^2(1-h)(Y_4 - Y_{14})$$
$$Y_{12}' = (h/(\phi^2+\psi^2))(\phi Y_8 - \psi Y_7 - \theta_1\theta_2\psi Y_{27} - \theta_1\psi Y_{17} + \theta_1\theta_2\phi Y_{28} + \theta_1\phi Y_{18})$$
$$+(1-h)(\theta_2 Y_{28} + Y_{18}) - 2\pi n h\epsilon^2 Y_3 - 2\pi n\epsilon^2(1-h)(Y_3 - Y_{13})$$

$$Y_{13}' = Y_{15}(1-h) - 2\pi n Y_{12}(1-h) + hY_5 + 2\pi n Y_2$$
$$Y_{14}' = Y_{16}(1-h) + 2\pi n Y_{11}(1-h) + hY_6 - 2\pi n Y_1$$

$$Y_{15}' = 0$$
$$Y_{16}' = 0$$

$$Y_{17}' = 2\chi^2\theta_2(2-h-H)(Y_1 - Y_{11} - Y_{21}) + 2\pi n\theta_2((H-h)Y_{30} + \epsilon^2(H-3+2h)Y_{26})$$
$$-2\pi n(1-h)Y_{20} + 6\pi n\epsilon^2(1-h)Y_{16} - 4\chi^2(1-h)(Y_1 - Y_{11})$$
$$-(1-h)\phi f_n\alpha_x^2 U_{\rm int}\sin(\pi(1-(1-h)X))/\sin(\pi h)$$
$$Y_{18}' = 2\chi^2\theta_2(2-h-H)(Y_2 - Y_{12} - Y_{22}) - 2\pi n\theta_2((H-h)Y_{29} + \epsilon^2(H-3+2h)Y_{25})$$
$$+2\pi n(1-h)Y_{19} - 6\pi n\epsilon^2(1-h)Y_{15} - 4\chi^2(1-h)(Y_2 - Y_{12})$$
$$-(1-h)\psi f_n\alpha_x^2 U_{\rm int}\sin(\pi(1-(1-h)X))/\sin(\pi h)$$

$$Y'_{19} = -2\pi n\epsilon^2((1-h)(Y_{18}+\theta_2 Y_{28}) - 3(H-1)\theta_2 Y_{28})$$
$$-4\chi^2\epsilon^2(H-1)\theta_2(Y_3 - Y_{13} - Y_{23}) - (1-h)\epsilon\psi g_n \alpha_y^2 V_{\rm int}\sin(\pi(1-(1-h)X))/\sin(\pi h)$$
$$Y'_{20} = 2\pi n\epsilon^2((1-h)(Y_{17}+\theta_2 Y_{27}) + 3(H-1)\theta_2 Y_{27})$$
$$+4\chi^2\epsilon^2(H-1)\theta_2(Y_4 - Y_{14} - Y_{24}) + (1-h)\epsilon\phi g_n \alpha_y^2 V_{\rm int}\sin(\pi(1-(1-h)X))/\sin(\pi h)$$
$$Y'_{21} = -Y_{17}(1-h) - 2\pi n\epsilon^2(1-h)(Y_4 - Y_{14}) - 2\pi n\epsilon^2(H-1)(Y_4 - Y_{14} - Y_{24})$$
$$-[H-1+\theta_2(1-h)]Y_{27}$$
$$Y'_{22} = -Y_{18}(1-h) + 2\pi n\epsilon^2(1-h)(Y_3 - Y_{13}) + 2\pi n\epsilon^2(H-1)(Y_3 - Y_{13} - Y_{23})$$
$$-[H-1+\theta_2(1-h)]Y_{28}$$
$$Y'_{23} = -(H-1)[Y_{25} + 2\pi n(Y_2 - Y_{12} - Y_{22})] - (1-h)[Y_{15} + 2\pi n(Y_2 - Y_{12})]$$
$$Y'_{24} = -(H-1)[Y_{26} - 2\pi n(Y_1 - Y_{11} - Y_{21})] - (1-h)[Y_{16} - 2\pi n(Y_1 - Y_{11})]$$
$$Y'_{25} = 0$$
$$Y'_{26} = 0$$
$$Y'_{27} = (H-1)[-2\pi n Y_{30} - 2\pi n\epsilon^2 Y_{26} + 2\chi^2(Y_1 - Y_{11} - Y_{21})]$$
$$Y'_{28} = (H-1)[2\pi n Y_{29} + 2\pi n\epsilon^2 Y_{25} + 2\chi^2(Y_2 - Y_{12} - Y_{22})]$$
$$Y'_{29} = (H-1)(2\pi n\epsilon^2 Y_{28} - 2\chi^2\epsilon^2(Y_3 - Y_{13} - Y_{23}))$$
$$Y'_{30} = (H-1)(-2\pi n\epsilon^2 Y_{27} - 2\chi^2\epsilon^2(Y_4 - Y_{14} - Y_{24}))$$

APPENDIX D

SINGULARITIES FOR STOKES FLOW IN A CONFINED DOMAIN

Below we repeat the expressions given for S^C_{jk} and D^C_{jk}, in the notation of chapter 3, given in Liron and Mochon (1976b) and Liron (1978) respectively. They were expressed in the form of exponentially decreasing infinite series, for more efficient computation. The singularities correspond to respectively a point force and a doubly-infinite array of point forces for Stokes flow in the confined domain $0 < x_3 < H$. For chapter 3, $H = 1$.

D.1 S^C_{jk}, the point force singularity

Following Liron and Mochon (1976b), for simplicity we write S^C_{jk} as S^k_j, which makes the solution slightly easier to express. For α, $\beta = 1, 2$,

$$
\begin{aligned}
S^\beta_\alpha \;=\;& \frac{1}{4\pi\mu}\frac{\partial}{\partial r_\beta}\frac{r_\alpha}{\rho}\frac{\pi}{H}\mathrm{Im}\left\{H\sum_{m=1}^{\infty}\mathrm{H}_1^{(1)}\left(\frac{\rho z_m}{H}\right)\left[\frac{1}{z_m}\sinh\frac{\xi_3 z_m}{H}\sinh\frac{x_3 z_m}{H}\right.\right.\\
&+\frac{x_3}{H}\cosh\frac{x_3 z_m}{H}\sinh\frac{\xi_3 z_m}{H}+\frac{\xi_3}{H}\cosh\frac{\xi_3 z_m}{H}\sinh\frac{x_3 z_m}{H}\\
&-\frac{1}{(1+z_m^2)^{1/2}-1}\left[z_m\frac{x_3+\xi_3}{H}\sinh\frac{\xi_3 z_m}{H}\sinh\frac{x_3 z_m}{H}+\frac{x_3}{H}\frac{\xi_3}{H}z_m\right.\\
&\left.\left.\left.\cdot\left(\cosh\frac{\xi_3-x_3}{H}z_m+z_m\sinh\frac{x_3+\xi_3}{H}z_m-(1+z_m^2)^{1/2}\cosh\frac{x_3+\xi_3}{H}z_m\right)\right]\right]\right\}\\
&+\frac{1}{4\pi\mu}\frac{\partial}{\partial r_\beta}\frac{r_\alpha}{\rho}\sum_{n=1}^{\infty}\frac{4}{n\pi}\sin\frac{n\pi\xi_3}{H}\sin\frac{n\pi x_3}{H}\mathrm{K}_1\left(\frac{n\pi\rho}{H}\right)\\
&+\frac{1}{4\pi\mu}\delta_{\alpha\beta}\frac{4}{H}\sum_{n=1}^{\infty}\sin\frac{n\pi\xi_3}{H}\sin\frac{n\pi x_3}{H}\mathrm{K}_0\left(\frac{n\pi\rho}{H}\right)\\
&-\frac{H}{4\pi\mu}\frac{6x_3}{H}\frac{\xi_3}{H}\left(1-\frac{x_3}{H}\right)\left(1-\frac{\xi_3}{H}\right)\frac{\partial}{\partial r_\beta}\left(\frac{r_\alpha}{\rho^2}\right). \qquad \text{(D.1)}
\end{aligned}
$$

$$
\begin{aligned}
S^{\alpha,3}_{3,\alpha} \;=\;& -\frac{1}{4\pi\mu}\frac{r_\alpha}{\rho}\frac{\pi}{H}\mathrm{Im}\left\{\sum_{m=1}^{\infty}\frac{z_m\mathrm{H}_1^{(1)}(\rho z_m/H)}{(1+z_m^2)^{1/2}-1}\left[\frac{\xi_3}{H}\frac{x_3}{H}z_m\cdot\right.\right.\\
&\left(\sinh\frac{x_3-\xi_3}{H}z_m\pm z_m\cosh\frac{x_3+\xi_3}{H}z_m\mp(1+z_m^2)^{1/2}\sinh\frac{x_3+\xi_3}{H}z_m\right)\\
&+z_m\left(\frac{x_3}{H}\cosh\frac{x_3 z_m}{H}\sinh\frac{\xi_3 z_m}{H}-\frac{\xi_3}{H}\sinh\frac{x_3 z_m}{H}\cosh\frac{\xi_3 z_m}{H}\right)\\
&\left.\left.+\sinh\frac{\xi_3 z_m}{H}\sinh\frac{x_3 z_m}{H}\left(\frac{\xi_3-x_3}{H}(1+z_m^2)^{1/2}\pm\left(\frac{x_3+\xi_3}{H}-1\right)\right)\right]\right\}. \qquad \text{(D.2)}
\end{aligned}
$$

The upper signs are for S^α_3, the lower signs for S^3_α.

$$
\begin{aligned}
S_3^3 \;=\; & -\frac{1}{4\pi\mu}\frac{\pi}{H}\mathrm{Im}\left\{\sum_{m=1}^{\infty}\frac{z_m \mathrm{H}_0^{(1)}(\rho z_m/H)}{(1+z_m^2)^{1/2}-1}\right. \\
& \cdot\left[[(1+z_m^2)^{1/2}+1]\left(\frac{x_3}{H}\sinh\frac{\xi_3 z_m}{H}\cosh\frac{x_3 z_m}{H}+\frac{\xi_3}{H}\sinh\frac{x_3 z_m}{H}\cosh\frac{\xi_3 z_m}{H}\right.\right. \\
& \left.-\frac{1}{z_m}\sinh\frac{x_3 z_m}{H}\sinh\frac{z_m\xi_3}{H}\right)-\frac{\xi_3}{H}\frac{x_3}{H}z_m \\
& \cdot\left((1+z_m^2)^{1/2}\cosh\frac{x_3+\xi_3}{H}z_m+\cosh\frac{x_3-\xi_3}{H}z_m-z_m\sinh\frac{x_3+\xi_3}{H}z_m\right) \\
& \left.\left.-z_m\frac{x_3+\xi_3}{H}\sinh\frac{\xi_3 z_m}{H}\sinh\frac{x_3 z_m}{H}\right]\right\}. \qquad \text{(D.3)}
\end{aligned}
$$

The functions K_n and $\mathrm{H}_n^{(1)}$ are the nth order modified Bessel function of the first kind and Hankel function respectively.

D.2 D^C_{jk}, the summed and integrated form of S^C_{jk}

The singularity $D^C_{jk}(x_1, x_3, \xi_1, \xi_3) := \sum_{q=-\infty}^{\infty} \int_{-\infty}^{\infty} S^C_{jk}(x_1, x_2, x_3, \xi_1 + q\lambda, 0, \xi_3)\ \mathrm{d}x_2$. Then writing D^k_j for D^C_{jk} and using κ for the wavenumber $1/\lambda$,

$$
\begin{aligned}
D^j_j(x_1, x_3, \boldsymbol{\xi}) \;=\; & \frac{\kappa}{2\pi\mu}\Bigg\{(\delta_{j1}+\delta_{j2})\frac{\xi_3(H-x_3)}{H} - 3\delta_{j1}\xi_3(H-\xi_3)x_3(H-x_3)/H^3 \\
& +(1+\delta_{j2})\sum_{q=1}^{\infty}\cos(\eta\kappa q)\frac{\sinh(\xi_3\kappa q)\sinh(H-x_3)\kappa q}{\kappa q\sinh(H\kappa q)} \\
& +(\delta_{j1}-\delta_{j3})\sum_{q=1}^{\infty}\cos(\eta\kappa q)\frac{\mathrm{d}}{\mathrm{d}t}\left[\frac{\sinh(\xi_3 t)\sinh(H-x_3)t}{\sinh(Ht)}\right]_{t=\kappa q} \\
& +(\delta_{j1}+\delta_{j3})\sum_{q=1}^{\infty}\kappa q\cos(\eta\kappa q)[x_3 H\cosh(x_3\kappa q)\sinh(\xi_3\kappa q) \\
& -x_3\xi_3\sinh(H\kappa q)\cosh(H-x_3-\xi_3)\kappa q + H\xi_3\sinh(x_3\kappa q)\cosh(\xi_3\kappa q) \\
& -H^2\sinh(x_3\kappa q)\sinh(\xi_3\kappa q)\coth(H\kappa q)]/[\sinh^2(H\kappa q)-(H\kappa q)^2] \\
& +(\delta_{j1}-\delta_{j3})\sum_{q=1}^{\infty}H(\kappa q)^2\cos(\eta\kappa q)[x_3\xi_3\cosh(x_3-\xi_3)\kappa q \\
& +H(x_3+\xi_3)\sinh(\xi_3\kappa q)\sinh(x_3\kappa q) \\
& -H\coth(H\kappa q)(x_3\sinh(\xi_3\kappa q)\cosh(x_3\kappa q)+\xi_3\sinh(x_3\kappa q)\cosh(\xi_3\kappa q) \\
& +H^2\sinh(x_3\kappa q)\sinh(\xi_3\kappa q)/\sinh^2(H\kappa q)]/[\sinh^2(H\kappa q)-(H\kappa q)^2]\Bigg\}, \\
& \quad j=1,2,3, \quad \eta = x_1-\xi_1, \quad \text{and} \quad \xi_3 < x_3. \qquad \text{(D.4)}
\end{aligned}
$$

For $x_3 < \xi_3$, replace x_3 by $H - x_3$ and η by $-\eta$.

$$
D^1_2 = D^2_1 = D^2_3 = D^3_2 = 0, \qquad \text{(D.5)}
$$

$$
\begin{aligned}
D_{3,1}^{1,3} \;=\; & \frac{\kappa}{2\pi\mu}\Bigg\{(x_3-\xi_3)\sum_{q=1}^{\infty}\sin(\eta\kappa q)\sinh(\xi_3\kappa q)\sinh(H-x_3)\kappa q/\sinh(H\kappa q) \\
& +\sum_{q=1}^{\infty}\kappa q\sin(\eta\kappa q)[\pm x_3 H\sinh(x_3\kappa q)\sinh(\xi_3\kappa q)+\xi_3 x_3\kappa q H\sinh(x_3-\xi_3)\kappa q \\
& \pm x_3\xi_3\sinh(H\kappa q)\sinh(H-\xi_3-x_3)\kappa q \mp H(H-\xi_3)\sinh(x_3\kappa q)\sinh(\xi_3\kappa q) \\
& +H^2\kappa q(x_3\sinh(\xi_3\kappa q)\sinh(H-x_3)\kappa q \\
& -\xi_3\sinh(x_3\kappa q)\sinh(H-\xi_3)\kappa q)/\sinh(H\kappa q)]/[\sinh^2(H\kappa q)-(H\kappa q)^2]\Bigg\} \\
& \eta = x_1-\xi_1, \quad \text{and} \quad \xi_3 < x_3. \qquad \text{(D.6)}
\end{aligned}
$$

The upper signs are to be used for D_3^1 and the lower signs for D_1^3. For $x_3 < \xi_3$ replace x_3 by $H - x_3$, ξ_3 by $H - \xi_3$, and η by $-\eta$.

Evaluating the singularities numerically is relatively efficient, since the series are exponentially decreasing. However, it is necessary to use an algorithm which monitors the size of the terms in each sum, since convergence of the series varies significantly with the parameters η, x_3 and ξ_3. It is also necessary to approximate certain parts of the formula in order to avoid overflow errors: for instance it is necessary to approximate $\sinh(H\kappa q)$ with $\frac{1}{2}e^{H\kappa q}$ for large q.

APPENDIX E

AN ADAPTATION OF THE ALTERNATING DIRECTION IMPLICIT (ADI) ALGORITHM

E.1 Introduction

An extension of the ADI algorithm, is used in chapter 4 to solve the advection diffusion tracer dispersion equation. Following the presentation of Douglas Jr. and Kim (1999), we briefly derive the algorithm. We have to solve the advection-diffusion equation

$$\frac{\partial c}{\partial t} = \frac{\partial^2 c}{\partial x^2} + \frac{\partial}{\partial z}\left(D\frac{\partial c}{\partial z}\right) - uc_x - vc_z, \tag{E.1}$$

on the domain $0 < x < X$, $0 < z < Z$ for the time period $0 < t < T$. This is discretised as $x_i = i\delta x$, $z_j = j\delta z$ and $t_n = n\delta t$, with $\delta x = X/N_X$, $\delta z = Z/N_Z$ and $\delta t = T/N_T$, so that the domain consists of $(N_X + 1)(N_Z + 1)$ grid points and there are N_T timesteps. We use the standard notation $c_{ij}^n = c(i\delta x, j\delta z, n\delta t)$.

E.2 ADI algorithm for diffusive terms

Applying a central differencing scheme about $t = (n + 1/2)\delta t$ for the time discretisation, we have

$$\begin{aligned} c^{n+1} - c^n &= \frac{\delta t}{2}\left(D\frac{\partial^2 c^{n+1}}{\partial x^2} + D\frac{\partial^2 c^n}{\partial x^2} + \frac{\partial}{\partial z}\left(D\frac{\partial c}{\partial z}\right)^{n+1} + \frac{\partial}{\partial z}\left(D\frac{\partial c}{\partial z}\right)^{n} \right. \\ &\quad \left. -uc_x^{n+1} - uc_x^n - vc_z^{n+1} - vc_z^n + O(\delta t^2)\right). \end{aligned} \tag{E.2}$$

Using the notation of Douglas Jr. and Kim (1999), the differential operators A_1 and A_2 are defined by

$$A_1 c = -(Dc_x)_x = -Dc_{xx}, \qquad A_2 c = -(Dc_z)_z, \tag{E.3}$$

and we write the advective terms as

$$A_3 c = uc_x, \qquad A_4 c = vc_z. \tag{E.4}$$

The operator A_1 is approximated by taking central differences,

$$A_1 c_{ij}^n = -(c_{i+1,j} - 2c_{ij} + c_{i-1,j})/(\delta x)^2 + O(\delta x^2), \tag{E.5}$$

again the error term is found by applying Taylor's theorem. In order to discretise the outer z derivative, we apply central differences about $y = j\delta z$, so that

$$\frac{\partial}{\partial z}\left(D\frac{\partial c}{\partial z}\right) = \frac{1}{\delta z}\left(D_{j+1/2}\frac{\partial c_{i,j+1/2}}{\partial z} - D_{j-1/2}\frac{\partial c_{i,j-1/2}}{\partial z}\right) + O(\delta z^2). \tag{E.6}$$

The diffusion terms $D_{j+1/2}$ and $D_{j-1/2}$ may be approximated by $(D_{j+1} + D_j)/2$ and $(D_j + D_{j-1})/2$ respectively. The remaining derivatives may again be approximated by central differ-

ences to give

$$\frac{\partial}{\partial z}\left(D\frac{\partial c}{\partial z}\right) = \frac{1}{2\delta z^2}\left(c_{i,j+1}(D_{j+1}+D_j) - c_{i,j}(D_{j+1}+2D_j+D_{j-1}) + c_{i,j-1}(D_{j-1}+D_j)\right) + O(\delta z^2). \tag{E.7}$$

E.3 QUICK discretisation for advective terms

It remains to calculate the advective terms. One could again use central differences, so that $c_x = (c_{i+1,j} - c_{i-1,j})/2\delta x + O(\delta x^2)$, but this approach may introduce unacceptable oscillations into the solution if there is insufficient diffusion. An alternative approach, used by Blake and Gaffney (2001) is first order upwind discretisation, in which the derivative is calculated from the 'upwind' or 'upstream' cell, so that for $u < 0$ we approximate $c_x = (c_{i+1,j} - c_{ij})/\delta x$. This is now numerically stable but only first order accurate and, as explained in Leonard (1979), introduces artificial numerical diffusion. Since diffusion will increase the tendency of the pulses to 'cotransport' in our problem, this may give misleading results. Instead we shall use the QUICK (Quadratic Upstream Interpolation for Convective Kinematics) scheme introduced by Leonard (1979), defined by

$$A_3 = \begin{cases} u((1/8)c_{i-2,j} - (7/8)c_{i-1,j} + (3/8)c_{ij} + (3/8)c_{i+1,j})/\delta x & \text{if} \quad u < 0 \\ u(-(3/8)c_{i-,j} - (3/8)c_{ij} + (7/8)c_{i+1,j} - (1/8)c_{i+2,j})/\delta x & \text{if} \quad u > 0, \end{cases} \tag{E.8}$$

and analogously for A_4. The properties of this scheme are briefly discussed in §4.3.2.

E.4 Solution

Writing $B_k = \delta t A_k/2$ for conciseness, we have the finite difference equation

$$(I + B_1 + B_2 + B_3 + B_4)c^{n+1} = (I - B_1 - B_2 - B_3 - B_4)c^n + O(\delta t(\delta x + \delta z + \delta t^2)), \tag{E.9}$$

which must be solved for each timestep $c^1, \ldots, c^{N_T}$, starting from the initial conditions c^0. After integrating over N_T timesteps, the solution will be accurate to $O(\delta x+\delta z+\delta t^2)$. At any timestep, the values on the right hand side will be known, the values on the right to be determined. For a 1D problem, only the operators B_1 and B_3 would be present, and the left hand side could be expressed in terms of a pentadiagonal matrix, leading to an efficient solution. However, since additionally the terms B_2 and B_4 are present, direct solution will require iteration. A more efficient approach, first proposed by Douglas, Peaceman and Rachford to solve the heat equation, is the ADI method (Douglas Jr. and Peaceman, 1955), extended here to make use of the QUICK method.

Adding $(B_1 + B_3)(B_2 + B_4)c^{n+1}$ to both sides and omitting the discretisation error we have

$$\begin{aligned}(I + B_1 + B_3)(I + B_2 + B_4)c^{n+1} = {} & (I - B_1 - B_3)(I - B_2 - B_4)c^n \\ & +(B_1 + B_3)(B_2 + B_4)(c^{n+1} - c^n).\end{aligned} \tag{E.10}$$

By neglecting the term $(B_1 + B_3)(B_2 + B_4)(c^{n+1} - c^n)$, we can solve equation (E.10) using the two step scheme

$$\begin{aligned}(I + B_1 + B_3)c^{n+1/2} &= (I - B_2 - B_4)c^n, \qquad (x - \text{sweep}) \\ (I + B_2 + B_4)c^{n+1} &= (I - B_1 - B_3)c^{n+1/2}. \quad (z - \text{sweep})\end{aligned} \tag{E.11}$$

For the nth timestep, c^n is known. For the first part of the timestep, the 'x-sweep', we find the

intermediate solution $c^{n+1/2}$ by inverting the pentadiagonal matrix arising from $I + B_1 + B_3$ for each $j = 1, \ldots, N_Z$. Once $c^{n+1/2}$ is known, we perform the 'z-sweep' by solving the pentadiagonal matrix arising from $I + B_2 + B_4$ for each $i = 1, \ldots, N_X$ to determine c^{n+1}.

E.5 No-flux boundary conditions

The no-flux boundary conditions $\partial c/\partial x = 0$ and $\partial c/\partial z = 0$ are discretised by $c^n_{i+1,j} = c^n_{ij}$ and by $c^n_{i,j+1} = c^n_{ij}$. This results in $c^n_{i,-1}$ being replaced by $c^n_{i,0}$, c^n_{i,N_Z+1} being replaced by $c^n_{iN_Z}$, $c^n_{0,j}$ being replaced by $c^n_{1,j}$ and $c^n_{N_X+1,j}$ being replaced by $c^n_{N_X j}$ wherever they occur in the discretised system.

LIST OF REFERENCES

Albers, G. M., Tomkiewicz, R. P., May, M. K., Ramirez, O. E., and Rubin, B. K. (1996). Ring distraction technique for measuring surface tension of sputum: relationship to sputum clearability. *J. Appl. Physiol.*, 81(6):2690–2695.

Barlow, E. (2000). Modelling muco-ciliary transport in the lung. Master's thesis, School of Mathematics and Statistics, University of Birmingham.

Bartha, E. and Liron, N. (1988a). Slender body interactions for low Reynolds Numbers. Part 1. Body-wall interactions. *SIAM J. Appl. Math.*, 48:992–1008.

Bartha, E. and Liron, N. (1988b). Slender body interactions for low Reynolds Numbers. Part 2. Body-body interactions. *SIAM J. Appl. Math.*, 48:1262–1280.

Barton, C. and Raynor, S. (1967). Analytical investigation of cilia induced mucous flow. *Bull. Math. Biophys.*, 29:419–428.

Blake, J. R. (1971). A spherical envelope approach to ciliary propulsion. *J. Fluid Mech.*, 46:199–208.

Blake, J. R. (1972). A model for the micro-structure in ciliated organisms. *J. Fluid Mech.*, 55:1–23.

Blake, J. R. (1973a). Flow in tubules due to ciliary activity. *Bull. Math. Biol.*, 35:513–523.

Blake, J. R. (1973b). Mucus flows. *Math. Biosci.*, 17:301–313.

Blake, J. R. (1975a). Fluid flow in fields of resistance. *Bull. Austral. Math. Soc.*, 13:129–145.

Blake, J. R. (1975b). On the movement of mucus in the lung. *J. Biomechanics*, 8:179–190.

Blake, J. R. (1977). An active porous medium model for ciliary propulsion. *J. Theor. Biol.*, 64:697–701.

Blake, J. R. (1984). Mechanics of muco-ciliary transport. *IMA J. Appl. Math.*, 32:69–87.

Blake, J. R. (1999). Fluid mechanics of ciliary propulsion. *University of Birmingham Preprint*, 99/18.

Blake, J. R. and Fulford, G. R. (1984). Mechanics of muco-ciliary transport. *PCH Physico-Chemical Hydrodynamics*, 5:401–411.

Blake, J. R. and Gaffney, E. A. (2001). Modeling aspects of tracer transport in mucociliary flows. In Salathe, M., editor, *Cilia and mucus: from development to respiratory defense*, pages 291–302. Dekker, New York.

Blake, J. R. and Sleigh, M. A. (1974). A model for the micro-structure in ciliated organisms. *Biol. Rev.*, 49:85–125.

Blake, J. R. and Winet, H. (1980). On the mechanics of muco-ciliary transport. *Biorheology*, 17:125–134.

Boucher, R. C. (1994). Human airway ion transport. Part 1. *Am. J. Respir. Crit. Care Med.*, 150:271–281.

Boucher, R. C. (2003). Personal communication.

Boucher, R. C., Knowles, M. R., and Yankaskas, J. R. (2000). Cystic fibrosis. In Murray, J. F. and Nadel, J. A., editors, *Textbook of respiratory medicine*, pages 1291–1323. W. B. Saunders Co., Philadelphia.

Cartwright, J. H. E., Piro, O., and Tuval, I. (2004). Fluid-dynamical basis of the embryonic development of left-right asymmetry in vertebrates. *PNAS*, 101(19):7234–7239.

Childress, S. (1981). *Mechanics of swimming and flying*. Cambridge University, New York.

Chilvers, M. A. and O'Callaghan, C. (2000). Analysis of ciliary beat pattern & beat frequency uing digital high speed imaging: comparison with the photomultiplier & photodiode methods. *Thorax*, 55:314–317.

Chwang, A. T. and Wu, T. Y. (1975). Hydrodynamics of the low-Reynolds number flows. Part 2. the singularity method for Stokes flows. *J. Fluid Mech.*, 67:787–815.

Davis, S. S. and Dippy, J. E. (1969). The rheological properties of sputum. *Biorheology*, 6:11–21.

Devalia, J. L., Sapsford, R. J., Rusznak, C., Toumbis, M. J., and Davies, R. J. (1992). The effects of salmeterol and salbutamol on ciliary beat frequency of cultured human bronchial epithelial cells, in vitro. *Pulm. Pharmacol.*, 5(4):257–263.

Douglas Jr., J. and Kim, S. (1999). On accuracy of alternating direction implicit methods for parabolic equations. `http://www.ms.uky.edu/~math/MAreport/PDF/00-02.pdf`.

Douglas Jr., J. and Peaceman, D. (1955). Numerical solution of two-dimensional heat flow problems. *A. I. Chem. E. J.*, 1:505–512.

Ekberg-Jansson, A., Larsson, S., and Löfdahl, C.-G. (2001). Preventing exacerbation of chronic bronchitis and COPD. *BMJ*, 322:1259–1261.

Foliguet, B. and Puchelle, E. (1986). Apical structure of human respiratory cilia. *Bull. Eur. Physiopathol. Respir.*, 22:43–47.

Fulford, G. R. and Blake, J. R. (1986). Muco-ciliary transport in the lung. *J. Theor. Biol.*, 121:381–402.

Fung, Y. C. (1993). *Biomechanics, 2nd edition*. Springer, New York.

Gibbs, B. F., Schmutzler, W., Vollrath, I. B., Brosthardt, P., Braam, U., Wolff, H. H., and Zwadlo-Klarwasser, G. (1999). Ambroxol inhibits the release of histamine, leukotrienes and cytokines from human leukocytes and mast cells. *Inflamm. Res.*, 48(2):86–93.

Gray, J. and Hancock, G. J. (1955). The propulsion of sea-urchin spermatozoa. *J. Exp. Biol.*, 32:802–814.

Gueron, S. and Levit-Gurevich, K. (1999). Energetic considerations of ciliary beating and the advantage of metachronal coordination. *Proc. Natl. Acad. Sci.*, 96(22):12240–12245.

Gueron, S. and Liron, N. (1992). Ciliary motion modeling, and dynamic multicilia interactions. *Biophys. J.*, 63:1045–1058.

Gueron, S. and Liron, N. (1993). Simulations of three-dimensional ciliary beats and cilia interactions. *Biophys. J.*, 65:499–507.

Guggino, W. B. (2001). Cystic fibrosis salt/fluid controversy: In the thick of it. *Nature Medicine*, 7(8):888–889.

Hancock, G. J. (1953). The self-propulsion of microscopic organisms through liquids. *Proc. Roy. Soc. B.*, 217:96–121.

Happel, J. (1959). Viscous flow relative to arrays of cylinders. *A. I. Chem. E. J.*, 5(2):174–177.

Hasani, A., Toms, N., O'Connor, J., Dilworth, J. P., and Agnew, J. E. (2003). Effect of salmeterol xinafoate on lung mucociliary clearance in patients with asthma. *Respir. Med.*, 94(6):667–671.

International Commission on Radiological Protection and Measurements (1994). Human respiratory tract model for radiological protection—ICRP Publication 66. *Annals of the ICRP*, 24:1+.

Jayaraman, S., Song, Y., Vetrivel, L., and Verkman, A. S. (2001). Noninvasive *in vivo* flouorescence measurement of airway-surface liquid depth, salt concentration, and pH. *J. Clin. Invest.*, 107(3):317–324.

Johnson, R. E. (1980). An improved slender-body theory for stokes flow. *J. Fluid Mech.*, 99(2):411–431.

Joseph, D. D. (1990). *Fluid dynamics of viscoelastic liquids*. Springer, New York.

Keller, S. R. (1975). *Fluid mechanical investigations of ciliary propulsion*. PhD thesis, California Institute of Technology.

Kerem, E., Bistritzer, T., Hanukoglu, A., Hofmann, T., Zhou, Z., Bennett, W., MacLaughlin, E., Barker, P., Nash, M., Quittell, L., Boucher, R., and Knowles, M. R. (1999). Pulmonary epithelial sodium-channel dysfunction and excess airway liquid in pseudohypoaldosteronism. *N. Engl. J. Med.*, 341:156–162.

King, M. (1980). Relationship between mucus viscoelasticity and ciliary transport in guaran gel/frog palate model system. *Biorheology*, 17:249–254.

King, M., Agarwal, M., and Shukla, J. B. (1993). A planar model for muco-ciliary transport: effect of mucus viscoelasticity. *Biorheology*, 30:49–61.

King, M. and Macklem, P. T. (1977). Rheological properties of microliter quantities of normal mucus. *J. Appl. Physiol.*, 42:797–802.

Landry, J. S. and Eidelman, D. H. (2001). Airway surface liquid: End of the controversy? *J. Gen. Physiol.*, 117:419–422.

Leonard, B. P. (1979). A stable and accurate convective modelling procedure based on quadratic upstream interpolation. *Comput. Methods Appl. Mech. Eng.*, 19:459–98.

Lighthill, M. J. (1952). On the squirming motion of nearly spherical deformable bodies through liquids at very small reynolds numbers. *Comm. Pure Appl. Math.*, 5:109–118.

Lighthill, M. J. (1958). *Fourier analysis and generalised functions*. CUP, Cambridge.

Lighthill, M. J. (1975). Mathematical biofluiddynamics. In *SIAM Regional conference series in applied mathematics*. Society for Industrial and Applied Mathematics, Philadelphia.

Liron, N. (1978). Fluid transport by cilia between parallel plates. *J. Fluid Mech.*, 86(4):705–726.

Liron, N. (1996). Stokes flow due to infinite arrays of stokeslets in three dimensions. *Journal of Engng. Math.*, 30(1–2):267–297.

Liron, N. (2001). The LGL (Lighthill–Gueron–Liron) Theorem–historical perspective and critique. *Math. Meth. Appl. Sci.*, 24:1533–1540.

Liron, N. and Mochon, S. (1976a). The discrete-cilia approach to propulsion of ciliated micro-organisms. *J. Fluid Mech.*, 75:593–607.

Liron, N. and Mochon, S. (1976b). Stokes flow for a stokeslet between two parallel flat plates. *J. Engng. Math.*, 10:287–303.

Liron, N. and Rozenson, M. (1983). Muco-ciliary transport. *J. Submicrosc. Cytol.*, 15(1):317–321.

Lutz, R. J., Litt, M., and Charkrin, L. W. (1973). Physical-chemical factors in mucus rheology. In Gabelnick, H. L. and Litt, M., editors, *Rheology of biological systems*, pages 119–157. Charles C. Thomas, Springfield, IL.

Matsui, H., Davis, C. W., Tarran, R., and Boucher, R. C. (2000). Osmotic water permeabilities of cultured, well-differentiated normal & cystic fibrosis airway epithelia. *J. Clin. Invest.*, 105(10):1419–1427.

Matsui, H., Grubb, B. R., Tarran, R., Randell, S. H., Gatzy, J. T., Davis, C. W., and Boucher, R. C. (1998a). Evidence for periciliary liquid layer depletion, not abnormal ion composition, in the pathogenesis of cystic fibrosis airways disease. *J. Clin. Invest.*, 95(7):1–20.

Matsui, H., Randell, S. H., Peretti, S. W., Davis, C. W., and Boucher, R. C. (1998b). Coordinated clearance of periciliary liquid and mucus from airway surfaces. *J. Clin. Invest.*, 102(6):1125–1131.

Meyer, F. A. and Silberberg, A. (1980). The rheology and molecular organization of epithelial mucus. *Biorheology*, 17:163–168.

NAG (1993). *The NAG Fortran library manual, mark 16*. The Numerical Algorithms Group Limited.

Nonaka, S., Shiratori, H., Saijoh, Y., and Hamada, H. (2002). Determination of left-right patterning of the mouse embryo by artificial nodal flow. *Nature*, 418:96–98.

Pavia, D., Bateman, J. R., Lennard-Jones, A. M., Agnew, J. E., and Clarke, S. W. (1986). Effect of selective and non-selective beta blockade on pulmonary function and tracheobronchial mucociliary clearance in healthy subjects. *Thorax*, 41(4):301–305.

Poole, P. J. and Black, P. N. (2001). Oral mucolytic drugs for exacerbations of chronic obstructive pulmonary disease: systematic review. *BMJ*, 322:1271–1274.

Pozrikidis, C. (1992). *Boundary integral and singularity methods for linearized viscous flow*. Cambridge University, Cambridge.

Puchelle, E., Herard, A. L., and Zahm, J. M. (1998). Airway mucociliary epithelium injury and repair. In Baum, G. L., Priel, Z., Roth, Y., Liron, N., and Ostfeld, E. J., editors, *Cilia, Mucus, and Mucociliary Interactions*, pages 203–217. Dekker, New York.

Puchelle, E., Zahm, J. M., Duvivier, C., Didelon, J., Jacquot, J., and Quemada, D. (1985). Elasto-thixotropic properties of bronchial mucus and polymer analogs. *Biorheology*, 22:415–423.

Puchelle, E., Zahm, J. M., and Quemada, D. (1987). Rheological properties controlling mucociliary frequency and respiratory mucus transport. *Biorheology*, 24:557–563.

Quemada, D. (1984). Towards a unified model of elasto-thixotropy of biofluids. *Biorheology*, 21:423–436.

Quinton, P. M. (1994). Viscosity versus composition in airway pathology (editorial). *Am. J. Respir. Crit. Med.*, 149:6–7.

Raptis, A. and Perkidis, C. (1973). A mathematical model of the cilia for pharyngeal epithelium of the frog. *J. Biomechanics*, 16(3):235–236.

Reid, L. (1973). Properties of mucus. *The Scientific Basis of Medicine Annual Reviews*, 149:130–150.

Rivera, J. A. (1962). *Cilia, ciliated epithelium, and ciliary activity*. Pergamon, New York.

Rochat, T., Lacroix, J. S., and Jornot, L. (2004). N-acetylcysteine inhibits Na^+ absorption across human nasal epithelial cells. *J. Cell Physiol.*, 201(1):106–116.

Rogers, D. F. (2004). Airway mucus hypersecretion in asthma: an undervalued pathology? *Curr. Opin. Pharm.*, 4:241–250.

Rogers, D. F. (2005). Mucociliary disfunction in COPD: effect of current pharmacotherapeutic options. *Pulm. Pharm. Ther.*, 18:1–8.

Ross, S. M. (1971). *A wavy wall analytic model of muco-ciliary pumping*. PhD thesis, John Hopkins University.

Salathe, M., O'Riordan, T. G., and Wanner, A. (1996). Treatment of muco-ciliary disfunction. *Chest*, 110:1048–1057.

Salathe, M., O'Riordan, T. G., and Wanner, A. (1997). Mucociliary clearance. In Crystal, R. G., West, P. J., Barnes, P. J., and Weibel, E. R., editors, *The Lung: Scientific Foundations*, pages 2295–2308. Lippincott–Raven, Philadelphia.

Sanderson, M. J. and Sleigh, M. A. (1981). Ciliary activity of cultured rabbit tracheal epithelium: beat pattern and metachrony. *J. Cell Sci.*, 47:331–341.

Shibuya, Y., Wills, P. J., and Cole, P. J. (2003). Effect of osmolality on mucociliary transportability and rheology of cystic fibrosis and bronchiectasis sputum. *Respirology*, 8(2):181–185.

Silberberg, A. (1983). Biorheological matching: Mucociliary interaction and epithelial clearance. *Biorheology*, 20:215–222.

Sleigh, M. A. (1962). *The biology of cilia and flagella*, page 5. Pergamon, Oxford.

Sleigh, M. A. (1977). The nature and action of respiratory tract cilia. In Brain, J. D., Proctor, D. F., and Reid, L. M., editors, *Respiratory defense mechanisms Part I*, pages 247–288. Dekker, New York.

Sleigh, M. A. and Blake, J. R. (1975). Hydromechanical aspects of ciliary propulsion. In Wu, T. Y., Brokaw, C. J., and Brennen, C., editors, *Swimming and flying in nature*, pages 185–210. Plenum, New York.

Sleigh, M. A., Blake, J. R., and Liron, N. (1988). The propulsion of mucus by cilia. *Am. Rev. Respir. Dis.*, 137:726–741.

Smith, J. J., Travis, S. M., Greenberg, E. P., and Welsh, M. J. (1996). Cystic fibrosis airway epithelia fail to kill bacteria because of abnormal airway surface liquid. *Cell*, 85:229–236.

Tarran, R., Grubb, B. R., Parsons, D., Picher, M., Hirsh, A. J., Davis, C. W., and Boucher, R. C. (2001). The CF salt controversy: in vivo observations and therapeutic approaches. *Mol. Cell*, 8(1):149–158.

Taylor, G. I. (1951). Analysis of the swimming of microscopic organisms. *Proc. Roy. Soc. Lond.*, A209:447–461.

Taylor, G. I. (1953). Dispersion of soluble matter in solvent flowing slowly throught a tube. *Proc. Roy. Soc. Lond.*, A219:186–203.

Toskala, E. (1994). *Normal and pathological respiratory cilia. An experimental and clinical study with special reference to scanning electron microscopy*. PhD thesis, University of Kuopio.

Winet, H., Yates, G. T., Wu, T. Y., and Head, J. (1984). On the mechanics of muco-ciliary flows III. Flow-velocity profiles in frog palate mucus. *J. Appl. Physiol.:Respirat. Environ. Exercise Physiol.*, 56(3):785–794.

Yoneda, K. (1976). Mucous blanket of rat bronchus: An ultrastructural study. *Am. Rev. Respir. Dis.*, 114:837–842.

Ziegler, G. R. and Foegeding, E. A. (1990). The gelation of proteins. *Adv. in Food and Nutr. Res.*, 34:203–298.